Structure and Properties of Cobalt Ferrite Nanoparticles, Bulk and Thin Films

A thesis submitted for the degree of

DOCTOR OF PHILOSOPHY

in PHYSICS

by

RAVI BABU KANCHARLA

(Reg. No: 13PHPH11)



SCHOOL OF PHYSICS

UNIVERSITY OF HYDERABAD

HYDERABAD – 500 046, INDIA

NOVEMBER 2019



DECLARATION

I, RAVI BABU KANCHARLA hereby declare that the thesis entitled "Structure and

Properties of Cobalt Ferrite Nanoparticles, Bulk and Thin Films" submitted by me for the

award of the degree of Doctor of Philosophy in Physics is done under the supervision of

Professor RAJENDER SINGH, School of Physics, University of Hyderabad, India, is a

bonafide research work and is free from plagiarism. I hereby declare that it has not been

submitted previously partially or fully to this University or any other university or institution

for the award of any degree or diploma.

Ravibabu Kancharla

Reg. No: 13PHPH11

Place: Hyderabad

Date:



CERTIFICATE

This is to certify that the research work presented in the thesis entitled "Structure and Properties of Cobalt Ferrite Nanoparticles, Bulk and Thin Films" bearing the registration no 13PHPH11 in fulfillment of requirements for the award of DOCTOR OF PHILOSOPHY (PhD) in Physics is a bonafide work carried out by RAVI BABU KANCHARLA under my supervision and guidance.

This thesis is free from plagiarism and has not been submitted previously in part or in full to this University or any other University or institution for the award of any degree or diploma. Further, the student has the following publications before submission of the thesis for adjudication.

- 1) Effect of RF Power on Structural, Magnetic, and Optical Properties of CoFe₂O₄ Thin Films, Kancharla Ravibabu and R. Singh, *Journal of Superconductivity and Novel Magnetism* (2018) 31:4029–4037 https://doi.org/10.1007/s10948-018-4680-1
- 2) Kancharla Ravibabu and R. Singh, "Morphology of Co-ferrite synthesized by co-precipitation method" at International Conference on Electron Microscopy EMSI-2014 during July 9-11, 2014 at University of Delhi, Delhi. (Poster presentation)
- 3) Kancharla Ravibabu and R. Singh, "Structure and magnetic properties of cobalt ferrite thin films synthesized by RF magnetron sputtering" International Conference on Magnetic Materials and Applications (ICMAGMA-2015) during Decrember 2-4, 2015 (Poster presentation)

Further, the student has passed the following course towards the fulfillment of course work required for Ph.D.

S. No.	Course code	Name	Credits	Pass/Fail
1	PY801	Advanced quantum mechanics	4	Pass
2	PY803	Advanced Statistical mechanics	4	Pass
3	PY804	Advanced electromagnetic theory	4	Pass
4	PY821	Research Methodology	4	Pass

Prof. Rajender Singh (Thesis Supervisor) School of Physics, University of Hyderabad.

Dr. Ashok Vudayagiri (Co-Supervisor) School of Physics, University of Hyderabad.

Dean, School of Physics, University of Hyderabad.

Place: Hyderabad

Date:

Dedicated to

My Parents and Family

Acknowledgements

I thank and praise *Almighty God* the Father, the *Son* and the *Holy Spirit* for *their* constant guidance in my life.

Coming to family members, I am grateful to my father and mother for their love and encouragement throughout my long studies. Thank you my dear mother for all the sacrifices to brought up me as I am today. Thank you my dear father you have endured immense troubles and inconveniences, I deeply feel that all these works are due to your blessings.

I am grateful to my elder sister Nagendram and my younger sister Suneetha and my brother-inlaw Ch. David Sharon Raju for their support and encouragement.

I thank my supervisor, Prof. Rajender Singh, for his relentless excellent guidance throughout the Ph. D program and for taking the time out of his busy schedules to correct and proof read this manuscript.

I am thankful to the former Deans and the present Dean for providing necessary facilities for carrying out my research work.

I would also like to thank DRC member and co-supervisor Dr. Ashok Vudayagiri for his help and generous support. I am also grateful to my DRC members Prof. S V S Nageswara Rao, Dr. Venkataiah Gorige and Prof. P.K. Suresh.

My thanks to the office staff, School of Physics, Mrs. Deepika, Mrs. Sailaja, Mrs. Vijaya Lakshmi, Mr. Sudarshan, Mr. Shekar, and Mr. K. Srinivas. I thank Ms. Sunitha (FESEM) and Mr. Naresh (XRD), NRC staff, Y. Jyothi and Mr. Laksminarayana for accepting to help with my experiments, CIL staff, Dr. S. Manjunath, Mr. Suresh, Mr. Pavan kumar, Mr. Sudhakar, Mr. Rajesh, Mr. Nagaraju, and CFN staff, S. Pankaj, Mr. Durgaprasad for their help and technical support. I also thank Mr. Sambasivsrao, Mr. Mantoo Kumar, Mr. Giri Bahadur and Mr. Sai for providing Liquid Nitogen for low temperature experiments.

I would like to thank University of Hyderabad, for BBL Fellowship for financial assistance.

I am thankful to the IGML and Computer center.

I am thankful to my fellow research students Pundareekam Goud, Andru Joseph, Shihab, Joshi, Binoy Krishna, Robertson, Sivarama Krishna, Nabil Abdlmomen Saad, B. Prakash, Y. Rajesh, Avisek, Naresh, Dhanunjaya Rao and Chinna Kandula. We have shared joy, laughter, excitement, frustration and most importantly love.

I thank my seniors, Dr. G.Thirupathi, Dr. Jasmeet Kaur, Dr. A. Ramesh, Dr. M. Venkaiah, Dr. P. Sandhyarani, and Dr. Saipriya and Dr. M. Padmavathi. I thank my juniors, Nisha Gautam and Atiya farheen for their support and lively atmosphere in the lab.

I thank my brother K. Nagendra Rao for financial help and P. Veeraswami for moral support and help.

Among other friends: Dr. B. Kishore Babu, Sk. Mastana, Manikya Rao, Jaya Rao, Dr. V. Ramesh, for your loving help. I thank, Dr. Sheshagiri Rao, Dr. Suneel and Dr. Venkata Rao for their inspiration and encouragement.

Close friends and loved ones Dr. M. Rama Krishna, K. Somaiah, Dr. G. Venkata Ramana and Dr. Neela Kishore Babu for their financial support.

I am thankful to all those I have not been able to name here, but have contributed to this work in various capacities. Thank you every body.

(Ravibabu Kancharla)

Table of Contents

List of Publications	169
Chapter 5 Summary and Conclusions	163
References	162
4.4 Studies on Co _{0.75} Cu _{0.25} Fe ₂ O ₄ thin films.	133
4.3 Effect of argon gas pressure on structure and properties of CoFe ₂ O ₄	
4.1 Effect of RF Power on structure and properties of CoFe ₂ O ₄	
Chapter 4 Structure and properties of CoFe ₂ O ₄ and Co _{0.75} Cu _{0.25} Fe ₂ O ₄ thin films 4.1 Effect of RF Power on structure and properties of CoFe ₂ O ₄	10
References	90
3.4 Effect of annealing temperature on structural, magnetic and dielectric properties of CoFe ₂ O ₄	
3.3 Structural, magnetic and dielectric properties of cobalt-copper ferrites Co _{1-x} Cu _x Fe ₂ O ₄ (x=0.0-1.0)	
3.1 CoFe ₂ O ₄ and Co _{1-x} Cu _x Fe ₂ O ₄ (x=0.0,0.2, 0.25 and 0.4) nanoparticles	
nanoparticles and bulk ferrites	
Chapter 3 Structure and properties of cobalt ferrite and copper doped cobalt ferrite	
References	20
2.9 Dielectric spectrometer	19
2.8 Profilometry	
2.7 Spectrophotometer	
Structural Characterization techniques Structural Characterization techniques Structural Characterization techniques	
2.4 CoFe ₂ O ₄ and Cu _{0.25} Co _{0.75} Fe ₂ O ₄ thin film preparation	
2.3 Target preparation	
2.2 Bulk and nanoparticles synthesis	12
2.1 RF-sputtering	1
Chapter 2 Synthesis of Nanoparticles, Bulk and Thin Films and Characterization Tec	chnique
References	
1.8 Thesis organization	
1.7 Objectives of the present work	
1.5 Literature survey of cobalt ferrite nanoparticles	
1.4 Optical properties	
1.3 Dielectric properties	
1.2 Superexchange interaction	
1.1 Structure and properties of CoFe ₂ O ₄	
Chapter 1 Introduction	
Abstract	
Abstract	
Table of contents	
Acknowledgements	v

Abstract

A great need for developing new multi-functional materials operating at high frequency (radio frequency) applications is demanding a better understanding of ferrimagnetic materials. In the present study, cobalt ferrite materials were synthesized in nanoparticles, bulk and thin film form by co-precipitation method and RF magnetron sputtering, respectively. The materials of choice, Cobalt ferrite (CoFe₂O₄), copper doped cobalt ferrites, $Co_{1-x}Cu_xFe_2O_4$ (x = 0, 0.2, 0.25, and 0.4) and cobalt-copper ferrites, $Co_{1-x}Cu_xFe_2O_4$ (x = 0.0, 0.2, 0.25, 0.4, 0.9 and 1.0) nanoparticles were synthesized using co-precipitation method. The synthesized samples were heat treated at various temperatures to understand its effect on structure and properties of materials. The magnetization and dielectric measurements on the samples heat treated at various temperatures were carried out to optimize these properties of the materials. The crystal structure was verified by X-ray diffraction and Rietveld refined XRD patterns show single phase spinel structure with Fd-3m space group. Surface morphology and microstructure was studied by employing FE-Scanning Microscopy (FESEM) and Transmission Electron Microscopy (TEM). Unusual features in magnetic hysteresis loops of nanoparticles and bulk materials were observed. The dielectric constant and the loss tangent decreases rapidly with increasing frequency, and then reaches almost constant value at high frequencies. CoFe₂O₄ nanoparticles of size 18 nm heated at 600 °C for 3 hours gives high saturation magnetization (M_s) of 137 emu/g and coercivity (H_c) of 582 G. CoFe₂O₄ pellets heated at 1200 °C for 4 h show very high M_s of 175 emu/g. The nanoparticles of $(Co_{0.8}Cu_{0.2}Fe_2O_4)$ annealed at 600 °C exhibit high H_c of 1217 G and M_s of 119 emu/g. CuFe₂O₄ pellets heated at 1200 °C exhibit high dielectric constant of 1015 at 40 MHz with low loss tangent of 0.112. This can be used as a filling material in capacitors. As-prepared $CoFe_2O_4$ nanoparticles of size 17 nm show a high H_c of 2875 G at RT which can be used in data storage applications. At 100 K, cobalt ferrite pellet heated at 600 °C show a very high H_c = 11.4 kG. CoFe₂O₄ pellet annealed at 1200 °C has dielectric constant of 19 between 1MHz to 40 MHz and very low tangent loss (0.021-0.028). This material can be used for insulating material for practical applications in high-frequency electrical circuits.

Cobalt ferrite (CoFe₂O₄) thin films were deposited on glass substrates under different sputtering conditions i.e. RF power variation, deposition time (film thickness) and argon gas pressure. Asdeposited films were amorphous and were post-annealed at 500°C for 3 h. The 164 nm (CFF-80) thick cobalt ferrite film exhibit M_s of 274 emu/cc which is equal to the M_s of bulk CoFe₂O₄

target. The 410-nm-thick annealed cobalt ferrite film deposited at 8 mTorr can be used for temperature sensor applications in the temperature range of 5-350 K.

The $Co_{0.75}Cu_{0.25}Fe_2O_4$ target show low H_c of 57 G and M_s of 293 emu/cm³. $Co_{0.75}Cu_{0.25}Fe_2O_4$ thin films were deposited onto quartz substrates at room temperature. The effect of sputtering conditions and post-annealing on structural, microstructural, magnetic and optical properties were investigated to understand the structure-property relation. Transmission electron microscopy (TEM) was used to correlate the nanostructure to the magnetic properties of nanoparticles and thin films. The surface morphology and elemental composition was investigated using field emission scanning electron microscopy (FESEM). The grazing incidence X-ray diffractometer was used to investigate structure. Magnetic properties were determined using vibrating sample magnetometer (VSM) and physical property measurement system (PPMS). Thin films of $Co_{0.75}Cu_{0.25}Fe_2O_4$ show high M_s of 250 emu/cm³ when annealed at 1000 °C with H_c of 1500 G. The H_c of 2670 G is obtained when annealing of the film is done at 800 °C. The M_s of thin films of $Co_{0.75}Cu_{0.25}Fe_2O_4$ increases with increase in RF power (i.e. with increase in film thickness) from 30 to 60 W. The annealed film deposited at 50 W exhibit high H_c of 3866 Oe and M_s of 243 emu/cc. The films grown at 40 W show H_c of 3449 Oe and M_s of 174 emu/cc. These films can be used for data storage applications.

The thin films of doped and undoped cobalt ferrite have 60- 85% optical transmittance. The optical band gap values of the doped and undoped cobalt ferrite films is between 1.90- 2.37 eV. The highest band gap value of 2.37 eV is obtained for $Co_{0.75}Cu_{0.25}Fe_2O_4$ film deposited on quartz substrate using 40 W RF power at 12 mTorr argon gas pressure and annealed post-deposition at $600^{\circ}C$ for 3 hrs.

Chapter 1

Introduction

The crystal structure and physical properties of cobalt ferrite (CoFe₂O₄) are discussed in this chapter. The superexchange interaction in ferrites and the dielectric properties are discussed. The literature on nanoparticles and thin films of cobalt ferrite is discussed. The objectives of the present work and thesis organization is presented.

1.1 Structure and properties of CoFe₂O₄

Ferrites are important class of magnetic materials due to their specific magnetic and electric properties. The magnetic parameters of the magnetic materials namely saturation magnetization (M_s) , coercivity (H_c) , and remanence (M_r) which are important can be measured from the magnetization hysteresis (M vs. H) loop, as depicted in Fig. 1.1.

1.1.1 Structure of CoFe₂O₄

CoFe₂O₄ is a member in the family of spinel ferrites. The spinel structure is an interesting one and has been widely studied because of the interesting physical properties exhibited by a number of compounds with this structure. Spinels commonly contain divalent and trivalent cations in a 1:2 ratio in a lattice structure built of divalent anions. An example is the mineral spinel itself, MgAl₂O₄. The compounds of spinel family have a general molecular formula MFe₂O₄ where the divalent M²⁺ and trivalent Fe³⁺ cations occupying tetrahedral (A) and octahedral (B) sites of the fcc lattice formed by O²⁻ ions. In this unit cell, the 32 O²⁻ anions are packed as already described and the 8 A and the 16 B cations fill a total of 24 of the 32 octahedral and 64 tetrahedral sites. The filling is systematic and there are two primary ways in which it occurs. In a normal spinel all the 8 divalent metal cations (A) fill tetrahedral holes and all the 16 trivalent metal cations (B) fill octahedral holes. On the other hand, if 8 of 16 trivalent metal cations (B) fill 8 tetrahedral holes, and remaining half trivalent cations fill 8 octahedral holes, and all the divalent metal cations (A) fill the remaining 8 spinel octahedral holes, the structure is called an inverse spinel. Many compounds are a hybrid of the normal and inverse spinel structures.

1.1.2 Magnetism of CoFe₂O₄

In ferrites the novel properties result from the distribution of different cations among the tetrahedral and octahedral sites [1-2]. CoFe₂O₄ is important because of its high magnetic anisotropy, high coercivity, high electrical resistivity and high thermal and chemical stability [3].

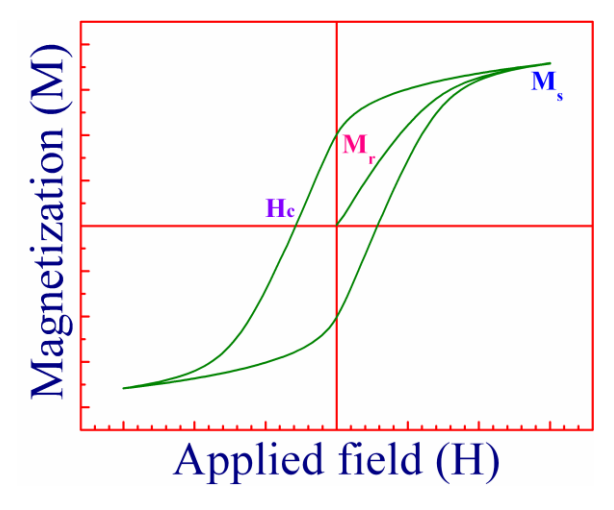


Fig. 1.1. Typical magnetization hysteresis loop of CoFe₂O₄.

The composition and microstructure of ferrite materials greatly influence their physical properties. Altering composition by doping of metal ions into cobalt ferrite is the best technique to change its physical as well as the chemical properties. The substitution of Co²⁺ in cobalt ferrite by other transition metals can alter its properties which can be tuned for a specific application. One of the important spinel ferrites is CuFe₂O₄ because it shows electrical switching and varying semiconducting properties (Sawant & Patil 1982). Copper ferrite is a complete inverse spinel with tetragonal phase at low temperature and exhibits a transition from tetragonal to cubic symmetry at high temperature. The hard and soft magnetic properties based on hysteresis loop are promising for recording technologies and for a variety of applications in biomedical and electronic devices (Ross 2001, Wood et al 2002, Tartaj et al 2003, Bader 2006). Therefore, copper substitution produces great potential for enhancing the magnetic and dielectric properties of cobalt-copper ferrites. Many studies [4-7] have reported on high amounts of substitution, where an increase in Cu content has resulted in a decrease of magnetization. Samavati et al. [7] made attempt to improve and optimize the antibacterial activities of cobalt ferrite nanoparticles by substitution of Co²⁺ with Cu²⁺.

Since ferrimagnetic materials are described as interpenetration of two sub lattices with unequal magnetic moments in direct opposition, the net magnetic moment, μ , of CoFe₂O₄ is equal to the vector sum of spin moments of cations in the A and B sub-lattices. Because the $Fe_{A,B}^{3+}$ (5 μ B) cations are in direct opposition in the antiferromagnetic A-O-B coupling, the net spin magnetic moment μ is equal the moment of Co²⁺. Therefore, for CoFe₂O₄ is μ CoFe₂O₄ = 3 μ B. The

magnetization of the copper doped CoFe₂O₄ decreases when Co²⁺ ions are substituted by less-magnetic Cu²⁺ ions. When all of Co²⁺ cations occupy tetrahedral holes and all Fe³⁺ occupy octahedral holes as in case of a *normal spinel*, μ increases dramatically to 7 μ _B [8].

1.2 Superexchange interaction

In case of ferromagnets, the atoms had to be very close for atomic orbital overlap, allowing application of the Pauli principle. In ferrimagnetic materials the material is so structured that all the elementary dipoles (magnetic ions) are separated by an intermediate ion (too far for direct overlap), a process called superexchange can occur. Superexchange is a mechanism by which coupling of spins occurs between nearest neighbor magnetic ions mediated by a non-magnetic ion. Even when the wave functions of the two magnetic ions do not overlap, such materials show appreciable spontaneous magnetization. Two magnetic ions interact with the mediation of non-magnetic ion.

1.3 Dielectric properties

All dielectric materials are insulators. The distinction between dielectric material and insulator lies in the applications of these materials and on the polarizing capacity of electrical charges. These materials are used to store electrical energy with minimum dissipation of power. In spite of being poor conductor of electricity or perhaps because of it, the dielectrics are most interesting and useful electrical engineering materials. The dielectric materials are characterized by dielectric constant, dielectric loss, dielectric strength and resistivity. Ferrites are considered as good dielectricmaterials which have many applications in high–frequency electrical devices that employ at microwave and radio-wave frequency-range [9] since they show very small conductivity [10]. Therefore, ferrites are used in many electromagnetic devices that employ at microwave frequencies. Modification in the microwave performance can be remarkably brought by varying the applied bias field [11].

1.3.1 Dielectric permittivity and loss tangent

Dielectric properties such as polarization, dielectric constant and loss tangent depends on frequency of the applied field and temperature. Under dc fields, the electric flux density D is proportional to the applied electric field E. Dielectric properties may be defined by the behavior of the material inserted between two plates a parallel plate capacitor. When a dielectric is subjected to an alternating field the polarization P and displacement D varies periodically with time. The time varying electric field E can be represented by

$$E(r,t) = E_0 \cos \omega t \tag{1.1}$$

The polarization and displacement might lag behind the driving field E(r,t) by introducing a phase angle δ ; we have

$$D = D_0 \cos(\omega t - \delta) = D_0 \cos\delta \cdot \cos\omega t + D_0 \sin\delta \cdot \sin\omega t = D_1 \cos\omega t + D_2 \sin\omega t \qquad (1.2)$$

As we know that

$$D = \in E(r, t) = (\in' + i \in'') E(r, t)$$
(1.3)

Introduction of phase angle is a perfectly satisfactory way of describing the phase lag. Electric field can be represented as the real part of a complex field.

$$E(r,t) = E_0 e^{-i\omega t} \tag{1.4}$$

Therefore, the two frequency dependent dielectric constants can be given as

$$\epsilon' = \frac{D_1}{E_0} = \frac{D_0}{E_0} \cos \delta \tag{1.5}$$

$$\epsilon'' = \frac{D_2}{E_0} = \frac{D_0}{E_0} \sin \delta \tag{1.6}$$

The dielectric loss tangent is defined as

$$Tan \,\delta = \frac{\epsilon''}{\epsilon'} \tag{1.7}$$

Since ϵ' and ϵ'' are frequency dependent, the phase angle δ is also frequency dependent.

1.4 Optical properties

When light is incident on matter, it interacts with the electronic structure of the material. If the frequency of the incident light matches with the band gap of the material, the incident EM radiation of wavelength equivalent to the band gap is absorbed. This occurs because the valence electrons of the material absorb the photon energy and move to higher energy states. Hence absorption occurs at various frequencies. The minimum photon energy required to excite and/or ionize a solids valence electrons is called absorption edge or absorption threshold. Reflection or Transmission occurs when the energy of the incident electromagnetic radiation does not match with the band gap energy of the material.

1.4.1 Direct and indirect band gap materials

The fundamental absorption is of two types. One is direct absorption without involving phonons and indirect absorption which involves phonons. If the minimum of the conduction band and the maximum of the valence band occur at the same value of k, the material is called direct band gap material. Absorption of light in these materials excites the electrons from the valence band to the conduction band directly without change in k (and, the momentum). In an indirect band

gap material the minimum of the conduction band and the maximum of the valence band do not occur at the same value of k. The change in momentum of electron generates electron transitions. For example in direct band gap semiconductors energy is released in the form of light during electron transition from conduction band to the valence band. In indirect band gap semiconductor non-radiative transitions occur through the defect states which lie inside the band gap and results in heating of the lattice.

The band gap values of direct band gap material can be estimated by using the well-known Tauc's formula [12],

$$\alpha h \nu = A \left(h \nu - E_g \right)^{1/2} \tag{1.8}$$

where A is constant, α is the optical absorption coefficient, and hv is the energy of the incident photon. The plots of $(\alpha hv)^2$ versus (hv) would be a straight line over a range of photon energies indicating the direct band gap transitions. The extrapolation of the straight-line graphs to $(\alpha hv)^2 = 0$ gives the value of the optical gap.

1.5 Literature survey of cobalt ferrite nanoparticles:

The nanocrystalline magnetic particles having a high surface to volume ratio show unique physical properties together with magnetic properties different from their bulk materials of the same chemical formula. Such properties would be affected highly by the particle size distribution and agglomeration of particles. The magnetic nature of the nanoparticles relies mainly on their size, structure, freshness, homogeneity and stability. The advantages of nanoferrites are due to their higher efficiency and lower cost and ease of manufacturing than other materials [13-14]. Magnetic nanoparticles research has increased over recent times because of their use in wide range of diagnosis and treatment such as genetic defect screening, biochemical field to enhanced delivery, and toxicity cleansing [15-18], targeted vectors for gene therapy, contrast agents for MR imaging and drug delivery [16,19], magnetic cell sorting schemes in electrochemical cell and spintronic devices [20]. Nanoparticles of cobalt ferrite can be used for purification of RNA and DNA, cell separation, targeted drug delivery, MRI [21], magnetic hyperthermia therapy for treatment of cancer [22] and biosensors [23].

Nanoparticles of cobalt ferrite (CoFe₂O₄) have also attracted great interest because their dielectric properties exhibit size dependence and change with frequency and measuring temperature [24]. Dielectric constant [25] and loss tangent (tan δ) [26] are the fundamental variables used to find the dielectric properties of CoFe₂O₄ nanoparticles. The above parameters

depend on three fundamental issues: (i) the phenomenon of ionic and dipolar relaxation, (ii) atomic (or ionic) polarization resulting due to displacement of atoms under vibration, and (iii) electronic resonance at high frequencies. Ionic and dipolar relaxation dominate over other two factors [27].

1.6 Literature survey of CoFe₂O₄ and Cu_{0.25}Co_{0.75} Fe₂O₄ thin films

Thin films of Cobalt ferrite possess potential in many applications including magnetic recording media with high density magneto—optical recording and micro-electromechanical system devices [28]. Cobalt ferrite film had been fabricated by different fabrication method. Cobalt ferrite thin film fabricated by sol—gel method on thermally oxidized Si wafer showed no preferred growth direction [29]. Also Cobalt ferrite film deposited by RF sputtering method on Si wafer and post—annealing at different temperature [30] and in situ annealing [31] showed no preferred direction. However Co_xFe_{2-x}O₄ film prepared by RF sputtering on quartz substrate and post—annealed showed different preferred direction [32]. Epitaxial CoFe₂O₄ thin film were deposited on (0 0 0 1) sapphire substrate by Pulsed laser deposition (PLD) technique by Yin et al. [33]. In this paper, structural property of CoFe₂O₄ thin film prepared by PLD on silicon substrate is reported.

The CFO has been used to fabricate active tunnel barriers (heterostructures) for spin filtering [34], resistive switching [35], and as coupling ferromagnetic and ferroelectric thin film layers [36]. The magnetic and optical studies on ferrites are reported in the literature [37-38]. The band gap of 2.55 eV for CoFe₂O₄ ferrite films deposited on (001)- oriented LaAlO₃ is reported by Ravindra et al. [39]. Whereas, band gap of Zinc ferrite is reported to be around 2.2 eV by Sultan et al. [40].

Because of their large magnetostriction epitaxial CoFe₂O₄ films have great potential applications for multiferroic devices [41-42]. For all the applications mentioned above magnetic anisotropy and coercivity are basic parameters which need to be studied. Different techniques were used to fabricate cobalt ferrite thin films. Cobalt ferrite films were fabricated by Sol-gel chemical method [43]. The maximal coercivity obtained by this method is 2720 Oe, when films were annealed at 950 °C. But after heating at such high temperature (950 °C), the grain size is extremely large to be used for high density magnetic recording. Kitamoto et al. [44] fabricated Co_xFe_{3-x}O₄ films at 90 °C by spin spray ferrite plating method. The coercivity obtained by this method reached 3 kOe for the Co_{0.43}Fe_{2.57}O₄ film of thickness 60 nm. Cobalt ferrite films

prepared using chemical methods exhibit low values of coercivity. Therefore, physical vapour deposition methods were used by many research groups in order to achieve high coercivity of cobalt ferrite thin films. Ding et al. deposited 90nm-thick-film on a silicon wafer by rf-sputtering using a 5 wt % SiO₂/CoFe₂O₄ target and post-annealed at 1000 °C. The annealed film exhibit very high perpendicular coercivity of 7.4 kOe and low in-plane coercivity of 4.4 kOe and has no magnetic texture and preferential crystallographic texture [30]. But the films deposited using the pure Co-ferrite target exhibited low coercivity. Jae-Gwang Lee et al. fabricated CoFe₂O₄ thin films at different substrate temperatures and post-annealing temperatures by RF magnetron sputtering [31]. The measured values of coercivity in perpendicular and in-plane directions were 3.873 and 2.70 kOe. Y.C. Wang et al. [28] reported the effect of film thickness, grain size and annealing temperature on magnetic properties of RF sputtered cobalt ferrite films deposited on a (100)-SiO₂ substrate showed high coercivity of 9.3 kOe for a 50nm-thick-film post-annealed at 900 °C. They explained the reason for large coercivity due to the presence of large lattice strain in the films. Gu et al. [32] reported coercivity of as-sputtered cobalt ferrite films is about 2 kOe and a maximal coercivity of 2.8 kOe and M_s of 455 emu/cm³ was obtained for Co_{0.5}Fe_{2.5}O₄ films annealed at 400 °C. Finally, Chambers et al. [45] deposited single-crystal CoFe₂O₄ films on MgO (0 0 1) substrates by oxygen-plasma-assisted molecular beam epitaxy (OPA-MBE). The measured moment per unit volume is 250 emu/cm³, and the saturation magnetization for films in the 1000 Å film thickness range is ~ 60% of that of bulk cobalt ferrite.

1.7 Objectives of the present work

The primary objectives of this research are:

- 1. To synthesize nanoparticles of cobalt ferrite by co-precipitation method.
- 2. To obtain bulk ferrite material by sintering CoFe₂O₄ nanopowder at different temperatures for densification.
- 3. To deposit thin film of ferrite by RF-magnetron sputtering.

Specific objectives

1. To synthesize bulk, nanoparticles of $CoFe_2O_4$, $Co_{1-x}Cu_xFe_2O_4$ (x=0, 0.2, 0.25 and 0.4) and $Co_{1-x}Cu_xFe_2O_4$ (x=0, 0.2, 0.25, 0.25, 0.25, 0.25 and 1.0) and thin films of $CoFe_2O_4$ and $Cu_{0.25}Co_{0.75}Fe_2O_4$.

- 2. To characterize bulk, nanoparticles and thin films of ferrites for their structure, composition and morphology.
- 3. To study the magnetic and dielectric properties of the bulk and nanoparticles of the synthesized ferrites.
- 4. To study the structural, magnetic and optical properties of the synthesized ferrite thin films.

1.8 Thesis organization

The thesis is organized in five chapters as follows:

Chapter 1 includes literature survey and general information on ferrites, description of the spinel structure, and dielectric properties. The objectives of the present work are also included in this chapter.

Chapter 2 consists of a detailed description of material synthesis methods and experimental techniques used in the present work.

Chapter 3 presents results obtained on $CoFe_2O_4$, $Cu_xCo_{1-x}Fe_2O_4$ (x=0, 0.2, 0.25 and 0.4) and $Cu_xCo_{1-x}Fe_2O_4$ (x=0, 0.2, 0.25, 0.4, 0.9 and 1.0) nanoparticles and bulk ferrites prepared by coprecipitation technique.

Chapter 4 contains a detailed study of structural, magnetic and optical properties of CoFe₂O₄ and Cu_{0.25}Co_{0.75}Fe₂O₄ thin films synthesized by rf-magnetron sputtering.

Chapter 5 gives summary and conclusions of the research work.

References

- [1] Handley, R.C.O. (2000) Modern Magnetic Materials: Principles and Applications. John Wiley & Sons, New York.
- [2] Chen, D., Zhang, Y. and Tu, C. *Materials Letters*, **82**, 10-12(2012).
- [3] M. Raghasudha, D. Ravinder, P. Veerasomaiah, J. Nanostruct. Chem. 3, 1–6 (2013).
- [4] J. Balavijayalakshmi, N. Suriyanarayanan, R. Jayaprakash, Mater. Lett. 81, 52-54 (2012).
- [5] A.Ghani, A. A. Sattar and J. Pierre, J. Magn. Magn. Mater. 97, 141 (1991).
- [6] S. Singhal Sonal Singhal , J. Singha , S.K Barthwal , K. Chandraa, *Journal of Solid State Chemistry* 178, 3183–3189 (2005).
- [7] Samavati, A., Mustafa, M. K., Ismail, A. F., Othman, M. H. D., Rahman, M. A., Mater. Express.6, 473 (2016).
- [8] Z. Szotek, W. M. Temmerman, D. Kodderitzsch, A. Svane, L. Petit, and H. Winter., *Phys. Rev. B*, **74**, 174431 (2006).
- [9] A.T. Raghavender and K.M. Jadhav, Bull. Mater. Sci., 32, 575 (2009).
- [10] G. Ranga Mohan, D. Ravinder, A.V. Ramana Reddy, and B.S. Boyanov, Mater. Let., 40, 39 (1999).
- [11] E. Schlömann, J. Phys. Colloq., 32, C1-443 (1971).
- [12] J. Tauc (Ed), Amorphous and liquid semiconductors, Plenum, Newyork (1974).
- [13] H.S. Mund, Shailja Tiwari, JagratiSahariya, M. Itou, Y. Sakurai Y, B.L. Ahuja, J. Appl. Phys., 110, 073914 (2011).
- [14] F. Bensebaa, F. Zavaliche, P. L'Ecuyer, R.W. Cochrane, T. Veres, *Journal of Colloid and Interface Science*277, 104–110 (2004).
- [15] K. Maaz, A. Mumtaz, S. K. Hasanain, A. Ceylan. J. Magn. Magn. Mater. 308, 289 (2007).
- [16] L. Ai, J. Jiang. Curr. Appl. Phys. 10,284 (2010).
- [17] L. Sonali, S. S. Suryavanshi, I. S. Mull.35,1793 (2009).
- [18] V. Cabuil, V. Dupuis, D. Talbot, S. Neveu. J. Magn. Magn. Mater. 323, 1238 (2011).
- [19] Huixia Wu, Gang Liu, Xue Wang, Jiamin Zhang, Yu Chen, Jianlin Shi, Hong Yang, He Hu, Shiping Yang, *Acta Biomaterialia***7**, 3496–3504 (2011).
- [20] M. Sertkol, Y. K. oseoglu, A. Baykal, H. Kavas, A. C. Basaran, J. Magn. Magn. Mater. 321, 157 (2009).
- [21] Tanaka, T., Shimazu, R., Nagai, H., Tada, M., Nakagawa, T., Shandhu, A., Handa, H., Abe, M.: J. Magn. Magn. Mater. 321, 1417 (2009)
- [22] Lee, S.W., Bae, S., Takemura, Y., Shim, I.B., Kim, T.M., Kim, J., et al.: J. Magn. Magn. Mater. **310**, 2868 (2007)
- [23] Pita, M., Abad, J.M., Dominguez, C.V., Briones, C., Martí, E.M., Gago, J.A.M., Morales, M.P., Fernández, V.M.: J. Colloid Interface Sci. 321, 484 (2008).
- [24] S.C. Watawe, B.D. Sarwade, S.S. Bellad, B.D. Sutar, and B.K. Chougule, *J. Magn. Magn. Mater.*, **214**, 55 (2000).
- [25] A.M. Bhavikatti, S. Kuikarni, and A. Lagashetty, Int. J. Eng. Sci. Technol., 3, 5985 (2011).

- [26] S.F. Mansour, Egypt. J. Solids, 28, 263 (2005).
- [27] E. Barsoukov and J.R. Macdonald, *Impedance Spectroscopy: Theory, Experiment, and Applications, Migration in the Absence of Concentration Gradients*, I.D. Raistrick, D.R.Franceschetti, and J.R. Macdonald, eds., John Wiley & Sons, Inc., Hoboken, New Jersey, 2005, p. 47.
- [28] Y. C. Wang, J. Ding, J. B. Yi, B. H. Liu, T. Yu, Z. X. Shen, Appl. Phys. Letters 84, 2596 (2004).
- [29] J. G. Lee, J. Y. Park, Y. J. Oh, C. S. Kim, J. Appl. Phys. 84, 2801(1998).
- [30] J. Ding, Y. J. Chen, Y. Shi, S. Wang, Appl. Phys. Letters 77, 3621 (2000).
- [31] J. G. Lee, K. P. Chae, J. C. Sur, J. Magn. Magn. Mater. 267, 161 (2003).
- [32] B. X. Gu, Z. H. Hua, J. Magn. Magn. Mater. 299, 392 (2006).
- [33] J. H. Yin, J. Ding, B. H. Liu, J. B. Yi, X. S. Miao, J. S. Chen, J. Appl. Phys. 101, 09K509 (2007).
- [34] Ramos, A.V., Santos, T.S., Miao, G.X., Guittet, M.-J., Moussy, J.-B., Moodera, J.S., *Phys. Rev. B78*, 180402 (R) (2008)
- [35] Bouet, L., Tailhades, P., Rousset, A., J. Magn. Magn. Mater. 153, 389 (1996).
- [36] Rondinone, A.J., Samia, A.C., Zhang, Z.J., Appl. Phys. Lett. 76, 3624 (2000)
- [37] Sultan, M., Singh, R., J. Appl. Phys. 105, 07A512 (2009).
- [38] Chavan, S.M., Babrekar, M.K., More, S.S., Jadhav, K.M., J. Alloy Comput. 507, 2 (2010).
- [39] Ravindra, A.V., Padhan, P., Prellier, W., Appl. Phys. Lett. 101, 161902 (2012).
- [40] Sultan, M., Singh, R., J. Phys. D42, 115306 (2009).
- [41] H. Zheng, J. Wang, S. E. Lofland, Z. Ma, L. Mohaddes-Ardabili, T. Zhao, L. Salamanca-Riba, S. R. Shinde, S. B. Ogale, F. Bai, D. Viehland, Y. Jia, D. G. Schlom, M. Wuttig, A. Roytburd, and R. Ramesh., *Science* 303, 661 (2004).
- [42] J. Slutsker, I Levin, J. H. Li, A. Artemev, and A. L. Roytburd, Phys. Rev. B73, 184127 (2005).
- [43] F. X. Cheng, J. T. Jia, Z. G. Xu, B. Zhou, C. S. Liao, C. H. Yan, L. Y. Chen, and H. B. Zhao, J. Appl. Phys. 86, 2727 (1999).
- [44] Y. Kitamoto, S. Kantake, F. Shirasaki, M. Abe, and M. Naoe, J. Appl. Phys. 85, 4708 (1999).
- [45] S. A. Chambers, R. F. C. Farrow, and S. Maat, J. Magn. Magn. Mater. 246, 124 (2002).

Chapter 2

Synthesis of Nanoparticles, Bulk and Thin Films and Characterization Techniques

The experimental details including preparation of bulk, nanoparticles using co-precipitation technique and thin film deposition by using RF magnetron sputtering and characterization of structure, microstructure, magnetic and optical properties are given in this chapter.

2.1 RF-sputtering

Radio frequency magnetron sputtering is a useful technique as the properties of the films can be controlled by changing the sputtering conditions such as substrate temperature, deposition time, pressure, and RF power. In sputtering the target of the material to be deposited will act as a cathode. The substrate is placed opposite to the target. The high energy ions formed from the plasma of an inert gas strikes the target. The material will be ejected from the target because of the momentum transfer from the impinging ions to the target surface. Atoms ejected from the target will be deposited on the substrate. The chamber is evacuated to ~ 10⁻⁶ Torr vacuum using a turbo molecular pump and gas is loaded into the vacuum chamber between the two electrodes. The sputter gas is typically an inert gas such as argon, nitrogen. For reactive sputtering it can be oxygen. Plasma is formed by the application of RF power. The high energy inert gas ions are accelerated towards the target due to coulomb attraction and make collisions onto the target and eject target atoms. A magnetic field is applied perpendicular to the target surface to sustain plasma near the target surface.

The details of sputtering system and film preparation are described in our earlier report [1]. Fig. 2.1 shows the photograph of the RF magnetron sputtering system. The target was mounted to the target holder of the magnetron gun (electron gun). The electron gun consists of a target backing plate, target holder, grounding shield, magnet pole pieces and cooling water inlet and the target is isolated from the grounding shield. The system is equipped with two sputter guns as shown in figure 2.1 (b)). The main chamber was pumped down to a high vacuum with a turbo-pump. The gas flow rate is maintained by mass flow controller.

2.1.1 RF-magnetron sputtering system

Rf-magnetron sputtering deposition techniques are used widely both in industrial processes and in advanced material fabrication or treatment [2]. We have synthesized thin films of cobalt

ferrite and Co_{0.75}Cu_{0.25}Fe₂O₄ using radio frequency magnetron sputtering under various sputtering conditions.

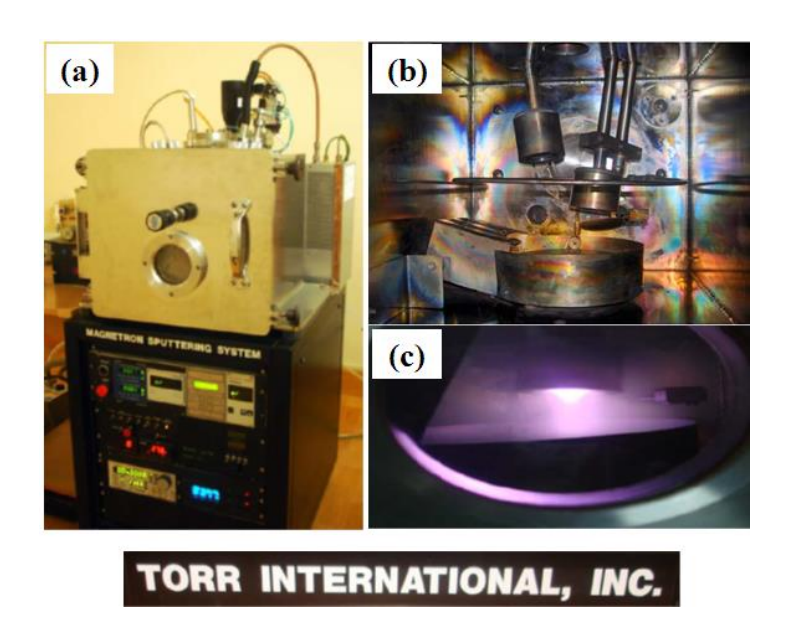


Figure 2.1: (a) The photograph of sputtering system used in this work, (b) view of the deposition chamber having two electron guns and (c) Plasma created during deposition process of ferrite thin films in Ar gas.

2.2 Bulk and nanoparticles synthesis

2.2.1 Synthesis of copper doped cobalt ferrite, Co_{1-x}Cu_xFe₂O₄ nanoparticles

Copper-substituted cobalt ferrites nanoparticles, Co_{1-x}CuxFe₂O₄ with *x* = 0.0, 0.2, 0.25 and 0.4, were prepared by co-precipitation method [3]. Stoichiometric amounts of cobalt (II) nitrate hexahydrate Co(NO₃)₂·6H₂O, copper (II) nitrate trihydrate Cu(NO₃)₂·3H₂O and Iron (III) nitrate nonahydrate Fe(NO₃)₃·9H₂O were dissolved separately in de-ionized water. Sodium hydroxide (NaOH) solution was used for neutralization. The reaction temperature was maintained at 60 °C under stirring for 2 hours. The pH of the solution was around 12-13. The precipitate was washed with double distilled water many times until the pH of the product becomes 7 and dried at 90 °C overnight. The dried product was cooled to room temperature and grinded with mortar and pestle for half an hour. This powder was further annealed at 600 °C for 3 h with 3°C/min both heating and cooling rate to decompose into well-crystalline nanopowders. The prepared Co_{1-x}Cu_xFe₂O₄ samples were characterized by standard techniques, such as X-ray diffraction (XRD), scanning electron microscope (SEM), energy dispersive spectroscopy (EDS), Transmission electron microscopy (TEM) and vibrating sample magnetometer (VSM).

2.2.2 Preparation of copper doped cobalt ferrite, Co_{1-x}Cu_xFe₂O₄ bulk ferrites

The $\text{Co}_{1-x}\text{Cu}_x\text{Fe}_2\text{O}_4$ nanopowder samples with x=0, 0.2, 0.25, and 0.4, were prepared by using Fe^{3+} , Co^{2+} and Cu^{2+} nitrates as precursors and sodium hydroxide as a precipitating agent by coprecipitation technique, as given in the above subsection 2.2.1, were pressed into pellets using mechanical press at a pressure of 3 tons after mixing with polyvinyl alcohol (PVA) as a binder (except pellets heated at 100 °C). Typical diameter and thickness of the pellets are 13 mm and 1-2 mm, respectively. The pellets were heat treated at 100, 600 and 1200 °C for 4 hours and also at 600 °C for 3 h with 3°C/min both heating and cooling rate, to get the grains of $\text{Co}_{1-x}\text{Cu}_x\text{Fe}_2\text{O}_4$ (x=0.0-0.4) of different grain sizes. The samples were coded as CoFe_2O_4 as (i) for x=0, $\text{Co}_{0.8}\text{Cu}_{0.2}\text{Fe}_2\text{O}_4$ as (ii) for Cu doping of x=0.2, $\text{Co}_{0.75}\text{Cu}_{0.25}\text{Fe}_2\text{O}_4$ as (iii) for Cu doping of x=0.25, $\text{Co}_{0.6}\text{Cu}_{0.4}\text{Fe}_2\text{O}_4$ as (iv) for Cu doping of x=0.4. The prepared $\text{Co}_{1-x}\text{Cu}_x\text{Fe}_2\text{O}_4$ samples were characterized by standard techniques, such as X-ray diffraction (XRD), scanning electron microscope (SEM), vibrating sample magnetometer (VSM) and dielectric spectrometer.

2.2.3 Synthesis of cobalt-copper ferrite, Co_{1-x}Cu_xFe₂O₄ nanoparticles and bulk materials

The synthesis of $\text{Co}_{1-x}\text{Cu}_x\text{Fe}_2\text{O}_4$, (x=0,0.2,0.25,0.4,0.9 and 1.0)nanopowders was carried out by the co-precipitation method [3] using high-purity cobalt (II) nitrate hexahydrate cobalt (II) nitrate hexahydrate $\text{Co}(\text{NO}_3)_2 \cdot 6\text{H}_2\text{O}$, copper (II) nitrate trihydrate $\text{Cu}(\text{NO}_3)_2 \cdot 3\text{H}_2\text{O}$ and Iron (III) nitrate nonahydrate $\text{Fe}(\text{NO}_3)_3 \cdot 9\text{H}_2\text{O}$ and sodium hydroxide, NaOH. The Fe/Co precursors ratio has been chosen in order to obtain $\text{Co}_{1-x}\text{Cu}_x\text{Fe}_2\text{O}_4$, (x=0.0-1.0) stoichiometry. Aqueous solutions of precursors were prepared separately under proper stirring at 60 °C for half an hour. We have increased concentration of precursor solutions as well as that of NaOH solution compared to concentration of solutions used in section 2.2.1. These solutions were mixed and NaOH solution was added until pH becomes 13.5. The beaker was covered during synthesis to avoid evaporation. Reaction mixture was continued at 60 °C with proper stirring for 2 hrs. Precipitates were washed several times with double distilled water to get rid of the impurities. The precipitated powders were dried overnight using hot air oven at 90 °C; the substance was collected and grinded for 20 min using agate mortar and pestle.

The synthesized powders were pressed into pellets using a mechanical press at a pressure of 3 tons after mixing with polyvinyl alcohol (PVA) as a binder (except pellets heated at 100 °C). These pellets were heat treated at 100, 600 and 1200 °C for 4 hours, to get the nano grains of $Co_{1-x}Cu_xFe_2O_4$ (x=0.0-1.0) of different grain sizes. The prepared $Co_{1-x}Cu_xFe_2O_4$ samples were

characterized by standard techniques, such as X-ray diffraction (XRD), scanning electron microscope (SEM), vibrating sample magnetometer (VSM) and dielectric spectrometer. The samples were coded CoFe₂O₄ as (i) for x=0, Co_{0.8}Cu_{0.2}Fe₂O₄ as (ii) for Cu doping of x=0.2, Co_{0.8}Cu_{0.25}Fe₂O₄ as (iii) for Cu doping of x=0.25, Co_{0.8}Cu_{0.4}Fe₂O₄ as (iv) for Cu doping of x=0.4, Co_{0.1}Cu_{0.9}Fe₂O₄ as (v) for x=0.9 and CuFe₂O₄ as (vi) for x=1.0.

2.2.4 Synthesis of CoFe₂O₄ nanoparticles and bulk ferrites

Cobalt ferrites nanoparticles with the general formula CoFe₂O₄ were synthesized by coprecipitation technique [3] using anhydrous FeCl₃ and CoCl₂·6H₂O as precursors and NaOH as a precipitating agent. In the co-precipitation method, stoichiometric quantities of ferric chloride, FeCl₃ and cobalt chloride, CoCl₂·6H₂O were dissolved in de-ionized water to get aqueous solutions of precursors separately with Fe/Co molar ratio of 2:1. To a mixed solution of Co²⁺ and Fe³⁺ chlorides, aqueous solution of NaOH was added within 10 seconds with stirring at 60°C. The precipitate formed was maintained at 60°C with constant stirring using hot plate for one and half an hour and the pH of the precipitate was 13. The precipitate obtained was washed many (15) times and dried at 90°C overnight. The acquired substance was uniformly grinded for 20 min using agate mortar and pestle. The powder is subjected to a pressure of 3000 PSI to obtain compact and dense pellets with a diameter of 13.6 cm and thickness of 1 mm. The pellets were then heated at 100°C, 400°C, 600°C and 1200°C for 4 hours with 3°C/min heating and cooling rate in air muffle furnace in order to carry out structural and magnetic and dielectric characterization.

2.3 Target preparation

2.3.1 CoFe₂O₄ and Cu_{0.25}Co_{0.75}Fe₂O₄ target preparation

The CoFe₂O₄ target material was prepared by co-precipitation method [3]. Stoichiometric quantities of ferric chloride, FeCl₃ and cobalt chloride, CoCl₂·6H₂O were used as the precursors and de-ionized water as solvent. To a mixed solution of Co²⁺ and Fe³⁺ chlorides, aqueous solution of NaOH was added within 10 seconds with stirring at 60 °C until a pH of 11-12 was attained and precipitation of the mixed material occurred. The precipitate obtained was washed many (15) times and dried at 80 °C overnight. The acquired substance was uniformly grinded for about 20 minutes. The powder was pressed into a disc of 3-in diameter and 5 mm thickness at a pressure of 3 tons after mixing with polyvinyl alcohol (PVA) as a binder. Calcination and final sintering of the target (resultant disk) was done at 1200 °C for 6 h and 1300 °C for 2 h

respectively. Finally the target was sintered at 1300°C for 4 hours to obtain a dense hard 2-in target disc.

The Co_{0.75}Cu_{0.25}Fe₂O₄ nanoparticles were prepared by using Fe³⁺, Co²⁺ and Cu²⁺ nitrates as precursors and sodium hydroxide as a precipitating agent by co-precipitation technique, as given in the above subsection 2.2.1. The precipitate was dried at 90°C overnight. The acquired substance was grinded for 20 minutes uniformly using mortar and pestle. To this powder poly vinyl alcohol (PVA) binder is added and pressed into a circular disc. The resultant disc was heated at 1200 °C for 5 h. Final sintering of the target was done at 1300 °C for 6 h.

2.4 CoFe₂O₄ and Cu_{0.25}Co_{0.75}Fe₂O₄ thin film preparation

Thin films of CoFe₂O₄ and Cu_{0.25}Co_{0.75}Fe₂O₄ were deposited by using various RF power at 13.6 MHz on unheated glass and quartz substrates, respectively, at room temperature. Prior to each deposition the vacuum chamber was pumped down to a base pressure of 4×10^{-5} and 4×10^{-6} Torr, respectively. The sputtering was done in Ar atmosphere with a target-to-substrate distance of 6 cm. The effect of RF power, thickness, gas pressure and post deposition heat treatment on the microstructure and properties of the deposited thin films was studied.

2.5 Structural Characterization techniques

The X-ray diffraction patterns of powders were recorded at room temperature in the 2θ range of 10° to 80° using PANalytical X'Pert³ Powder diffractometer equipped with Cu-K α source (λ = 1.5405Å) operating at 45 kV and 40 mA and were refined using Rietveld method with HighScore Plus software. The structure of the films was characterized by grazing incidence X-ray diffractometer (Bruker D8 DISCOVER) with Cu-K α source operating at 40 kV and 30 mA. The X-ray diffraction patterns of films were recorded at room temperature in 2θ range of 20° to 70° .

2.5.1 X-ray diffraction

When incident X-ray wave strikes on the sample, the diffracted beams interfere and produce maximum intensity. If θ is the incident angle of X-rays with respect to the plane of the crystal, intensity of the diffracted beam will be maximum when [4]:

$$2d_{hkl}\sin\theta_{hkl} = n\lambda\tag{2.1}$$

where n is order of diffraction, λ is the wavelength of X-rays, d_{hkl} is interplanar distance. Eq. (2.1) is known as Bragg's law. The crystallite size of the sample is estimated using the Debye-Scherrer equation [5] given by

$$D = \frac{0.9\lambda}{\beta\cos\theta} \tag{2.2}$$

where, D is crystallite size in Å, λ is the wavelength of X-rays, β is the full width of the diffraction line at half the maximum intensity and θ_{hkl} is the diffraction angle.

Powder X-ray diffraction is used to identify phase of the unknown crystalline powder sample, by comparing its diffraction pattern with standard pattern given by the ICDD data. Grazing incident angle X-ray diffraction is used to identify the phase of the thin films and estimate their crystallite size, lattice constant, interplanar spacing, etc.

2.5.2 Field emission scanning electron microscopy (FESEM)

FESEM employs a beam of electrons to produce magnified and high resolution images of the samples. In FESEM, focused beam of electrons is scanned systematically over the sample. When high energy electron beam hits the sample surface placed in the microscope, the desired image of the surface of the sample will be built up by the secondary electrons emitted by the sample. The X-rays generated by the specimen are used for elemental analysis of the sample composition in energy dispersive X-ray spectroscopy.

The surface morphology of cobalt ferrite, copper doped cobalt ferrite nanoparticles, thin films and bulk ferrite samples were studied using CARL ZEISS Gemini ULTRA 55 Field Emission Scanning Electron Microscope. FESEM images were taken at different accelerating voltages of 5 kV, 10 kV, 20 kV at different magnifications of between 1KX and 500 KX under different working distances between 4 to 8 mm.

2.5.3 Transmission electron microscopy

In transmission electron microscope, a tungsten filament produce electrons which are accelerated by applying a high voltage of 200 kV. The wavelength of electrons is related to the accelerating voltage, V by

$$\lambda = \frac{h}{\sqrt{2meV}} \tag{2.3}$$

where m and e are the mass and charge of the electron. Since the wavelengths of electrons are much smaller than wavelength of the X-rays, the Bragg angles for electron diffraction are small. Therefore electron diffraction pattern seems as a narrow cone centered on the undiffracted or direct beam. Diffraction pattern of the polycrystalline sample can be taken by changing the relative position of the viewing screen, which is called selected area diffraction pattern. To increase the quality of photographs where the particles of interest are difficult to find out from

the background, dark field imaging is employed. With HRTEM, it is possible to look at the atomic structure of our sample. The microstructure of cobalt ferrite, copper doped cobalt ferrite nanoparticles and thin films were studied using FEI Tecnai G² S-Twin 200 kV Transmission Electron Microscope.

2.6 Vibration sample magnetometer (VSM)

The VSM used for measuring magnetization of magnetic samples works on Faraday's law. If a magnetic sample is suspended in a uniform magnetic field from a vibrator which vibrates the sample in the magnetic field up and down, the sample is magnetized which also acts as a magnet and creates changing magnetic flux. This changing magnetic flux will induce a current in the pick-up coils. This current will induce a magnetic moment which is equal to the magnetic moment of the sample.

The induced emf across the coil is given by [6]

$$\varepsilon = -C \frac{d\phi}{dt} \tag{2.4}$$

where ϕ represents the changing flux in the coils. The output measurement displays the magnetic moment, m (or magnetization, M) as a function of the applied filed, H.

Magnetic properties of the samples in the present studies were measured by using LakeShore-7400 vibrating sample magnetometer and Physical Property Measurement System (Quantum Design).

2.7 Spectrophotometer

By studying a fraction of light energy transmitted through a sample of known thickness, one can determine α , the absorption coefficient, refractive index (n) and band gap energy (E_8). Spectrophotometer is an instrument used to measure the transmittance, absorbance and reflectance of a material. The instrument consists of a source of light, a sample holder and a detector. As light passes through the sample, the energy of the photon is partially transferred to the atoms in the material. The absorbed photons help in exciting the electrons from the valence band to conduction band. The unabsorbed photons which pass through the sample are detected by the detectors. Figure 2.2 represents a block diagram showing the working of a spectrophotometer. Single beam ones lost their popularity due to their unstable light source, detectors and the inbuilt electronics. Tungsten and deuterium lamps are used to generate EM waves corresponding to UV and visible-NIR region respectively.

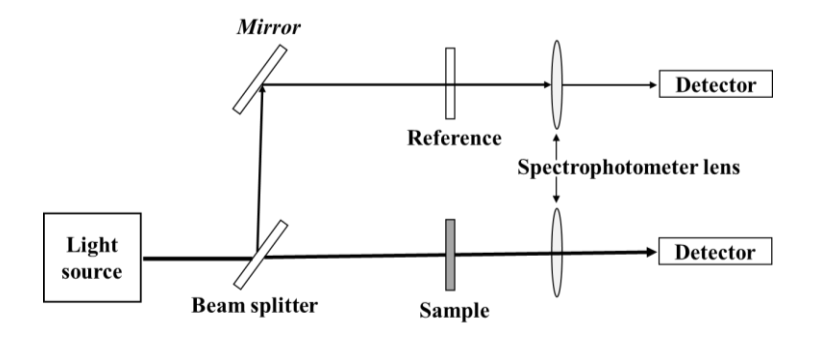


Fig. 2.2. An experimental arrangement used to measure direct transmittance spectra.

The deuterium lamp is used to produce EM radiation in the wavelength range 190-240 nm and the tungsten lamp is used to produce EM waves of wavelength in the range 240-2500 nm. The sample compartment contains two holders: (1) to contain the sample in the measurement-side and (2) to contain the reference on the reference-side. The detectors receive the light transmitted through the sample and the reference simultaneously. The difference in the energy of the incident photons is converted into electronic signals by a photomultiplier tube connected to the detector. Unlike the transmittance and absorbance the reflectance of the material is measure by measuring the difference in the intensity of the reflected by the sample and the reference surfaces. The optical transmission spectra of the films were measured in the wavelength range of 200–2500 nm by using JASCO V670 spectrophotometer and Agilent Cary 5000 spectrophotometer.

2.8 Profilometry

The general operating technique of surface stylus profilometer is shown in figure 2.3. A mechanical diamond tip stylus is scanned over the film across the step and height is recorded. The step height generated by the probe is equal to the film thickness. For this study the films (substrates on which films were deposited) were partially masked with a tape (to obtain a step) before deposition. After film deposition the tape is removed.

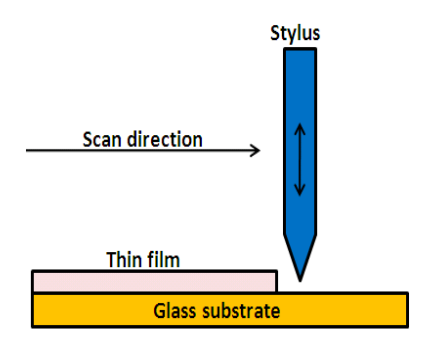


Fig. 2.3 Operating concept for a stylus profilometer.

Thickness of thin films of CoFe₂O₄ and Cu_{0.25}Co_{0.75}Fe₂O₄ were measured using AMBIOS Tech Model XP-1 surface stylus profilometer. Film thickness measurements were done at three different positions to average over the variations in the film thickness.

2.9 Dielectric spectrometer

In addition to the magnetic properties, ferrites also exhibit good dielectric properties. The dielectric properties determine the response of a material when placed in an electric field. Spinel ferrite nanoparticles have high electrical resistivity and low eddy current and dielectric losses. The dielectric properties (permittivity, ϵ' and dielectric loss, $\tan \delta$) of ferrites rely on their preparation method and material processing conditions sintering temperature, substitution used, the ratio of Fe³⁺/Fe²⁺ions and AC conductivity. Dielectric properties are always presented relative to the dielectric constant of the vacuum (ϵ_0). The electric permittivity is given by

$$\varepsilon' = \frac{c \cdot t}{\varepsilon_{0} \cdot A} \tag{2.5}$$

where C is measured capacity, t is sample thickness, A is surface area of the pellet and $\epsilon_0 = 8.85 \times 10^{-12} \text{ F/m}$.

$$\varepsilon' = \frac{4 \, C \cdot t}{\varepsilon_0 \pi D^2} \tag{2.6}$$

Here $A = (\pi D^2)/4$, where D is diameter of capacitor electrodes.

The loss of energy is generally characterized by dielectric loss tangent tan $\delta = \epsilon''/\epsilon'$, where δ is phase lag between induced polarization and applied electric field.

2.9.1 Method of dielectric measurement

The sample cells used in our dielectric spectrometers are shown below. Dielectric properties were measured using Novocontrol Technologies (Germany) dielectric spectrometer with an ac voltage of '1volt' at frequencies ranging from 100 Hz–40 MHz (and at RT) for copper doped cobalt ferrites $Co_{1-x}Cu_xFe_2O_4$ with x=0.0, 0.2, 0.25 and 0.4. For these measurements, pellets of $Co_{1-x}Cu_xFe_2O_4$ powders were made using mechanical press. These pellets were sintered in a furnace at different temperatures $100^{\circ}C$ for 4 h, $600^{\circ}C$ for 3 h, $600^{\circ}C$ and $1200^{\circ}C$ for 4 h. The pellets obtained by sintering were then polished and painted with silver paste on both the faces. The sample material is prepared by placing the silver coated pellets between additional gold plated parallel plate external electrodes in order to form a sandwich capacitor as shown below (Fig.2.4). Finally for the measurements, the sandwich capacitor is mounted between upper and lower electrodes of Alpha active sample cell BDS 1200 as shown in figure 2.5. This procedure

simplifies the sample preparation, protects the electrodes from contamination and allows removing the sample easily. A signal of 1 V is applied to the samples and dielectric measurements were carried out using Novocontrol Alpha active cell interfaced to a PC.

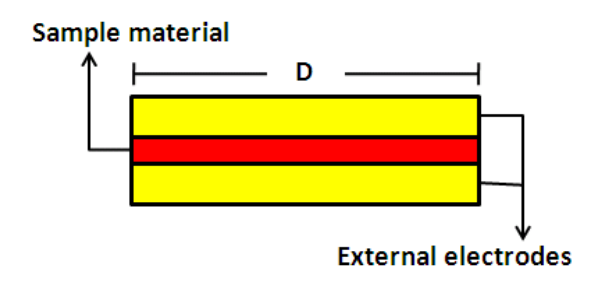


Fig. 2.4. Sample capacitor prepared with two round disposable plate electrodes.

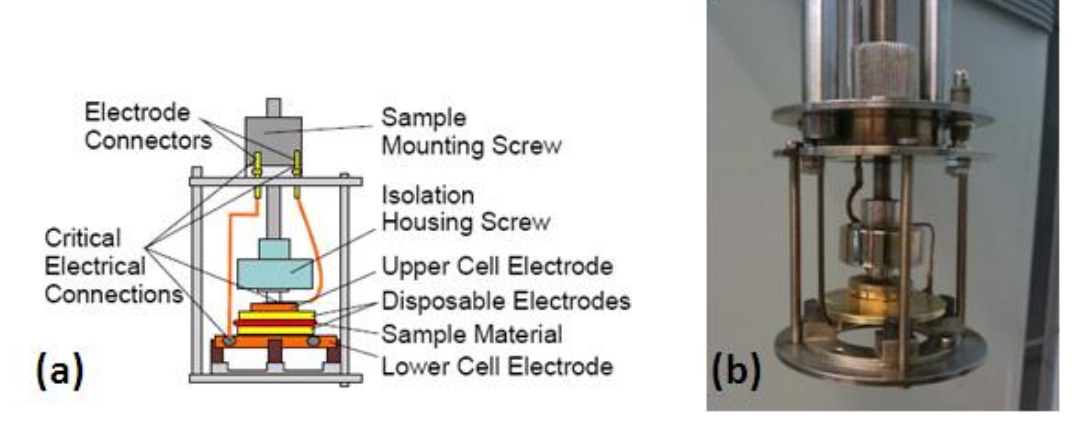


Fig. 2.5. Lower sample cell part with sample mounted between disposable electrodes; (a) block diagram and (b) photograph.

Measurements on the samples were done at room temperature as a function of frequency and composition in the frequency range 100 Hz to 40 MHz at room temperature.

References

- [1] Sultan, M., Singh, R.: Structural and optical properties of RF sputtered ZnFe₂O₄ thin films. J. Phys. D **42**, 115306 (2009).
- [2] Li, N., Allain, J., Ruzic, D.N. (2002) Enhancement of aluminium oxide physical vapour deposition with secondary plasma. Surface and Coating Technology, no. 149, P. 161, ISSN0257-8972.
- [3] Thirupathi, G., Singh, R.: Magnetic Properties of Zinc Ferrite Nanoparticles. IEEE Trans. Mag. 48, 3630 (2012)
- [4] B. D. Cullity and S. R. Stock, *Elements of X-Ray Diffraction* (Prentice-Hall, International, 2001).
- [5] Patterson, A.L.: The Scherrer formula for X-ray particle size determination. Phys. Rev. 56, 978 (1939).
- [6] H. S. Nalwa, Hand book of Thin Film materials (2002) Academic press.

Chapter 3

Structure and properties of cobalt ferrite $(CoFe_2O_4)$ and copper doped cobalt ferrite $Co_{1-x}Cu_xFe_2O_4$ nanoparticles and bulk ferrite synthesized by co-precipitation technique

This chapter is divided into four major sections. Section 3.1 describes structure and magnetic properties of CoFe₂O₄ and copper doped cobalt ferrite Co_{1-x}Cu_xFe₂O₄ (*x*=0.0, 0.2, 0.25, 0.4) nanoparticles. Section 3.2 describes the structure, magnetic and dielectric properties of bulk CoFe₂O₄ and Co_{1-x}Cu_xFe₂O₄ (*x*=0.0, 0.2, 0.25, 0.4) ferrites annealed at different temperatures. Section 3.3 describes the structure, magnetic and dielectric properties of cobalt-copper ferrites Co_{1-x}Cu_xFe₂O₄ (*x*=0.0, 0.2, 0.25, 0.4, 0.9 and 1.0) annealed at different temperatures. Section 3.4 describes the influence of sintering temperature on structure, magnetic and dielectric properties of cobalt ferrite.

3.1 Structural and magnetic properties of $CoFe_2O_4$ and copper doped cobalt ferrite Co_1 $_xCu_xFe_2O_4$ (x=0.0, 0.2, 0.25 and 0.4) nanoparticles.

3.1.1 Introduction

The aim of the present work is to investigate the effect of Cu doping on crystal structure and magnetic properties of cobalt ferrite nanoparticles. We succeeded in synthesizing Cu-substituted cobalt ferrite nanoparticles of size 10-22 nm with stoichiometry exhibiting high saturation magnetization, high coercivity and remanence.

3.1.2 Structural analysis

The XRD patterns of $\text{Co}_{1-x}\text{Cu}_x\text{Fe}_2\text{O}_4$ (x = 0.0, 0.2, 0.25 and 0.4) nanoparticles heated at 90 °C (as-synthesized) and 600 °C are shown in Fig. 3.1. The X-ray diffraction pattern reveals that samples are crystallized in single-phase spinel structure with Fd-3m space group and all the diffraction peaks matches with JCPDS file No. 98-016-0059. There is no second phase such as α -Fe₂O₃, CuO, and so on detected. It has been noticed that, none of the peaks undergo a shift in 2 θ .

Furthermore, the intensity of (311) peak was found to decrease with Cu-doping up to x=0.25 followed by a small increase. The addition of Cu at Co-site is broadening the peaks which indicate a decrease in crystallite size, in the case of as-synthesized samples heated at 90 °C. On

heating the samples at 600°C, large increase in peak intensity is observed. This indicates the enhanced crystallinity of nanoparticles.

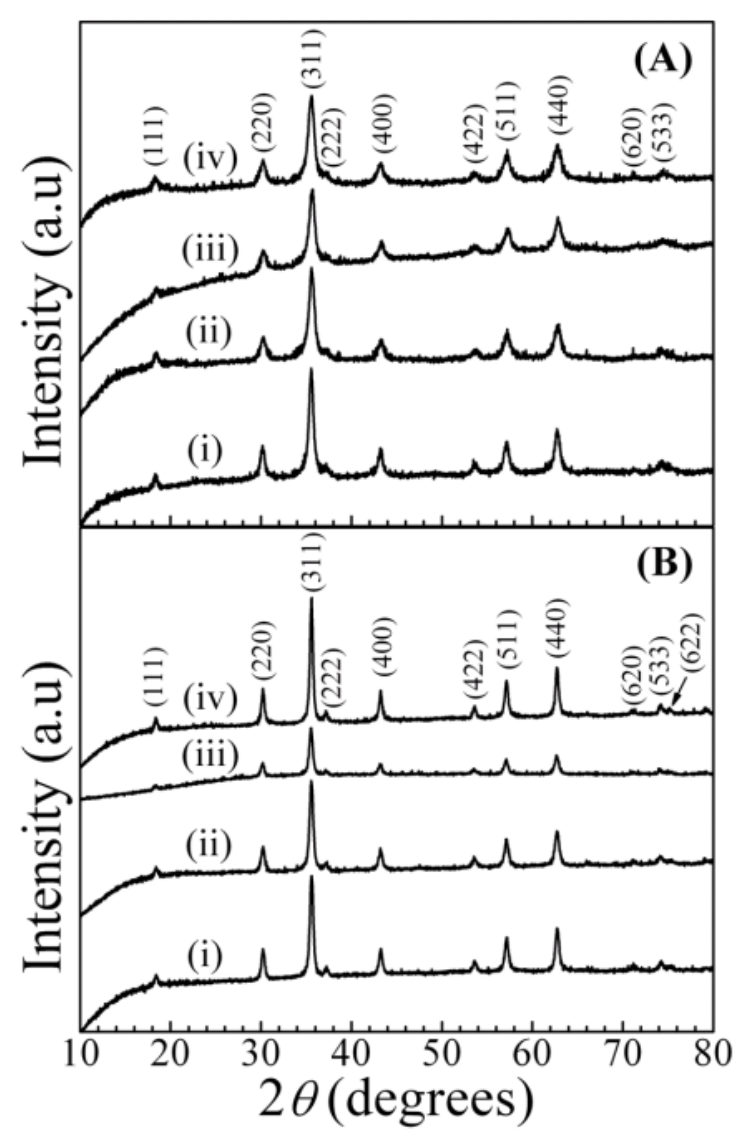


Fig. 3.1 RT-XRD spectra of as-synthesized $Co_{1-x}Cu_xFe_2O_4$ (x=0.0-0.4) nanoparticles heated at 90 °C overnight, (A) and nanoparticles heated at 600 °C for 3 h, (B) for (i) $CoFe_2O_4$ (ii) $Co_{0.8}Cu_{0.2}Fe_2O_4$ (iii) $Co_{0.75}Cu_{0.25}Fe_2O_4$ (iv) $Co_{0.6}Cu_{0.4}Fe_2O_4$.

The XRD patterns were Rietveld refined using Xpert HighScore Plus software to determine the lattice parameter of Cu doped nanoparticles as shown in Figs. 3.2 and 3.3. The lattice parameters obtained from Rietveld method agree well with those reported by Stein et al. [1]. The crystallite size of nanoparticles was evaluated by Scherrer formula [2]

$$D = \frac{0.9\lambda}{\beta_{hkl}\cos\theta} \tag{3.1}$$

where D is crystallite size, λ is the wavelength of X-rays, β is the full width of the diffraction line at half the maximum intensity and θ is the diffraction angle. The average crystallite size is evaluated from β values of all diffraction peaks. The average crystallite size for CoFe₂O₄, Co_{0.8}Cu_{0.2}Fe₂O₄, Co_{0.75}Cu_{0.25}Fe₂O₄ and Co_{0.6}Cu_{0.4}Fe₂O₄ nanoparticles heated at 90 °C and 600 °C are 14, 11, 11 and 10 nm, respectively and 20, 19, 18 and 22 nm, respectively. Annealing induces structural distortion by increasing the crystallite size. Lattice parameter is found to increase on annealing (Table 3.1). The average crystallite size evaluated by employing the Debye–Scherer formula are listed in table 3.1. Various R factors and goodness of fit values are also presented in table 3.1. G.O.F. are around 1.16–1.78 and 1.98–2.34 for nanoparticles heated at 90 °C and 600 °C (for 3 h), respectively. The average crystallite size is in agreement with the particle size estimated from TEM micrographs. X-rays (ρ_x) density decreases slightly on annealing sample at 600 °C (Table 3.1).

Table 3.1 Rietveld parameters and calculated values of Lattice parameter, average crystallite size (XRD), average particle size (TEM) and average grain size (FESEM) for $Co_{1-x}Cu_xFe_2O_4$ (x=0.0-0.4) nanoparticles.

$Co_{1-x}Cu_xFe_2O_4(x=0.0-0.4)$	x = 0	x = 0.2	x = 0.25	x = 0.4			
Co _{1-x} Cu _x Fe ₂ O ₄ (Nanoparticles heated at 90 °C overnight)							
Lattice parameter (±0.001 Å)	8.3685	8.3733	8.3622	8.3699			
$\mathrm{D}_{\mathrm{XRD}}$	14	11	11	10			
$\mathrm{D}_{\mathrm{TEM}}$	14	15	13	13			
G_{FESEM} (±1 nm)	38	35	39	34			
R (expected)/ %	0.4928	0.5073	0.5583	0.5212			
R (profile)/ %	0.4715	0.7083	0.5149	0.6045			
R (weighted profile)/ %	0.6135	0.9021	0.6482	0.7872			
G.O.F	1.2448	1.7782	1.1611	1.5104			
Density (calculated)/ g/cm ³	5.3174	5.3083	5.3295	5.3148			
Unit cell volume V (Å ³)	586.0738	587.0764	584.7416	586.3556			
Co _{1-x} Cu _x Fe ₂ O ₄ (Nanoparticles heated at 600 °C for 3 h)							
Lattice parameter (±0.001 Å)	8.3784	8.3807	8.3791	8.3807			
$\mathrm{D}_{\mathrm{XRD}}$	20	19	18	22			
$\mathrm{D}_{\mathrm{TEM}}$	15	17	-	20			
G_{FESEM} (±1 nm)	33	31	35	38			
R (expected)/ %	0.4960	0.5454	0.7401	0.5506			
R (profile)/ %	0.8929	0.9228	1.2863	0.8929			
R (weighted profile)/ %	1.1634	1.1420	1.6748	1.0906			
G.O.F	2.3455	2.0940	2.2630	1.9809			
Density (calculated)/ g/cm ³	5.2987	5.2942	5.2972	5.2942			
Unit cell volume V (Å ³)	588.1438	588.637	588.3091	588.6441			

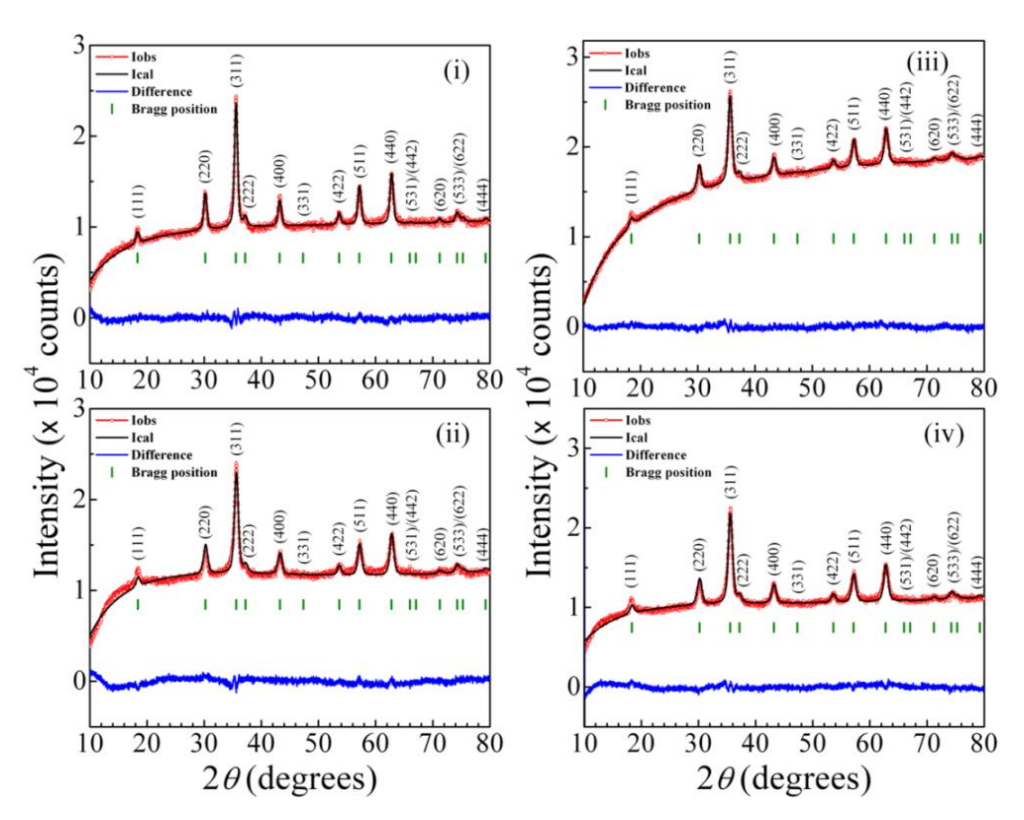


Fig. 3.2 Rietveld refined XRD patterns of as-synthesized Co_{1-x}Cu_xFe₂O₄ (x=0.0-0.4) nanoparticles heated at 90 °C overnight: (i) CoFe₂O₄ (ii) Co_{0.8}Cu_{0.2}Fe₂O₄ (iii) Co_{0.7}Cu_{0.2}Fe₂O₄ (iv) Co_{0.6}Cu_{0.4}Fe₂O₄.

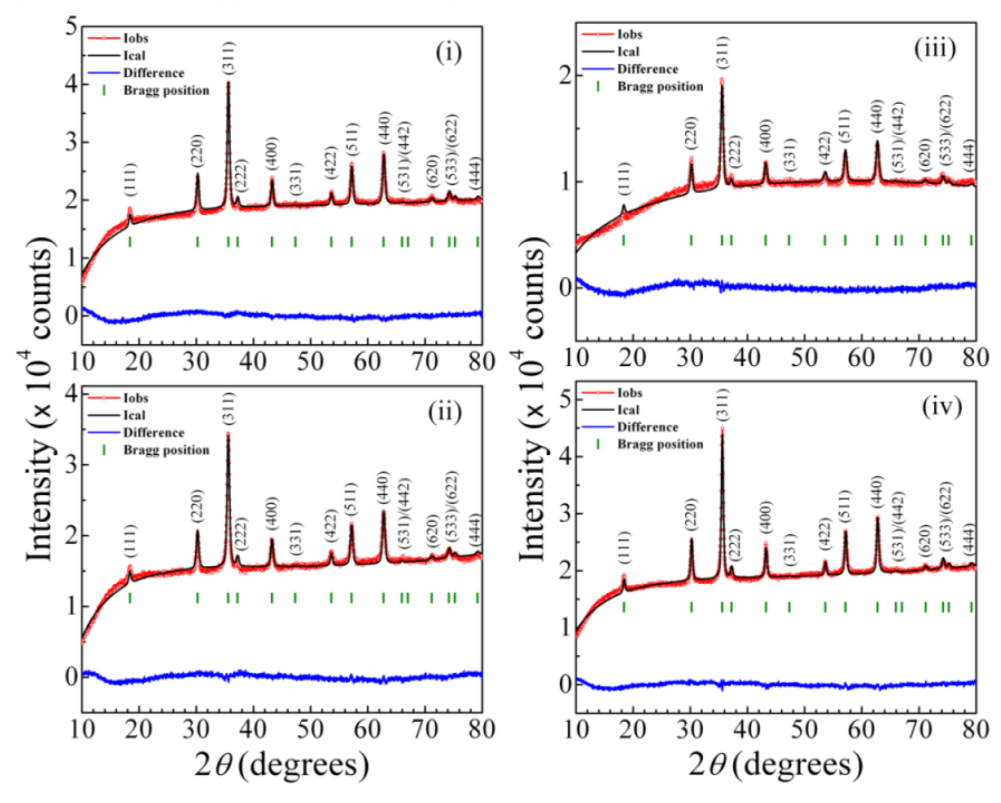


Fig. 3.3 Rietveld refinement of the XRD data of $Co_{1-x}Cu_xFe_2O_4$ (x=0.0-0.4) nanoparticles heated at 600 °C for 3 h: (i) $Co_{E_2O_4}$ (ii) $Co_{E_2O_4}$ (iii) $Co_{E_2O_4}$ (iii) $Co_{E_2O_4}$ (iv) $Co_{E_2O_4}$

3.1.3 Surface morphology

Figs. 3.4 and 3.5 show the FESEM micrographs and histograms for $Co_{1-x}Cu_xFe_2O_4$ (x=0.0 to 0.4) nanoparticles heated at 90 °C and 600 °C, respectively. The FSEM images reveal that the sample comprises homogeneous grains that do not connect with each other tightly and larger grains seem to be well separated by smaller grains. The grains have excellent crystallinity and show agglomeration. After heat treatment at 600 °C for 3 h grains with nearly spherical shape became apparent.

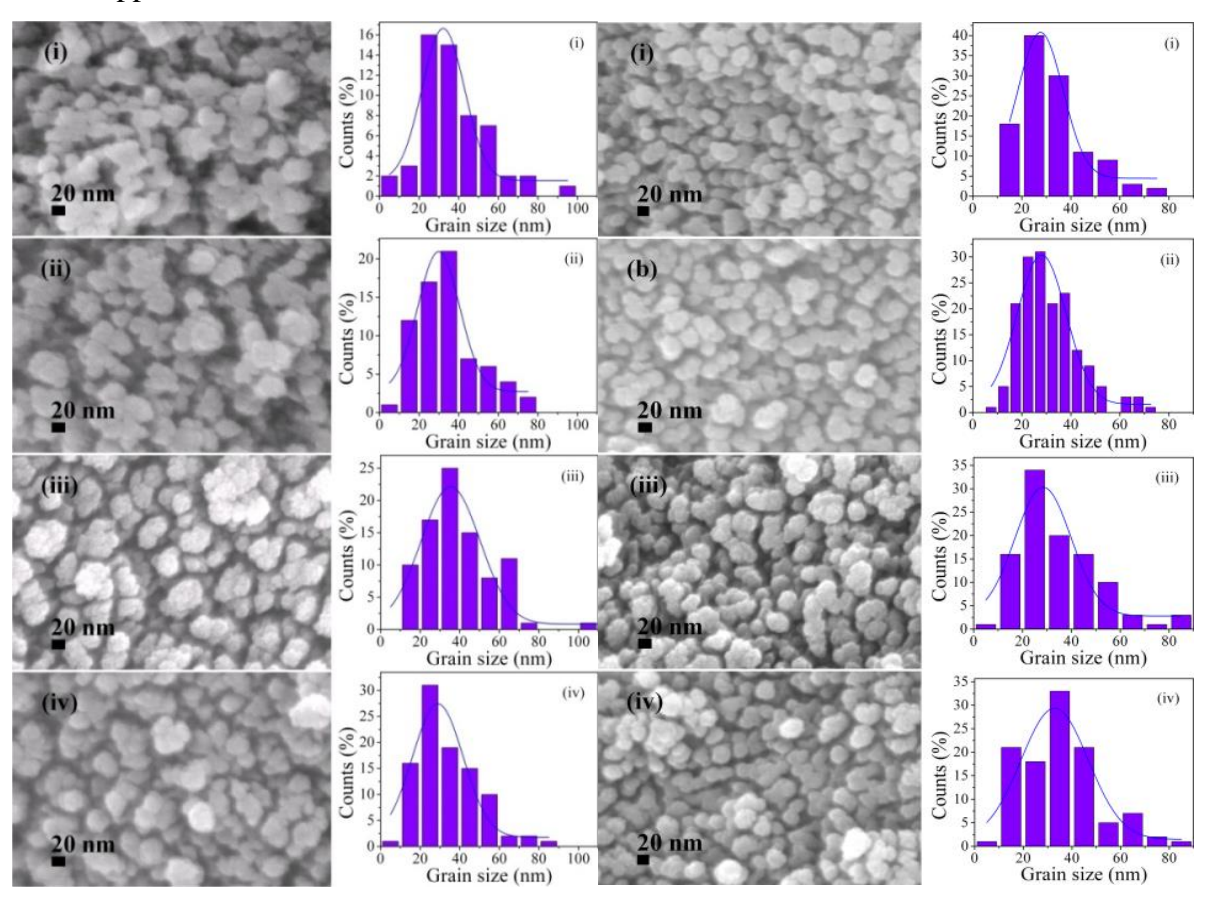


Fig. 3.4 FESEM images of as-synthesized $Co_{1-x}Cu_xFe_2O_4$ (x=0.0-0.4) nanoparticles heated at 90 °C overnight: (i) $CoFe_2O_4$ (ii) $Co_{0.8}Cu_{0.2}Fe_2O_4$ (iii) $Co_{0.75}Cu_{0.25}Fe_2O_4$ (iv) $Co_{0.6}Cu_{0.4}Fe_2O_4$ and grain size distributions.

Fig. 3.5 (right) FESEM images of $Co_{1-x}Cu_xFe_2O_4$ (x = 0.0-0.4) nanoparticles heated at 600 °C for 3 h:

The average grain size was determined using the ImageJ software by measuring the size of 100–200 individual grains. The average grain size of nanoparticles of CoFe₂O₄, Co_{0.8}Cu_{0.2}Fe₂O₄, Co_{0.75}Cu_{0.25}Fe₂O₄ and Co_{0.6}Cu_{0.4}Fe₂O₄ are 38, 35, 39, and 34 nm, and 33, 31, 35 and 38 nm for as-synthesized samples heated at 90 °C and 600 °C, respectively. For samples annealed at 600

°C, the histogram of CoFe₂O₄, Co_{0.8}Cu_{0.2}Fe₂O₄, Co_{0.75}Cu_{0.25}Fe₂O₄ sample show maximum size distribution in the range of 20–30 nm. For Co_{0.6}Cu_{0.4}Fe₂O₄ sample it is in the range of 30–40 nm. The average values of grain size are listed in Table 3.1.

EDAX spectrum (Fig. 3.6) shows that there is no new element in samples under study. This means that the compositional stoichiometry of the compound is confirmed within the experimental limits. For powders sintered at 600 °C for 3 h, the ratio of Fe/Co is 2.22 in CoFe₂O₄, close to the expected value of 2. The Cu/Co ratio is 0.301 for Co_{0.8}Cu_{0.2}Fe₂O₄, which is slightly higher than the expected value of 0.25. For Co_{0.75}Cu_{0.25}Fe₂O₄ the Cu/Co ratio is 0.255, which is slightly lower than the expected value 0.333. The value of Cu/Co is 0.66 for Co_{0.6}Cu_{0.4}Fe₂O₄, which is same as its theoretical value of 0.666.

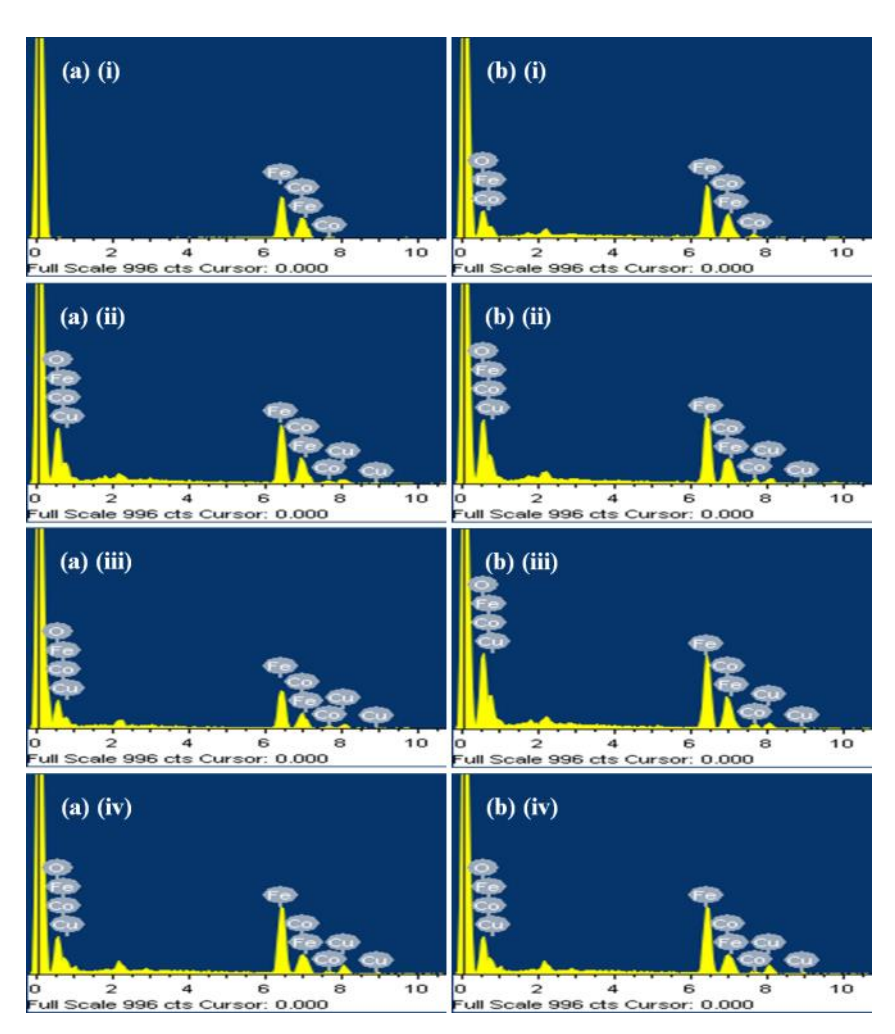


Fig. 3.6 EDAX spectrum of copper-substituted cobalt ferrite nanoparticles $Co_{1-x}Cu_xFe_2O_4$ (x = 0.0-0.4); (i) $CoFe_2O_4$ (ii) $Co_{0.8}Cu_{0.2}Fe_2O_4$ (iii) $Co_{0.75}Cu_{0.25}Fe_2O_4$ (iv) $Co_{0.6}Cu_{0.4}Fe_2O_4$ (a) as-synthesized nanoparticles heated at 90 °C, and (b) nanoparticles heated at 600 °C for 3 h.

For as-synthesized powders, the ratio of Fe/Co is 1.97 in CoFe₂O₄, and the ratio of Cu/Co is 0.24 in Co_{0.8}Cu_{0.2}Fe₂O₄, which is very close to the expected value 0.25. The ratio Cu/Co is 0.452 and 0.729 for Co_{0.75}Cu_{0.25}Fe₂O₄ and Co_{0.6}Cu_{0.4}Fe₂O₄ which are higher than the theoretical values of 0.333 and 0.666, respectively.

3.1.4 Transmission Electron Microscopy

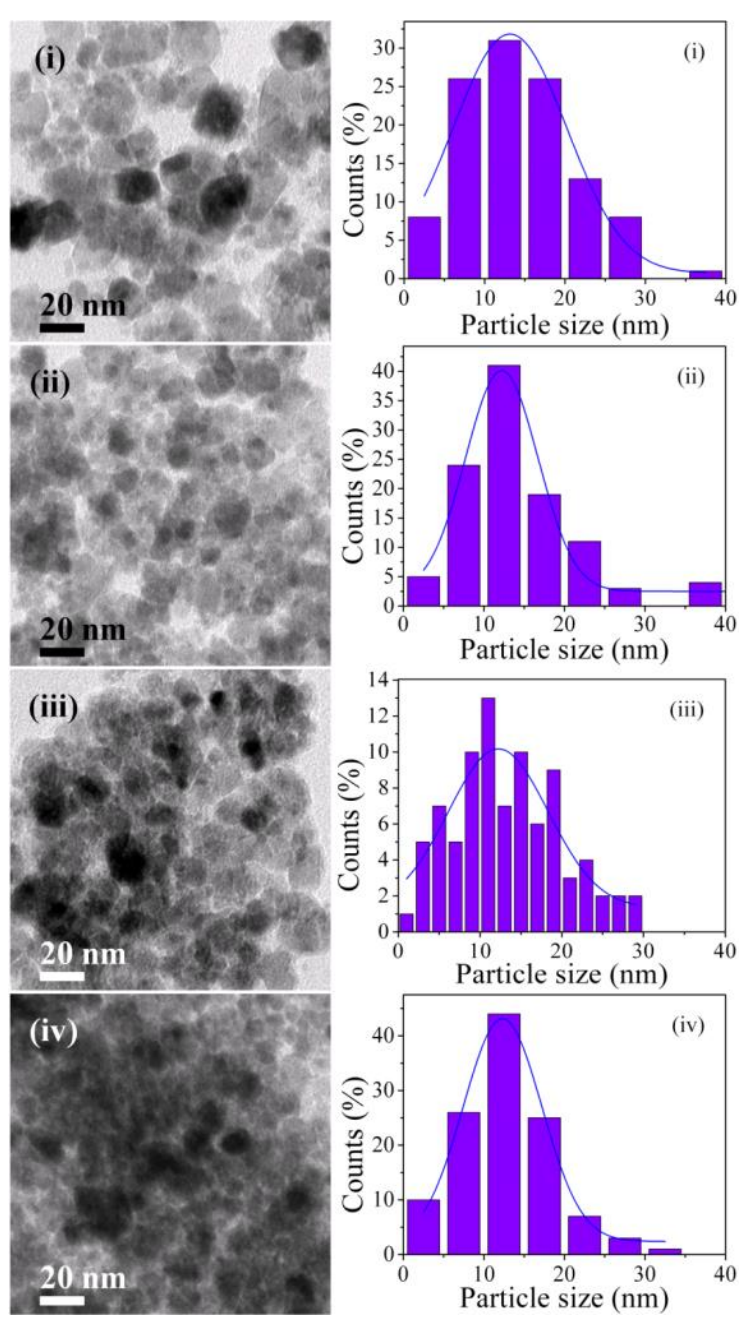


Fig. 3.7 TEM micrograph and particle size distribution of as-synthesized nanoparticles heated at 90 °C: (i) $CoFe_2O_4$ (ii) $Co_{0.8}Cu_{0.2}Fe_2O_4$ (iii) $Co_{0.75}Cu_{0.25}Fe_2O_4$ (iv) $Co_{0.6}Cu_{0.4}Fe_2O_4$.

TEM micrographs of as-synthesized Co_{1-x}Cu_xFe₂O₄ nanoparticles heated at 90 °C and 600 °C and the corresponding histograms are presented in Figs. 3.7 and 3.10, respectively. The results indicate that the samples are uniform in both morphology and particle size distribution. TEM images of nanoparticles heated at 90 °C exhibit spherical shape whereas the nanoparticles sintered at 600 °C showed hexagonal, cubic and spherical shape. The average size is in the range of 13-15 nm and 15-20 nm for as-synthesized nanoparticles heated at 90 °C and 600 °C, respectively. The particle sizes increase slightly on heat treatment.

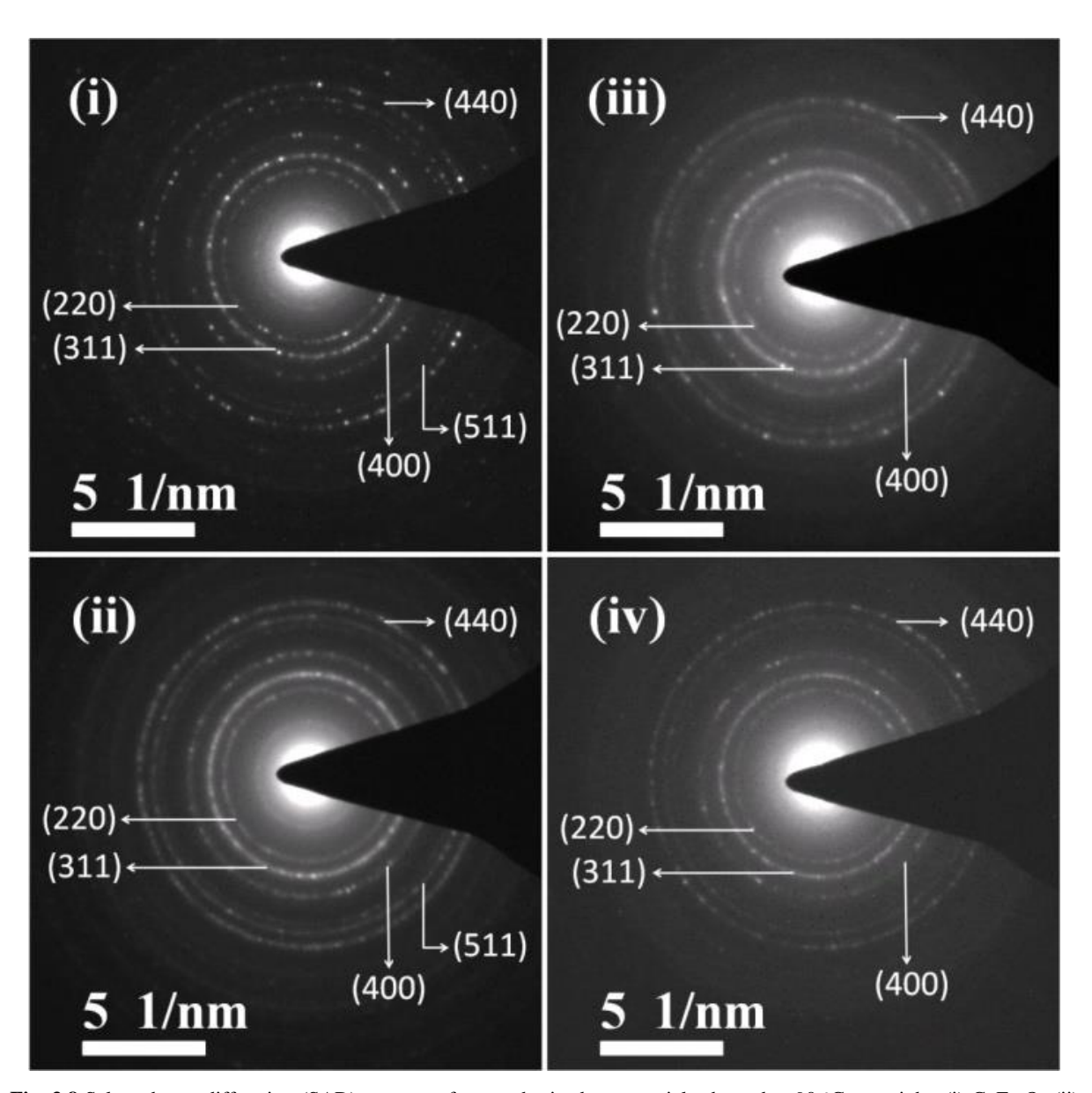


Fig. 3.8 Selected area diffraction (SAD) patterns of as-synthesized nanoparticles heated at 90 °C overnight: (i) CoFe₂O₄ (ii) Co_{0.8}Cu_{0.2}Fe₂O₄ (iii) Co_{0.75}Cu_{0.25}Fe₂O₄ (iv) Co_{0.6}Cu_{0.4}Fe₂O₄.

The selected area electron diffraction (SAED) patterns of the as-synthesized nanoparticles heated at 90 °C and 600 °C shown in Figs. 3.8 and 3.11, respectively, confirm their crystalline nature. Each diffraction ring corresponds to a set of parallel planes. The lattice plane is identified by measuring the radius of each circle, which is equal to d-spacing, and compared them with JCPDS (card no # 98-016-0059). The images in Fig. 3.8 show distinct diffraction circles in the (220), (311) (400) (511) and (440) crystal planes of CoFe₂O₄.

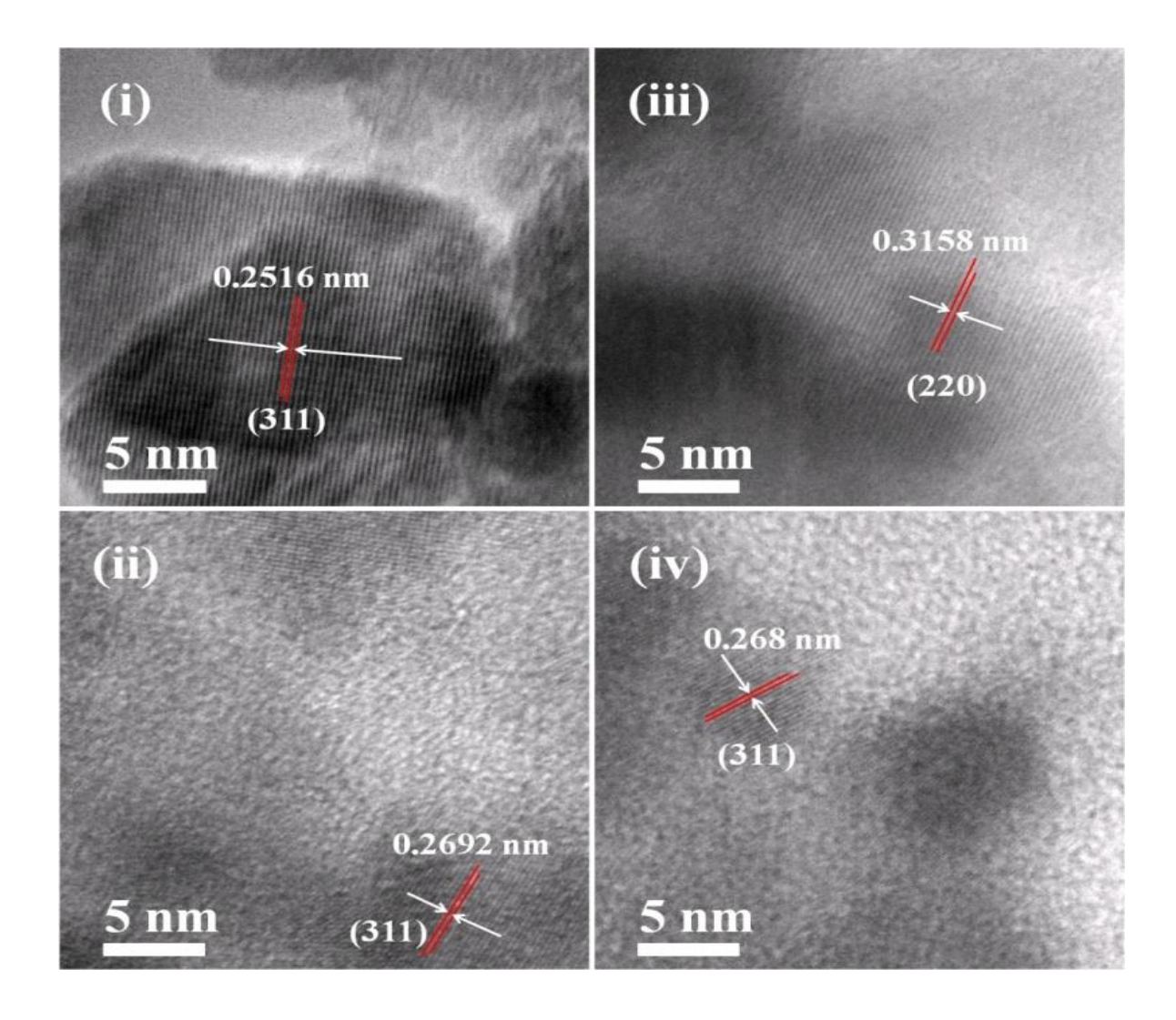


Fig. 3.9 HRTEM lattice fringes of nanoparticles heated at 90 $^{\circ}$ C overnight: (i) CoFe₂O₄ (ii) Co_{0.8}Cu_{0.2}Fe₂O₄ (iii) Co_{0.75}Cu_{0.25}Fe₂O₄ (iv) Co_{0.6}Cu_{0.4}Fe₂O₄.

The high resolution TEM (HRTEM) images of as-synthesized nanoparticles heated at 90 °C and 600 °C in Figs. 3.9 and 3.11 show the lattice fringes of the nanocrystallites. The interplanar

spacing calculated from the lattice fringes reveal formation of $(2\ 2\ 0)$, $(3\ 1\ 1)$ and $(4\ 0\ 0)$ planes of cobalt ferrite. The HRTEM analysis reveals that $CoFe_2O_4$ nanoparticles have spherical/squares shape. The histograms of as-synthesized nanoparticles heated at 90 °C show that the maximum size distribution is in the range of 10–15 nm for all the samples. For nanoparticles heated at 600 °C, except for $Co_{0.6}Cu_{0.4}Fe_2O_4$, maximum size distribution is in the range of 20–25 nm.

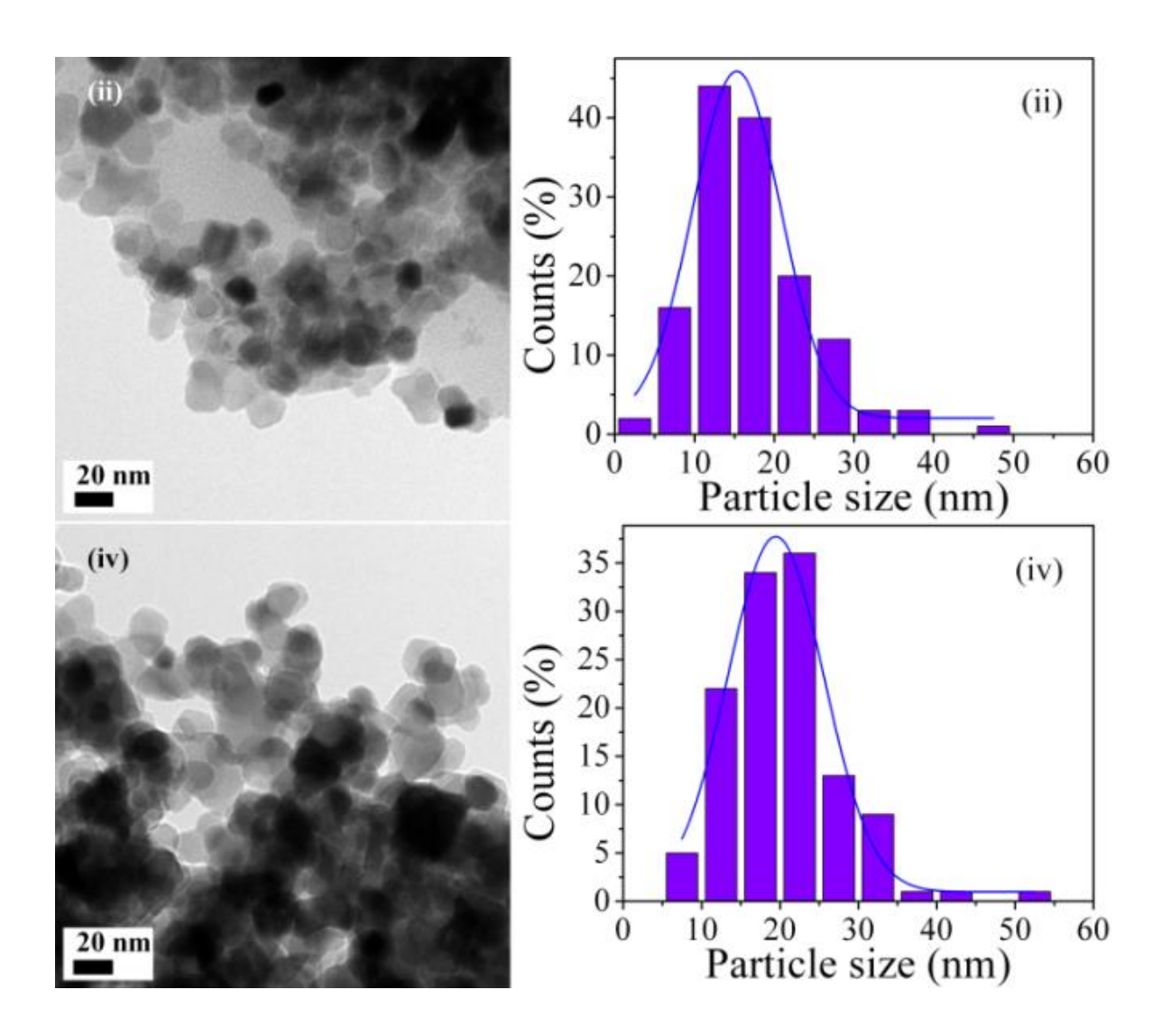


Fig. 3.10 TEM micrograph and particle size distribution of nanoparticles heated at 600 °C for 3 h: (i) CoFe₂O₄ (ii) Co_{0.8}Cu_{0.2}Fe₂O₄ and (iv) Co_{0.6}Cu_{0.4}Fe₂O₄.

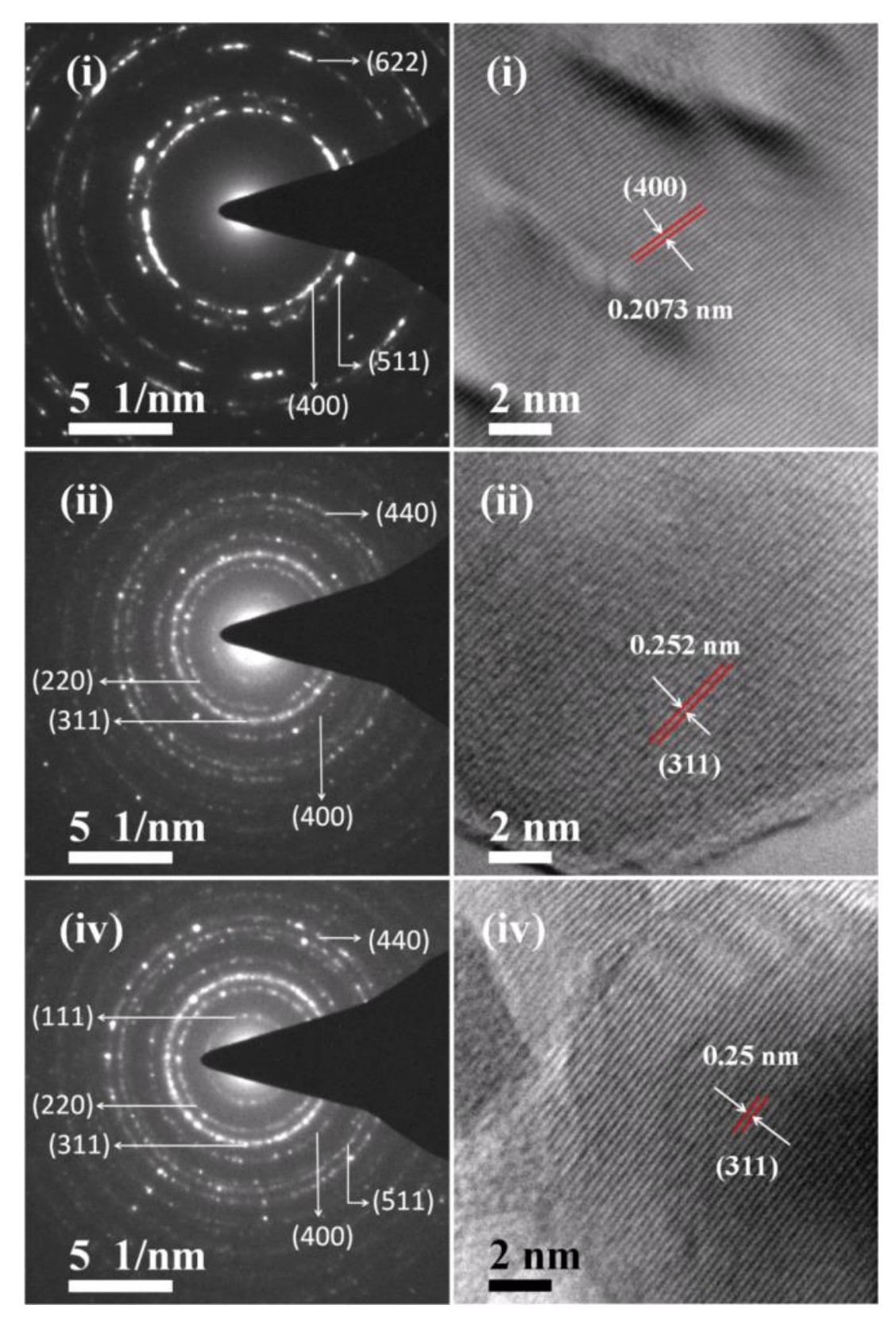


Fig. 3.11 Selected area diffraction (SAD) patterns [Left Panel] and HRTEM images [Right Panel] of nanoparticles heated at $600\,^{\circ}\text{C}$ for 3 h: (i) CoFe_2O_4 (ii) $\text{Co}_{0.8}\text{Cu}_{0.2}\text{Fe}_2\text{O}_4$ and (iv) $\text{Co}_{0.6}\text{Cu}_{0.4}\text{Fe}_2\text{O}_4$.

3.1.5 Magnetic properties

The M-H loops of $\text{Co}_{1-x}\text{Cu}_x\text{Fe}_2\text{O}_4$ (x=0.0 to 0.4) samples as-synthesized (heated at 90 °C) and annealed at 600 °C are shown in Fig. 3.12. An expanded view is shown in the inset of the figure. The magnetization at 1.5 T (M_s), remanent magnetization (M_R), and coercivity (H_c) of the samples are tabulated in Table 3.2. For as-synthesized CoFe_2O_4 nanoparticles heated at 90 °C the maximum H_c and M_s are 636 G and 134 emu/g. M_s value of nanoparticles is higher than the bulk CoFe_2O_4 . The M_s value is much larger than previously reported for CoFe_2O_4 nanoparticles heated at 95 °C by Stein *et al.* [1].

For samples heated at 90 °C the M(H) loops clearly indicate that M_s , M_r and H_c decreases gradually as the doping concentration of Cu increases from 0 to 40% (x=0.0 to 0.4). The magnetic measurements of the CoFe₂O₄ nanoparticles indicate an H_c = 636G, M_r = 43 emu/g, and $M_s=134$ emu/g. The high M_s value CoFe₂O₄ can be explained on the basis of random distribution of cations. In an ideal inverse spinel cobalt ferrite, the O²⁻ anions pack in the fcc positions of the unit cell, and half of Fe³⁺ cations (5µ_B) occupy 8 (of 64) tetrahedral holes and the remaining half occupy 8 (of 32) octahedral holes, and all the Co²⁺ cations fill the remaining 8 octahedral (B) sites. As the spin magnetic moments of the cations in the tetrahedral (A) sites and octahedral (B) sites are oriented antiparallel because of the superexchange interaction across oxygen involving the cations (Fe³⁺ and Co²⁺), the magnetic moments of Fe³⁺ ions gets cancelled. The net moment of ideal inverse spinel CoFe₂O₄ arises only from the magnetic moment of Co²⁺ ions. Sometimes, CoFe₂O₄ can be a partial normal spinel, while the tetrahedral (A) sites are partially occupied by Co²⁺. If a fraction of Co²⁺ ions occupy tetrahedral holes then the octahedral holes which are not filled by Co²⁺ ions are filled by Fe³⁺ cations, leading to a mixed spinel structure, and consequently, a large increase in the saturation magnetization (M_s) . The M_S decreases systematically as the Cu doping increases from x=0.2 to 0.4, acopanied by decrease in crystallite size (Table 3.1).

The M_S decreases from 134 to 107 emu/g as x increases from 0 to 0.2, which is a decrease of about 20%. There is a decrease of M_S (104 emu/g) about 22.4% for the sample with x = 0.25, whereas the 40% Cu doped sample show a decrease of about 36.57% of M_S (85 emu/g). The decrease in M_S with increase in Cu²⁺ is because of substitution of Co²⁺ by Cu²⁺ at octahedral sites. Noting that the directions of magnetization for the A and B sublattices in ferromagnetic materials are antiparallel, the net magnetization (in μ_B) can be written as M (μ_B) = M_B - M_A ,

where M_A and M_B are magnetic moments of A and B sublattices. Substitution of Cu might displace cations of Co and Fe to A-sites from B-sites leading to a decrease in saturation magnetization (M_S). At higher Cu content (x= 0.25 and 0.4) fraction of Co²⁺ might be substituted at tetrahedral sites also leading to decrease in magnetization (M_S) which is not linear at x=0.25 to 0.4. The decrease in H_c value with the Cu doping is due to decrease in crystallite size (Tables 3.1 and 3.2).

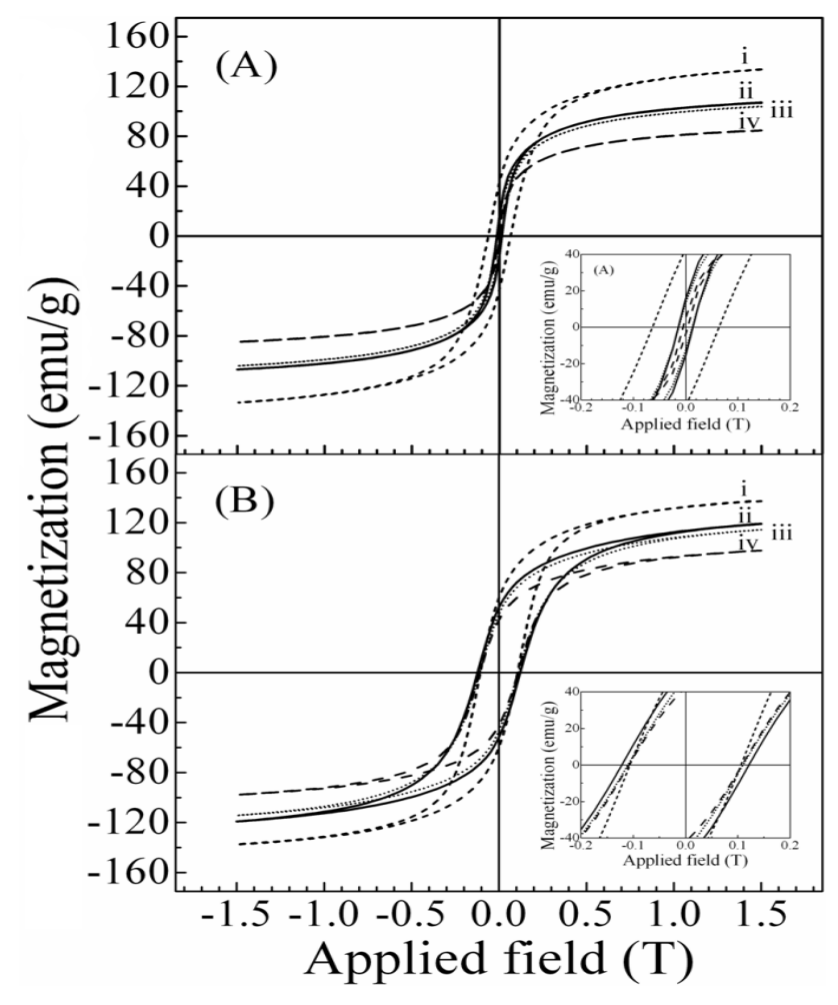


Fig. 3.12 M(H) hysteresis loops of copper-substituted cobalt ferrite nanoparticles $Co_{1-x}Cu_xFe_2O_4$ (x = 0.0-0.4); (i) x = 0 (ii) x = 0.2 (iii) x = 0.2 (iv) x = 0.4 (**A**) as-synthesized nanoparticles heated at 90 °C, and (**B**) nanoparticles heated at 600 °C.

After heating the nanopowders at 600 °C for 3 h, a slight increase in M_s , significant increase in M_r , and a large increase in H_c (except pure CoFe₂O₄) is observed for all compositions. The M_s obtained for (x = 0) sample is 137 emu/g which is smaller than reported by Jeppson et al. [3]. They reported M_s of 144 emu/g for CoFe₂O₄ annealed in nitrogen at 600 °C [3]. We attribute

this increase in M_s due to the presence of Co^{3+} (4 μ_B) ion in the octahedral site leading to an increase in M_B , magnetic moment of B site. The M_s reduced from 137 to 98 emu g⁻¹, as x changes from 0 to 0.4. The decrease in M_s might be due to the migration of more Fe^{3+} and smaller fraction of Fe^{2+} (4 μ_B) to A site from B site so that net magnetic moment decreases. Also when both Cu^{2+} and Co^{2+} occupy octahedral site, M_s decrease due to decrease in M_B . However, the reduction in M_s is small with increasing copper content as compared to the samples heated at 90 °C. This could be due to the formation of a fraction of non-magnetic Cu^+ (0 μ_B) ion in tetrahedral site [4] which will lead to an increase in the net magnetic moment so that the decrease in M_s is only 13%, 16.8% and 28.5% as Cu content increases between x=0.2-0.25-0.4, respectively (Table 3.2). The M_s value for $CoFe_2O_4$ nanoparticles annealed at 600 °C is greater than that of cobalt ferrite nanoparticle reported earlier [5-12] and that of bulk $CoFe_2O_4$ (90 emu/g) [13].

Table 3.2 Magnetic properties of $Co_{1-x}Cu_xFe_2O_4$ (x=0.0, 0.2, 0.25 and 0.4) nanoparticles

Co _{1-x} Cu _x Fe ₂ O ₄	M_r	M_s	H_c				
(x)	(emu/g)	(emu/g)	(G)				
Co _{1-x} Cu _x Fe ₂ O ₄ (Nanoparticles heated at 90 °Covernight)							
0	43	134	636				
0.2	16	107	137				
0.25	13	104	131				
0.4	5	85	58				
$Co_{1-x}Cu_xF$	e ₂ O ₄ (Nanoparti	cles heated at 600 °	C for 3 h)				
0	60	137	582				
0.2	52	119	1217				
0.25	47	114	1102				
0.4	42	98	1081				

For CoFe₂O₄, H_C is found to be reduced to lower value of 582 G, whereas for samples with x = 0.2, 0.25 and 0.4, a large increase in H_c is observed. The value of coercivity, H_c decreases from 1217 to 1081G as Cu concentration increase from x=0.2–0.4. This might be due to reduction in anisotropy and grain size with increase in Cu²⁺ doping [14-15]. As the orbital moment of Co²⁺ occupied at B-sites of the spinel structure is relatively large, the magnetocrystalline anisotropy is not negligible even though the crystal structure of CoFe₂O₄ is face-centered cubic [16]. The spin-orbit coupling would increase anisotropy energy resulting increase in H_c and decrease of M_s .

The remanence (M_r) values exhibit a large increase on heat treating samples at 600 °C and decreases with increase in Cu doping level. The change in M_r value is due to the change in

magneto crystalline anisotropy resulting from cation distribution. Bulk cobalt ferrite is inverse spinel but in nano dimension the occupation tendency of Co^{2+} among tetrahedral and octahedral sites is arbitrary so that fraction of smaller Fe^{3+} (0.645 Å) [17] can migrate to octahedral site and replace the heavier Co^{2+} (0.745 Å) cations [18-20]. The substitution of bigger Cu^{2+} (3d⁹) ion (0.87 Å) at B-site by replacing smaller Co^{2+} (3d⁷) ion (0.74 Å) distorts octahedral symmetry and hence the substitution of Cu reduces the magneto-crystalline anisotropy. Therefore, this might be the reason for a decrease in remanence (M_r).

3.1.6 Conclusions

Nanoparticles of cobalt ferrite and copper doped cobalt ferrite $Co_{1-x}Cu_xFe_2O_4$, (x = 0, 0.2, 0.25, and 0.4) were synthesized successfully using co-precipitation method. Rietveld refined XRD patterns confirm single phase spinel structure with Fd-3m space group. As-synthesized nanoparticles (heated at 90 °C) size is in the range of 10-14 nm. After annealing particle size increases to 18-22 nm. Particle size estimated from TEM are in agreement with crystallite sizes. Grain size estimated from FESEM show that grain is made up of few crystallites. The M_s values increases slightly on heat treatment. Highest magnetization (137 emu/g) is observed for $CoFe_2O_4$ NPs which were heated at 600 °C for 3 hours. The nanoparticle of composition with x = 0.2, annealed at 600 °C exhibit high coercivity of 1217 G and saturation magnetization of 119 emu/g.

3.2 Structural, magnetic and dielectric properties of bulk $CoFe_2O_4$ and copper doped cobalt ferrites $Co_{1-x}Cu_xFe_2O_4$ (x=0.0, 0.2, 0.25 and 0.4)

3.2.1 Introduction

Studies on the influence of particle interactions of increasing strength on nanoparticles (γ -Fe₂O₃) with different particles sizes and particle interactions show a change from the superparamagnetic to ferrimagnetic state [21-22]. In addition to the magnetic properties iron ferrite nanoparticles can be used in developing supercapacitors with stable cycling performance [23], for absorption of electromagnetic radiation [24], metal-oxide-semiconductor capacitors [25], and chemical sensors [26]. Jonker [27] explained two regions of low and high conductivity due to the different ionic structures Co²⁺ and Co³⁺ and Fe²⁺ and Fe³⁺in cobalt ferrite, causes the mechanism of hole and electron hopping, respectively. For cobalt ferrite, the dielectric constant is found to increase with increase of particle size while dielectric loss (tan δ) decreases as of

particle size increases and may have no clear correlation with particle size [28-30]. Several reports on electrical conductivity and dielectric properties of bulk CoFe₂O₄ are available in the literature [31-33].

In this study the $Co_{1-x}Cu_xFe_2O_4$, (x = 0, 0.2, 0.25, and 0.4) nanopowders fabricated by coprecipitation technique (as given in Section 2.2.1) are pressed into pellets to study their magnetic and dielectric properties by heating them at different annealing temperatures. Substitution of Co with Cu ions improved the magnetic properties, and dielectric properties. The effects of copper substitution on structural, magnetic and dielectric properties of $Co_{1-x}Cu_xFe_2O_4$ bulk ferrites are reported.

3.2.2 Structural characterization

The X-ray diffraction patterns of $\text{Co}_{1-x}\text{Cu}_x\text{Fe}_2\text{O}_4$ (x = 0.0, 0.2, 0.25 and 0.4) nano-particles sintered at 100, 600 (and 600 °C for 3 h) and 1200 °C for 4 h, are shown in Fig. 3.13. The indexed peaks of the crystal planes (1 1 1), (2 2 0), (3 1 1), (2 2 2), (4 0 0), (4 2 2), (5 1 1), (4 4 0), (5 3 1) (6 2 0), (5 3 3), (6 2 2) and (4 4 4) corresponds to spinel structure consistent with JCPDS # 98-016-0059 and confirms highly pure crystalline $\text{Co}_{1-x}\text{Cu}_x\text{Fe}_2\text{O}_4$ bulk and nanoparticles. XRD pattern of the samples matches to spinel structure with space group Fd-3m.

Rietveld refinement method using Xpert HighScore plus software program (Figs. 3.14, 3.15, 3.16 and 3.17) was used to estimate structural parameter of $Co_{1-x}Cu_xFe_2O_4$ bulk materials. Rietveld refinement was done without background correction. The Rietveld refined X-ray diffraction patterns are shown in Figures 3.14, 3.15, 3.16 and 3.17. The various R factors and "goodness of fit" values are listed in Table 3.3. Low values of χ^2 (goodness of fit) establish the goodness of refinement. Each panel (i, ii, iii, and iv) in the figures represent the samples $CoFe_2O_4$, $Co_{0.8}Cu_{0.2}Fe_2O_4$, $Co_{0.75}Cu_{0.25}Fe_2O_4$ and $Co_{0.6}Cu_{0.4}Fe_2O_4$, respectively. Crystallite size (D_{XRD}) of the samples was estimated using the Debye-Scherrer equation [2] $D = 0.9\lambda/\beta \cos\theta$ where λ is the wavelength of X-rays, β is the full width of the diffraction line at half the maximum intensity and θ is Bragg angle. The evaluated average crystallite sizes are tabulated in Table 3.3 for the different sets of the four samples sintered at different temperatures used in the experiments. The crystallite sizes were small for samples heated at 100 °C (below 14 nm) and increased with increasing annealing temperature. The average crystalline sizes are 14, 11, 11 and 10 nm for (a) (i) $CoFe_2O_4$, (ii) $Co_{0.8}Cu_{0.2}Fe_2O_4$, (iii) $Co_{0.75}Cu_{0.25}Fe_2O_4$, and (iv) $Co_{0.6}Cu_{0.4}Fe_2O_4$, pellets heated at 100 °C for 4 h, respectively, 19.5, 18, 19.2, and 21.3 nm for

(b) (i), (ii), (iii) and (iv), pellets heated at 600 °C for 3 h, respectively, and 20, 19, 17, and 22 nm for (c) (i), (ii), (iii) and (iv), pellets heated at 600 °C for 4 h, respectively, 84, 83, 87 and 93 for (d) (i), (ii), (iii) and (iv), pellets sintered at 1200 °C for 4 h respectively.

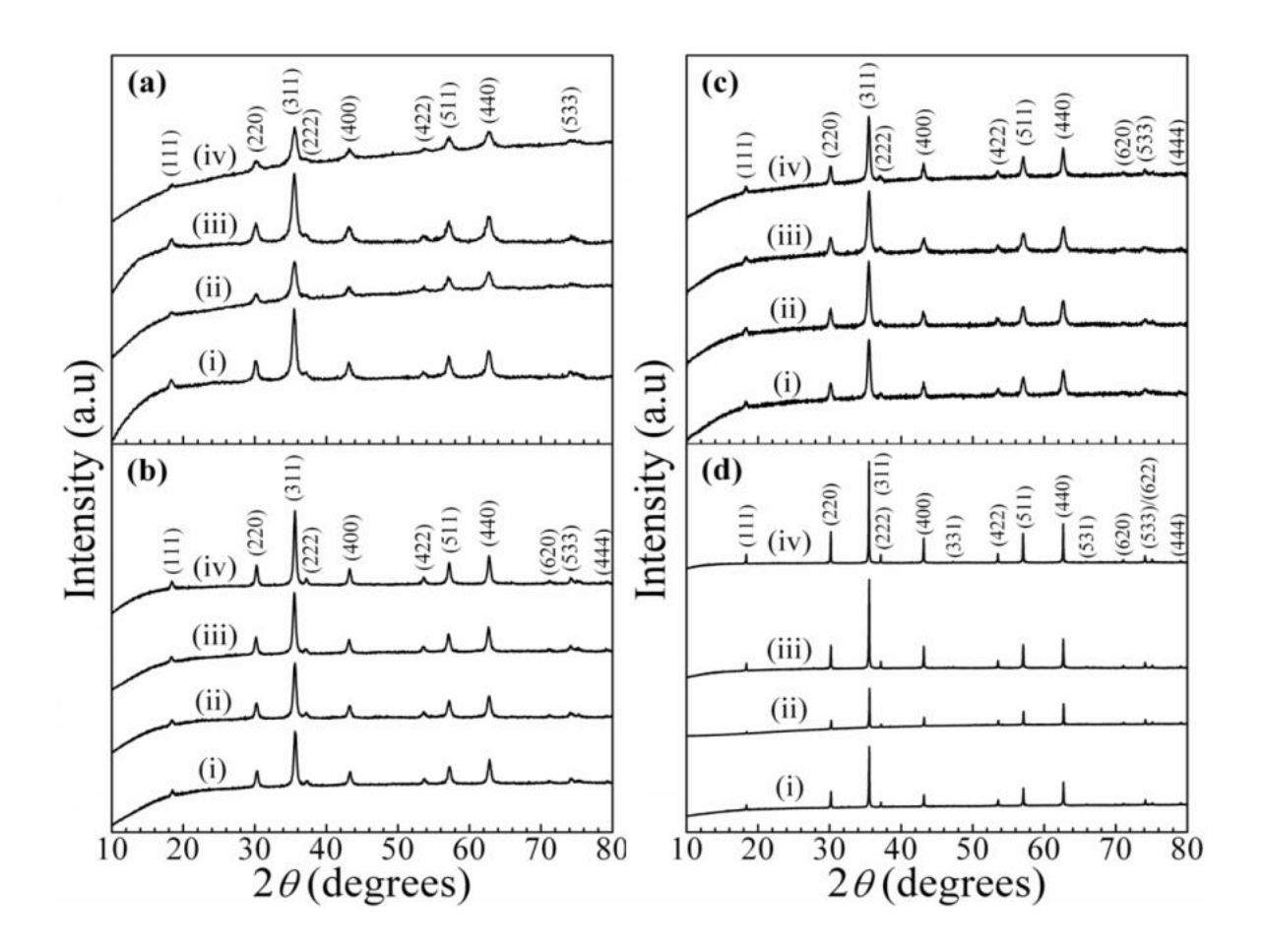


Fig. 3. 13 XRD pattern of copper doped cobalt ferrite samples $Co_{1-x}Cu_xFe_2O_4$ (x = 0.0, 0.2, 0.25 and 0.4); (i) $CoFe_2O_4$ (ii) $Co_{0.8}Cu_{0.2}Fe_2O_4$ (iii) $Co_{0.75}Cu_{0.25}Fe_2O_4$ and (iv) $Co_{0.6}Cu_{0.4}Fe_2O_4$ which are heated at (\boldsymbol{a}) 100 °C for 4 h, (\boldsymbol{b}) 600 °C for 3 h, (\boldsymbol{c}) 600 °C for 4 h and (\boldsymbol{d}) 1200 °C for 4 h.

Table 3.3 Rietveld parameters, estimated Lattice parameter, crystallite size (XRD), and average grain size (FESEM)

$Co_{1-x}Cu_xFe_2O_4$	$\mathbf{x} = 0 \; (\mathbf{i})$	x = 0.2 (ii)	x = 0.25 (iii)	x = 0.4 (iv)			
Co _{1-x} Cu _x Fe ₂ O ₄ Pellets Heated at 100 °C for 4 h							
Lattice parameter (Å)	8.372(1)	8.374(2)	8.376(1)	8.374(2)			
D_{XRD}	13.8	11	11	9.8			
G_{FESEM} (±1 nm)	51	40	45	49			
R (expected)/%	0.6496	0.7624	0.6518	0.7810			
R (profile)/%	0.8456	0.8038	0.8257	0.6203			
R (weighted profile)/ %	1.0872	1.0143	1.0729	0.7810			
G.O.F	1.6736	1.3303	1.6459	1.0000			
Theoretical density, $\rho_{hkl}(g/cm^3)$	5.3109	5.3062	5.3041	5.3077			
Measured density ρ (g/cm ³)	2.027	2.5746	2.7131	2.26			
Porosity (%)	61.83	51.48	48.45	57.42			
Volume of the unit cell (Å ³)	586.7864	587.3138	587.5419	587.1424			
	22O4 Pellets Heate			207.1121			
Lattice parameter (Å)	8.3766	8.3797	8.38093	8.37952			
D _{XRD}	19.5	18	19.2	21.3			
G _{FESEM} (±1 nm)	43	48	44	58			
R (expected)/ %	0.5071	0.5233	0.5220	0.51895			
R (profile)/ %	0.5954	0.6373	0.6477	0.8345			
R (weighted profile)/ %	0.7750	0.7828	0.8185	1.0692			
G.O.F	1.5282	1.4957	2.2630	2.0604			
Theoretical density, $\rho_{hkl}(g/cm^3)$	5.3021	5.2962	5.2939	5.2966			
Measured density ρ (g/cm ³)	2.5748	2.4843	3.3438	3.1366			
Porosity (%)	51.44	53.09	36.83	40.78			
Volume of the unit cell (Å ³)	587.7667	588.4228	588.6772	588.3796			
	2204 Pellets Heate			9 2910(5)			
Lattice parameter (Å)	8.3812(7)	8.3820(6)	8.3801(7)	8.3819(5)			
D _{XRD}	20	19 128	17	22 92			
GFESEM (±1 nm)	65		71				
R (expected)/ %	0.6958	0.6997	0.7037	0.7984			
R (profile)/%	0.7425	0.7143	0.6508	0.7237			
R (weighted profile)/ %	0.9441	0.9042	0.8137	0.9298			
G.O.F	1.3569	1.2923	1.1562	1.1646			
Theoretical density, $\rho_{hkl}(g/cm^3)$	5.2934	5.2919	5.2954	5.2921			
Measured density ρ (g/cm ³)	3.1464	2.5038	3.3016	3.825			
Porosity (%)	40.55	52.68	37.65	27.72			
Volume of the unit cell (Å ³)	588.7323	588.8979	588.506	588.8762			
$Co_{1-x}Cu_xFe_2O_4$ Pellets Heated at 1200 °C for 4 h							
Lattice parameter (Å)	8.384689	8.38806(7)	8.386540	8.38646(5)			
D_{XRD}	76	73	76	88			
G_{FESEM} (±1 nm) [μ m]	66 [4]	48 [10]	56 [14]	62 [26]			
R (expected)/ %	0.56535	0.52042	0.53253	0.52222			
R (profile)/ %	0.68661	0.68517	0.72230	0.84068			
R (weighted profile)/ %	1.12613	1.31439	1.33278	1.39145			
G.O.F	1.99192	2.52565	2.50273	2.66451			
Theoretical density, $\rho_{hkl}(g/cm^3)$	5.2868	5.2804	5.2833	5.2834			
Measured density ρ (g/cm ³)	4.125	4.5326	4.7451	3.995			
Porosity (%)	21.97	14.16	10.18	24.38			
Volume of the unit cell ($Å^3$)	589.4687	590.1803	589.8592	589.8417			

Errors of lattice parameters are shown in parentheses. Average grain sizes estimated in 'µm' scale from right panel of Fig. 3.23 are given in square brackets.

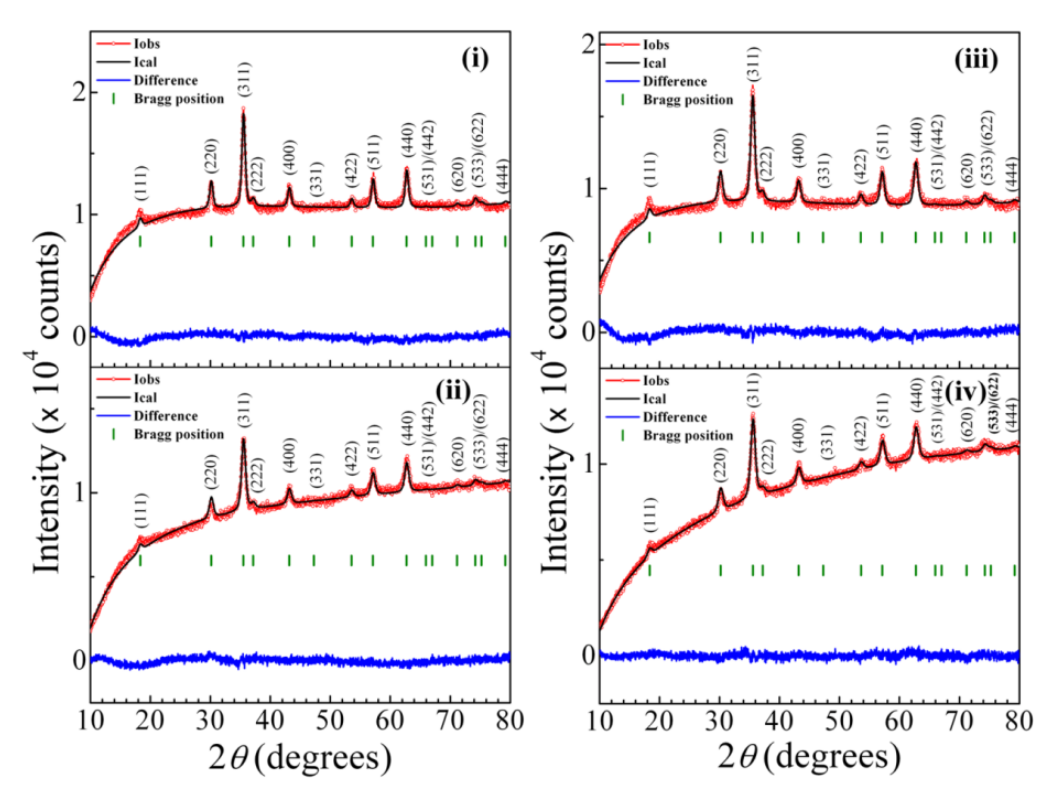


Fig. 3.14 Rietveld refined XRD patterns of copper-substituted cobalt ferrite samples $Co_{1-x}Cu_xFe_2O_4$ (x=0.0, 0.2, 0.25 and 0.4); (i) $CoFe_2O_4$ (ii) $Co_{0.8}Cu_{0.2}Fe_2O_4$ (iii) $Co_{0.75}Cu_{0.25}Fe_2O_4$ and (iv) $Co_{0.6}Cu_{0.4}Fe_2O_4$ which are heated at $100^{\circ}C$ for 4 hrs.

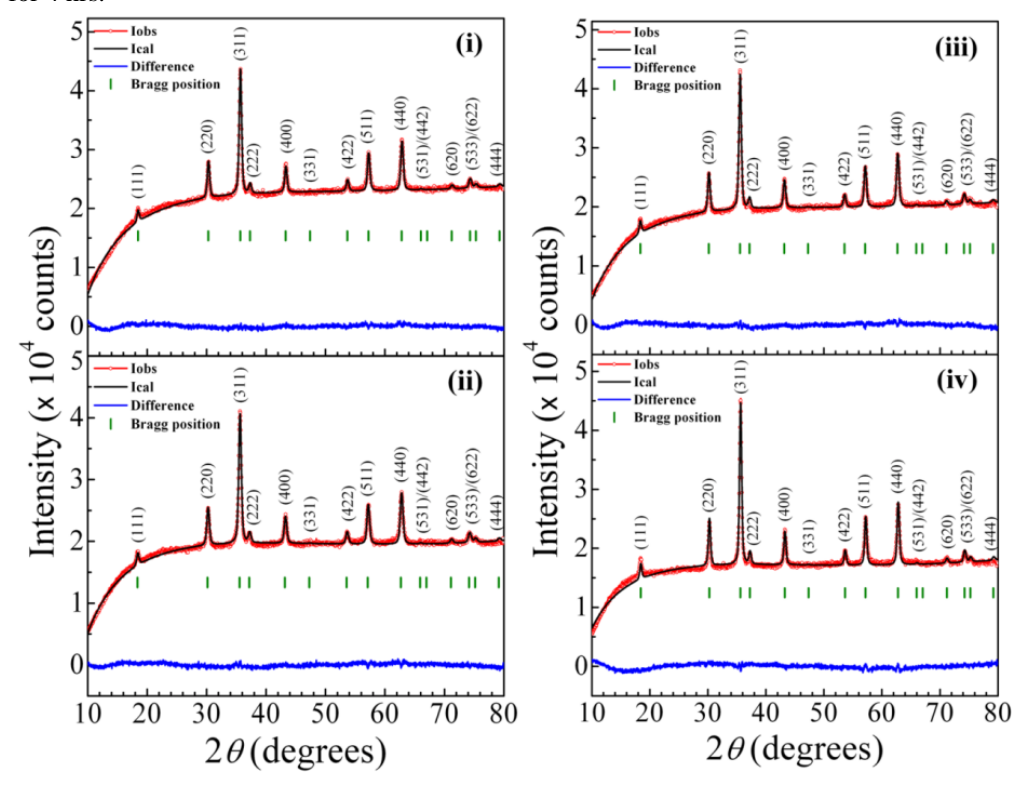


Fig. 3.15 Rietveld refined XRD patterns of copper-substituted cobalt ferrite $Co_{1-x}Cu_xFe_2O_4$ (x=0.0-0.4) samples; (i) $Co_{0.8}Cu_{0.2}Fe_2O_4$, (iii) $Co_{0.8}Cu_{0.2}Fe_2O_4$, (iii) $Co_{0.8}Cu_{0.2}Fe_2O_4$, (iii) $Co_{0.8}Cu_{0.2}Fe_2O_4$, and (iv) $Co_{0.6}Cu_{0.4}Fe_2O_4$ which are heated at $600^{\circ}C$ for 3 h.

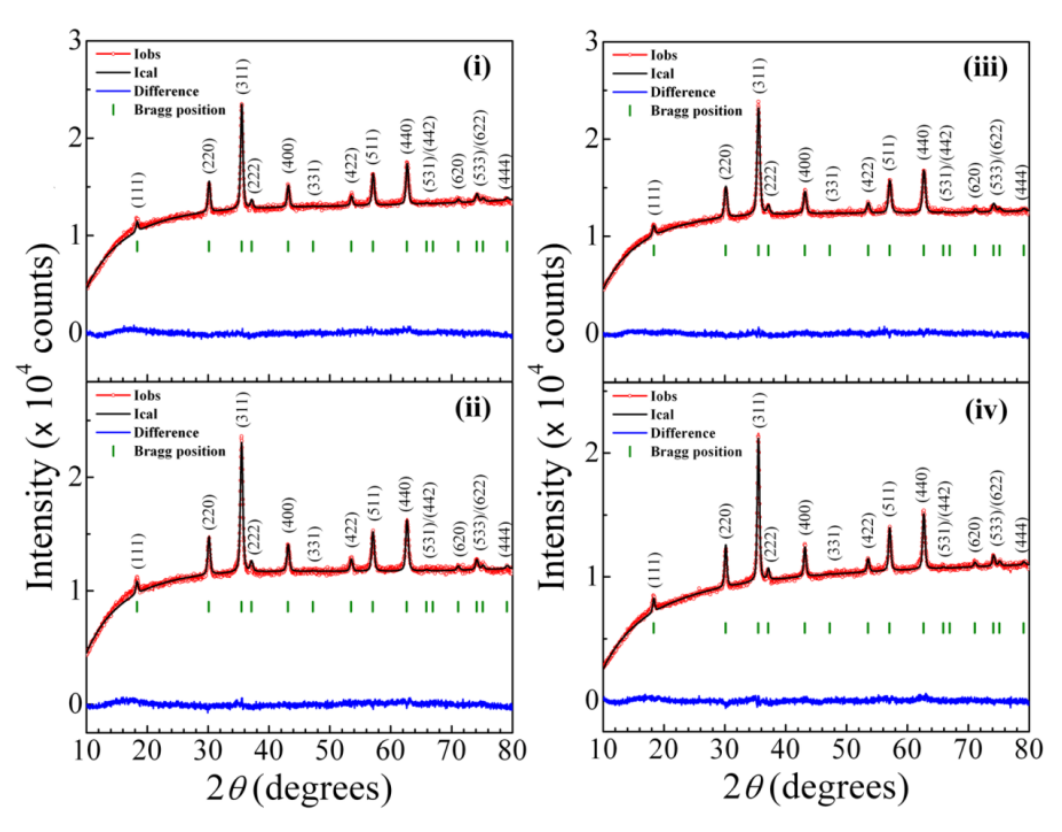


Fig. 3.16 Rietveld refined XRD patterns of copper-substituted cobalt ferrite $Co_{1-x}Cu_xFe_2O_4$ (x = 0.0-0.4) samples; (i) $Co_{0.8}Cu_{0.2}Fe_2O_4$, (iii) $Co_{0.8}Cu_{0.2}Fe_2O_4$, (iii) $Co_{0.75}Cu_{0.25}Fe_2O_4$, and (iv) $Co_{0.6}Cu_{0.4}Fe_2O_4$ which are heated at $600^{\circ}C$ for 4 h.

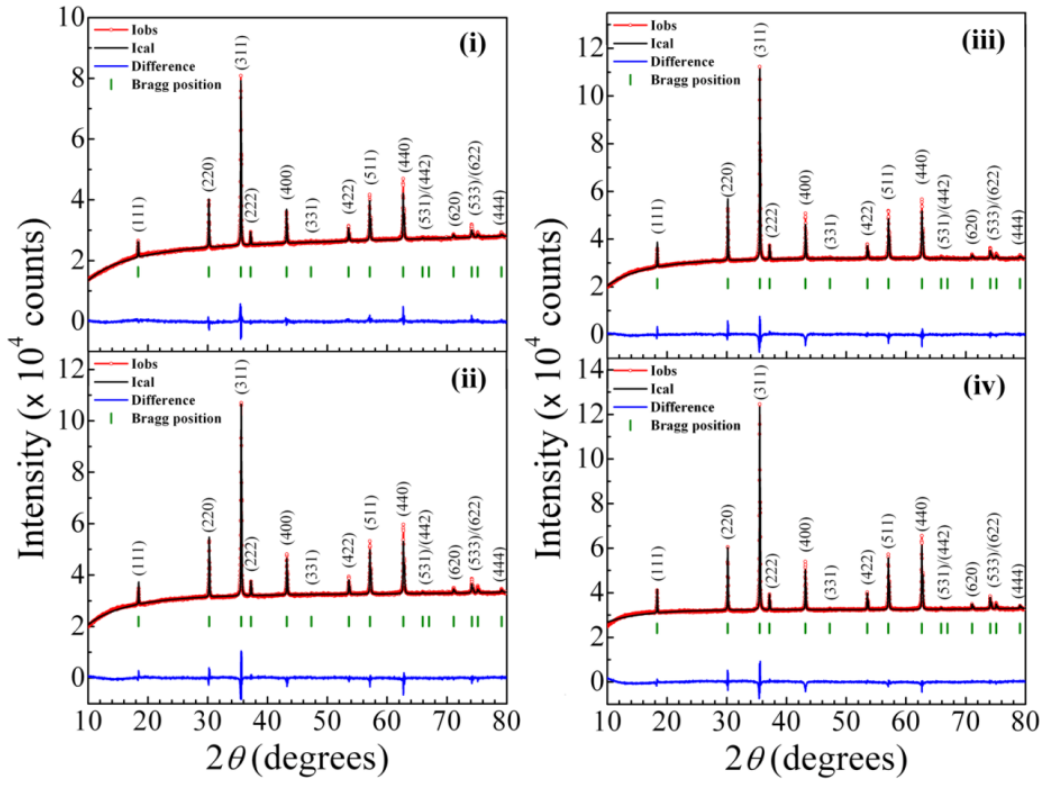


Fig. 3.17 Rietveld refined XRD patterns of copper-substituted cobalt ferrite $Co_{1-x}Cu_xFe_2O_4$ (x = 0.0-0.4) samples; (i) $CoFe_2O_4$, (ii) $Co_{0.8}Cu_{0.2}Fe_2O_4$, (iii) $Co_{0.8}Cu_{0.2}Fe_2O_4$, (iii) $Co_{0.8}Cu_{0.2}Fe_2O_4$, and (iv) $Co_{0.6}Cu_{0.4}Fe_2O_4$ which are sintered at $1200^{\circ}C$ for 4 h.

The values of ρ_x (calculated) from Rietveld method are presented in Table 3.3. Lattice parameters of CoFe₂O₄ pellets heated at 100 °C and 600 °C for 3 h are in the range of 8.37Å [34]. While Lattice parameters of CoFe₂O₄ pellets sintered at 600 °C and 1200 °C for 4 h are in the range of 8.38 Å match with the values reported in the literature [35-36].

The density of pellets ρ_m was estimated by the formula [37]

$$\rho_m = \frac{m}{\pi r^2 l} \tag{3.2}$$

where m is mass, r is radius and l is pellet thickness. The porosity is given by [37]

$$P = 1 - \frac{\rho_m}{\rho_x} \tag{3.3}$$

The values of porosity are presented in Table 3.3. Bulk density increases at higher sintering temperatures due to consequent decrease in porosity.

3.2.3 Surface morphology

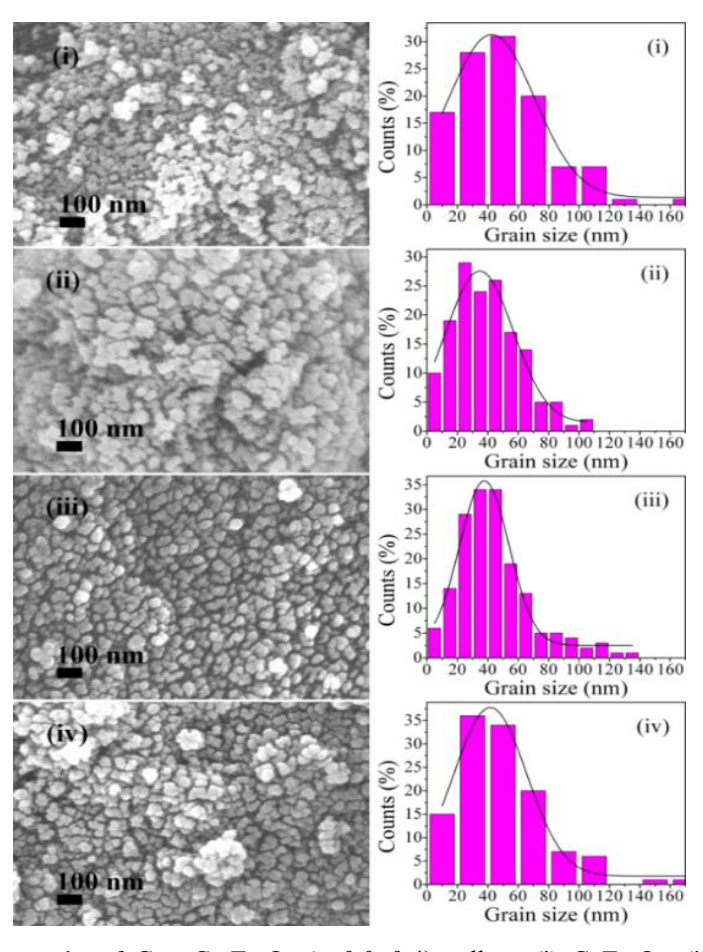


Fig. 3.18 FESEM micrographs of $Co_{1-x}Cu_xFe_2O_4$ (x=0.0-0.4) pellets; (i) $CoFe_2O_4$, (ii) $Co_{0.8}Cu_{0.2}Fe_2O_4$, (iii) $Co_{0.75}Cu_{0.25}Fe_2O_4$, and (iv) $Co_{0.6}Cu_{0.4}Fe_2O_4$ which are heated at $100^{\circ}C$ for 4 hrs and grain size distributions.

Figs. 3.18, 3.19, 3.20, and 3.21 shows FESEM images and grain size distibutions of samples sintered at $100\,^{\circ}$ C for 4 h, $600\,^{\circ}$ C for 3 h, $600\,^{\circ}$ C for 4 h. The FESEM images of all the samples heated at $100\,^{\circ}$ C and $600\,^{\circ}$ C exhibit homogeneous, almost spherical nanocrystalline morphology, whereas samples heated at $1200\,^{\circ}$ C show most of the grains irregular in shape with few spherical, tetragonal, rectangular/square and also hexagonal shape domains made up of nanocrystalline grains. Average grain sizes of the prepared samples of composition (x = 0.00 to 0.4) have been estimated by FESEM images using imageJ software and are reported in Table 3.3.

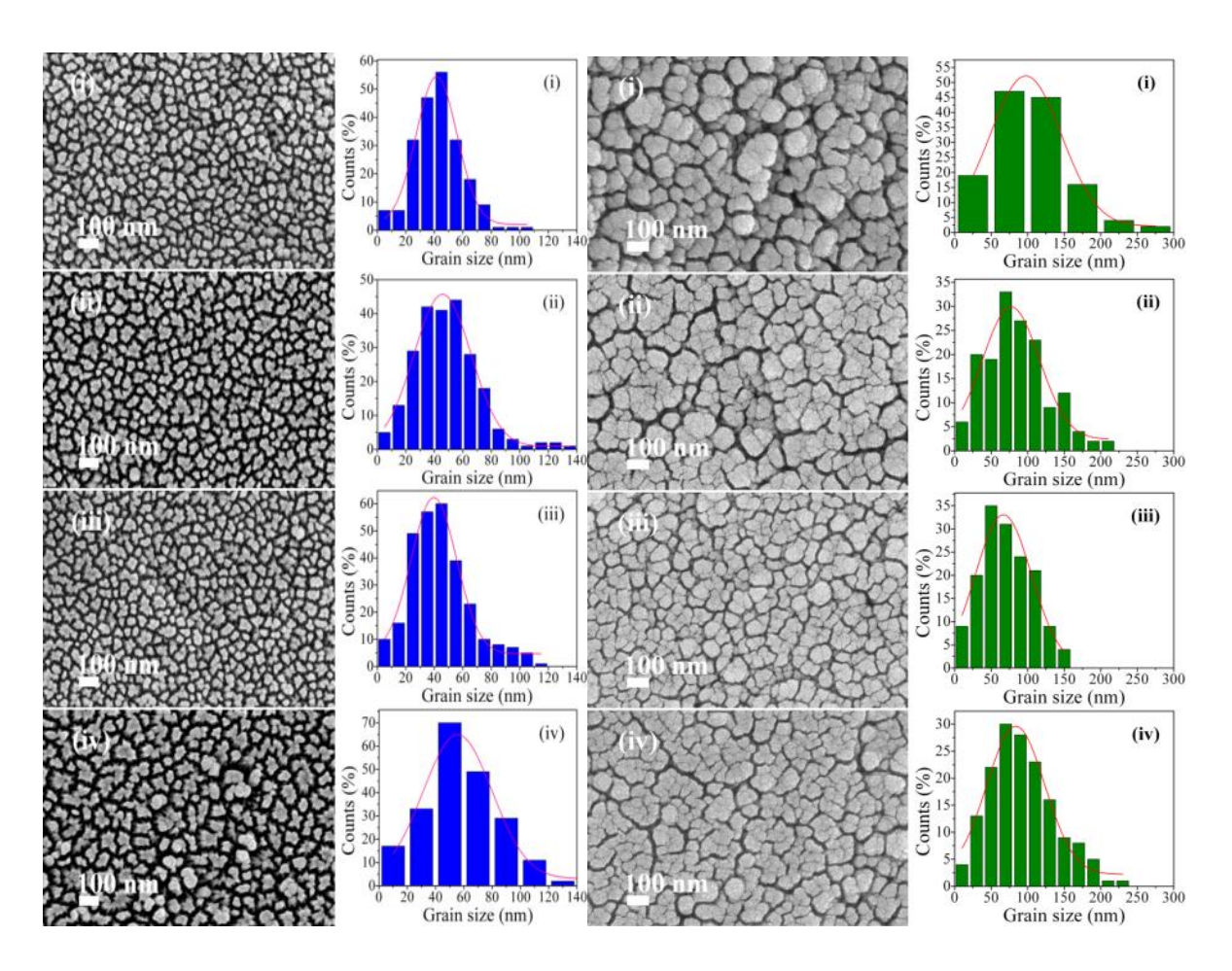


Fig. 3.19 (left) FESEM micrographs of $Co_{1-x}Cu_xFe_2O_4$ (x=0.0-0.4) pellets; (i) $CoFe_2O_4$, (ii) $Co_{0.8}Cu_{0.2}Fe_2O_4$, (iii) $Co_{0.75}Cu_{0.25}Fe_2O_4$, and (iv) $Co_{0.6}Cu_{0.4}Fe_2O_4$ which are heated at 600°C for 3 hrs and grain size distributions.

Fig. 3.20 (right) FESEM micrographs of $Co_{1-x}Cu_xFe_2O_4$ which are heated at 600°C for 4 hrs and grain size distributions.

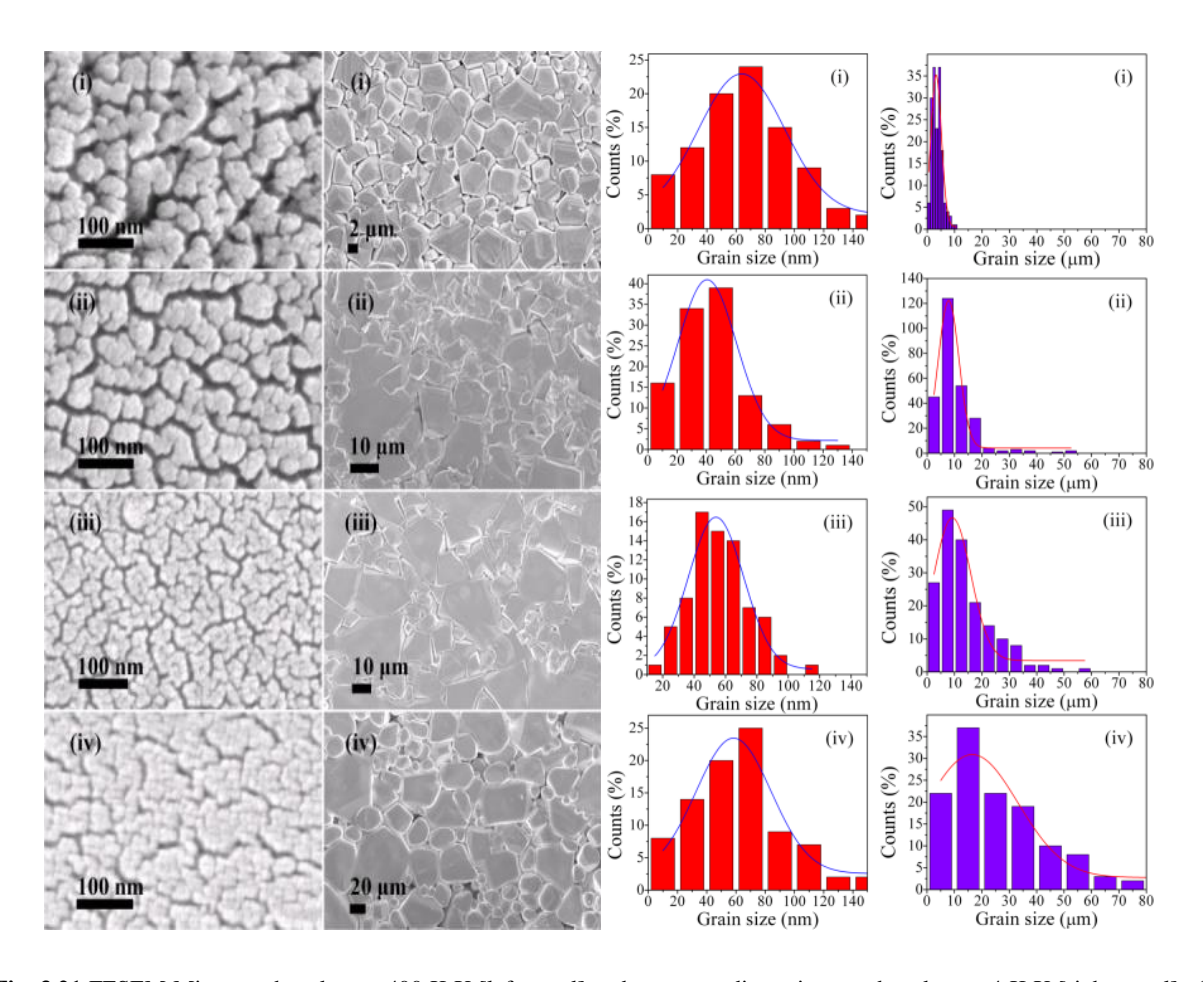


Fig. 3.21 FESEM Micrographs taken at 400 K X [left panel] and corresponding micrographs taken at 4 K X [right panel] of $Co_{1-x}Cu_xFe_2O_4$ (x=0.0-0.4) pellets; (i) $Co_{6.8}Cu_{0.2}Fe_2O_4$, (iii) $Co_{0.75}Cu_{0.25}Fe_2O_4$, and (iv) $Co_{0.6}Cu_{0.4}Fe_2O_4$ which are sintered at $1200^{\circ}C$ for 4 h.

Fig. 3.22 (right) Grain size distributions.

The average grain sizes were oscillating with Cu^{2+} ion doping for samples sintered at 600 °C, whereas average grain sizes first decreased at x=0.2 and increased thereafter with Cu^{2+} concentration for samples heated at 1200 °C. Moreover average grain sizes determined from FESEM are much greater than crystallite sizes determined by XRD, indicating that each grain is composed of a few nanocrystallites.

EDS spectra of the samples are depicted in Fig. 3.23. The EDS analysis shows presence of all constituent elements Co, Fe, Cu and O. The atomic % of all elements are given in Table 3.4. The gold peak in spectrum comes from thin conduction coating of gold on the sample. We have estimated the concentrations of the cations only because the EDS is not enough sensitive to oxygen. The atomic % ratio Fe/Co of all CoFe₂O₄ samples is 2 and for Cu doped samples the Fe/Co is >2.

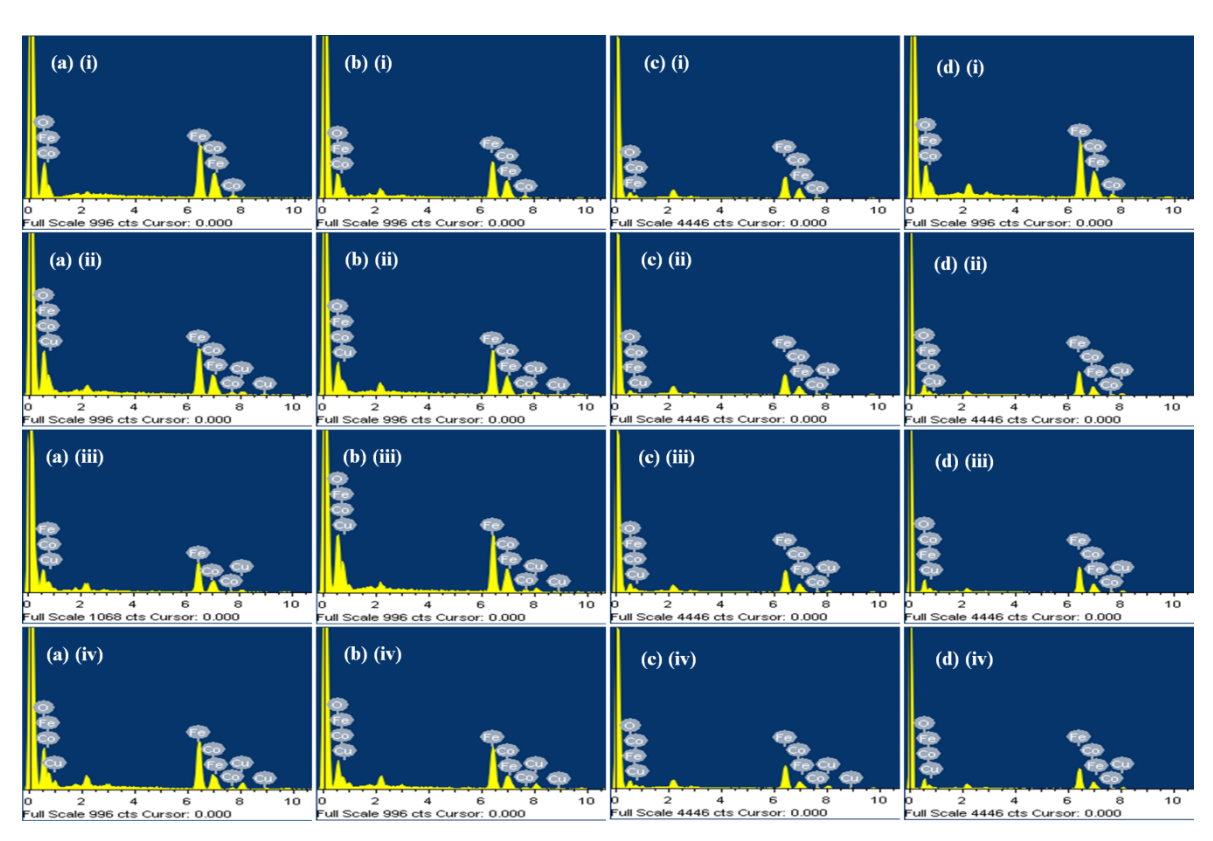


Fig. 3.23. The energy dispersive spectroscopic spectra of $Co_{1-x}Cu_xFe_2O_4$ (x=0.0-0.4) pellets; (i) $CoFe_2O_4$, (ii) $Co_{0.8}Cu_{0.2}Fe_2O_4$, (iii) $Co_{0.75}Cu_{0.25}Fe_2O_4$, and (iv) $Co_{0.6}Cu_{0.4}Fe_2O_4$ which are heated at (\boldsymbol{a}) $100^{\circ}C$, (\boldsymbol{c}) $600^{\circ}C$, (\boldsymbol{d}) $1200^{\circ}C$ for 4 h and (\boldsymbol{b}) $600^{\circ}C$ for 3 h.

Table 3.4. Composition of the prepared pellets measured from EDS

$Co_{1-x}Cu_xFe_2O_4$ $(x = 0.0-0.4)$	Elements in EDS					
	Co (atomic %)	Fe (at. %)	Cu (at. %)	Fe/Co	Cu/Co	
	$Co_{1-x}Cu_xFe_2c$	O4 (Pellets Heated	at 100 °C for 4 h)			
x=0	26.04	48.79	-	1.87	-	
x = 0.2	19.89	44.32	5.42	2.22	0.272	
x=0.25	17.60	44.59	7.48	2.53	0.425	
x = 0.4	14.29	45.20	10.66	3.16	0.746	
	$Co_{1-x}Cu_xFe_2C$	O4 (Pellets Heated	at 600 °C for 3 h)			
x=0	26.15	49.71	-	1.9	-	
x = 0.2	20.38	48.58	5.28	2.38	0.259	
x=0.25	19.64	43.66	5.02	2.22	0.256	
x = 0.4	16.14	48.66	11.69	3.01	0.724	
	$Co_{1-x}Cu_xFe_2C$	O4 (Pellets Heated	at 600 °C for 4 h)			
x=0	29.39	57.02	-	1.94	-	
x = 0.2	25.64	56.88	6.07	2.21	0.237	
x=0.25	22.82	51.95	7.45	2.28	0.326	
x = 0.4	17.02	52.92	13.02	3.1	0.765	
	$Co_{1-x}Cu_xFe_2C$	04 (Pellets Heated o	at 1200 °C for 4 h)			
x=0	26.48	51.64	-	1.95	-	
x = 0.2	21.08	51.99	8.42	2.47	0.399	
x = 0.25	20.54	53.80	8.56	2.61	0.416	
x = 0.4	20.72	53.66	9.15	2.59	0.441	

3.2.4 Magnetic properties

The room temperature magnetic properties of samples are measured by vibrating sample magnetometer (VSM) under an applied field of ± 15 kG. Fig. 3.24, shows the magnetization hysteresis loops of samples $\text{Co}_{1-x}\text{Cu}_x\text{Fe}_2\text{O}_4$ (x=0.0-0.4) samples which exhibit a typical ferrimagnetic property at room temperature. The values of coercivity (H_c), remanent magnetization (M_r) and saturation magnetization (M_s) of the samples are given in Table 3.3. The magnetic saturation (M_s) values are 137, 140, 55 and 175 emu/g for CoFe_2O_4 heated at 100, 600 and 1200 °C for 4 h, respectively which is much higher than the theoretical value of 71.2 emu·g⁻¹ [38]. The enhancement of saturation magnetization (M_s) of pure CoFe_2O_4 , might be because of occupation of Co^{2+} ions in tetrahedral holes. Co^{2+} actually goes to octahedral site. If Co^{2+} goes to tetrahedral site instead of octahedral site, the occupancy of tetrahedral site in inverse spinel structure cannot be increased, and forces transfer of same number of Fe^{3+} ions to octahedral sites. Hence magnetic moment per unit volume/unit mass (M_s), i.e. saturation magnetization increases.

The M_s of CoFe₂O₄ pellets heated at 100 °C decreased with increasing Cu doping. For pellets heated at 100 °C, the values of M_s , M_r and H_c reduced as the Cu²⁺content increased. The decrease of M_s values is due to the combined effect of grain size and substitution of Co²⁺ by a less-magnetic Cu²⁺ ion, whereas the decrease of coercivity with increasing Cu²⁺ is because of decrease in the size of the crystallite, as observed from XRD (Table 3.3). These M_s values are much larger than previously reported CoFe₂O₄ nanoparticles [6].

A slight decrease of M_s values is observed as copper doping increases for pellets sintered at 600 °C for 3 h because of the corresponding change in the grain size (Tables 3.3 & 3.5). But both H_c and M_r initially decreased for x=0.2 Cu^{2+} doping ($Co_{0.8}Cu_{0.2}Fe_2O_4$), while a slight increase was observed for x=0.25 doped samples, and again for further high doping of Cu (x=0.4) both H_c and M_r increased. The decrease in the coercive field at x=0.2 is related to the corresponding increase in grain size, and increase in H_c at x=0.25 is related to a small decrease of grain size. Finally, the decrease of coercivity at x=0.4 is related to the increase on the grain size.

Similarly, for pellets sintered at 600 °C for 4 h, both M_s and M_r decreased drastically and showed a decreasing trend, while H_c decreased from x=0.0 to 0.25 and finally increased at x=0.4. The observed changes in the M_s , M_r and H_c are due to the large grain sizes and small x-ray density values as compared to the other group of samples (Tables 3.3 and 3.5). Additionally, the

concentration of Co^{2+} in B-sites might be more in samples annealed at 600 °C for 4 h and exhibit high amount of inversion (near ideal inverse spinel) than for samples annealed at 100, and 1200 °C for 4 h resulting in lower saturation magnetization (M_s)

Finally, for pellets heated at 1200 °C for 4 h, all properties M_s , M_r and H_c exhibited a decrease at x=0.2 Cu doping and an increase at x=0.25 followed by a decrease at x=0.4. The observed changes in the M_s , M_r and H_c values are due to the corresponding changes in the grain sizes (Tables 3.3 & 3.5).

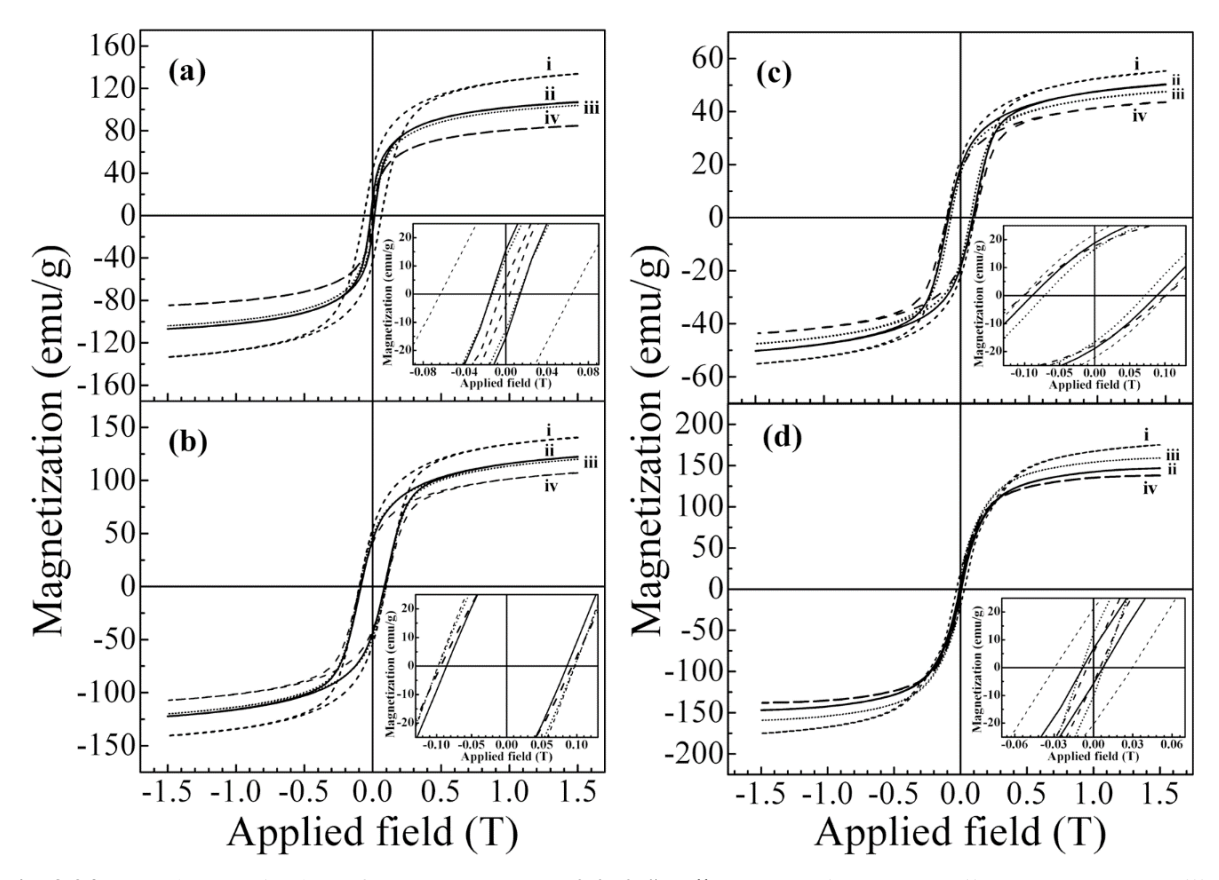


Fig. 3.24. M(H) hysteresis plots of $Co_{1-x}Cu_xFe_2O_4$ (x=0.0-0.4) pellets at RT; (i) $CoFe_2O_4$, (ii) $Co_{0.8}Cu_{0.2}Fe_2O_4$, (iii) $Co_{0.75}Cu_{0.25}Fe_2O_4$, and (iv) $Co_{0.6}Cu_{0.4}Fe_2O_4$ which are heated at (a) $100^{\circ}C$, (c) $600^{\circ}C$ and (d) $1200^{\circ}C$ for 4 h and (b) $600^{\circ}C$ for 3 h.

Due to the surface effects, in nano crystalline ferrites the density of magnetization is lower than submicron ferrites or bulk of the same alloy systems [39]. Because of this reason samples heated at 600 °C for 4 h (Fig. 3.24(c)) shows very lower M_s compared to the magnetization of the samples annealed at 1200 °C. It can also be seen that the samples heated at 100 °C, 600 °C for 3 h exhibit smaller M_s compared to M_s of samples heated at 1200 °C. Changes in magnetic

properties with heat treatment could be due to increased grain size with increasing temperature. Since pellets were heated at different temperatures cation distribution might change resulting in increase of M_s . Formation mechanism of different samples might involve different rates of grain growth when the materials were brought through a different annealing temperature even though both heating and the cooling rate are the same [40-42].

As coercivity of a material depends on its magnetocrystalline anisotropy, the increase in M_r and H_c when temperature increases from 100 to 600 °C is due to an increase of anisotropy whereas the decrease in M_r and H_c with increasing annealing temperature from 600 to 1200 °C can be due to decrease in anisotropy of CoFe₂O₄.

Table 3.5 Magnetic properties of $Cu_xCo_{1-x}Fe_2O_4$ with x = 0.0, 0.2, 0.25 and 0.4

$Cu_xCo_{1-x}Fe_2O_4$	M_r	M_s	H_c				
(x = 0.0 - 0.4)	(emu/g)	(emu/g)	(G)				
Cu_xCo_{1-x}	Cu _x Co _{1-x} Fe ₂ O ₄ (Pellets Heated at 100 °C for 4 h)						
x=0	43	134	636				
x = 0.2	16	107	137				
x = 0.25	13	104	133				
x = 0.4	5	85	44				
Cu _x Co _{1-x} Fe ₂ O ₄ (Pellets Heated at 600 °C for 3 h)							
x=0	54	140	977				
x = 0.2	44	122	858				
x = 0.25	48	120	970				
x = 0.4	41	107	937				
Cu_xCo_{1-x}	Fe ₂ O ₄ (Pellets He	ated at 600 °C for	4 h)				
x=0	22	55	1019				
x = 0.2	26	50	891				
x = 0.25	24	48	717				
x = 0.4	16.5	44	1010				
$Cu_xCo_{1-x}Fe_2O_4$ (Pellets Heated at 1200 °C for 4 h)							
x=0	21	175	296				
x = 0.2	6	146	76				
x = 0.25	11	159	83				
x=0.4	5	138	50				

The higher M_s value of the CoFe₂O₄ could be related to the disorder in the distribution of Fe³⁺ and Co²⁺ cations among A and B sites compared with a perfectly ordered inverse spinel structure. In complete inverted structure, the Fe³⁺ moments are cancelled and the net moment comes only from Co²⁺ ions. The occupation of Co²⁺ ions to octahedral sites might be less than the full. The octahedral holes which are not occupied by the Co²⁺ ions might be filled with Fe³⁺ ions which lead to the increase in M_s of the pure CoFe₂O₄. The decrease in M_s with Cu concentration could be related to the increase in cation ordering among A and B sites.

The increase in M_s with annealing temperature might be due increase in the microscopic magnetic domain size (see Fig. 3.21[left panel]) and a large number of atomic spins tend to align with the applied field direction [43-44]. Similar explanation holds for the effect of annealing on magnetic properties of Cu doped samples $Co_{0.8}Cu_{0.2}Fe_2O_4$, $Co_{0.75}Cu_{0.25}Fe_2O_4$ and $Co_{0.6}Cu_{0.4}Fe_2O_4$. The study shows that annealing temperature used for preparing the samples has strong effect on the microstructure and magnetic properties of copper doped cobalt ferrite, $Co_{1-x}Cu_xFe_2O_4$ (x=0.2, 0.25 and 0.4) materials. Fig. 3.25 show M(H) loops measured at a temperature of 100 K for the $Co_{1-x}Cu_xFe_2O_4$ (x=0, 0.2, 0.25 and 0.4) pellets heated at 1200 °C for 4 h, for the applied fields of up to ± 15 kG. Magnetization attains its saturation value, at ± 15 kG (Fig. 3.25), when compared to the samples measured at room temperature (Fig. 3.24). This might be due to the decrease in the thermal randomizing energy minimize thermal fluctuations of the spins at the surface of the grains and orient them easily along the field direction, which leads to saturation magnetization faster in these grains at 100 K.

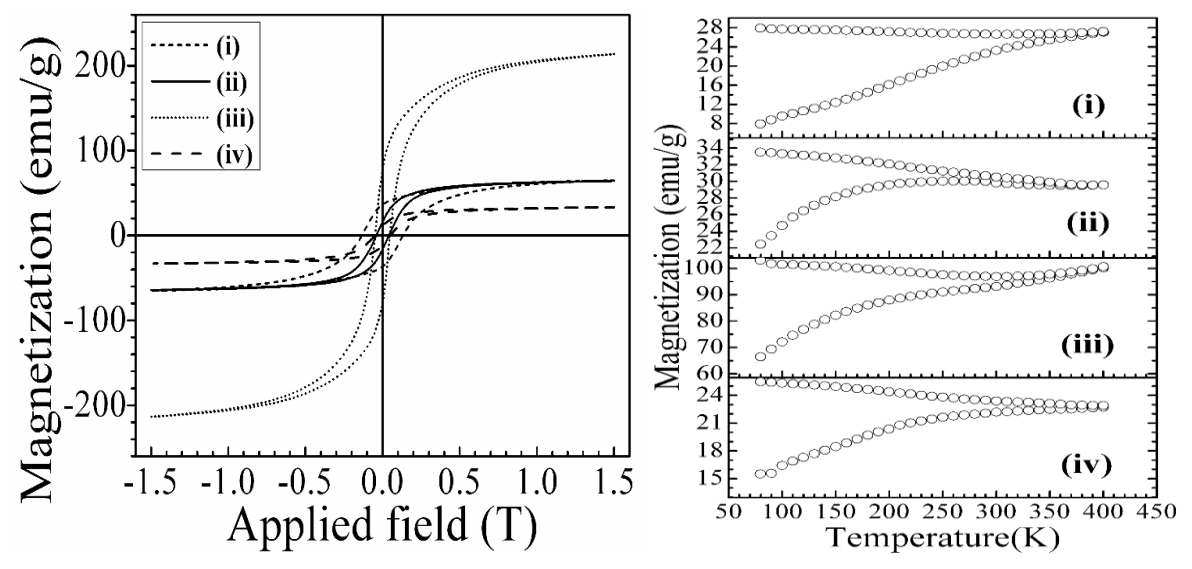


Fig. 3.25 M(H) hysteresis curves measured at 100 K of $Co_{1-x}Cu_xFe_2O_4$ (x = 0.0–0.4) pellets; (i) $CoFe_2O_4$ (ii) $Co_{0.8}Cu_{0.2}Fe_2O_4$ (iii) $Co_{0.75}Cu_{0.25}Fe_2O_4$ (iv) $Co_{0.6}Cu_{0.4}Fe_2O_4$ which are heated at 1200 °C for 4 h.

Fig. 3.26 (right) Zero field cooled and field cooled magnetizations for $Co_{1-x}Cu_xFe_2O_4$ (x = 0.0-0.4) pellets measured at an applied field of 1kG.

We observed an increase in coercivity and decrease of M_s at temperature of 100 K. The observed values of M_s are 65 emu/g, 64 emu/g, 213 emu/g and 33 emu/g and H_c values are 1332, 407, 476 and 499 G and M_r values are 37, 16, 88 and 12 emu/g, respectively for x = 0.0, 0.2, 0.25 and

0.4. When temperature is decreased, thermal fluctuations are reduced tending to make magnetic moments anisotropic, resulting in increase of coercivity [45]. At 100 K, decrease in H_c with increasing Cu amount is due to increasing particles size [13,46]. From Fig. 3.21 [right panel], we observed that the samples consist of microscopic domains which are made up of few nanocrystallites [left panel]. The decrease of saturation magnetization value of the bulk materials may be attributed to the reduced number of moments contributing [47-49].

All the samples show a large decrease in M_s compared with the value at room temperature except $Co_{0.75}Cu_{0.25}Fe_2O_4$ which exhibited very large increase in M_s at 100 K (Table 3.6). The decrease in magnetization observed at 100 K is due to increase in the anisotropy. The Mössbauer spectroscopy studies of Nakagomiet al. [48], showed that octahedral site is most occupied by Co^{2+} ions resulting in increase of anisotropy. Therefore the maximum applied magnetic field is not enough to align dipoles leading to a decrease in magnetization of the samples.

To get information about magnetic properties of $\text{Co}_{1-x}\text{Cu}_x\text{Fe}_2\text{O}_4$ samples which are heated at 1200 °C, ZFC and FC magnetizations were measured at 1 kG. The composition $\text{Co}_{0.8}\text{Cu}_{0.2}\text{Fe}_2\text{O}_4$ show a broader peak in the ZFC curve around T_{max} =260 K as shown in Fig. 3.26(ii) might be due to broad distribution of relaxation time for metastable states. CoFe_2O_4 shows no sharp peak in the curves and there is no irreversibility point up to 400 K.

The irreversibility temperatures (T_{irr}) for Co_{0.8}Cu_{0.2}Fe₂O₄ and Co_{0.75}Cu_{0.25}Fe₂O₄ are 360 K, 380 K, respectively. Similarly, Co_{0.6}Cu_{0.4}Fe₂O₄ shows no irreversibility point up to 400 K. T_{irr} decreased with the decreasing cobalt content at x=0.2 because of decrease in grain size. Similarly, a slight increase of T_{irr} for x=0.25 is because of increase in grain size (Table 3.3). Moreover, we observed a broad peak in ZFC for Cu doping of x=0.2 which becomes broader with increase in Cu doping. All samples would have blocking temperature higher than 400 K except Co_{0.8}Cu_{0.2}Fe₂O₄ sample. The nature of the ZFC and FC curves remain same, only blocking temperature of Co_{0.8}Cu_{0.2}Fe₂O₄ is due to decrease in grain size (Table 3.3). The decrease in blocking temperature may also be attributed to a decrease in anisotropy.

3.2.5 Dielectric properties

The change of dielectric permittivity (ε') with frequency for all compositions $\text{Co}_{1-x}\text{Cu}_x\text{Fe}_2\text{O}_4$ (x=0.0-0.4) is depicted in Fig. 3.27. Dielectric constants obtained at different frequencies are

listed in the Table 3.6. The dielectric constant decreases rapidly at lower frequencies and as frequency increases it decreases and becomes almost constant at high frequencies.

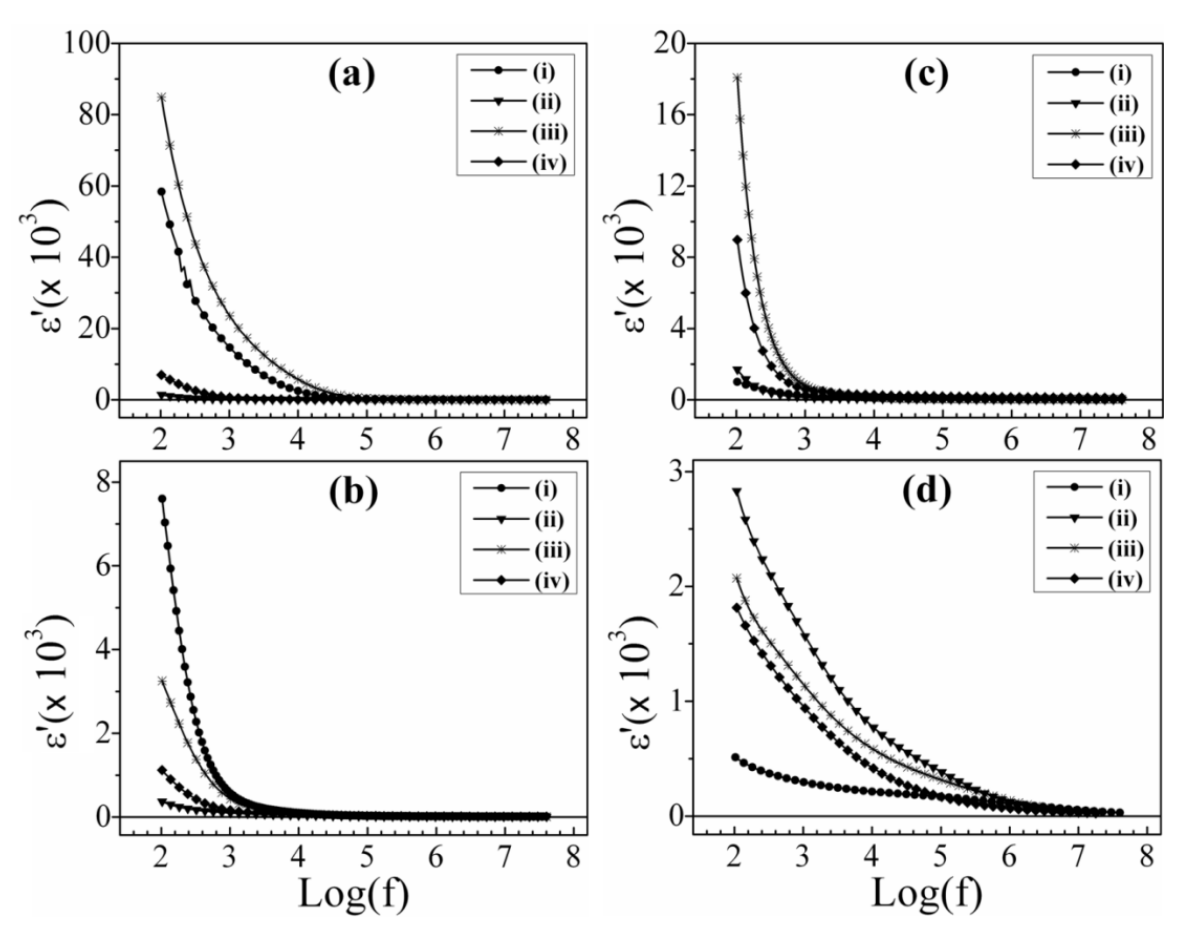


Figure 3.27. Dependence of dielectric permittivity, (ε') with logarithmic frequency in case of $Co_{1-x}Cu_xFe_2O_4$ (x = 0.0, 0.2, 0.25 and 0.4); (i) $CoFe_2O_4$ (ii) $Co_{0.8}Cu_{0.2}Fe_2O_4$ (iii) $Co_{0.75}Cu_{0.25}Fe_2O_4$ (iv) $Co_{0.6}Cu_{0.4}Fe_2O_4$ which are heated at (α) 100 °C, (α) 600°C and (α) 1200 °C for 4 h and (α) 600 °C for 3 h.

Polycrystalline materials exhibit an interfacial or space charge polarization arising from the difference in the polarization of different phases present. Even if the solid has no net charge, it is composed of positive atomic cores and electrons which experience oppositely directed forces under the action of an applied electric field. Electrons migrate through the dielectric material across the boundaries by hopping conduction. The positive atomic cores form a periodic coulomb potential with electrons localized within the potential wells. Electrons in potential wells can either hope over the potential well or tunnel through the barrier. Hopping requires an activation energy whereas tunneling does not. At ordinary temperatures the tunneling

probability is less than that for jumping over the potential barriers and the electron hopes from Fe³⁺ site to Fe²⁺ site. The motion of electrons is interrupted at the grain boundaries and some charges get trapped at the grain boundaries. Charges of opposite sign give rise to dipole moment. Even if the charges are predominantly of one type the electric field due to these trapped charges affect dielectric constant, since their presence alters the applied field inside the dielectric.

At low frequencies the polarization adjusts itself to the instantaneous value of the driving field and so dielectric constant is very high. As the frequency becomes higher, it becomes increasingly impossible for all of the charge carriers to move fast enough to stay in step with the field and hence polarization lags behind the driving field. Therefore, dielectric constant decreases with increasing frequency. At very high frequencies, the fastest moving charge carriers can no longer respond there will be no polarization resulting in a very low dielectric constant. The dielectric constant in the present study is of the same order of magnitude as compared to that reported by Balavijayalakshmi et al. [33].

For samples heated at 100 °C, introduction of Cu doping of x=0.2, Co_{0.8}Cu_{0.2}Fe₂O₄ decrease dielectric constant to lowest value since grain size and porosity decreased as compared to pure CoFe₂O₄ as shown in Fig. 3.27 (a)(see Table 3.3). As the doping concentration increases to (x=0.25) Co_{0.75}Cu_{0.25}Fe₂O₄ dielectric constant increases and becomes maximum due lowest value of porosity and small increase in grain size as compared to Co_{0.8}Cu_{0.2}Fe₂O₄. Dielectric constant is found to decrease for Cu doping x=0.4, Co_{0.6}Cu_{0.4}Fe₂O₄ due to increase in grain size and porosity as compared to that of Co_{0.75}Cu_{0.25}Fe₂O₄. The value of dielectric constant varies from 84.943 × 10³ to 14. Therefore, Cu doped sample heated at 100 °C show highest dielectric constant for Cu concentration of x =0.25 (Fig.3.27 (a)).

Similarly, for samples heated at 600 °C for 3 h (Fig.3.27(b)), CoFe₂O₄ shows highest dielectric constant because of smallest grain size. Co_{0.8}Cu_{0.2}Fe₂O₄ shows lowest dielectric constant due to high porosity and increase in grain size compared to that of CoFe₂O₄. Even though Co_{0.75}Cu_{0.25}Fe₂O₄ has small grain size when compared to that of Co_{0.8}Cu_{0.2}Fe₂O₄, dielectric constant increases significantly because of lowest value of porosity. Finally, the dielectric constant is found to decrease for *x*=0.4, Co_{0.6}Cu_{0.4}Fe₂O₄ due to small increase in porosity and bigger grain size of 58 nm, when compared to that of Co_{0.75}Cu_{0.25}Fe₂O₄ (Table 3.3). But for samples heated at 600 °C for 4 h (Fig.3.27 (c)), CoFe₂O₄ exhibits lowest dielectric constant because of small grain size. Co_{0.8}Cu_{0.2}Fe₂O₄ shows almost same dielectric constant as that of

CoFe₂O₄ due to high porosity and grain size. High dielectric constant for Co_{0.75}Cu_{0.25}Fe₂O₄ is because of significant reduction in porosity and grain size compared to that of Co_{0.8}Cu_{0.2}Fe₂O₄ Finally, the dielectric constant of Co_{0.6}Cu_{0.4}Fe₂O₄ decreased slightly due to increase in grain size even though it has smallest porosity value.

Similarly for samples sintered at 1200 °C (Fig. 3.27 (d)), CoFe₂O₄ shows lowest dielectric constant because of large grain size and high porosity. $Co_{0.8}Cu_{0.2}Fe_2O_4$ shows highest dielectric constant because of decrease in grain size and porosity compared to that of $CoFe_2O_4$. Dielectric constant of $Co_{0.75}Cu_{0.25}Fe_2O_4$ decreased due to increase in grain size even though porosity decreased slightly at x=0.25 followed by a small decrease at x=0.4, $Co_{0.8}Cu_{0.2}Fe_2O_4$ due to increase in grain size and porosity.

Table 3.6: Dielectric Constant ε' at Different Frequencies

Samples	ε΄						
Cu _x Co _{1-x} Fe ₂ O ₄	100Hz	1kHz	1MHz	5MHz	40MHz		
(x = 0.0 - 0.4)							
Cu _x Co _{1-x} Fe ₂ O ₄ (Pellets Heated at 100 °C for 4 h)							
x=0	58371	14786	84	42	24		
x=0.2	1425	215	17	15	13		
x=0.25	84943	23719	74	38	21		
x=0.4	6987	705	22	18	14		
Cu _x Co _{1-x} Fe ₂ O ₄ (Pellets Heated at 600 °C for 3 h)							
x=0	7602	580	19	16	14		
x=0.2	371	102	13	11	10		
x=0.25	3252	439.5	16.5	12.5	10.4		
x=0.4	1121	166	15.8	13	11.5		
Cu _x Co ₁ -	x Fe ₂ O ₄ (Pelle	ts Heated a	at 600 °C for	· 4 h)			
x=0	1007	253	35	35	32.4		
x=0.2	1701.6	142.6	20	13	9.4		
x=0.25	18078	798	48	41	33.4		
x=0.4	8971	591	149	135	119		
Cu _x Co _{1-x} Fe ₂ O ₄ (Pellets Heated at 1200 °C for 4 h)							
x=0	513	295	110	69	30		
x=0.2	2830	1594	126	51	-		
x=0.25	2072	1147	136	55	-		
x=0.4	1815	956	67	37	-		

Dielectric loss behaviour

Dielectric tangent loss ($tan\delta$) was calculated using the relation [50]

$$\tan \delta = \frac{\varepsilon''}{\varepsilon'} \tag{3.4}$$

where ε' and ε'' are real and imaginary parts of complex dielectric constant.

The polarization that lags behind can be resolved in to two components. One component χ' (or ε') in phase with applied field and another component χ'' (or ε'') out of phase with electric field by 90°. The out phase component of polarization continuously drains away energy from the field and appears as joule heating of the material. The energy associated with the in phase component of polarization is alternately store in the material and released twice during each cycle of the driving field and thus makes no contribution to the energy balance.

Variation of Tan δ (loss tangent) with frequency for all compositions is shown in Figure 3.28. For samples heated at 100 °C for 4 h, the loss tangent decreases with increasing frequency from 100 Hz and becomes minimum at 1640 Hz exhibiting the relaxation peak between the frequency 1600 Hz and 2.5 MHz for the pure CoFe₂O₄. For Co_{0.8}Cu_{0.2}Fe₂O₄, the loss tangent increases with increasing frequency from 100 Hz and becomes maximum around 350 Hz and decreases thereafter with further increase in frequency showing a shift in the relaxation peak between the frequency 100 Hz to 1350 Hz. Whereas Co_{0.75}Cu_{0.25}Fe₂O₄ exhibits a relaxation peak between 4250 Hz to 20 MHz, Co_{0.6}Cu_{0.4}Fe₂O₄ exhibits a relaxation peak between 100 Hz to 159 kHz, followed by a decrease with increasing frequency. The position of loss tangent maxima shifted towards low frequency (350 Hz) for Cu doping of x=0.2, and shifts towards higher frequency (192.3 kHz) for x=0.25 and finally again shifts towards lower frequency (2.6 kHz) for Cu content of x=0.4. Therefore, peak in the loss tangent occurs if the frequency of the electric field is in phase with the relaxation frequency of the dielectric, resonance occurs and maximum energy is absorbed. The value of the dielectric tangent loss (tan δ) at different frequencies is tabulated in the Table 3.7.

For samples heated at 600 °C for 3 h, the loss tangent increases with increasing frequency from 100 Hz and becomes maximum at 1640 Hz showing the relaxation peak between the frequency 1640 Hz to 1.5 MHz for the pure CoFe₂O₄. For Co_{0.8}Cu_{0.2}Fe₂O₄, the loss tangent decreases with frequency without any characteristic peak in the measured frequency region. Whereas Co_{0.75}Cu_{0.25}Fe₂O₄ exhibits a peak a relaxation peak between 180 Hz to 280 kHz followed by a decrease with increasing frequency, Co_{0.6}Cu_{0.4}Fe₂O₄ exhibits a peak a relaxation peak between 220 Hz to 840 Hz and decreases rapidly with increasing frequency. The relaxation peak can be explained according to the Debye relaxation theory (Tridevi et al 2005) [51].

For samples heated at 600 °C for 4 h, the loss tangent is very small which decreases very slowly with frequency without any characteristic peak in the measured frequency region for the pure

 $CoFe_2O_4$. For $Co_{0.8}Cu_{0.2}Fe_2O_4$ and $Co_{0.6}Cu_{0.4}Fe_2O_4$ the loss tangent increases up to 475 Hz and 695 Hz, respectively, decreases rapidly up to 10 kHz exhibiting a relaxation peak between 100 Hz and 6.2 kHz beyond which it decreases slowly becomes almost constant at higher frequencies. Whereas loss tangent increases up to 1490 Hz beyond which it decreases rapidly up to 60 kHz showing a relaxation peak between 100 Hz to 60 kHz followed by a slow decrease at higher frequencies for $Co_{0.6}Cu_{0.4}Fe_2O_4$.

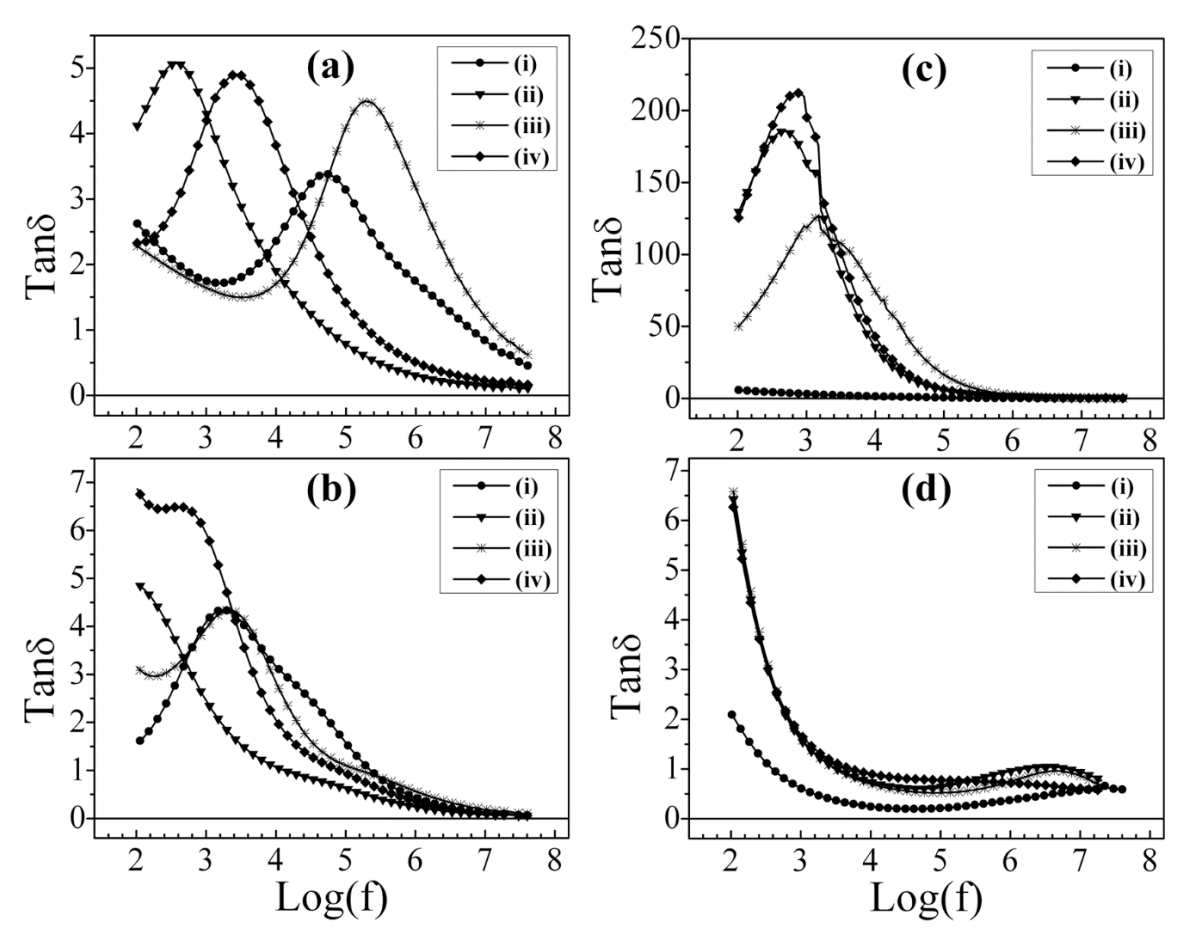


Fig. 3.28. The variation of dielectric loss with log of frequency of copper doped cobalt ferrite samples $Co_{1-x}Cu_xFe_2O_4$ (x = 0.0, 0.2, 0.25 and 0.4); (i) $CoFe_2O_4$ (ii) $Co_{0.8}Cu_{0.2}Fe_2O_4$ (iii) $Co_{0.75}Cu_{0.25}Fe_2O_4$ (iv) $Co_{0.6}Cu_{0.4}Fe_2O_4$ which are heated at (a) 100 °C, (c) 600°C and (d) 1200 °C for 4 h and (b) 600 °C for 3 h.

For samples heated at 1200 °C for 4 h, no relaxation peak appears in the loss tangent which decreases with frequency. CoFe₂O₄ exhibits small loss tangent value and decreases gradually with frequency from 100 Hz and becomes minimum at 41.9 kHz and increases slowly thereafter with frequency.

Table 3.7: Loss Tangent (tan δ)

Samples	tan δ						
CuxCo _{1-x} Fe ₂ O ₄	100Hz	1kHz	1MHz	5MHz	40MHz		
(x = 0.0-0.4)							
Cu _x Co _{1-x} Fe ₂ O ₄ (Pellets Heated at 100 °C for 4 h)							
x=0	2.624	1.75	1.743	1.092	0.456		
x=0.2	4.118	4.328	0.309	0.182	0.1087		
x=0.25	2.283	1.648	3.176	1.644	0.626		
x = 0.4	2.327	4.18	0.502	0.284	0.163		
Cu _x Co _{1-x} Fe ₂ O ₄ (Pellets Heated at 600 °C for 3 h)							
x=0	1.57	4.097	0.429	0.178	0.064		
x=0.2	4.893	2.472	0.24	0.115	0.054		
x=0.25	3.147	3.972	0.567	0.27	0.101		
x=0.4	6.858	5.955	0.359	0.162	0.057		
Cu _x Co	o _{1-x} Fe ₂ O ₄ (Pe	ellets Heate	d at 600 °C fo	r 4 h)			
x=0	5.7	3.1	0.145	0.064	0.044		
x=0.2	129.3	164.7	1.752	0.742	0.244		
x=0.25	50	118.9	2.333	0.649	0.178		
x=0.4	125.4	197.9	0.982	0.273	0.069		
Cu _x Co _{1-x} Fe ₂ O ₄ (Pellets Heated at 1200 °C for 4 h)							
x=0	2.095	0.614	0.3746	0.516	0.587		
x=0.2	6.428	1.592	0.953	1.033	-		
x=0.25	6.578	1.631	0.746	0.962	-		
x=0.4	6.267	1.692	0.7216	0.646	-		

For all doped samples Co_{0.8}Cu_{0.2}Fe₂O₄ and Co_{0.75}Cu_{0.25}Fe₂O₄, the loss tangent decreases rapidly till 1 kHz and decreased slowly thereafter, becomes minimum at 48.3 kHZ and 94.1 kHZ, respectively and then increases slowly up to 3.9 MHz beyond which a small decrease is observed at higher frequencies. Whereas Co_{0.6}Cu_{0.4}Fe₂O₄ shows a rapid decrease till 1 kHz beyond which it decreases very slowly.

3.2.6 Conclusions

The cobalt ferrite and copper doped cobalt ferrite nanoparticles of composition $Co_{1-x}Cu_xFe_2O_4$ (x = 0.2, 0.25 and 0.4) prepared by co-precipitation were pressed into pellets which were heated at 100 °C, 600 °C and 1200 °C for 4 hours and also at 600 °C for 3 hours with 3 °C/min heating and cooling rate. The rietveld refined XRD patterns of all samples exhibit single phased spinel structure. The saturation magnetization increased significantly with increase of annealing temperature due to increase in grain size. The M_s of CoFe₂O₄ pellet heated at 600 °C for 3 h is 140 emu·g⁻¹. CoFe₂O₄ pellets heated at 1200 °C for 4 h show very high saturation magnetization (M_s) of 175 emu/g. The copper doped samples $Co_{1-x}Cu_xFe_2O_4$ with x = 0.2, 0.25 and 0.4 annealed at 600 °C for 3 h exhibited M_s values of 122, 120 and 107 emu·g⁻¹ with coercivity of 858 G, 970 G and 939 G, respectively. The M_s values of samples annealed at 1200 °C for 4 h are 122,

120 and 107 emu·g $^{-1}$, with low coercivity of 76 G, 83 G and 50 G respectively. The dielectric constant value is in the range 84.943×10^3 to 14 when frequency of applied electric field increases from 100 Hz to 40 MHz. The dielectric constant and loss tangent show a decreasing trend with increasing frequency.

3.3 Structural, magnetic and dielectric properties of cobalt-copper $Co_{1-x}Cu_xFe_2O_4$ (x=0.0, 0.2, 0.25, 0.4, 0.9 and 1.0) ferrites synthesized by co-precipitation method 3.3.1 Introduction

We have used co-precipitation method for synthesizing a complete series of Cu doped, Co_{1-x}Cu_xFe₂O₄ (x=0.0, 0.2, 0.25, 0.4, 0.9 and 1.0), cobalt-copper ferrite nanoparticles. Detailed systematic studies of structural, magnetic and dielectric properties of these materials were carried out. In order to increase the M_s of Co_{1-x}Cu_xFe₂O₄ nanoparticles, we processed Pellets of Cobalt-Copper ferrite samples with thermal annealing at different temperatures 100, 600 and 1200 °C. These studies are helpful in tuning the properties of the ferrite materials.

3.3.2 Structural analysis

For the different compositions, cobalt-copper ferrite samples $Co_{1-x}Cu_xFe_2O_4$ (x = 0.0, 0.2, 0.25, 0.4, 0.9 and 1.0) show single phased spinel structure from x = 0.0–0.4 (space group Fd-3m) and for x = 0.9 and 1.0 spinel-(Cu,Fe) structure with space group I 41/a m d. Fig. 3.29 depicts the XRD patterns of $Co_{1-x}Cu_xFe_2O_4$ (x = 0.0, 0.2, 0.25, 0.4, 0.9 and 1.0) nano-particles heated at 90 °C (overnight), 100, 600 and 1200 °C. Peaks are indexed to (111), (220), (311), (222), (400), (331), (422), (511), (440), (531), (422), (620), (533), (622) and (444) planes of spinel structure (JCPDS PDF # 98-016-0059) from x=0.0–0.4. No peaks of impurities were observed which confirms highly pure crystalline $Co_{1-x}Cu_xFe_2O_4$ (x=0.0–0.4). The pattern of the samples (v) (x=0.9) and (vi) (x=1.0) were indexed to a single phase of tetragonal $CuFe_2O_4$ spinel with a=5.891 Å and c=8.565 Å (JCPDS PDF # 98-018-8861(3)).

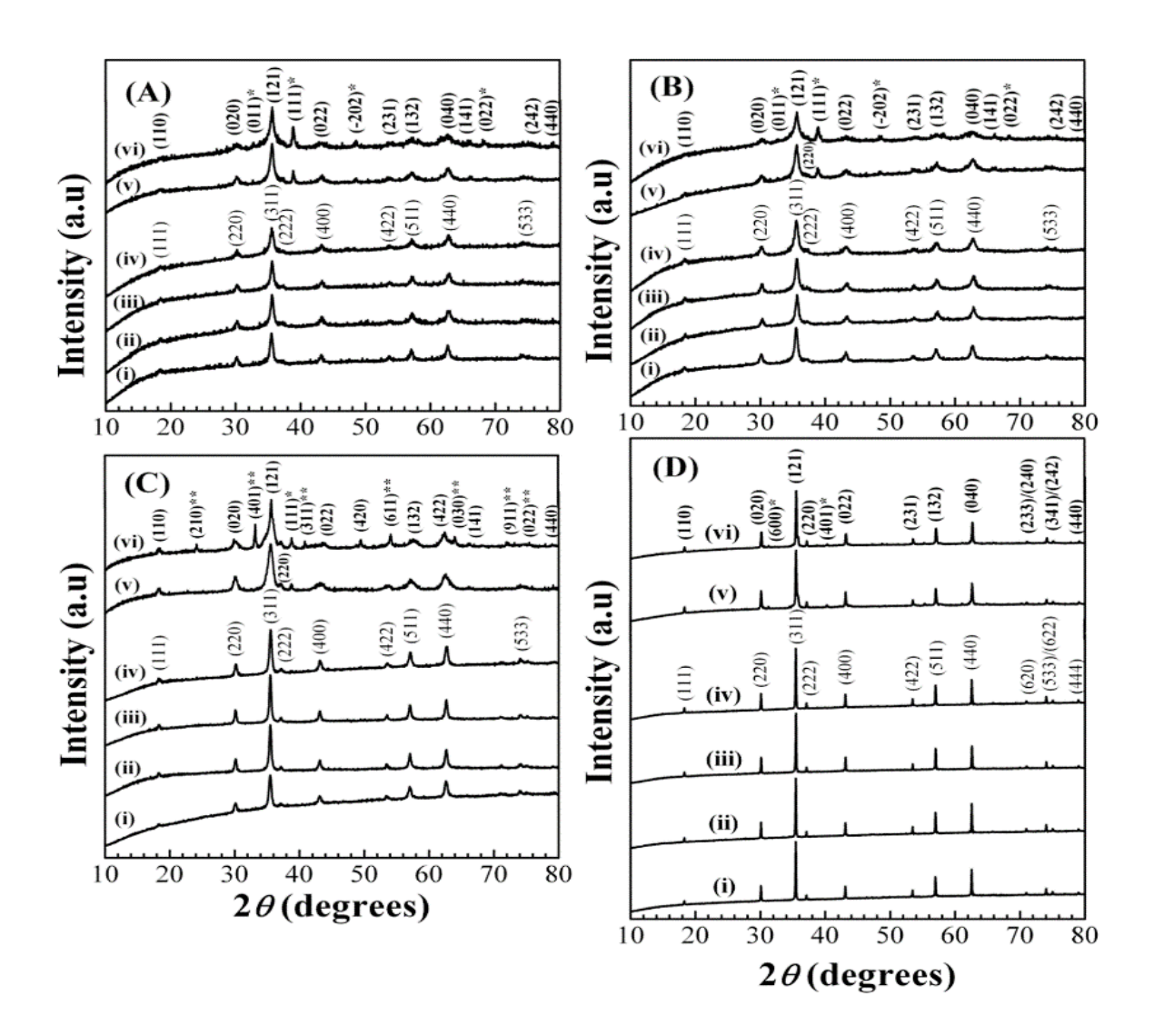


Fig. 3.29 X-ray diffraction patterns of cobalt-copper ferrites $Co_{1-x}Cu_xFe_2O_4$ (x = 0.0, 0.2, 0.25, 0.4, 0.9 and 1.0); (i) $CoFe_2O_4$, (ii) $Co_{0.8}Cu_{0.2}Fe_2O_4$, (iii) $Co_{0.75}Cu_{0.25}Fe_2O_4$, (iv) $Co_{0.6}Cu_{0.4}Fe_2O_4$, (v) $Co_{0.1}Cu_{0.9}Fe_2O_4$ and (vi) $CuFe_2O_4$ which are heated at (**A**) 90 °C (overnight), (**B**) 100 °C, (**C**) 600 °C and (**D**) 1200 °C for 4 h.

Samples with *x*=0.9 and *x*=1.0 have three phases, namely, presence of a major phase of spinel-(Cu,Fe) with (ICDD:98-018-8861(3), space group I 41/a m d), a minor phase of CuO (98-009-2364, space group C 1 2/c 1), Fe₂O₃ (98-005-6372, space group R-3c for samples heated at 600 °C) and Cu₁Fe₁O₂ (98-0059-2184, space group R-3m for samples heated at 1200 °C). For Cu_{0.9}Co_{0.1}Fe₂O₄ and CuFe₂O₄ samples heated at low temperature were observed to have a major spinel-(Cu, Fe) phase COD (ICDD: 98-018-8861, space group I 41/a m d) and a minor phases of Fe₂O₃, CuO. However, the intensity of the CuO in Cu_{0.9}Co_{0.1}Fe₂O₄ and CuFe₂O₄ is very small indicating the presence of 12% and 16% CuO phase, respectively, in the sample heated at 100

°C, 4.2% and 6.9%, in the sample heated at 600 °C which indicates the insignificant loss of Cu²⁺. But samples heated at high temperature 1200 °C indicate the presence of 12.2% and 7.4 % Delafossite (CuFeO₂) phase, respectively. Only CuFe₂O₄ heated at 600 °C indicates the presence of 21.7% of unreacted Hematite, Fe₂O₃. At high temperature, the phases are more pure which indicates that the unreacted CuO and Fe₂O₃ are also converted into CuFe₂O₄. All ICDD files were used in Rietveld refinement. All the X-ray diffraction (XRD) patterns were analyzed with the help of HoghScore Plus software program using Rietveld refinement.

The XRD patterns were refined using the Fd-3m space group [69], I 41/a md tetragonal space group [70], C 1 2/c 1 monoclinic space group [71] and R-3m space group [72]. The goodness of fit (χ^2) and the R factors (Rp = profile factor, R_B = Bragg factor, and R_F = crystallographic factor) show quality of fitting. Rietveld refinement was done without background correction. The values R factors and χ^2 (goodness of fit) are enlisted in Table 3.8. Rietveld refined XRD patterns are shown in Figures 3.30, 3.31, 3.32 and 3.33 for the samples heated at 90, 100, 600 and 1200 °C, respectively. Each panel (i, ii, iii, iv, v and vi) in the figures represent the samples CoFe₂O₄, Co_{0.8}Cu_{0.2}Fe₂O₄, Co_{0.75}Cu_{0.25}Fe₂O₄, Co_{0.6}Cu_{0.4}Fe₂O₄, Co_{0.1}Cu_{0.9}Fe₂O₄ and CuFe₂O₄ respectively.

The crystallite size (D_{XRD}) was calculated using the Debye-Scherrer's equation [2] given by Eq. (3.1). An increase in the crystalline nature of the $Co_{1-x}Cu_xFe_2O_4$ (x = 0.0, 0.2, 0.25, 0.4, 0.9 and 1.0) ferrite powders was observed as the sintering temperature was increased. Average crystallite sizes are in the range of 6.6–15 nm, 13–24 nm and 48–82 nm for the samples heated at 100, 600 and 1200 °C, respectively (Table 3.8). The crystallite sizes were small for samples heated at 100 °C (below 15 nm) and increased with increasing annealing temperature.

The average crystalline sizes are 15, 13.6, 13, and 10.8 nm for (a) (i) $(CoFe_2O_4)$, (ii) $(Co_{0.8}Cu_{0.2}Fe_2O_4)$, (iii) $(Co_{0.75}Cu_{0.25}Fe_2O_4)$, and (iv) $(Co_{0.6}Cu_{0.4}Fe_2O_4)$, pellets annealed at 100 °C for 4 h, respectively, 18, 22, 24, and 20 nm for (b) (i), (ii), (iii) and (iv), pellets annealed at 600 °C for 4 h, respectively, and 71, 82, 63 and 60 nm for (i), (ii), (iii), (iv) and (v), pellets annealed at 1200 °C for 4 h, respectively.

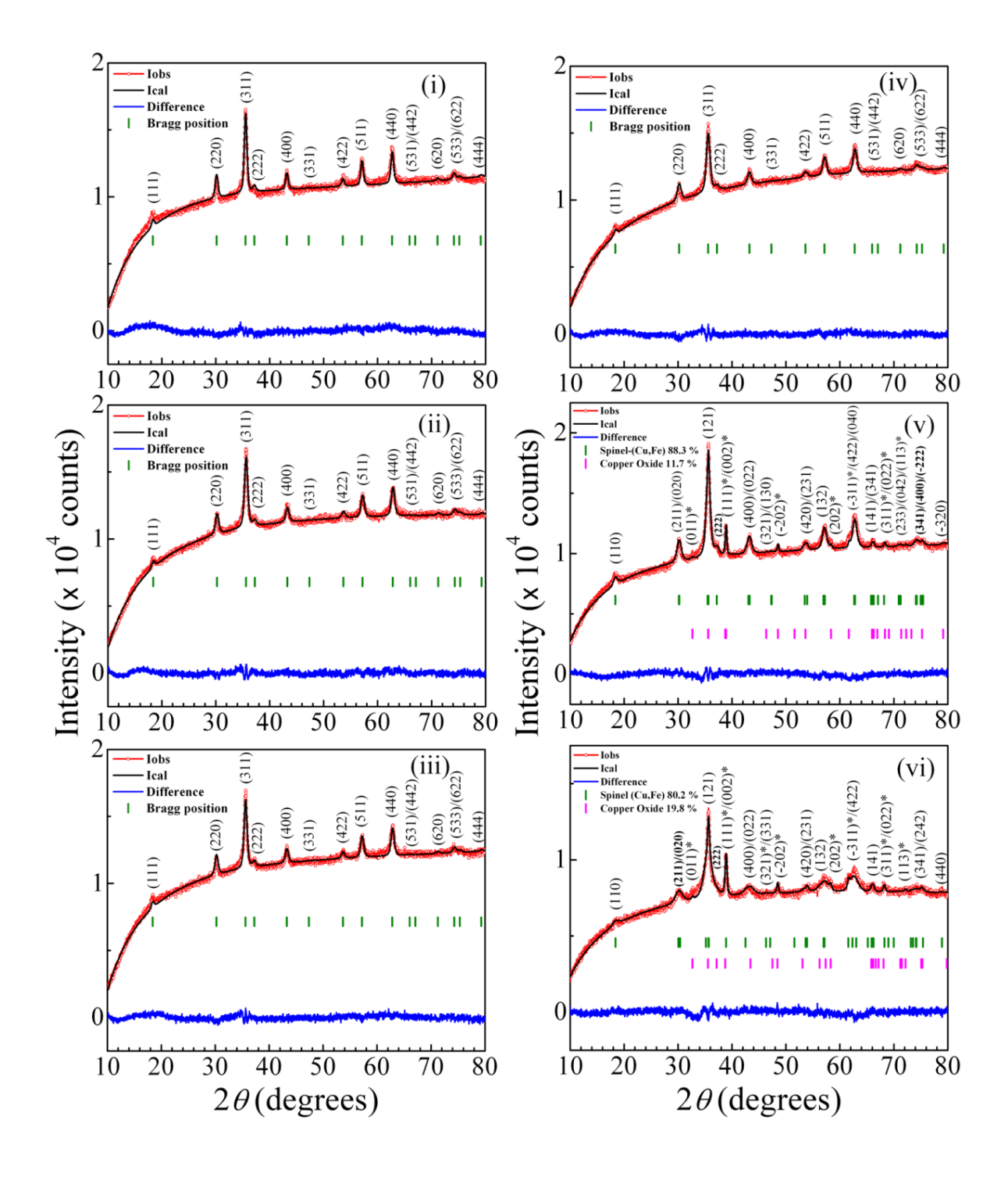


Fig. 3.30. Rietveld refined XRD patterns of as-synthesized cobalt-copper ferrite nanoparticles $Co_{1-x}Cu_xFe_2O_4$ (x = 0.0, 0.2, 0.25, 0.4, 0.9 and 1.0) nanoparticles; (i) $CoFe_2O_4$, (ii) $Co_{0.8}Cu_{0.2}Fe_2O_4$, (iii) $Co_{0.75}Cu_{0.25}Fe_2O_4$, (iv) $Co_{0.6}Cu_{0.4}Fe_2O_4$, (v) $Co_{0.1}Cu_{0.9}Fe_2O_4$ and (vi) $CuFe_2O_4$ which are dried at 90 °C overnight.

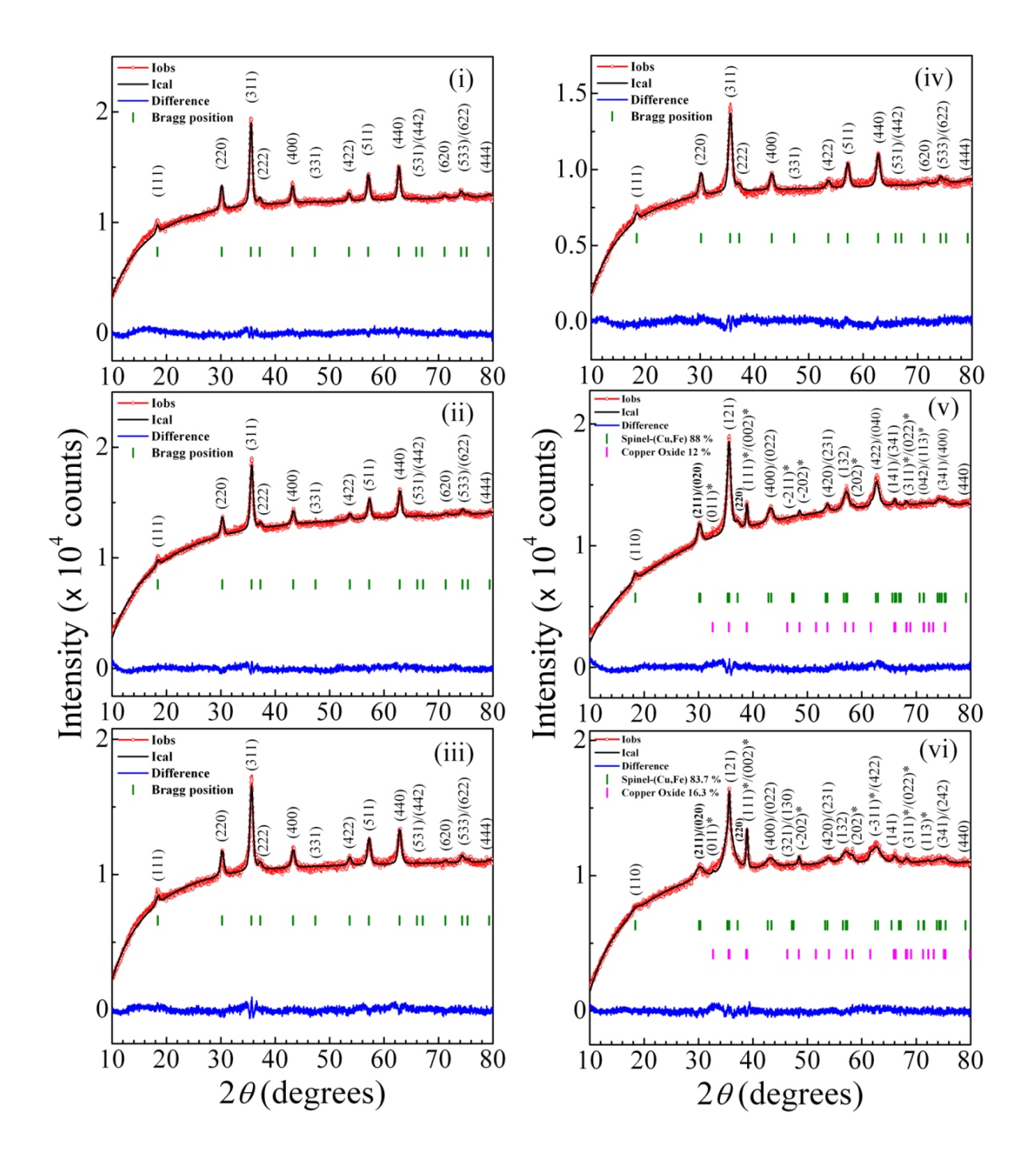


Fig. 3.31. Rietveld refined XRD patterns of cobalt-copper ferrite samples $Co_{1-x}Cu_xFe_2O_4$ (x = 0.0, 0.2, 0.25, 0.4, 0.9 and 1.0); (i) $CoFe_2O_4$, (ii) $Co_{0.8}Cu_{0.2}Fe_2O_4$, (iii) $Co_{0.75}Cu_{0.25}Fe_2O_4$, (iv) $Co_{0.6}Cu_{0.4}Fe_2O_4$, (v) $Co_{0.1}Cu_{0.9}Fe_2O_4$ and (vi) $CuFe_2O_4$ which are heated 100 °C for 4 h.

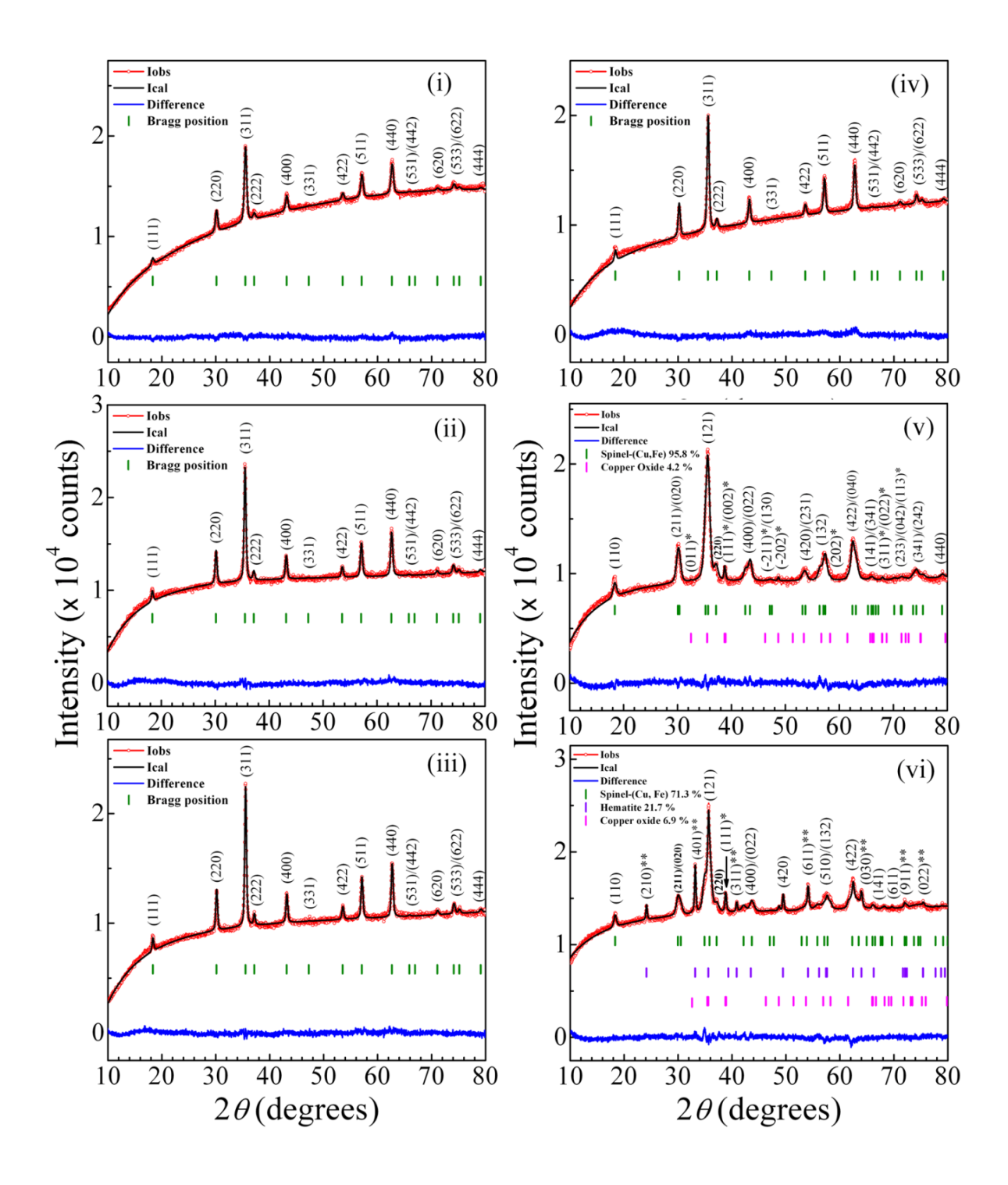


Fig. 3.32. Rietveld refined XRD patterns of cobalt-copper ferrite samples $Co_{1-x}Cu_xFe_2O_4$ (x=0.0, 0.2, 0.25, 0.4, 0.9 and 1.0); (i) $CoFe_2O_4$, (ii) $Co_{0.8}Cu_{0.2}Fe_2O_4$, (iii) $Co_{0.75}Cu_{0.25}Fe_2O_4$, (iv) $Co_{0.6}Cu_{0.4}Fe_2O_4$, (v) $Co_{0.1}Cu_{0.9}Fe_2O_4$ and (vi) $CuFe_2O_4$ which are heated 600 °C for 4 h.

The X-ray density, ρ_x and these values are presented in Table 3.8. The values of lattice parameter are comparable to the values reported in the literature [1].

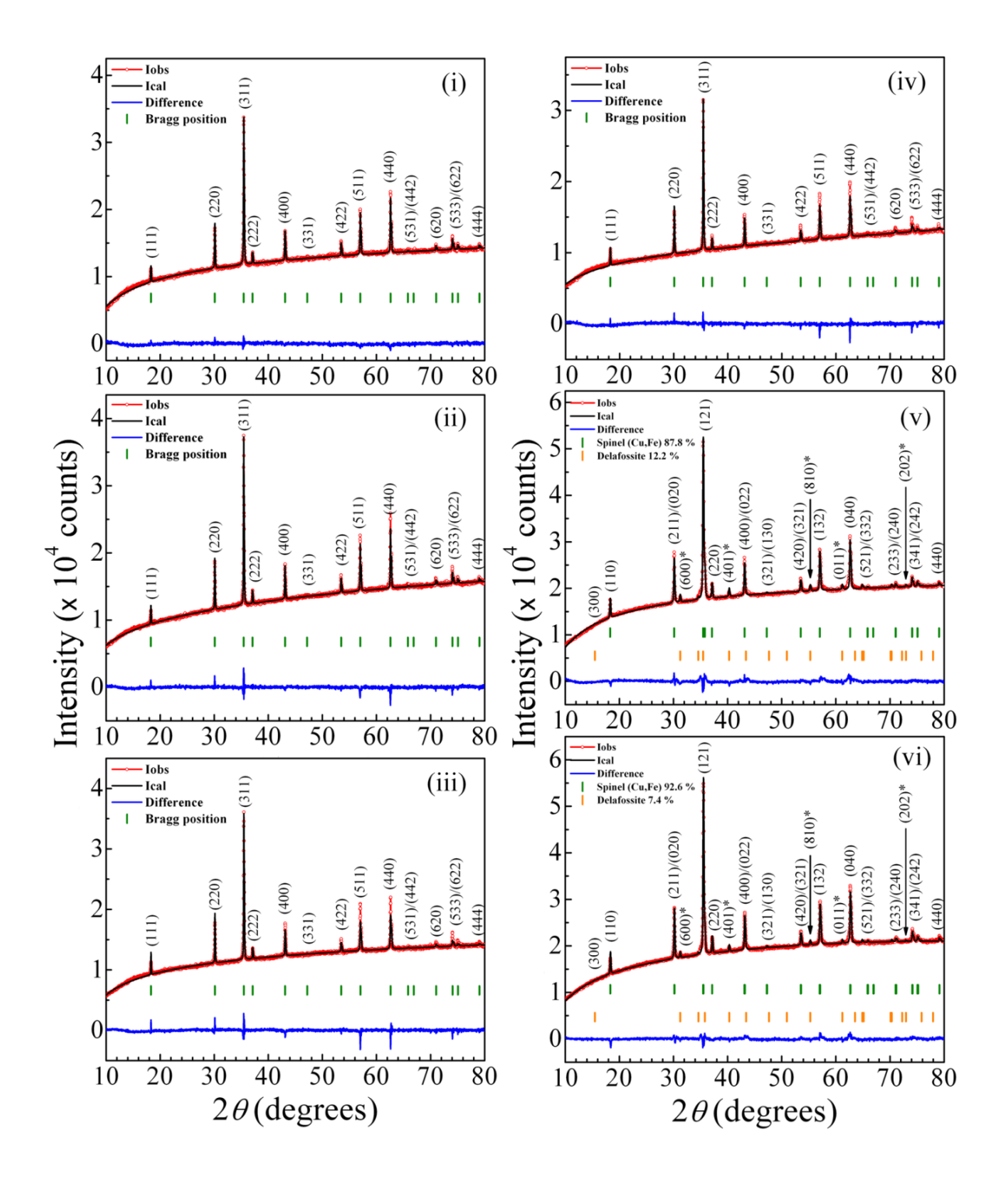


Fig. 3.33. Rietveld refined XRD patterns of cobalt-copper ferrite samples $Co_{1-x}Cu_xFe_2O_4$ (x = 0.0, 0.2, 0.25, 0.4, 0.9 and 1.0); (i) $CoFe_2O_4$, (ii) $Co_{0.8}Cu_{0.2}Fe_2O_4$, (iii) $Co_{0.75}Cu_{0.25}Fe_2O_4$, (iv) $Co_{0.6}Cu_{0.4}Fe_2O_4$, (v) $Co_{0.1}Cu_{0.9}Fe_2O_4$ and (vi) $CuFe_2O_4$ which are heated 1200 °C for 4 h.

Table 3.8 Rietveld parameters and calculated values Lattice parameter, crystallite size (XRD), and average grain size (FESEM). *Errors of lattice parameters are shown in parentheses*. Average grain sizes estimated in 'µm'scale from right panel of Fig. 3.38 are given in square brackets.

$Co_{1-x}Cu_xFe_2O_4$	x = 0	x = 0.2	x = 0.25	x = 0.4	x = 0.9	x = 1.0
	(i)	(ii)	(iii)	(iv)	(iv)	(iv)
(04Pellets Heat				
Lattice parameter (Å)	8.379(1)	8.368(2)	8.365(2)	8.372(2)	5.916(3)	5.905(4)
Zamie parameter (c.1)	0.077(1)	0.000(2)	0.000(2)	0.072(2)	8.406(8)	8.52(1)
D_{XRD}	15.4	12.5	13.5	11	14	6.4
G _{FESEM} (±1 nm)	60	55	54	62	19	15
R (expected)/ %	0.73155	0.73711	0.74717	0.77457	0.69330	0.73317
R (profile)/%	0.90377	0.68421	0.74350	0.70673	0.71209	0.67266
R (weighted profile)/ %	1.14594	0.87996	0.94034	0.90185	0.89007	0.85826
G.O.F	1.56645	1.19380	1.25853	1.16433	1.28381	1.17062
Theoretical density, $\rho(g/cm^3)$	5.2973	5.3183	5.3242	5.3109	5.3999	5.3464
Unit cell volume V (\mathring{A}^3)	588.2955	585.9751	585.3282	586.79340	294.23130	297.1742
		O ₄ Pellets Hea			27 1.23130	2,7,17,12
Lattice parameter (Å)	8.378663	8.359(1)	8.366(1)	8.372(2)	5.904(2)8.	5.904(5)
Zamire parameter (12)	0.070000	0.000 (1)	0.200(1)	0.072(2)	444(4)	8.47(1)
D_{XRD}	15	13.6	13	10.8	13	6.6
G _{FESEM} (±1 nm)	58	52	55	54	23	26
R (expected)/%	0.67224	0.70779	0.69604	0.74786	0.72968	0.71594
R (profile)/%	0.68752	0.68820	0.69108	0.78539	0.80556	0.65745
R (weighted profile)/ %	0.87526	0.89807	0.87403	0.97730	1.07890	0.83073
G.O.F	1.30200	1.26884	1.25573	1.30680	1.47860	1.16033
Theoretical density, ρ (g/cm ³)	5.2982	5.3361	5.3226	5.3103	5.3978	5.3795
Apparent density ρ (g/cm ³)	2.5814	2.6898	2.5372	2.6557	2.51051	2.3243
Porosity (%)	50.27	49.59	52.33	49.99	53.49	56.79
Unit cell volume V (Å ³)	588.1989	584.01790	585.5054	586.8588	294.3497	295.3489
		O ₄ Pellets Hea			274.5471	273.3407
Lattice parameter (Å)	8.3800(9)	8.3817(5)	8.3822(5)	8.3809(6)	5.8954,	5.857,
Lattice parameter (11)	0.3000())	0.3017(3)	0.3022(3)	0.3007(0)	8.498(1)	8.573(2)
D_{XRD}	18	22	24	20	13.2	14.55
G _{FESEM} (±1 nm)	64	60	66	62	43	36
R (expected)/%	0.76989	0.69806	0.75021	0.76780	0.66406	0.67760
R (profile)/ %	0.69995	0.76056	0.66689	0.86406	0.74637	0.68074
R (weighted profile)/ %	0.89647	0.96057	0.84967	1.12376	0.95541	0.90046
G.O.F	1.16440	1.37605	1.13258	1.46360	1.43874	1.32890
Theoretical density, ρ (g/cm ³)	5.2956	5.2925	5.2915	5.2939	5.3797	5.4024
Apparent density ρ (g/cm ³)	2.682	2.7524	2.576	2.954	2.7864	2.7901
Porosity (%)	49.35	47.99	51.32	44.2	48.2	48.35
Unit cell volume V (Å ³)	588.4873	588.8294	588.9435	588.6692	295.33650	294.095
		04Pellets Heat			293.33030	294.093
Lattice parameter (Å)	8.3857(1)	8.3850(1)	8.3842(2)	8.3825(2)	5.9276(5)	5.9225
Lattice parameter (A)	0.3037(1)	6.3630(1)	0.3042(2)	0.3023(2)	8.386(1)	8.3908(3)
D	71	82	63	60	48.3	54.4
D_{XRD}						
G_{FESEM} (±2 nm)[μ m]	70[3.2]	83[5.3]	64[9.3]	64[20]	40[34.7]	57[26]
R (expected)/%	0.75859	0.80165	0.83091	0.86340	0.74292	0.73154
R (profile)/%	0.71194	0.75857	0.89673	0.94236	1.03231	0.81729
R (weighted profile)/ %	0.93986	1.17278	1.45315	1.37788	1.47739	1.19144
G.O.F Theoretical density: a (a/am ³)	1.23897	1.46295	1.74887	1.59588	1.98861	1.62867
Theoretical density, ρ (g/cm ³)	5.2849	5.2862	5.2877	5.2909	5.3923	5.3984
Apparent density ρ (g/cm ³)	4.8437	4.744	4.8424	4.162	3.8472	4.0697
Porosity (%)	8.35	10.25	8.42	21.33	28.65	24.61
Unit cell volume V (Å ³)	589.6779	589.53170	589.3631	589.006	294.6461	294.3123

Measured density ρ_m of pellets was estimated by $\rho_m = (m/\pi r^2 l)$ given by Eq. (3.2). The porosity of the pellets was calculated using the formula $P = 1 - (\rho_m/\rho_x)$ given by Eq. (3.3), where ρ_m and ρ_x measured and theoretical (from Rietveld) densities. The values of porosity are presented in Table 3.8. Bulk density increases at higher sintering temperatures due to consequent decrease in porosity.

3.3.3 Surface morphology

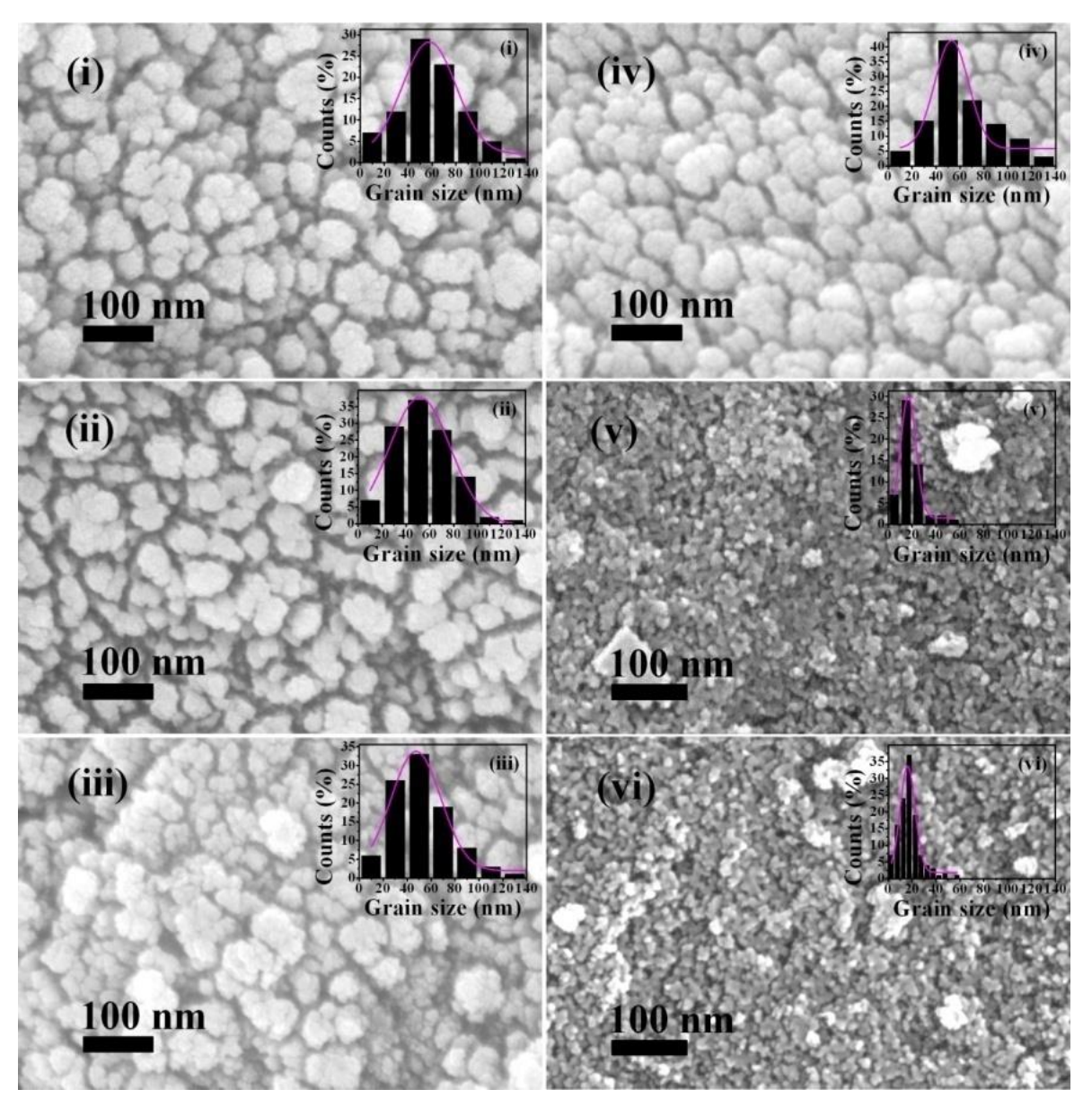


Fig. 3.34 FESEM micrographs of as-synthesized $Co_{1-x}Cu_xFe_2O_4$ (x = 0.0, 0.2, 0.25, 0.4, 0.9 and 1.0) nanoparticles; (i) $CoFe_2O_4$, (ii) $Co_{0.8}Cu_{0.2}Fe_2O_4$, (iii) $Co_{0.75}Cu_{0.25}Fe_2O_4$, (iv) $Co_{0.6}Cu_{0.4}Fe_2O_4$, (v) $Co_{0.1}Cu_{0.9}Fe_2O_4$ and (vi) $CuFe_2O_4$ which are dried at $90^{\circ}C$ overnight.

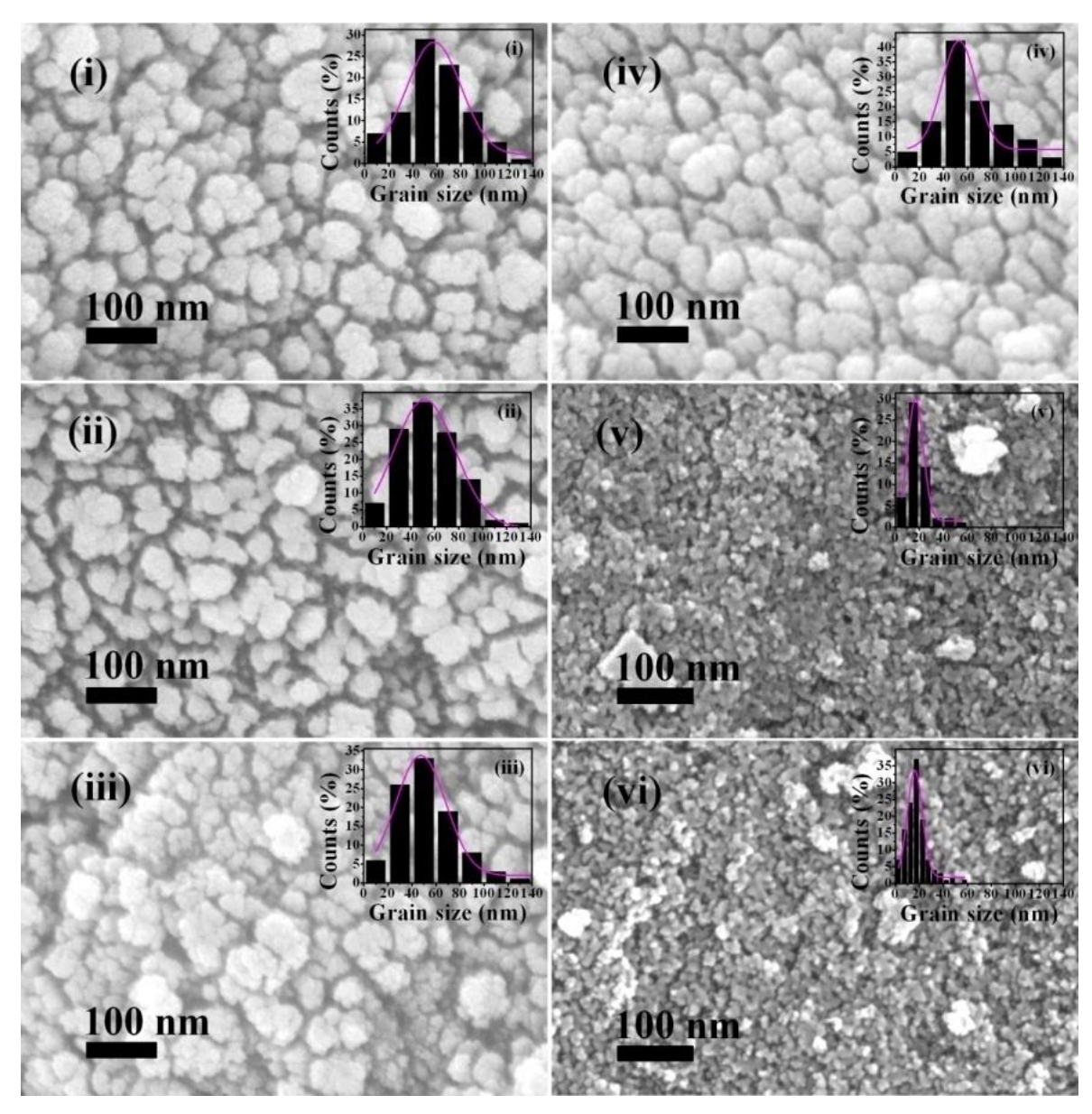


Fig. 3.34 FESEM micrographs of as-synthesized $Co_{1-x}Cu_xFe_2O_4$ (x = 0.0, 0.2, 0.25, 0.4, 0.9 and 1.0) nanoparticles; (i) $CoFe_2O_4$, (ii) $Co_{0.8}Cu_{0.2}Fe_2O_4$, (iii) $Co_{0.75}Cu_{0.25}Fe_2O_4$, (iv) $Co_{0.6}Cu_{0.4}Fe_2O_4$, (v) $Co_{0.1}Cu_{0.9}Fe_2O_4$ and (vi) $CuFe_2O_4$ which are dried at $90^{\circ}C$ overnight.

Figs. 3.34, 3.35, 3.36 and 3.37 shows representative FESEM micrographs of $Co_{1-x}Cu_xFe_2O_4$ (x = 0.0, 0.2, 0.25, 0.4, 0.9 and 1.0) samples heated at 90, 100, 600, and 1200 °C. In the FESEM micrographs of samples heated at 100 and 600 °C most of grains are spherical with some elongated particles with uniformly distributed grains. Agglomeration increase with increase of Cu substitution concentration due to decrease in crystallite size, especially in the case of samples heated at 100 °C (Fig. 3.35) and the agglomerated grains appear like a single big grain in the

images. This agglomeration affects the different physical properties. It is observed that the crystallite sizes estimated from the XRD pattern are much less than grain sizes estimated from FESEM due to aggregation of few number of nanocrystallites.

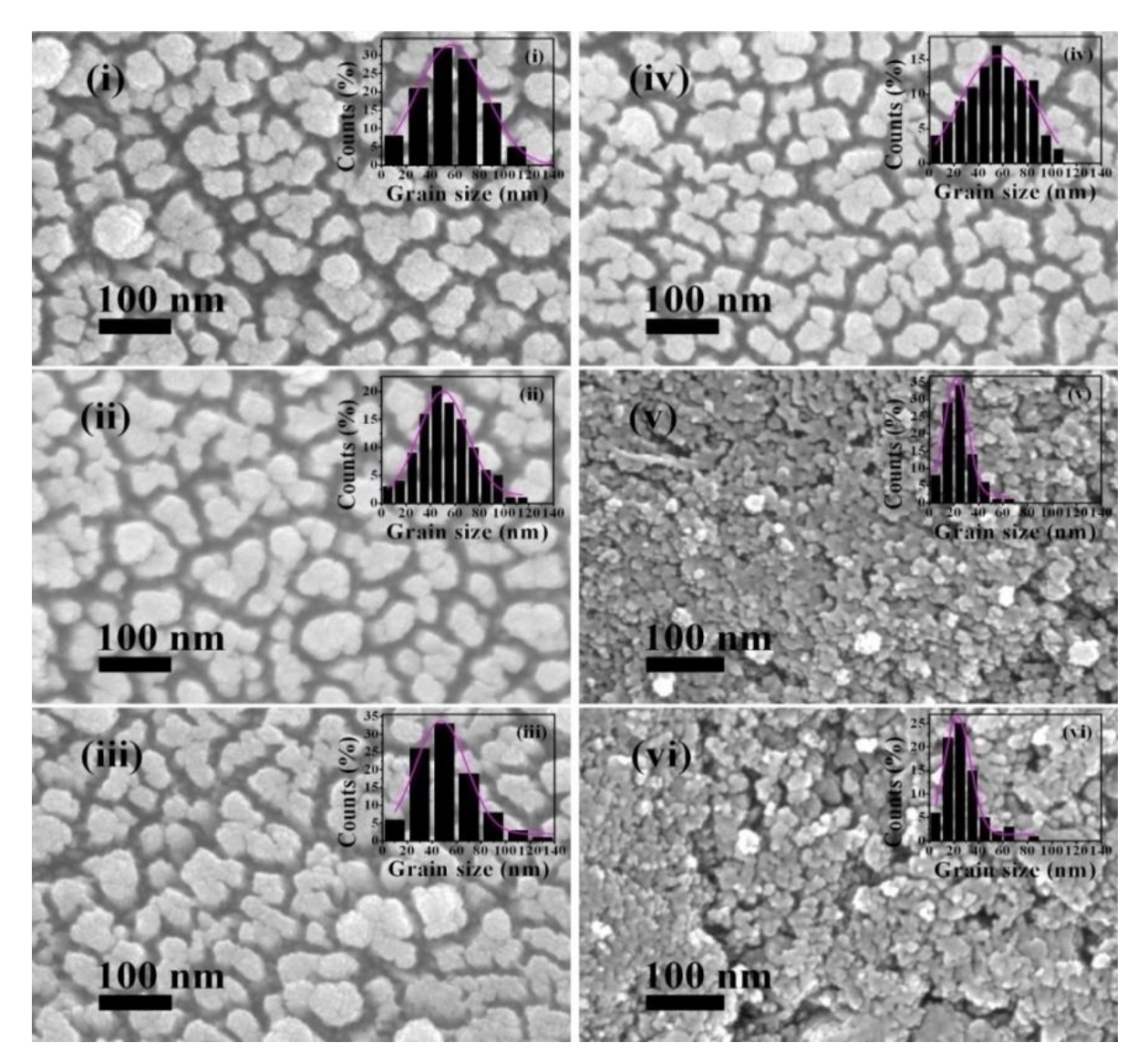


Fig. 3.35 FESEM micrographs of $Co_{1-x}Cu_xFe_2O_4$ (x=0.0, 0.2, 0.25, 0.4, 0.9 and 1.0) pellets; (i) $CoFe_2O_4$, (ii) $Co_{0.8}Cu_{0.2}Fe_2O_4$, (iii) $Co_{0.75}Cu_{0.25}Fe_2O_4$, (iv) $Co_{0.6}Cu_{0.4}Fe_2O_4$, (v) $Co_{0.1}Cu_{0.9}Fe_2O_4$ and (vi) $CuFe_2O_4$ which are heated 100 °C for 4 h.

In the case of as-synthesized nanoparticles dried at 90 °C overnight (Fig. 3.34), the average grain sizes decreases with increasing Cu doping up to x=0.25 but increase at x=0.4, and a large decrease at x=0.9 with a small decrease finally at x=1.0. The average grain sizes first decreased

at Cu doping concentration of x=0.2 (20%) and increased thereafter till x=0.4 and decreased at x=0.9 followed by slight increase at x=1.0 for samples heated at 100 °C (Table 3.8 and Fig. 3.35) whereas the average grain size decreased at x=0.2 and then increased at x=0.25 followed by a gradual decrease with increase in Cu doping from x=0.4 to x=1.0, in case of samples heated at 600 °C (Fig. 3.36).

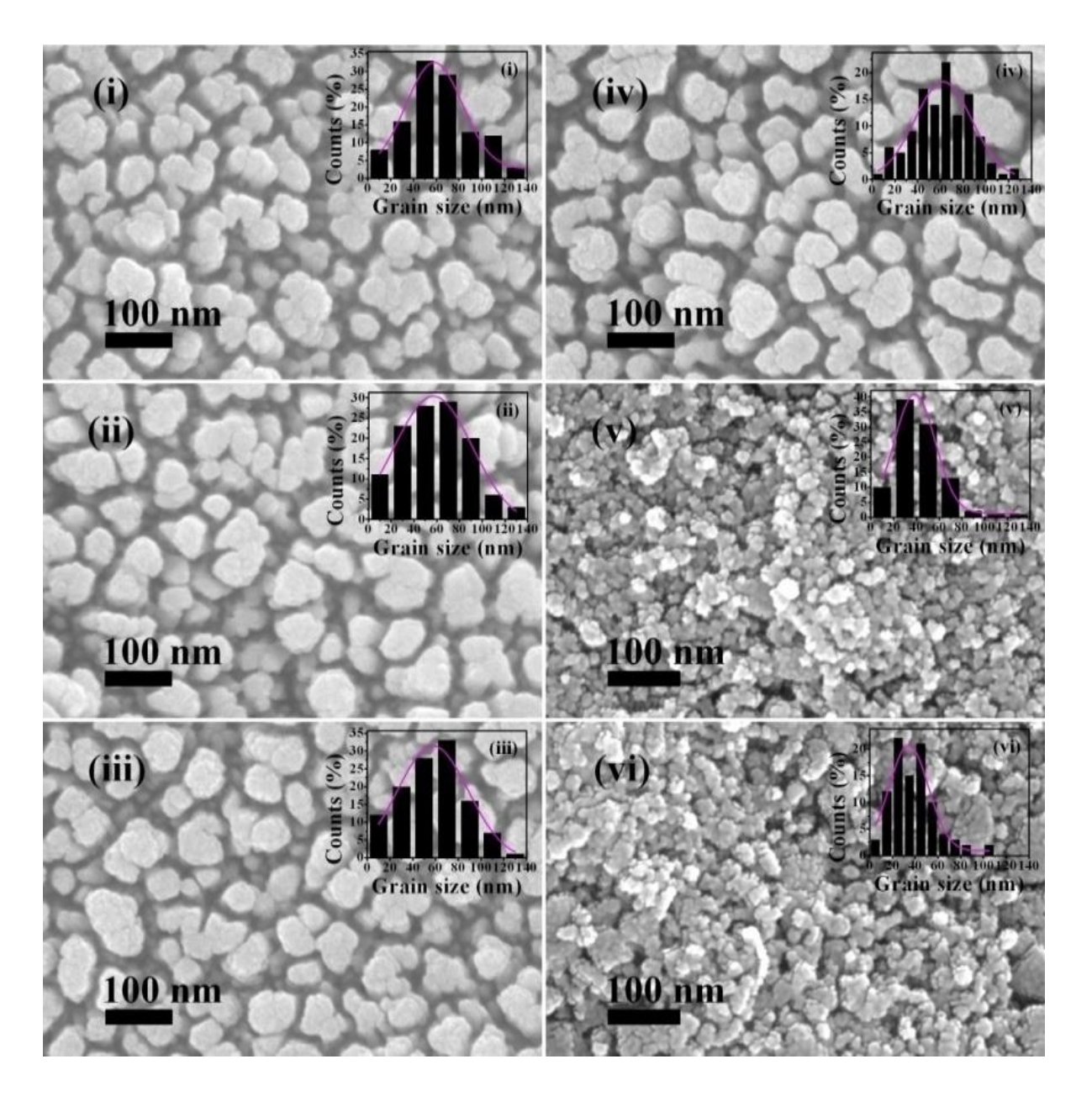


Fig. 3.36 FESEM micrographs and grain size distributions of $Co_{1-x}Cu_xFe_2O_4$ (x = 0.0, 0.2, 0.25, 0.4, 0.9 and 1.0) pellets; (i) $CoFe_2O_4$, (ii) $Co_{0.8}Cu_{0.2}Fe_2O_4$, (iii) $Co_{0.75}Cu_{0.25}Fe_2O_4$, (iv) $Co_{0.6}Cu_{0.4}Fe_2O_4$, (v) $Co_{0.1}Cu_{0.9}Fe_2O_4$ and (vi) $CuFe_2O_4$ which are heated 600 °C for 4 h.

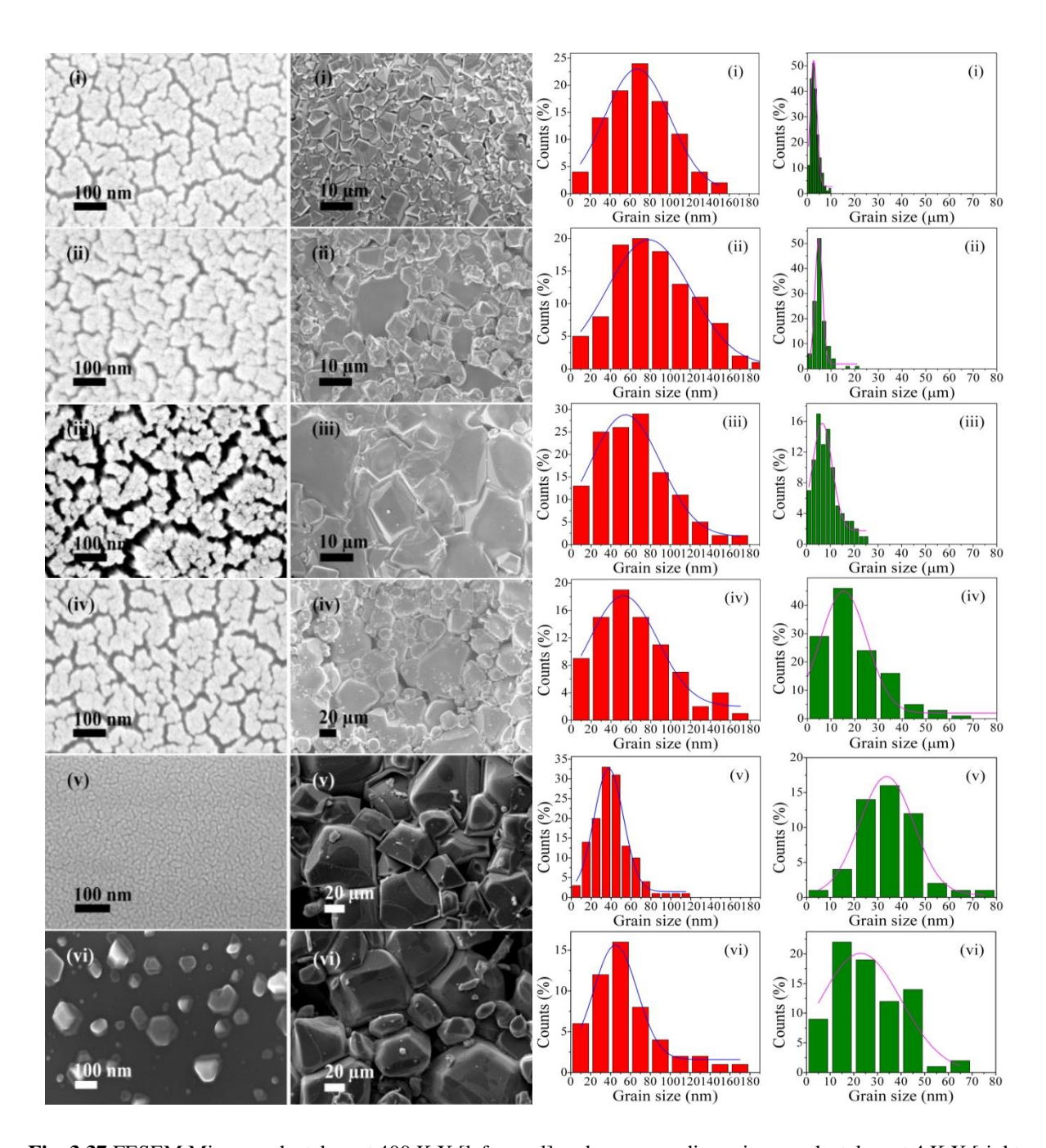


Fig. 3.37 FESEM Micrographs taken at 400 K X [left panel] and corresponding micrographs taken at 4 K X [right panel] ((iv), (v) and (vi) were taken at 1 K X) of $Co_{1-x}Cu_xFe_2O_4$ (x=0.0, 0.2, 0.25, 0.4, 0.9 and 1.0) pellets; (i) $CoFe_2O_4$, (ii) $Co_{0.8}Cu_{0.2}Fe_2O_4$, (iii) $Co_{0.75}Cu_{0.25}Fe_2O_4$, (iv) $Co_{0.6}Cu_{0.4}Fe_2O_4$, (v) $Co_{0.1}Cu_{0.9}Fe_2O_4$ and (vi) $CuFe_2O_4$ which are heated 1200 °C for 4 h.

Fig. 3.38 (right) Grain size distributionstaken for the samples.

For samples annealed at 1200 °C, the average grain size decreased up to x=0.9 with final increase at x=1.0. For samples sintered at 1200 °C the morphology shows that the samples

consists of few tetragonal, hexagonal rectangular/square, spherical and elliptical shape particles but most of them are irregular in shape as can be seen in the right panel of the Fig. 3.37. With increasing Cu⁺² concentrations an increase in the average particle size was observed. The observed increase in particle size could be due to increase of agglomeration. Because of the high agglomeration of grains during sintering at high temperature 1200 °C which resulted in high sintered density there is a large increase in particle size compared to those obtained from samples heated at 100, 600 °C. The grain size distributions of the samples heated at 1200 °C are shown in Fig. 3.38. Images taken at a higher magnification 400 KX (left panel of Fig. 3.37) show uniformly distributed nano-grains with average grain sizes 70, 83, 64, 64, 40 and 57 nm for CoFe₂O₄, Co_{0.8}Cu_{0.2}Fe₂O₄, Co_{0.75}Cu_{0.25}Fe₂O₄, Co_{0.6}Cu_{0.4}Fe₂O₄, Co_{0.1}Cu_{0.9}Fe₂O₄ and CuFe₂O₄ respectively (Table 3.8).

Table 3.9. Element composition of pellets measured from EDS

$Co_{1-x}Cu_xFe_2O_4$ $(x = 0.0-1.0)$		"Con	position m	easured from	n EDS"	
(x - 0.0 - 1.0)	Co (at.	Fe (at. %)	Cu (at.	Fe/Co	Cu/Co	Fe/Cu
	%)	, ,	%)			
	$Co_{1-x}Cu_x$	Fe ₂ O ₄ (Powder	Dried at 90	0 °C for 12 l	<u>(h)</u>	
x=0	12.94	27.04	_	2.09	· -	
x = 0.2	11.39	31.33	3.04	2.75	0.267	
x = 0.25	12.41	33.03	3.78	2.66	0.304	
x = 0.4	13.03	47.67	9.56	3.65	0.733	
x = 0.9	3.88	48.78	19.02	12.57	4.902	2.56
x=1.0	_	48.62	24.58	-	_	1.98
	$Co_{1-x}Cu_xI$	Fe ₂ O ₄ (Pellets)	Heated at 1	00 °C for 4	h)	
x=0	18.00	36.04	-	2.00	_	
x = 0.2	15.42	36.75	4.49	2.38	0.291	
x = 0.25	13.11	34.05	4.18	2.60	0.319	
x = 0.4	10.18	34.13	6.03	3.35	0.592	
x = 0.9	3.92	49.27	23.01	12.57	5.87	2.14
x = 1.0	_	50.16	24.82	-	-	2.02
	$Co_{1-x}Cu_x$	Fe ₂ O ₄ (Pellets)	Heated at 6	00 °C for 4	h)	
x=0	19.22	39.53	_	2.06	· -	
x = 0.2	21.82	50.23	4.80	2.30	0.219	
x = 0.25	13.95	35.43	3.66	2.53	0.262	
x = 0.4	12.93	39.70	7.05	3.07	0.545	
x = 0.9	4.56	51.14	22.66	-	4.96	2.256
x = 1.0	_	52.37	25.68	-	_	2.04
	$Co_{1-x}Cu_xF$	Te ₂ O ₄ (Pellets H	Heated at 12	200 °C for 4	(h)	
x=0	26.03	51.67	_	1.99	_	
x = 0.2	22.27	52.02	5.49	2.33	0.269	
x = 0.25	15.88	41.84	3.78	2.63	0.238	
x = 0.4	15.26	50.05	10.25	3.28	0.671	
x = 0.9	2.43	49.72	23.37	_	9.6	2.127
x=1.0	_	48.68	24.98	_	-	1.95

It is to be noted that the average grain sizes estimated from FESEM has been found in good matching with crystallite sizes determined by XRD, indicating that each particle (tetragonal, hexagonal rectangular/square, spherical and elliptical shape) is formed by aggregation of number of nanograins/nanocrystallites. Average grain sizes of all the samples of composition (x = 0.00 to 1.0) have been estimated by FESEM images using imageJ software and are reported in Table 3.8. In addition, it can clearly be seen from Figs. 3.34, 3.35, 3.36 and 3.37 that the grain size seems to increase with increasing temperature.

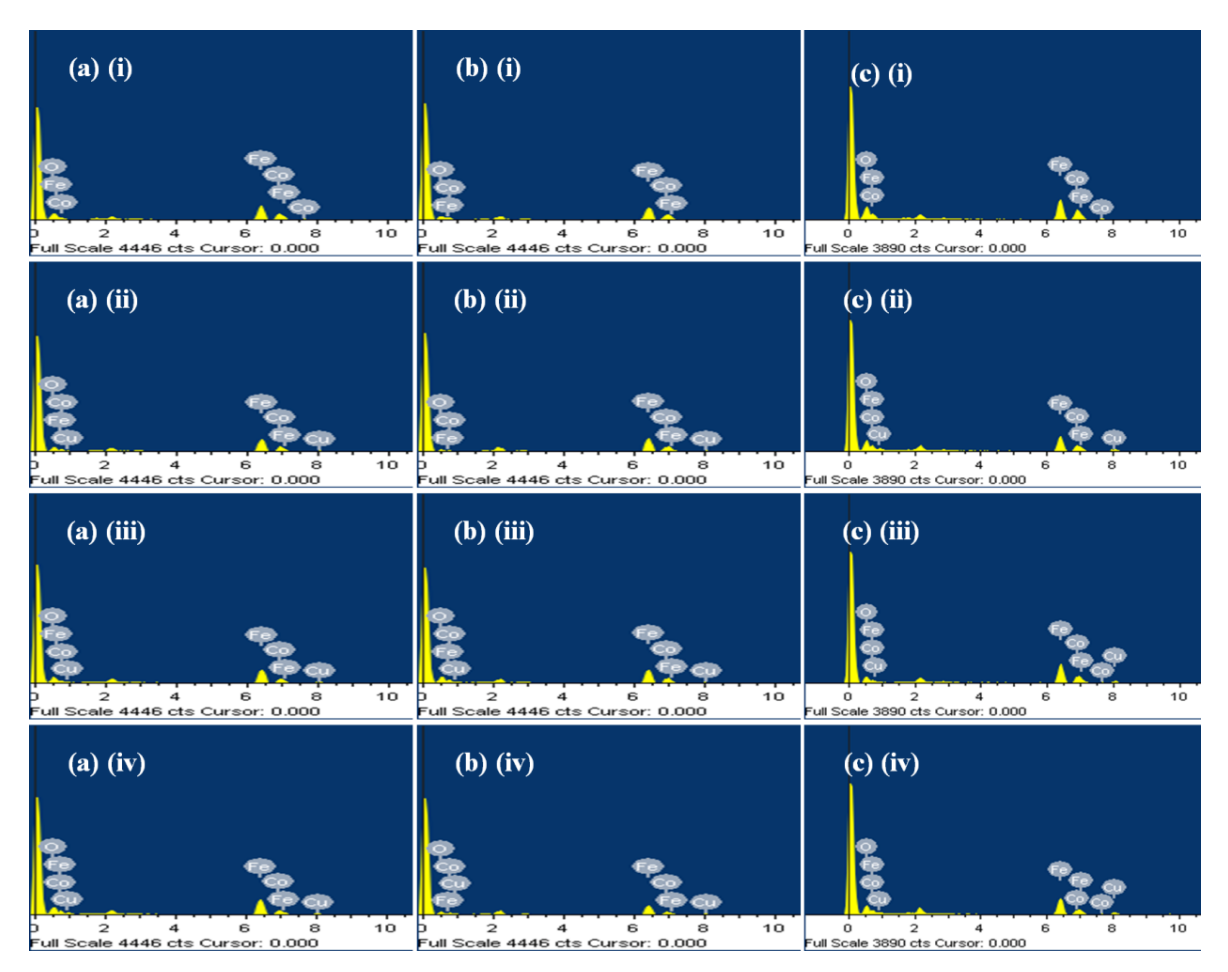


Fig. 3.39. The EDAX spectra of $Co_{1-x}Cu_xFe_2O_4$ (x = 0.0, 0.2, 0.25, 0.4, 0.9 and 1.0) pellets; (i) $CoFe_2O_4$, (ii) $Co_{0.8}Cu_{0.2}Fe_2O_4$, (iii) $Co_{0.75}Cu_{0.25}Fe_2O_4$, (iv) $Co_{0.6}Cu_{0.4}Fe_2O_4$, (v) $Co_{0.1}Cu_{0.9}Fe_2O_4$ and (vi) $CuFe_2O_4$ which are sintered at (a) $100^{\circ}C$, (b) $600^{\circ}C$ and (c) $1200^{\circ}C$ for 4 h.

The EDAX spectra (Fig. 3.39) of the $Co_{1-x}Cu_xFe_2O_4$ (x = 0.0-1.0) samples shows the presence of all Co, Fe, Cu and O elements. Except the gold (Au) peak, no additional peaks due to impurities appear in the EDS spectrum. Table 3.9 shows the concentration of elements present

in the samples and the at. % ratios Fe/Co and Cu/Co. From the Table 3.9 we can observe that the ratios of the elements slightly deviate from the stoichiometric ratios.

3.3.4 Magnetic properties

As shown in Fig. 3.40, magnetization hysteresis loops of all $Co_{1-x}Cu_xFe_2O_4$ (x = 0.0, 0.2, 0.25, 0.4, 0.9 and 1.0) samples exhibited a typical characteristic features of ferro- or ferri-magnetic materials ferromagnetic property at room temperature. Expanded view is given in the inset. Saturation magnetization (M_s), remanent magnetization (M_R), and coercivity (H_c) of the samples are tabulated in Table 3.10. The saturation magnetization (M_s) of $Co_{1-x}Cu_xFe_2O_4$ (x = 0.0, 0.2, 0.25, 0.4, 0.9 and 1.0) nanoparticles (samples heated at 90 °C) decreases with increase of copper substitution. This is because of decrease in grain size as can be seen from Table 3.8. The results are consistent with earlier Copper-substituted cobalt ferrite nanoparticles [6], which also showed a decreasing M_s after the doping of Cu element. A small increase of M_s at x = 0.25, 0.4 may be due to occupation of Cu^{2+} in tetrahedral (A) site which forces Fe^{3+} ions migrate to octahedral sites leading to small increase of M_s .

Our value of highest saturation magnetization (M_s) of CoFe₂O₄ nanoparticles is 47.6 emu·g⁻¹, which is smaller than the value reported by Fonseca et al. [34]. The M_s consistently decreases with decreasing crystallite size as crystallite size decrease with Cu content and it becomes relatively much lower at x = 1.0 i.e. CuFe₂O₄ which exhibit superparamagnetism. The CuFe₂O₄ exists in the tetragonal phase. In the tetragonal phase, CuFe₂O₄ exhibits inverse spinel structure. In CuFe₂O₄, all (8) Cu²⁺ (1µ_B) ions occupy octahedral sites, while half Fe³⁺ ions occupy octahedral sites and remaining half occupy tetrahedral [73]. The net magnetic moment is only due to the Cu²⁺ ions. Therefore, M_s of CuFe₂O₄ is smaller than that of CoFe₂O₄. The values of saturation magnetization (M_s), residual magnetization (M_r), coercivity (H_c) are given in Table 3. Cobalt ferrite heated at 90 °C and 100°C show low M_s compared to that of bulk material (80 emu g⁻¹) [74] which may be due to small crystallite size.

Coercivity H_c decreases with increasing Cu concentration (Table 3.11). CuFe₂O₄ nanoparticles heated at 90 °C and 100 °C show zero coercivity (H_c). The verage crystallite size and average grain size of CuFe₂O₄ nanoparticles heated at 90 °C are 6, 15 nm and that of sample heated at 100 °C are 7 and 26 nm, respectively. At very small size, magnetic nanoclusters have single magnetic domain, and the strongly coupled magnetic spins on each atom combine to produce a particle with a single gaint spin. Therefore ferromagnetic CuFe₂O₄ particle show the effect of

superparamagnetism at about 15 nm to 26 nm. That is the CuFe₂O₄ particles rotate freely at room temperature.

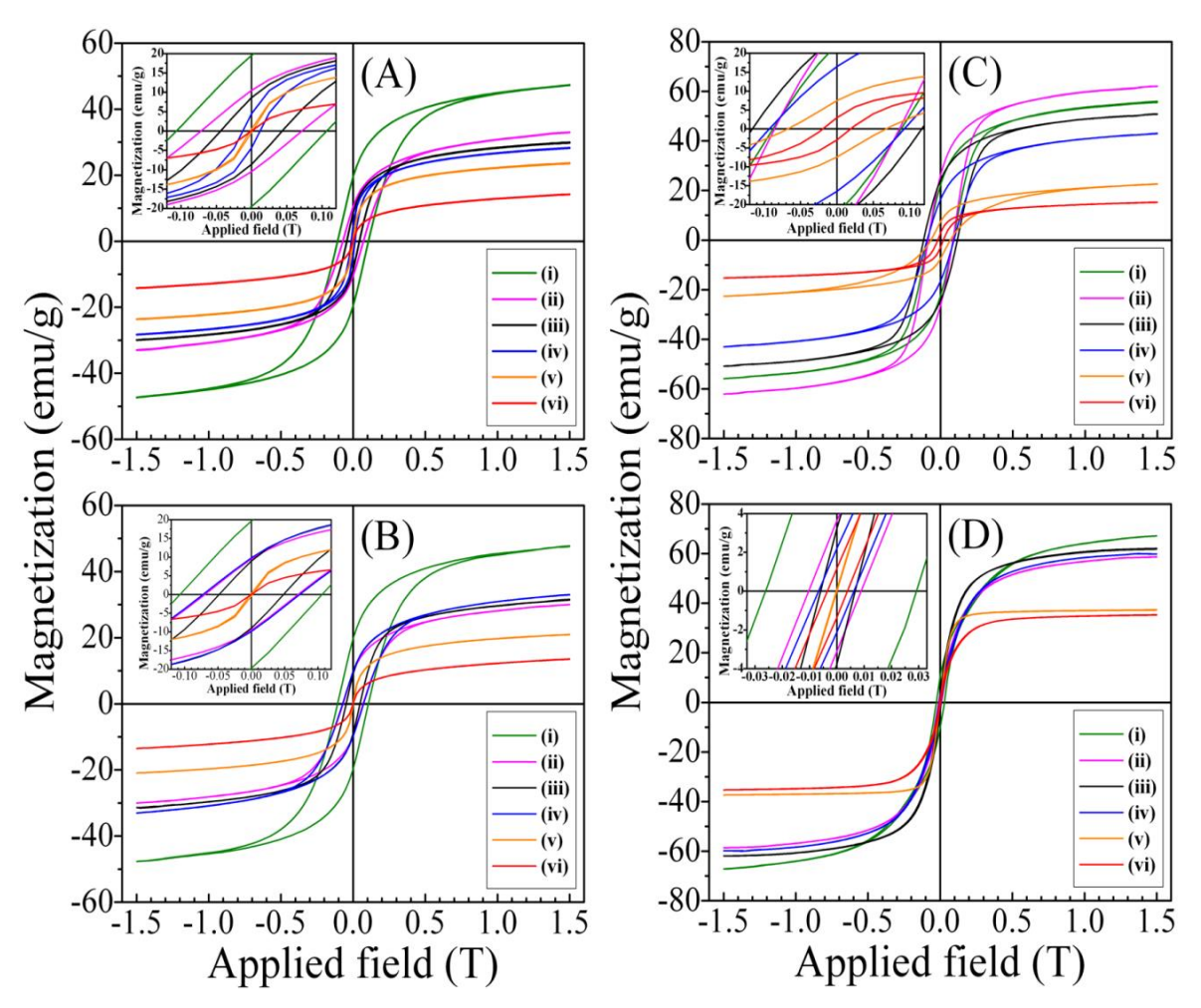


Fig. 3. 40. M-H loops of cobalt-copper ferrite samples $\text{Co}_{1-x}\text{Cu}_x\text{Fe}_2\text{O}_4$ (x = 0.0, 0.2, 0.25, 0.4, 0.9 and 1.0); (i) CoFe_2O_4 , (ii) $\text{Co}_{0.8}\text{Cu}_{0.2}\text{Fe}_2\text{O}_4$, (iii) $\text{Co}_{0.75}\text{Cu}_{0.25}\text{Fe}_2\text{O}_4$, (iv) $\text{Co}_{0.6}\text{Cu}_{0.4}\text{Fe}_2\text{O}_4$, (v) $\text{Co}_{0.1}\text{Cu}_{0.9}\text{Fe}_2\text{O}_4$ and (vi) CuFe_2O_4 which are heated at (**A**) 90 °C (overnight), (**B**) 100 °C, (**C**) 600 °C and (**D**) 1200 °C for 4 h.

As the Cu concentration increases remanence (M_R) decreased. The reduction in remanence (M_R) with increasing Cu doping (see Table 3.10) is because of decrease of anisotropy. As the net magnetic moment of fully inverted cobalt ferrite is only due Co^{2+} ($3\mu_B$) ions. But, cobalt ferrite normally shows mixed spinel structure. As the orbital moment of Co^{2+} occupied at octahedral sites of spinel structure is relatively large, the magnetocrystalline anisotropy is not negligible even though the crystal structure of CoFe_2O_4 is face-centered cubic [16]. Moreover, the substitution of Cu reduces the magneto-crystalline anisotropy. Therefore, this might be the reason for a decrease in remanence (M_r). For samples annealed at 600 °C, the M_s first increased

at x=0.2 and decreased thereafter with increase in copper substitution. The increase in M_s at x=0.2 is due to increase of crystallite size. Decrease in M_s at x=0.25 even though crystallite size increased, is due to the combined effect of crystallite size and decrease in the magnetization of the octahedral sites (M_B) due to substitution of Co^{2+} (3 μ_B) by less magnetic Cu^{2+} ions (1 μ_B). Further decrease in M_s at x=0.4, 0.9 and 1.0 is also attributed to decrease in crystallite size together with substitution of Co^{2+} by Cu^{2+} ions at B-sites. The H_C value of $CoFe_2O_4$ is 880 G for an average grain size of D_{FESEM} = 64 nm. A decrease of H_C is observed among the Cu substituted samples: initially, H_C value of 854 G is observed for Cu substitution of x = 0.2 with grain size of D_{FESEM} = 60 nm. For x = 0.25, H_C value increased to 1165 G due to increase of grain size (D_{FESEM} = 66 nm). As Cu doping increases to x = 0.4, H_C decreased to 922 G due to the corresponding reduction in grain size (D_{FESEM} = 62) as shown in the Table 3.8. The decrease in H_C (676 G) values at x=0.9 is due to decrease in magnetic anisotropy which arises due to substitution of Co^{2+} on octahedral sites by Cu^{2+} ions. Further decrease in H_C (192 G) at x =1.0 is due to the smallest crystallite size (15 nm) of $CuFe_2O_4$.

Table 3.10 Magnetic properties of $Cu_xCo_{1-x}Fe_2O_4$ (x = 0.0-1.0)

$Cu_xCo_{1-x}Fe_2O_4$	M_r	M_s	H_c
(x = 0.0 - 1.0)	(emu/g)	(emu/g)	(G)
Cu_xCo_{1-x}	Fe ₂ O ₄ (Powder	Dried at 90 °	<u>C)</u>
x=0	19.6	47	1080
x = 0.2	10	33	716
x = 0.25	8.6	30	432
x = 0.4	4	28	120
x = 0.9	0.4	23.6	16
x=1.0	0.023	14.2	2
$Cu_xCo_{1-x}Fe_2Co_{1-x}$	4 (Pellets Heat	ed at 100 °C f	for 4 h)
x=0	19.7	47.6	1067
x = 0.2	9.5	30	687
x=0.25	9	30	478
x = 0.4	4	29	135
x = 0.9	0.4	21	16
x=1.0	0.02	13.5	3
$Cu_xCo_{1-x}Fe_2C$	4 (Pellets Heat	ed at 600 °C f	for 4 h)
x=0	22	56	880
x = 0.2	26	62	854
x = 0.25	24	51	1165
x = 0.4	16.5	43	922
x = 0.9	7.4	22.6	676
x=1.0	3	15	192
$Cu_xCo_{1-x}Fe_2O_x$,		,
x=0	10.5	67	277
x = 0.2	3.4	58.6	96
x = 0.25	3.5	62	64
x = 0.4	2	60	65
x = 0.9	0.04	37	1
x=1.0	1	35	36.6

The remanence (M_r) values exhibited an increase at Cu doping of x = 0.2 and decreases thereafter with increasing Cu concentration. The change in the remanent magnetization (M_r) is due to change in magnetic anisotropy resulting from cation distribution as discussed above.

Copper-cobalt ferrites $\text{Co}_{1-x}\text{Cu}_x\text{Fe}_2\text{O}_4$ (x=0.0, 0.2, 0.25, 0.4, 0.9 and 1.0) synthesized using the co-precipitation technique which were sintered at 1200 °C for 4 h became spinel ferrite phase with high purity, resulting in high magnetic properties. From Table 3.10, M_s value decreases from 67 to 58.6 emu/g when Cu doping increases from x=0 to 0.2 and increased to 62 emu/g when x=0.25 which then decreased to 60, 37 and 35 emu/g, respectively, at x=0.4, 0.9 and 1.0 (Fig. 3.40 and Table 3.10). The decrease in M_s at x=0.2 might be substitution of Co^{2+} by Cu^{2+} at B-sites. The M_s values of all compositions from x=0.0 to 1.0 increases with annealing temperature from 100 °C to 1200 °C because of increase in crystallite size.

Table 3.10 also shows that the coercivity (H_c) decreases from 277 G to 37 G as x is increased from 0 to 1.0. This is because of substitution of Co^{2+} ions by small anisotropic of Cu^{2+} ions resulting in decrease of magnetocrystalline anisotropy [14,15]. The decrease of H_c is due to the development of domain walls because the grain size/crystallite sizes are $D_{XRD}/D_{FESEM}>40$ nm The samples annealed at 1200 °C are made up of bigger grains (Fig.3.37 right panel) of irregular shape with few spherical, tetragonal, square and hexagonal shape grains. Demagnetizing fields may be generated at the corners of the larger grains and spins may be incoherent with increasing grain size leading to a decrease of H_c [43].

The remanent magnetization for pure $CoFe_2O_4$ is 10.5 emu/g. The decrease in M_r values for copper-cobalt ferrites $Co_{1-x}Cu_xFe_2O_4$ (x = 0.0, 0.2, 0.25, 0.4, 0.9 and 1.0) which vary from 1.5 emu/g to 1 emu/g can be due to interactions between grains which are affected grain size distribution [33,75]. From the M(H) loops of $CuFe_2O_4$ annealed at 100 °C, 600 °C and 1200 °C we conclude that $CuFe_2O_4$ is a soft magnetic material.

3.3.5 Dielectric properties

Figure 3.41 shows dielectric constant (ε') versus Logarithm of frequency plots of Co_{1-x}Cu_xFe₂O₄ (x = 0.0, 0.2, 0.25, 0.4, 0.9 and 1.0) ferrites measured at RT in the range of 100 Hz–40 MHz frequencies. It is evident that for each sample the dielectric permittivity is very high at low frequencies initially decrease sharply with increasing frequency. At high frequencies, it decreases slowly and becomes almost constant. Very high dielectric constant at lower frequencies is because of contribution from hoping conduction including space charge.

Electrons are able to follow reversal of the field and polarization is in phase with driving electric field. The decrease of dielectric constant (ϵ') with increasing frequency is due to lagging of species that contribute to polarization behind the driving electric field [76]. When frequency of driving field is low, the electron hoping adjusts itself to the instantaneous value of electric field. But as the frequency becomes higher it is not possible for electrons to follow reversal of the field and lag behind it. This reduces space charge polarization and hence dielectric constant also decreased [77]. The polarization at lower frequencies is due electron jumping between $Fe^{3+} \leftrightarrow Fe^{2+}$ ions in the ferrite material (Mallapur et al 2009). At high frequencies, fluctuating dipole moments of atoms polarized by external electric field scatters the hopping electrons. Therefore the induced polarization and dielectric constant becomes small.

The dielectric constant in the present study is of the order of 10³ which is one order of magnitude higher (up to 1kHZ) as compared to that reported by Balavijayalakshmi et al. [33] and of the same order when compared to that reported by Sivakumar et al. [28]. In case of samples heated at 100 °C for 4 h (Fig. 3.41(a)), introduction of Cu doping of $x=0.2 \text{ Co}_{0.8}\text{Cu}_{0.2}\text{Fe}_2\text{O}_4$ results in a large increase in dielectric constant than pure cobalt ferrite. The substitution of Co²⁺ by Cu²⁺ ions increases the number of mobile charge carriers that is electrons which produce dipole moment locally by hopping conduction. Therefore, Cu^{2+} doping of at x=0.2 causes an increase in the polarization, and hence dielectric constant (Fig. 3.41 & Table 3.11). High dielectric constant at x=0.2 (Co_{0.8}Cu_{0.2}Fe₂O₄) may be because of decrease in grain size/crystallite size. The increase in dielectric constant, ε' value might also be due to the decrease of porosity and grain size of the sample (Table 3.8). As the doping concentration increases to (x=0.25)Co_{0.75}Cu_{0.25}Fe₂O₄ dielectric constant value decreases due to increase in the porosity and small increase in grain size as compared to Co_{0.8}Cu_{0.2}Fe₂O₄. Dielectric constant is found to increase for Cu doping x=0.4 (Co_{0.6}Cu_{0.4}Fe₂O₄) due to decrease in porosity as compared to that of $Co_{0.75}Cu_{0.25}Fe_2O_4$. A large decrease of ε' as Cu concentration increase from x=0.4 to x=0.9 is due to increase in porosity (53.49%) and smallest grain size and at x = 1.0, CuFe₂O₄ exhibits lowest dielectric constant which is because of small grains and very high porosity.

But for samples heated at 600 °C for 4 h (Fig. 3.41(b)), CoFe₂O₄ shows lower dielectric constant due to bigger grain size compared to that of Co_{0.8}Cu_{0.2}Fe₂O₄. Decrease in dielectric constant at x=0.2 is because of reduced grain size and porosity. Cu doping at x=0.4 (Co_{0.8}Cu_{0.4}Fe₂O₄), shows increase of dielectric constant because of reduced grain size and porosity. Lowest

dielectric constant value for $Co_{0.75}Cu_{0.25}Fe_2O_4$ (x=0.25) is due to highest porosity and biggest grain size. At x=0.4, small increase in the dielectric constant of $Co_{0.6}Cu_{0.4}Fe_2O_4$ is due to smallest porosity, followed by a very slight increase at x=0.9 is due to decrease in grain size even though porosity of $Co_{0.1}Cu_{0.9}Fe_2O_4$ increased by 4 % and finally, at x=1.0, $CuFe_2O_4$ exhibits highest dielectric constant than all other compositions is due to very small grain size even though it has same porosity as that of $Co_{0.1}Cu_{0.9}Fe_2O_4$.

Similarly for samples heated at 1200 °C for 4 h, the 20% Cu doped cobalt ferrite i.e. $Co_{0.8}Cu_{0.2}Fe_2O_4$ exhibit lowest dielectric constant because of biggest grain size than all other compositions. A slight increase of dielectric constant at x=0.25 ($Co_{0.75}Cu_{0.25}Fe_2O_4$) is because of decrease of grain size and porosity followed by a significant increase at x=0.4 ($Co_{0.6}Cu_{0.4}Fe_2O_4$) due to decrease in grain size and even though the porosity increased significantly. Further increase in Cu doping at x=0.9 ($Co_{0.1}Cu_{0.9}Fe_2O_4$), results in a large increase in dielectric constant due to smallest grain size even though the porosity attains its highest value and at x=1.0, $CuFe_2O_4$ exhibits a small increase due to the decrease in porosity. The significant change in dielectric constant of samples from x = 0.2–1.0 is ascribed to the structural changes caused by Cu^{2+} in the cobalt ferrite material.

Table 3.11: Dielectric Constant ϵ' at Different Frequencies

Samples			ε΄		
CuxCo _{1-x} Fe ₂ O ₄	100Hz	1kHz	1MHz	5MHz	40MHz
(x = 0.0 - 0.4)					
Cu	Co _{1-x} Fe ₂ O ₄ (Pe	ellets Heated	at 100 °C for	4 h)	
x=0	2014	2291	43	25	16
x=0.2	75648	30197	69	39	24
x=0.25	30902	13066	41	25.4	16
x=0.4	85121	34878	70.7	47	31
x=0.9	2242	190	12.6	11	9.6
x=1.0	200	48	10.7	10	9
Cu	Co _{1-x} Fe ₂ O ₄ (Po	ellets Heated	at 600 °C for	4 h)	
x=0	24499	6280	22	16	11.9
x=0.2	122197	37994	57	25	16.6
x=0.25	2243	281	13	11	9.3
x=0.4	15128	2024	18	15	12.3
x=0.9	19795	59328	21.3	15.5	11.8
x=1.0	275929	4770	1507	1206	1015
Cux	Co _{1-x} Fe ₂ O ₄ (Pe	llets Heated a	at 1200 °C for	· 4 h)	
x=0	20531	8467	2155	1334	219
x=0.2	1391	599	119	64	26.7
x=0.25	1393.6	820	134	83	31.5
x=0.4	3531	1667	57	37	22
x=0.9	57699	18227	178.7	79	49
x=1.0	74289	24955	225.6	109.4	76

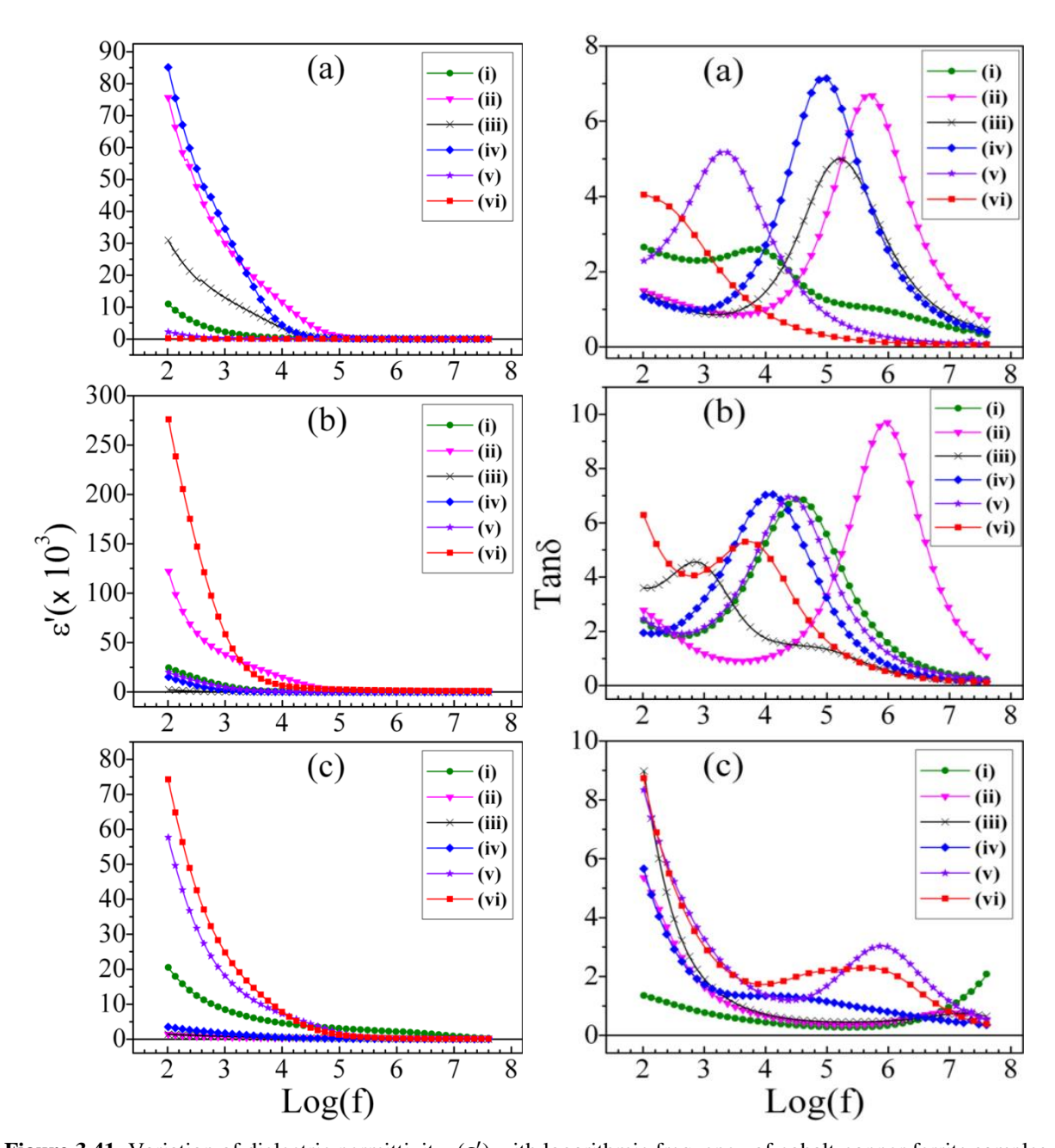


Figure 3.41. Variation of dielectric permittivity, (ϵ') with logarithmic frequency of cobalt-copper ferrite samples $Co_{1-x}Cu_xFe_2O_4$ (x=0.0, 0.2, 0.25, 0.4, 0.9 and 1.0); (i) $CoFe_2O_4$, (ii) $Co_{0.8}Cu_{0.2}Fe_2O_4$, (iii) $Co_{0.75}Cu_{0.25}Fe_2O_4$, (iv) $Co_{0.6}Cu_{0.4}Fe_2O_4$, (v) $Co_{0.1}Cu_{0.9}Fe_2O_4$ and (vi) $CuFe_2O_4$ which are heated at (α) 100 °C, (α) 600°C and (α) 1200 °C for 4 h measured at RT.

Fig. 3.42. (**right**) The variation of dielectric loss with log of frequency of cobalt-copper ferrite samples $Co_{1-x}Cu_xFe_2O_4$.

Dielectric loss behavior

Fig. 3.42 illustrates $\tan \delta$ as a function of frequency. Dielectric loss decreases with increasing frequency. In general, $\tan \delta$ is a measure of, the rate at which the driving field does work upon the medium, $\underline{E} \cdot \underline{J}$ which must be averaged over one complete cycle to obtain the net power per unit volume absorbed from the field and dissipated within the medium. As the frequency becomes higher, the polarization begins to lag behind the driving electric field because the hopping rate of charge carriers cannot stay in step with the field. Due to this dielectric loss decreases with frequency. The power absorbed from the field is proportional to $\omega \chi''$, as the frequency of the applied field approaches resonance frequency, if the hopping rate or mobility of charge carriers increases their relaxation frequency increases. When the relaxation frequency reaches the frequency of driving electric field, resonance occurs maximum energy is absorbed and a peak is observed in $\tan \delta$ versus frequency graph. Only in this region of strongest absorption (at resonance) the polarization response is large and significantly out of phase with the driving electric field. This out of phase component of polarization continuously drains away energy from the field and appears as Joule heating of the material.

Table 3.12: Dielectric Loss Tangent (tan δ) at different frequencies

Samples			tan δ					
Cu _x Co _{1-x} Fe ₂ O ₄	100Hz	1kHz	1MHz	5MHz	40MHz			
(x = 0.0 - 0.4)								
Cu _x Co _{1-x} Fe ₂ O ₄ (Pellets Heated at 100 °C for 4 h)								
x=0	2.652	2.298	0.954	0.666	0.323			
x = 0.2	1.496	0.972	5.789	2.372	0.740			
x=0.25	1.430	0.877	2.767	1.189	0.467			
x=0.4	1.340	0.977	2.533	1.027	0.389			
x=0.9	2.286	4.6	0.256	0.133	0.086			
x=1.0	4.047	2.6	0.120	0.078	0.067			
Cu _x Co	1-x Fe ₂ O ₄ (P	ellets Heate	ed at 600 °C	for 4 h)				
x=0	2.406	2.037	1.559	0.633	0.237			
x=0.2	2.778	1.181	9.655	4.578	1.082			
x=0.25	3.602	4.447	0.562	0.267	0.118			
x = 0.4	1.945	3.184	0.763	0.336	0.147			
x=0.9	2.46	2.153	1.204	0.516	0.222			
x=1.0	6.29	4.204	0.505	0.248	0.122			
Cu _x Co	I-x Fe ₂ O ₄ (Pe	ellets Heate	d at 1200 °C	for 4 h)				
x=0	1.335	0.779	0.339	0.676	2.084			
x=0.2	5.353	1.645	0.455	0.740	0.534			
x=0.25	8.982	1.925	0.492	0.646	0.650			
x=0.4	5.663	1.738	0.798	0.572	0.354			
x=0.9	8.341	3.28	2.997	1.689	0.534			
x=1.0	8.734	3.025	2.165	1.195	0.385			

For samples heated at 100 °C for 4 h, the loss tangent decreases with increasing frequency from 100 Hz, becomes low at 764 Hz and increases slowly exhibiting the relaxation peak at 6.844 kHz between the frequencies 1 kHz to 158.96 kHz followed by a feeble peak at 664 kHz for the pure $CoFe_2O_4$. For $Co_{0.8}Cu_{0.2}Fe_2O_4$, $tan\delta$ decreases with increasing frequency from 100 Hz, becomes low around 498.8 kHz and increases thereafter with frequency showing a peak shifted to high frequency between 4.25 kHz to 40 MHz with a peak at 498.88 kHz. Thus at x = 0.2, the dielectric relaxation time decreased. While $Co_{0.75}Cu_{0.25}Fe_2O_4$ exhibits a relaxation peak between 1638 Hz to 40 MHz showing maximum at 158.96 kHz, $Co_{0.6}Cu_{0.4}Fe_2O_4$ exhibits a peak a relaxation peak between 764 Hz to 40 MHz showing maximum at 89.73 kHz. For high Cu doping concentration at x = 0.9, the dielectric relaxation peak is further shifted to lower frequency exhibiting a peak at 2.18 kHz, but at x = 0.9, $CuFe_2O_4$ show no relaxation peak. Peak in dielectric loss tangent shifted to higher frequency 498.88 kHz for Cu doping of x = 0.2, and then shifts towards lower frequencies 158.96 kHz, 89.73 kHz and 2.18 kHz with increase of Cu concentration at x = 0.25, 0.4 and 0.9, respectively. The shift of relaxation towards lower frequencies is an indication of increase in the dielectric relaxation time.

For samples heated at 600 °C for 4 h, the loss tangent decreases slowly from 100 Hz to 431 Hz and then increases with increasing frequency becomes maximum at 34.594 kHz showing the relaxation peak between the frequency 430 Hz to 40 MHz for the pure CoFe₂O₄. At x = 0.2(Co_{0.8}Cu_{0.2}Fe₂O₄), the loss tangent decreases from 100 Hz up to 3.863 kHz beyond which it increases and becomes maximum at 883.8 kHz showing the relaxation peak between the frequency 3863 Hz to 40 MHz. Whereas $Co_{0.75}Cu_{0.25}Fe_2O_4$ (for x = 0.25) exhibits a relaxation peak between 100 Hz to 31.5 kHz showing maximum at 695 Hz followed by a feeble peak at 74.15 kHz and decreases thereafter. For x = 0.4, $Co_{0.6}Cu_{0.4}Fe_2O_4$ exhibits a peak a relaxation peak between 100 Hz to 40 MHz showing maximum absorption at 12.13 kHz and decreased beyond that. At high doping level x = 0.9 and x = 1.0, the samples show up relaxation peaks at 25.99 kHz (between 431 Hz to 40 MHz) and 5.14 kHz (between 574 to 119.4 kHz), respectively. For samples heated at 1200 °C for 4 h, CoFe₂O₄ exhibits small loss tangent value and decreases gradually with frequency from 100 Hz and becomes minimum at 211.5 kHz and increases slowly thereafter with frequency and acquire highest value at 40 MHz. For Cu doping at x = 0.2, the loss tangent decreases rapidly up to 211.5 kHz and increases slowly thereafter showing a feeble relaxation peak at 8.7 MHz beyond which it decreases up to 40 MHz while at x = 0.25

the feeble relaxation peak is shifted to 20.5 MHz followed by a small decrease. Whereas at x = 0.4, $Co_{0.6}Cu_{0.4}Fe_2O_4$ shows a rapid decrease till 4.25 kHz beyond which it increases up to 26 kHz and decreases gradually. Finally, for x = 0.9 and x = 1.0 dielectric loss decreases from 100 Hz up to 23.63 kHz and 9.1 kHz, respectively showing relaxation peaks between 23.63 kHz to 40 MHz and 9.1 kHz to 40 MHz, respectively with peaks at 803.4 kHz and 453.5 kHz. It is further observed from the Fig. 3.42(c) that on sintering the samples 1200 °C the relaxation peaks appears at high frequencies, this may be attributed to the low resistivity and the dissipation factor increases at high frequencies. In addition, $CoFe_2O_4$ has high permittivity and low dielectric loss in comparison to Cu doped samples $Co_{1-x}Cu_xFe_2O_4$ (x = 0.2, 0.25, 0.4, and 0.9) whereas $CuFe_2O_4$ exhibit high dielectric constant at low frequencies till 1 kHz and low loss at 40 MHz.

3.3.6 Conclusions

The cobalt ferrite and copper-cobalt ferrite nanoparticles with composition $Co_{1-x}Cu_xFe_2O_4$ (x =0.0, 0.2, 0.25, 0.4, 0.9 and 1.0) synthesized by co-precipitation pressed into pellets and were heated at 100 °C, 600 °C and 1200 °C for 4 hours. The rietveld refinement of X-ray diffraction patterns reveal the formation of single phase spinel structure from x = 0.0 to 0.4 and the compositions with x = 0.9 to 1.0 show tetragonal spinel-(Cu,Fe) structure with I41/amd space group. The samples with x = 0.9 and 1.0 had trace amounts of CuO, and Fe₂O₃ in case of NPs dried at 90 °C and pellets heated at 100 °C, 600 °C shown by lines in the XRD pattern, while samples heated at 1200°C indicate small amount of delafossite (Cu₁Fe₁O₂) phase. CoFe₂O₄ sample heated at 100 °C, 600 °C and 1200 °C showed saturation magnetization (M_s) 47.6 emu/g, 56 emu/g and 67 emu/g, while coercivity decreased as 1067, 880 and 277 G. As-prepared CuFe₂O₄ nanoparticles of size 6 nm heated at 90 °C and CuFe₂O₄ pellet heated at 100 °C exhibit superparamagnetism with M_s of 14 emu/g. Co_{0.1}Cu_{0.9}Fe₂O₄ annealed at 1200 °C also exhibit superparamagnetism showing M_s of 37 emu/g, while CuFe₂O₄ annealed at 1200 °C exhibit M_s of 35 emu/g and low coercivity of 37 G. CuFe₂O₄ heated at 100 °C exhibits dielectric constant value 10 and 9 at 10 MHz and 40 MHz with low loss tangent values of 0.078 and 006, respectively. CuFe₂O₄ heated at 1200 °C exhibits high dielectric constant of 1015 at 40 MHz with low loss tangent value (0.112). Low dielectric constant materials can be used for insulating materials application and high dielectric constant materials could be used as a medium in capacitors.

3.4 Effect of annealing on structural, magnetic and dielectric properties of CoFe₂O₄ nanoparticles.

3.4.1 Introduction

The present work reports synthesis of CoFe₂O₄ nanoparticles and the effect of sintering temperature on structure and magnetic and dielectric properties of CoFe₂O₄ pellets heated at different temperatures 100°C, 400°C, 600°C and 1200°C. We have used co-precipitation method for synthesizing cobalt ferrite nanoparticles. The magnetic properties of the CoFe₂O₄ samples have been correlated with the change of microstructural changes evolved during sintering. Room temperature and low temperature magnetization from 90-400 K of the synthesized (dried at 90 °C) and annealed CoFe₂O₄ samples has also been measured. Room temperature dielectric properties of the heat treated CoFe₂O₄ samples have also been measured.

3.4.2 Structural analysis

XRD pattern of as-synthesized CoFe₂O₄ powder heated at 90 °C (as depicted in Fig. 3.43) show single phase spinel structure (JCPDS no. 98-016-0059). Fig. 3.46 shows x-ray diffraction patterns of CoFe₂O₄ pellets heated at 100 °C, 400 °C, 600 °C and 1200 °C. These patterns show spinel structure of cobalt ferrite according to JCPDS card no 98-016-0059 and all the planes of (111), (220), (311), (222), (400), (331), (422), (511), (440), (531), (422), (620), (533), (622) and (444) were identified. The Rietveld refined data for pellets heated at 100 °C, 400 °C, 600 °C and 1200 °C is shown in Figure 4.47. The various R factors are listed in Table 3.13. The value of χ^2 (goodness of fit) lies in the range of 1.155 to 1.33.

The crystallite size of samples was calculated using Debye-Scherrer's formula [2] D = $0.9\lambda/\beta\cos\theta$ given by Eq. (3.1). Average crystallite sizes are 18, 17.3, 24 and 83 nm for CoFe₂O₄ samples annealed at 100°C, 400°C, 600°C and 1200°C, respectively as shown in Table 3.13. The average crystallite size increased with increase in the annealing temperature. For sample treated at 400°C there is no increase in the average crystallite size. Lattice constant 'a' and unit cell volume 'V' obtained from Rietveld method are given in Table 3.13. The lattice constants are same as the values reported in the literature [91]. All results of Rietveld Method are tabulated in Table 3.13.

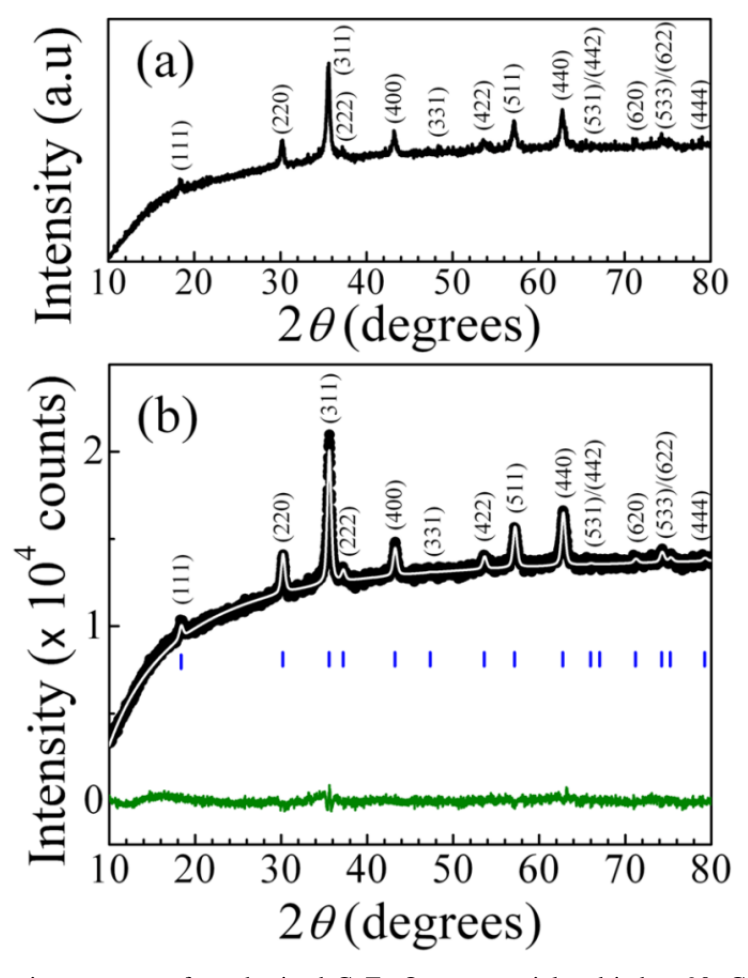


Fig. 3.43. X-ray diffraction patterns of synthesized $CoFe_2O_4$ nanoparticles dried at 90 °C (a), and its Rietveld refinement (b).

Table 3.13 Rietveld parameters and Lattice parameter, average crystallite size (D_{XRD}) , and average grain size (G_{FESEM})

CoFe ₂ O ₄	annealing temperature (°C)					
	90 °C	100 °C	400 °C	600 °C	1200 °C	
Lattice parameter (Å)	8.372(1)	8.373(1)	8.3561(7)	8.3806(5)	8.38988	
D_{XRD} (±1 nm)	17.4	17.5	17.3	24	83	
G_{FESEM} (±1 nm) [μ m]	67	53	40	56	82 [3.5]	
R (expected)/%	0.67306	0.73725	0.70746	0.69207	0.77076	
R (profile)/ %	0.60250	0.72954	0.66815	0.72142	0.73686	
R (weighted profile)/ %	0.77755	0.95095	0.86070	0.92111	1.00538	
G.O.F	1.15525	1.28986	1.21661	1.33096	1.30440	
Theoretical density, $\rho_{hkl}(g/cm^3)$	5.3113	5.3092	5.3413	5.2944	5.2770	
Measured density ρ (g/cm ³)	-	2.51051	2.6778	2.744	4.8655	
Porosity (%)	-	52.71	49.867	48.17	7.798	
Unit cell volume V (Å ³)	586.7489	586.9791	583.4536	588.6157	590.565	

Errors of lattice parameters are shown in parentheses. Average grain size estimated in 'µm' scale from (d)-(ii) of Fig. 3.49 is given in square brackets.

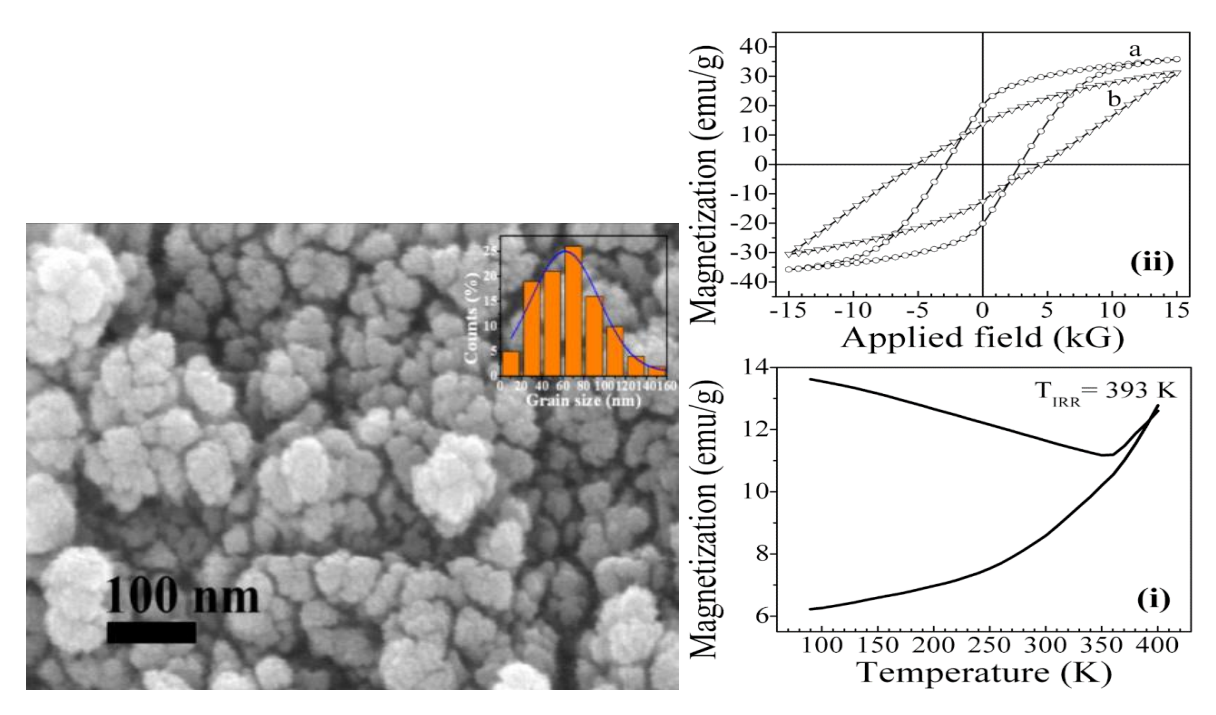


Fig. 3.44 FESEM micrograph of as-synthesized CoFe₂O₄ nanoparticles dried at 90 °C. Inset of the figure show the histogram.

Fig. 3.45 (**right**) ZFC-FC magnetization curves (**i**), and M(H) hysteresis loops (**ii**), measured at (a) 300 K, (b) 100 K; for as-synthesized CoFe₂O₄ nanoparticles dried at 90 °C.

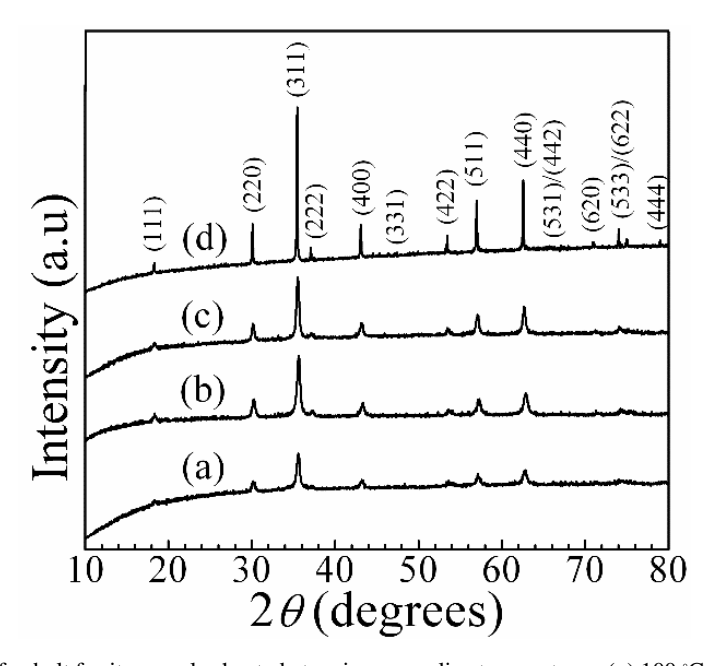


Fig. 3.46. XRD patterns of cobalt ferrite samples heated at various annealing temperatures: (a) $100 \,^{\circ}$ C, (b) $400 \,^{\circ}$ C, (c) $400 \,^{\circ}$ C and (d) $1200 \,^{\circ}$ C for 4 h.

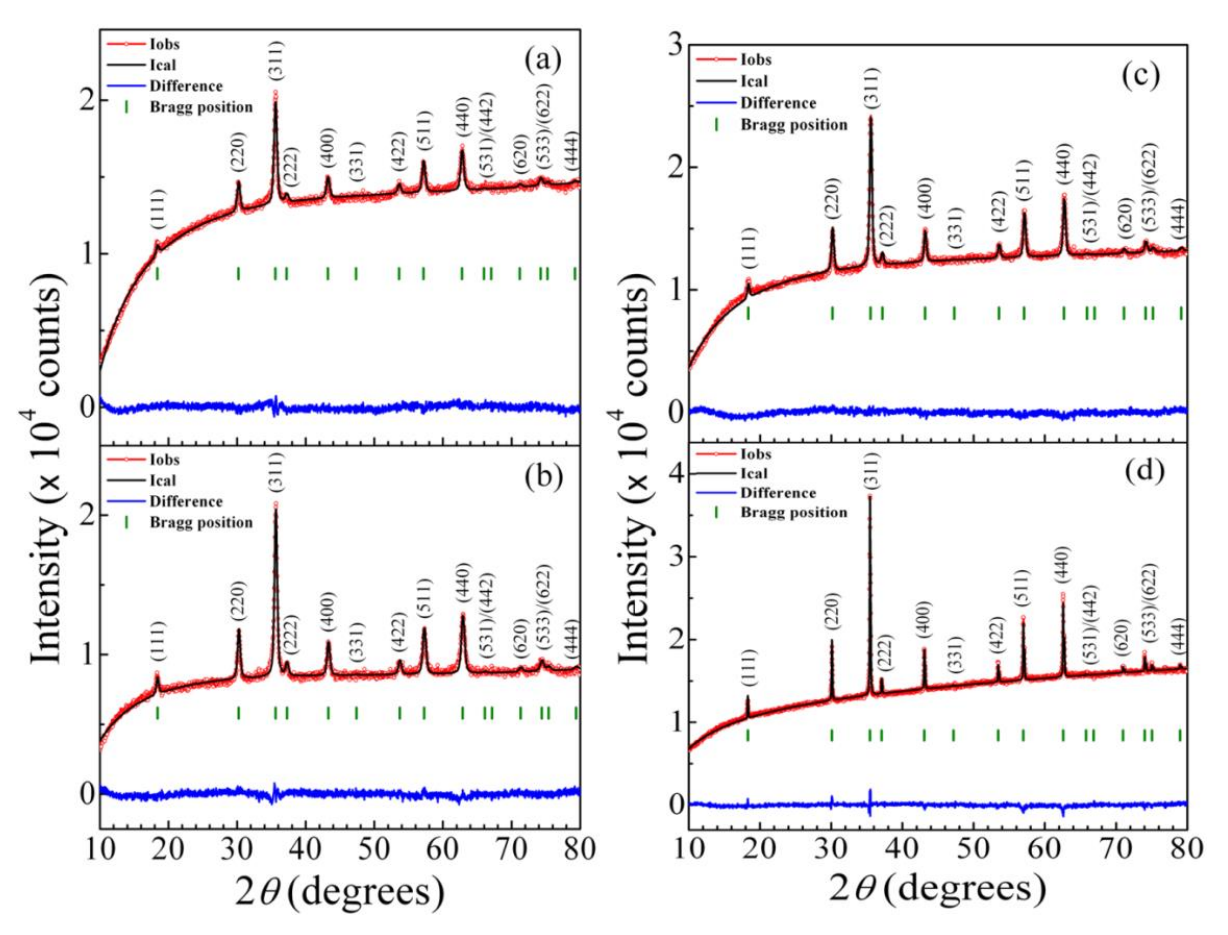


Fig. 3.47 Rietveld refined XRD patterns of cobalt ferrite samples heated at various annealing temperatures: (*a*) 100 °C, (*b*) 400 °C, (*c*) 400 °C and (*d*) 1200 °C for 4 h.

The X-ray densities obtained from Rietveld method were presented in Table 3.13. The density ρ_m of pellets was estimated using the standard formula $\rho_m = m/(\pi r^2 l)$ [37] given by Eq. (3.2). The porosity of the samples was measured using the formula $P = 1 - (\rho_m/\rho_x)$ given by Eq. (3.3). The values of porosity are presented in Table 3.13. Bulk density increases at higher sintering temperatures due to consequent decrease in porosity.

3.4.3 Surface morphology

Fig. 3.44 shows a FESEM image of as-synthesized cobalt ferrite nanoparticles dried at 90 °C. The FESEM show that CoFe₂O₄ nanoparticles are nearly spherical. The insets in Fig. 3.44 show the grain size distribution and average grain size estimated using ImageJ software is 67 nm. The changes in the grain size of CoFe₂O₄ samples annealed at 100, 400, 600 and 1200 °C were observed by FESEM. FESEM images were taken at 4 KX and 400 KX magnifications and 10 kV. FESEM micrographs of samples heated at 100 and 600 °C (Fig. 3.48 (a) and (c)) show

grains with uniform morphology with almost spherical shape and agglomerated because of their magnetic behaviour. The agglomeration can be due to van der Waals "intermolecular" interactions. The histograms of grain size for samples are shown in the insets of Fig. 3.48. Agglomeration is more in the case of samples heated at 100, 400 and 600 °C (Fig. 3.48 (a) and (c)) due to small crystallite size and the agglomerated grains appear like a single big grain in the images. This agglomeration affects the different physical properties. Average grain sizes of all the samples have been estimated from FESEM images using imageJ software and are reported in Table 3.13. Crystallite sizes found from the XRD pattern are much less than grain sizes estimated from FESEM due to agglomeration of few number of nanocrystallites.

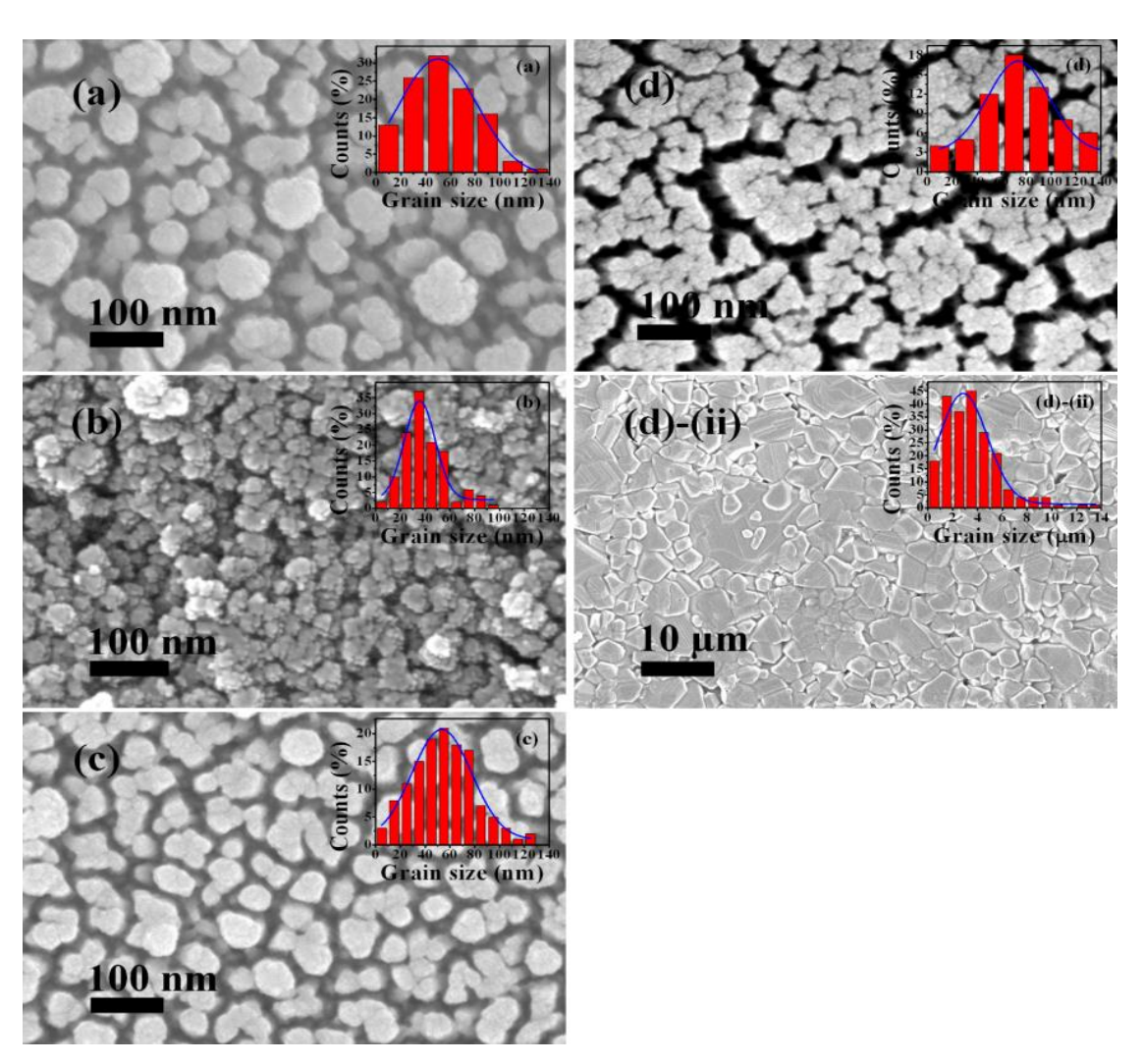


Fig. 3.48 FESEM images CoFe₂O₄ samples heated at (a) 100 °C; (b) 400 °C; (c) 600 and (d) 1200 °C for 4 h. (d)-(ii) is the image taken at low magnification of 4 KX for the sample (d).

But for samples heated at 1200 $^{\circ}$ C the average crystallite size estimated from XRD matches well with the average grain size measured from FESEM. Images taken at low magnification of 4 KX (right panel of Fig. 3.48(d)-(ii)) show the formation grains with irregular shape with few tetragonal, hexagonal rectangular/square shape microscopic domains with average grain size of 3.3 μ m.

The EDAX spectrums (Fig. 3.49) of the CoFe₂O₄ samples show all Co, Fe and O elements. Except gold, no impurities appear in the EDS spectrum. Table 3.14 shows the concentration (atomic %) of elements present in the samples and the at. % ratio of Fe/Co. From the Table 3.14 we can observe that the ratios of the elements slightly deviate from the stoichiometric ratio of 2:1.

Table 3.14. Composition of the preparedpellets measured from EDS

CoFe ₂ O ₄	Composition measured from EDS					
(annealing Tamp. (°C))	Co (at. %)	Fe (at. %)	Fe/Co			
90 °C	21.97	41.89	1.906			
100 °C	15.95	31.54	1.98			
400 °C	-	-	-			
600 °C	19.14	37.49	1.96			
1200 °C	18.33	36.57	1.995			

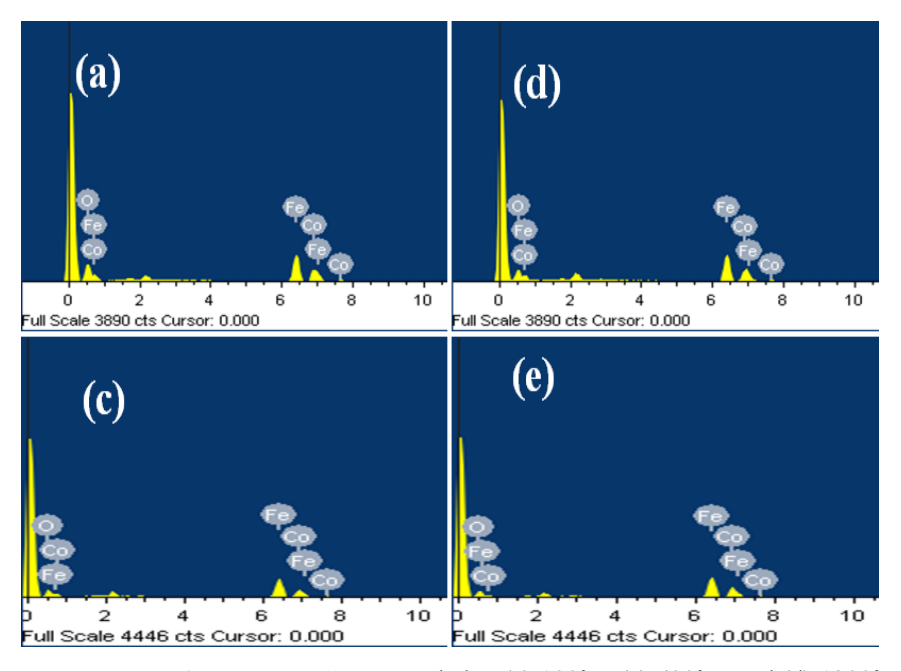


Fig. 3.49. The EDAX spectra of $CoFe_2O_4$ pellets annealed at (a) $100^{\circ}C$, (c) $600^{\circ}C$, and (d) $1200^{\circ}C$ for 4 h. (e) assynthesized $CoFe_2O_4$ nanoparticles heated at $90^{\circ}C$.

3.4.4 Magnetic properties

Fig. 3.45(ii) shows M(H) plots of as-synthesized CoFe₂O₄ nanoparticles heated at 90 °C measured at temperatures of 100 and 300 K. The M_s is less than that of CoFe₂O₄ value, which is due to surface spin canting [92-93]. The reason for the increasing coercivity at 100 K is due to increase in the magnetic anisotropy. Magnetic hysteresis loops of CoFe₂O₄ samples measured at RT and 100 K on the samples treated at different temperatures are shown in Fig. 3.50 (i) and 3.50 (ii), respectively. All results from VSM analysis at room temperature ("magnetic properties like M_S , H_C , M_R ") are summarized in Table 3.15

Fig. 3.50 (i) show the M(H) hysteresis loops measured at RT. The saturation magnetization (M_s) of CoFe₂O₄ samples measured at RT (Fig. 3.50(i)) increased with annealing temperature 100, 400, 600 and 1200 °C, while the coercivity (H_c) and the remanence (M_r) first decreased at 400 °C followed by an increase at 600 °C and then decreased at 1200 °C. As the annealing temperature increases from 100, 400, 600 °C and 1200 °C the M_s increases from 39, 43, 58 and 71 emu/g, respectively. The increase in saturation magnetization (M_s) might be due to increase in crystallite size as can be seen from Tables 3.13 and 3.15.

The increase in saturation magnetization also depends on heating rate. We have used heating rate 3 °C/min. Our value of saturation magnetization (M_s) of CoFe₂O₄ pellet heated at 600 °C is 58 emu·g⁻¹, which is very slightly greater than M_s (56.72 emu/g) reported by Fonseca et al. [34]. Highest M_s of 71 emu/g sample annealed at 1200 °C, which is slightly smaller than that of bulk cobalt ferrite (74.08 emu/g) [94].

Coercive field (H_c) shows a decreasing trend from 3046 G to 118 G with increase of annealing temperature (Table 3.16). When annealing temperature increased from 100 °C to 400 °C, coercivity decreased from 3046 G up to 530 G (Table 3.16) when the crystallite/grain size is same 17.3/40 nm and increased to 951 G at 600 °C since crystallite/grainsize increased to 24/56 nm at 600 °C and finally decreased to 118 G at 1200 °C and crystallite size of 83 nm. The decrease in M_r and H_c is because of decrease in magnetic anisotropy with annealing temperature. The Mössbauer spectroscopy results of [48,49] reported that B site is most populated by Co^{2+} ions resulting in increase of anisotropy. Large anisotropy nanoparticles compared to its bulk counterpart is due to extra contribution from surface anisotropy and certain size-related effects [95]. Therefore, the as-synthesized powder dried at 90 °C and sample heated at 100 °C for 4 h show highest coercivity (H_c) values.

When Co^{2+} shift from octahedral to tetrahedral sites, H_c decreases because of a less anisotropic environment of tetrahedral sites [96]. The decrease in H_C for sample heated at 400 °C for 4 h might be due to migration of Co^{2+} ions from B site to A site resulting in decrease of coercivity (H_C) and increase of M_s . The M_R was also found with a reduction from 20 emu/g to 14 emu/g with increasing annealing temperature from 100 °C to 400 °C and then increased to 27 emu/g at 600 °C followed by a decrease to 6 emu/g at 1200 °C. The change in remanence (M_R) with increasing annealing temperature is because of change of magnetic anisotropy. The decrease in M_r values could also be interparticle interactions which are affected by the grain size distribution [33,75]. Sample heated at 600 °C show a significant increase in M_s , M_R and H_C when compared to that of sample heated at 400 °C (Table 3.16). This is due to combined effect of grain size, porosity and cation distribution of pellet heated at 600 °C. The sample annealed at 1200 °C shows a high M_s , low M_r and H_c , implying multi-domain nature.

If squareness $M_r/M_s \ge 0.5$ the material has single domain structure. If $M_r/M_s < 0.5$ synthesized material contain multi domain structure [97-98]. All samples are multi domain type except assynthesized CoFe₂O₄ powder dried at 90 °C which has $M_r/M_s = 0.513$ and the sample heated at 100 °C ($M_r/M_s = 0.564$). Therefore, as-synthesized CoFe₂O₄ powder heated at 90 °C and pellets heated 100 °C show high coercivity and low M_s .

The magnetization measurements at 100 K for synthesized cobalt ferrite nanoparticles (heated at 90 °C) is presented in Fig. 3.45(ii)(b). Saturation magnetization (M_S) decreased at 100 K. The $M_S = 31$ emu/g is observed at 100 K and 1.5 T for the as-prepared nanopowders composed of shellcore nanograins. The increase in H_c for samples dried at 90 °C and sample heated at 100 °C (Fig. 3.50(ii)(a)) at 100 K can be explained by core-shell model. Because of the exchange coupling between the shell and the core spins, cooling can select a surface spin configuration. Spins (shell spins) freeze in their random/disordered sates with decreasing temperature of the sample up to 100 K, thereby increasing the surface anisotropy that is responsible for the exchange bias effects in the magnetic domains, giving no further response to the applied field so that the core spins need little extra field to align along the applied field direction. Therefore in addition to anisotropy the exchange bias and hence coercivity increased when the sample temperature is decreased to 100 K.

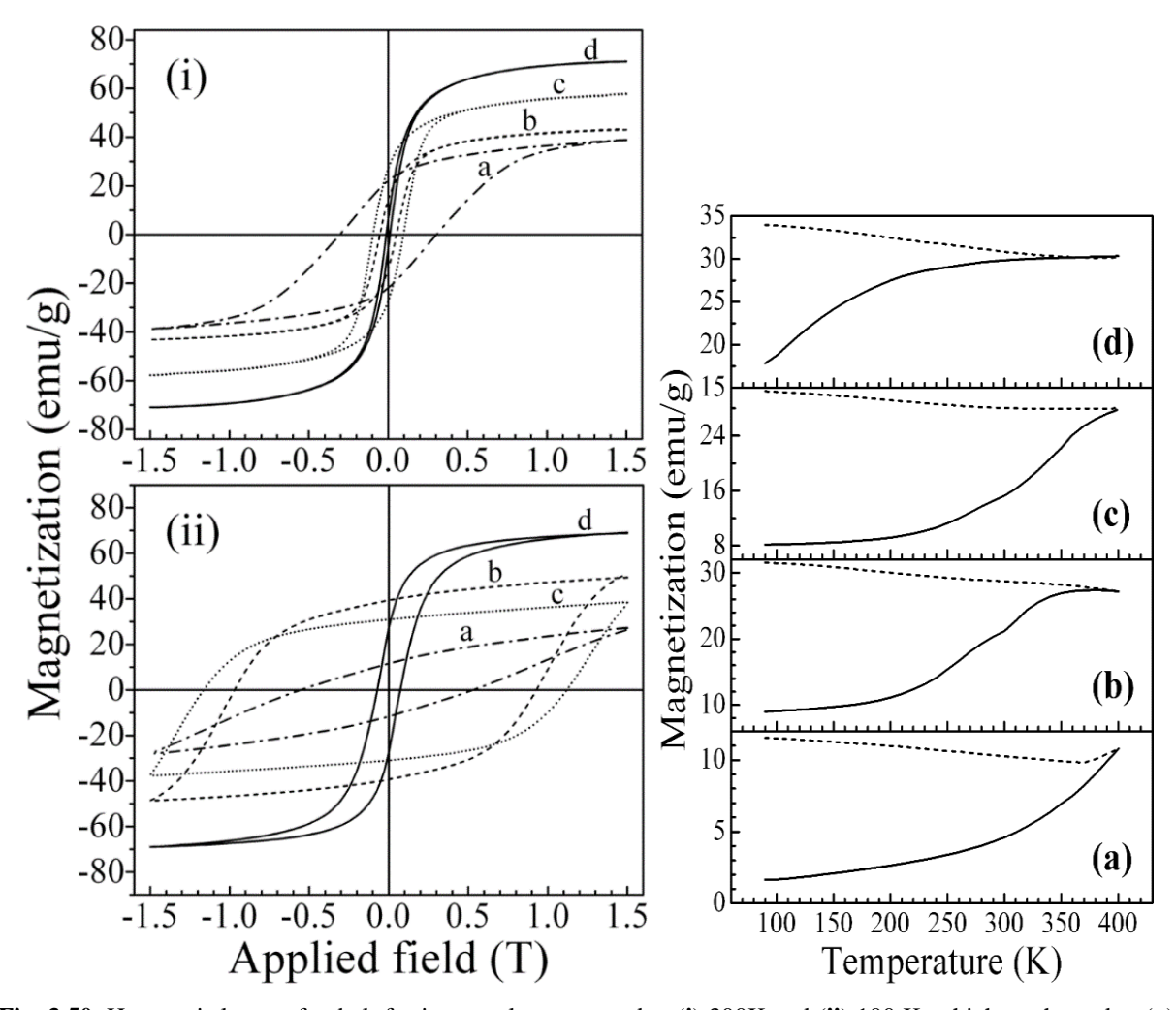


Fig. 3.50. Hysteresis loops of cobalt ferrite samples measured at (i) 300K and (ii) 100 K, which are heated at (a) 100 °C, (b) 400 °C, (c) 600 °C and (d) 1200 °C for 4 h.

Fig. 3.51. (right) ZFC and FC magnetization curves of cobalt ferrite samples, measured at 1 kG applied field

Table 3.15. Magnetic Parameters obtained from the hysteresis loops of CoFe₂O₄ heated at different temperatures: saturation magnetization (M_s), coercive field (H_c), and the remanent magnetization (M_r).

CoFe ₂ O ₄	M_r	M_s	H_c	M_r	M_s	H_c
(Annealing Temp. (°C))	(emu/g)	(emu/g)	(G)	(emu/g)	(emu/g)	(G)
		M(H) at RT		M(H) at 1	00 K	
90 °C	20	39	2875	13	31	4830
100 °C	22	39	3046	11.5	29	5394
400 °C	14	43	530	39	49	9484
600 °C	27	58	951	31	39	11400
1200 °C	6	71	118	27	69	724

Fig. 3.50(ii) show the dependence of the M(H) hysteresis loop measured at 100 K in the range of ± 1.5 T for pellets heated at 100 °C, 400, 600 and 1200 °C, respectively. In Table 3.15 the saturation magnetization (M_s), the coercive field (H_c), and the remanent magnetization (M_r) are

reported. Significant reduction of M_s is observed for samples when compared to that of RT except pellet heated at 400 °C which show an increase in M_s at 100 K. Maaz et al. [67] reported M_s value of 36 emu/g at 77 K for 24-nm CoFe₂O₄ NPs, which is slightly less compared to observed M_s of 39 emu/g at 100 K in the present study (our sample annealed at 600 °C show crystallite size of 24 nm, see Table 3.13). All samples exhibit a large increase of coercivity at 100 K. The coercivity increases tremendously with increase of annealing temperature of the samples up to 600 °C. Similar increase of the coercivity was reported by Maaz et al. [67] and Gopalan et al. [99]. Another effect observed by Maaz et al. [67] and Gopalan et al. [99] which is also observed in the present study is the increase remanence ratio (M_r/M_S) . The M_S and M_r obtained at at room temperature are 39, 43, 58 and 71 emu/g, and 22, 14, 27 and 6 emu/g, respectively, while at 100 K they are 29, 49, 39, 69 emu/g and 12, 39, 31, 27 emu/g. These values show increase of (M_r/M_s) , from 0.56, 0.32, 0.46 and 0.08, respectively to 0.41, 0.796, 0.795 and 0.39 when temperature decreases from 300 K to 100 K. The M_r/M_s value (at RT) of the sample heated 600 °C (0.46) is close to 0.5, which is the case of non-interacting single domain particles with uniaxial anisotropy [44,100]. Kodama [44] attributed the existence uniaxial anisotropy in magnetic nanoparticles to the surface effect. Golapan et al. [99] suggested that increase of M_r/M_S ratio at lower temperatures is due to enhanced cubic anisotropy.

Fig. 3.45(i) show the magnetization variation with temperature of as-prepared nanoparticles between 90 –400 K. ZFC and FC temperature dependences of magnetizations were measured for an applied field of 1 kG. The origin of the difference between ZFC and FC magnetization curves in as-prepared nanopowder which is dried at 90 °C is domain wall pinning and/or reorientations of weak ferrimagnetic domains in cobalt ferrite phase. The temperature below which an irreversible magnetic behavior (i.e. bifurcation of FC and ZFC) occurs is called the irreversibility temperature ($T_{\rm irr}$). The irreversible temperature of as-synthesized nanoparticles dried at 90 °C is 393 K. There is no maximum in the ZFC curve below 400 K. FC magnetization increases monotonously with temperature (see Fig. 3.45(i)) exhibiting Curie-law behavior of noninteracting particles.

Figure 3.51 show ZFC-FC magnetizations of pellets sintered at 100, 400, 600 and 1200 °C, respectively. The irreversibility temperature ($T_{\rm irr}$) of pellets heated at 100 °C is 400 K. The average grain size of this sample is 67 nm. $T_{\rm irr}$ decreased from 400 K to 390 K when annealing temperature of pellets increased from 100 °C to 400 °C and again increased to 400 K for sample

annealed at 600 °C, finally T_{irr} decreased to 365 K in case of sample annealed at 1200 °C. Actually, the slow variation (increase with decreasing temperature) of the FC magnetization below T_{irr} for the sample heated at 100 °C indicates that the interparticle interactions are high. As the annealing temperature of samples increased to 1200 °C, the FC magnetization increases bit faster due to decrease of interparticle interactions as grain size increased. The increase in FC magnetization with decreasing temperature is due to decrease in A sub-lattice magnetization [101]. Similar behavior is also observed cobalt ferrite prepared by various methods [101-103].

3.4.5 Dielectric properties

Figure 3.52 shows change of dielectric permittivity (ε ') versus log of frequency for CoFe₂O₄ samples heated at different temperatures 100 °C, 400 °C, 600 °C and 1200 °C, measured at room temperature between 100 Hz–40 MHz. The polarization in ferrites is due to electronic exchange (i.e. hoping), Fe²⁺ \leftrightarrow Fe³⁺ as well as space charge polarization on application of an electric field. Ferrite materials contain well-conducting grains separated by non-conducting grain boundaries [104]. Under the influence of an electric field, electrons migrate through the material across the grain boundaries to reach the electrodes of opposite polarity through hopping. The motion of electrons is interrupted at grain boundaries and some electrons get trapped at the grain boundaries. Charges of opposite sign give rise to dipole moment. Even if the charges are predominantly of one type, the electric field due to these trapped charges affect dielectric constant since their presence alters the applied field inside the dielectric.

At low frequencies the polarization is in phase or leads the applied electric field leading to high dielectric constant. As the frequency is raised, all of the electrons cannot move fast enough to stay in step with the driving field. Consequently, the polarization begins to lag behind the driving field and hence dielectric constant decreases. At very high frequencies the fastest moving electrons can no longer respond and at radio frequencies ($\sim 10^6 \, \mathrm{Hz}$) electrons are relaxed there will be no space charge polarization and so the dielectric constant decreases to a small value.

Dielectric constant (ε') of sample heated at 100 °C decreases less rapidly (at 10 kHZ) with frequency when compared to samples heated at high temperatures than 100 °C. This is due lagging of electron hopping behind the driving field with increasing frequency [27,28]. Beyond 10 kHz of driving electric field hopping electrons cannot follow the alternation of the field which results into such type of behaviour. The dielectric constant in the present study is almost

ten times higher than that reported by Balavijayalakshmiet al. [33] and of the same order to that reported by Sivakumar et al. [28].

Table 3.16: Dielectric Constant ϵ' at Different Frequencies

CoFe ₂ O ₄	ε΄					
(annealing temp. (°C))	100Hz	1kHz	1MHz	5MHz	40MHz	
100 °C	40031	11737	35.5	23	16	
400 °C	1155	169	13	11	9	
600 °C	3800	571	18	14	11	
1200 °C	62.89	30.5	19	19	19	

Table 3.18: Dielectric Loss Tangent (tan δ) at Different Frequencies of the Samples

CoFe ₂ O ₄	tan δ					
(annealing temp. (°C))	100Hz	1kHz	1MHz	5MHz	40MHz	
100 °C	1.491	1.529	1.58	0.731	0.309	
400 °C	3.78	3.625	0.314	0.179	0.111	
600 °C	5.904	5.332	0.799	0.38	0.167	
1200 °C	6.09	1.609	0.021	0.016	0.028	

In case of samples heated at 100 °C, CoFe₂O₄ shows highest dielectric constant because of smallest grain size of 53 nm and highest porosity (52.71%). Annealing at 400 °C for 4 h results in the decrease in dielectric constant due to small decrease in porosity (49.86%) and grain size (40 nm). A small increase of dielectric constant, ε' of sample heated at 600 °C for 4 h might be due to the further decrease in porosity (48.17%) and increase in grain size (56 nm) of the sample (Table 3.13). As the annealing temperature increases to 1200 °C dielectric constant decreases to lowest value due to lowest porosity (7.79%) and highest grain size. The values of dielectric constant at various frequencies are enlisted in Table 3.16. The value of dielectric constant varies from 4 x 10³ to 16, 1155 to 9, 3800 to 11 and 63 to 19, respectively, for samples heated at 100 °C, 400 °C, 600 °C and 1200 °C. The dielectric constant of the sample annealed at 1200 °C is 19 at 1 MHz and remains constant till 40 MHz.

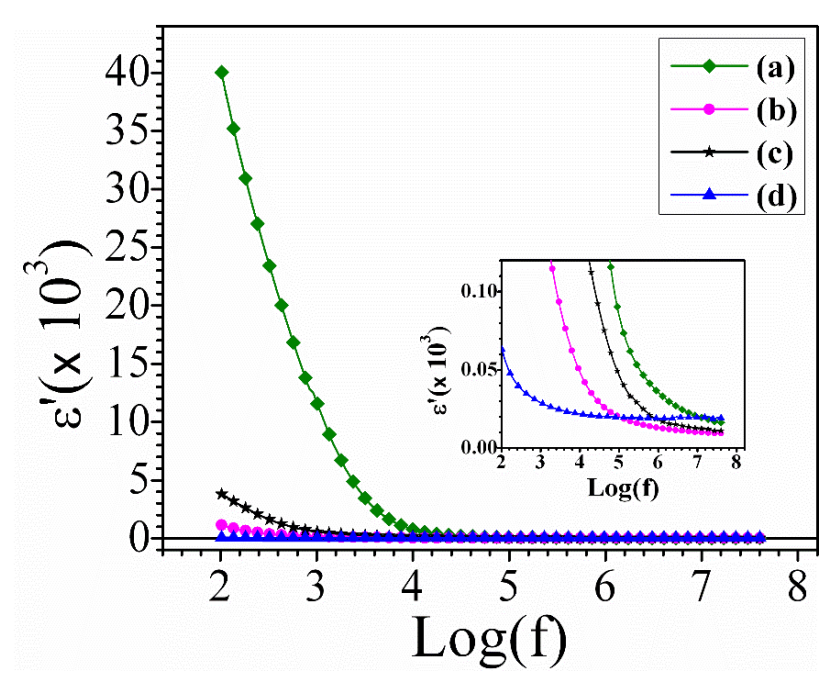


Figure 3.52. Change in dielectric permittivity, (ϵ') with logarithmic frequency. For CoFe₂O₄ samples heated at (a) 100 °C, (c) 600 °C, and (d) 1200 °C for 4 h.

Dielectric loss behaviour

The change of dielectric loss ($\tan \delta$) versus frequency at RT is illustrated in Fig. 3.53. Dielectric loss tangent ($\tan \delta$) was calculated using the relation given by Eq. (3.6). The ($\tan \delta$) values at different frequencies are tabulated in Table 3.17. Similar to the dielectric constant, the dielectric loss ($\tan \delta$) also exhibit decreasing trend with increase of frequency for all samples except the sample heated at 100 °C. As the frequency increases loss tangent decreases very rapidly at low frequencies and becomes small in high frequency region. The decrease in ($\tan \delta$) with frequency is because hopping rate of electrons lag behind driving electric field. Space charge polarization gives rise to dielectric absorption usually at low frequencies. Dielectric loss occurs because polarization lags behind the driving field. This time varying polarization gives rise to current. The current has a component $\omega \chi'' E(r) \cos(\omega t)$ that is in phase with electric field E. The in phase component of current E gives rise to power loss as heat.

For sample heated at 100 °C for 4 h, dielectric loss ($\tan \delta$) decreases with increase of frequency from 100 Hz and reaches minimum at 324 Hz exhibiting the relaxation peak (at 3406 kHz) between the frequency 630 Hz to 4.91 MHz. Absorption peak is shifted to lower frequency to 324 Hz with a decrease in peak height after heating the sample at 400 °C. Another feeble peak

appears at high frequency side around 13.33 kHz. The sample heated at 600 °C shows a relaxation peak at 840 Hz at low frequency side and a broad peak around 144.5 kHz.

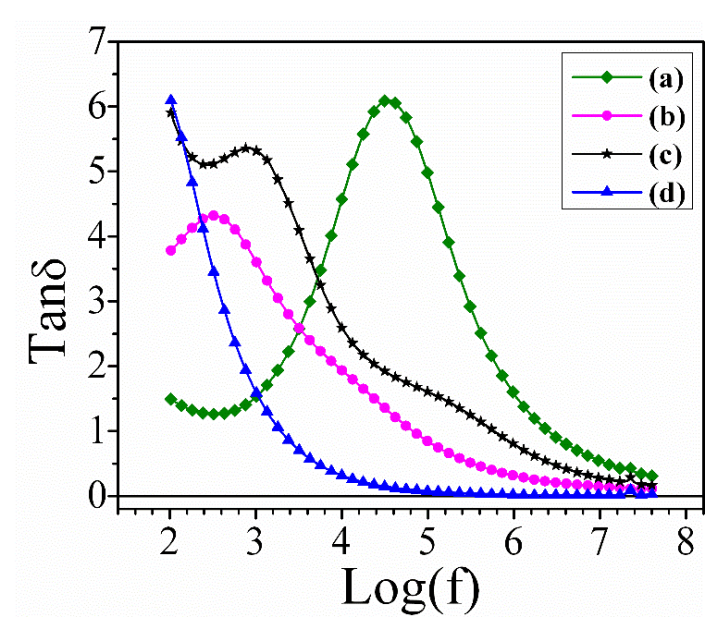


Fig. 3.53. The variation of dielectric loss tangent with logarithmic frequency of $CoFe_2O_4$ samples heated at (*a*) 100 °C, (*b*) 400 °C, (*c*) 600 °C, and (d) 1200 °C for 4 h.

For sample heated at 1200 °C the loss tangent decreases rapidly up to 5.14 kHz beyond that it decreases slowly up to 1.7 MHz and remains almost constant thereafter. For sample sintered at 1200 °C no relaxation peak appears because of its very high resistance. Low density results in low dielectric constant and higher dielectric loss [105]. The samples annealed at 1200 °C exhibit very low loss tangent values between 1 MHz-40 MHz due to high density of the material (porosity is 7.798%).

The appearance of relaxation peak can be explained according to the Debye relaxation theory (Tridevi et al 2005) [51]. Hoping of electrons between Fe²⁺⇔Fe³⁺ and holes between Co²⁺⇔Co³⁺ is responsible for relaxation behaviour. The peak in the loss spectrum appears if jumping frequency of electrons is equal to that of driving electric field, resonance occurs maximum power is absorbed [106]. The low loss tangent at high frequencies of sample heated at 1200 °C suggests that it can be used in high frequency applications. The very low values of dielectric loss show that the sample is structurally prefect.

3.4.6 Conclusions

Cobalt ferrite nanoparticles of 17 nm size prepared by co-precipitation were pressed into pellets and annealed at 100, 400, 600 and 1200 °C for 4 h. Rietveld refined XRD patterns show single phased spinel structure with Fd-3m space group. Grain size increases with increase of annealing temperature. As-prepared CoFe₂O₄ NPs show a high coercivity of 2875 G at RT and M_s of 39 emu/g. The RT saturation magnetization (M_s) increases with increasing temperature due to the increase of grain size. Cobalt ferrite heated at 100 °C and 1200 °C show coercivity, 3046 G and 118 G and saturation magnetization (M_s) of 39 emu/g and 71 emu/g, respectively, at RT. All the samples show a large increase in coercivity and a slight decrease in M_s at 100 K. The CoFe₂O₄ sample heated at 600 °C exhibit high coercivity of 11.4 kG at 100 K. Dielectric constant of CoFe₂O₄ annealed at 1200 °C is 19 between 1 MHz to 40 MHz showing low loss tangent values (0.021-0.028). This sample can be used as an insulating material in high–frequency electrical circuits to reduce power losses and skin effect.

References

- [1] C. R. Stein, M. T. S. Bezerra, G. H. A. Holanda, J. André-Filho, and P. C. Morais, *AIP Advances8*, 056303 (2018).
- [2] Patterson, A.L.: The Scherrer formula for X-ray particle size determination. Phys. Rev. **56**, 978 (1939).
- [3] P. Jeppson, R. Sailer, E. Jarabek, J. Sandstrom, B. Anderson, M. Bremer, D. G. Grier, D. L. Schulz, A. N. Caruso, S. A. Payne, P. Eames and Mark Tondra, Hongshan He, and D. B. Chrisey, J. Appl. Phys. 100, 114324 (2006).
- [4] M. Sultan and R. Singh, J. Appl. Phys. 107, 09A510 (2010).
- [5] E. Tirosh, G. Shemer, and G. Markovich, Chemistry of Materials 18, 465 (2006).
- [6] Samavati, A., Mustafa, M. K., Ismail, A. F., Othman, M. H. D., Rahman, M. A., Mater. Express.6, 473 (2016).
- [7] Ponce A.S., Chagas E.F., Prado R.J., Fernandes C.H.M., Terezo A.J., Baggio-Saitovitch E., *J. Magn. Magn. Mater.* **344**, 182–187 (2013).
- [8] V. Masheva, M. Grigorova, N. Valkov, H. J. Blythe, T. Midlarz, V. Blaskov, J. Geshev, and M. Mikhov, J. Magn. Magn. Mater. 196–197, 128 (1999).
- [9] G. C. Papaefthymiou, S. R. Ahmed, and P. Kofinas, Rev. Adv. Mater. Sci. 10, 306 (2005).
- [10] M. Grigorova et al., J. Magn. Magn. Mater. 183, 163 (1998).
- [11] S. Chakrabarti, S. K. Mandal, and S. Chaudhuri, Nanotechnology 16, 506 (2005).
- [12] R. Betancourt-Galindo, O. Ayala-Valenzuela, L. A. Garcia-Cerda, O. Rodriguez Fernandez, J. Matutes-Aquino, G. Ramos, and H. Yee-Madeira, *J. Magn. Magn. Mater.* **294**, e33 (2005).
- [13] B. D. Cullity, Introduction to magnetic materials (Addison Wesley Publishing Company, 1972).
- [14] S. Ammar, A. Helfen, N. Jouini, F. Fiévet, I. Rosenman, F. Villain, P. Molinie and M. Danot, J. Mater. Chem. 111, 86–192 (2001).
- [15] S. Ayyappan, S. Mahadevan, P. Chandramohan, M. P. Srinivasan, J. Philip and B. Raj, *J. Phys. Chem.* C, 114, 6334–6341 (2010).
- [16] S. Chikazumi, Physics of Ferromagnetism (Wiley, New York, 1964).
- [17] A.S. Group. *Database of Ionic Radii*; 1976. Available from: http://abulafia.mt.ic.ac.uk/shannon/ptable.php>. Access in: 17/11/2017.
- [18] Attaur Rahman, M. A. Rafiq, K. Maaz, S. Karim, Sung Oh Cho and M. M. Hasan, *Journal of applied physics* 112, 063718 (2012).
- [19] A. Franco, Jr. and F. C. e Silva, Journal of applied physics 113, 17b513 (2013).
- [20] I. C. Nlebedim, R. L. Hadimani, R. Prozorov, and D. C. Jiles, *Journal of applied physics* 113, 17A928 (2013).
- [21] S. Morup and E. Tronc, *Phys. Rev. Lett.* **72**, 3278–3281 (1994).
- [22] D. Fiorani, J. L. Dormann, R. Cherkaoui, E. Tronc, F. Lucari, F. D'Orazio, L. Spinu, M. Nogues, A. Garcia and A. M. Test, *J. Magn. Magn. Mater.* **196**, 143–147 (1999).

- [23] W. Shi, J. Zhu, D. H. Sim, Y. Y. Tay, Z. Lu, X. Zhang, Y. Sharma, M. Srinivasan, H. Zhang, H. H. Hng and Q. Yan, *J. Mater. Chem.* **21**, 3422–3427 (2011).
- [24] A. Caprile, M. Coi"sson, F. Fiorillo, P. Kabos, O. M. Manu, E. S. Olivetti, M. A. Olariu, M. Pasquale and V. A. Scarlatache, *IEEE Trans. Magn.* **48**, 3394–3397 (2012).
- [25] A. M. Yashchenok, D. A. Gorin, M. Badylevich, A. A. Serdobintsev, M. Bedard, Y. G. Fedorenko, G. B. Khomutov, D. O. Grigoriev and H. Mohwald, *Phys. Chem. Chem. Phys.* 12, 10469–10475 (2010).
- [26] C. J. Belle, A. Bonamin, U. Simon, J. Santoyo-Salazar, M. Pauly, S. Begin-Colin and G. Pourroy, *Sens. Actuators* B **160**, 942–950 (2011).
- [27] G. H. Jonker, J. Phys. Chem. Solids 9, 165-175 (1959).
- [28] N. Sivakumar, A. Narayanasamy, C. N. Chinnasamy and B. Jeyadevan, *J. Phys.: Condens. Matter* 19, 386201 (2007).
- [29] X. H. Guo, Y. H. Deng, D. Gu, R. C. Che and D. Y. Zhao, J. Mater. Chem. 19, 6706–6712 (2009).
- [30] G. B. Sun, B. X. Dong, M. H. Cao, B. Q. Wei and C. W. Hu, Chem. Mater. 23, 1587–1593 (2011).
- [31] Na J G, Lee T D and Park S J., IEEE Trans. Magn. 28 2433 (1992).
- [32] Na J G, Kim M C, Lee T D and Park S J 1993 IEEE Trans. Magn. 29 3520.
- [33] J. Balavijayalakshmi, N. Suriyanarayanan, R. Jayaprakash, V. Gopalakrishnan, *Physics Procedia* 49, 49–57 (2013).
- [34] Saulo Gregory Carneiro Fonseca, LaédnaSouto Neiva, Maria Aparecida Ribeiro Bonifácioc, Paulo Roberto Cunha dos Santos, Ubiratan Correia Silva, João Bosco Lucena de Oliveira, *Mat. Res.* 21 (3)e20170861 (2018).
- [35] Vaidyanathan G, Sendhilnathan S, Arulmurugan R., J MagnMagn Mater 313, 293-299 (2007).
- [36] Yogendra Kumar and Parasharam M. Shirage, J Mater Sci52, 4840-4851 (2017).
- [37] Gul, I.H., Amin, F., Abbasi, A.Z., Anis-ur-Rehman, M., Maqsood, A. Scr. Mater. 56, 497-500 (2007).
- [38] Bao, N., Shen, L., Wang, Y., Padhan, P. & Gupta, A., J. Am. Chem. Soc. 129, 12374–12375 (2007).
- [39] J. I. Mrtin, J. Nogues, K. Liu, J. L. Vicent, and I. K. Schiller, J. Magn. Magn. Mater. 256, 449 (2003).
- [40] T.A. Anhøj, B. Bilenberg, B. Thomsen, C.D. Damsgaard, H.K. Rasmussen, C.S. Jacobsen, J. Mygind and S. Mørup, *J. Magn. Magn. Mater.* **260**, 115 ((2003).
- [41] S. Mørup, J. Magn. Magn. Mater. 266, 110 (2003).
- [42] G. Concas, G. Spano, C. Cannas, A. Musinu, D. Peddis and G. Piccaluga, J. Magn. Magn. Mater.321, 1893 (2009).
- [43] B.G. Toksha, S.E. Shirsath, S.M. Patange and K.M. Jadhav, Solid State Comm. 147 (2008) p.479.
- [44] R.H. Kodama, J. Magn. Magn. Mater. 200 (1999) p.359.
- [45] Koseoglu, Y.; Baykal, A.; Gozuak, F.; Kavas, H., Polyhedron28, 2887–2892 (2009).
- [46] S. Chikazumi, Physics of Magnetism, Chapter 11, Wiley, New York, 1959, p.224.
- [47] A. Franco Júnior, V. Zapf, and P. Egan, J. Appl. Phys. 101, 09M506 (2007).
- [48] F. Nakagomi, S. W. da Silva, V. K. Garg, A. C. Oliveira, P. C. Morais, A. Franco, Jr., and E. C. D. Lima, J. Appl. Phys. 101, 09M514 (2007).

- [49] J. Park, K. Na, Y. Hwang, J.-G. Park, H.-J. Noh, J.-Y. Kim, J.-H. Park, N.-M. Hwang, and T. Hyeon, *Nature (London)*3, 891 (2004).
- [50] Magsood, A., Khan, K.: J. Alloys Compd. 509, 3393-3397 (2011).
- [51] U. N. Trivedi, M. C. Chhantbar, K. B. Modi and H. H. Johi, *Indian Journal of Pure and Applied Physics*, 43, 688-690 (2005).
- [52] A.T. Raghavender and K.M. Jadhav, Bull. Mater. Sci., 32, 575 (2009).
- [53] G. Ranga Mohan, D. Ravinder, A.V. Ramana Reddy, and B.S. Boyanov, Mater. Let., 40, 39 (1999).
- [54] E. Schlömann, J. Phys. Collog., 32, C1-443 (1971).
- [55] Naik SR, SalKer AV., J Mater Chem22, 2740–2750 (2012).
- [56] Zan F, Ma Y, Ma Q, Xu Y, Dai Z, Zheng G, Wu M, Li G, J Am Ceram Soc 96, 3100-3107 ((2013)).
- [57] S.C. Watawe, B.D. Sarwade, S.S. Bellad, B.D. Sutar, and B.K. Chougule, *J. Magn. Magn. Mater.*, 214, 55 (2000).
- [58] A.M. Bhavikatti, S. Kuikarni, and A. Lagashetty, Int. J. Eng. Sci. Technol., 3, 5985 (2011).
- [59] S.F. Mansour, Egypt. J. Solids, 28, 263 (2005).
- [60] Dos, J.G., Duque, S., Macedo, M.A., Moreno, N.O., Lopez, J.L., Pfanes, H.D., J. Magn. Magn. Mater. 1424, 226–230 (2001)
- [61] Panda, R.N., Shih, J.C., Chin, T.S., J. Magn. Magn. Mater. 257, 79 (2003)
- [62] Sartale, S.D., Lokhande, C.D., Ceram. Int.28, 467 (2002)
- [63] Yan, C.H., Xu, Z.G., Cheng, F.X., Wang, Z.M., Sun, L.D., Liao, C.S., Jia, J.T., Solid State Commun. 111, 287 (1999)
- [64] Godinho, M.I., Catarino, M.A., da Silva Pereira, M.I., Mendonc, M.H., Costa, F.M., *Electrochim. Acta* 47, 4307 (2002)
- [65] Ding, J., Miao, W.M., McCormick, P.G., Street, R., Appl. Phys. Lett. 65, 3135 (1994)
- [66] Blaskov, V., Petkov, V., J. Magn. Magn. Mater. 162, 331 (1996).
- [67] K. Maaz, A. Mumtaz, S.K. Hasanain, and A. Ceylan, J. Magn. Magn. Mater., 308, 289 (2007).
- [68] T.M. Meaz, M.A. Amer, and M.K. El-Nimr, Egypt. J. Solids, 31(2008), No. 1, p. 147.
- [69] Ishii, Y.; Hoshikawa, A.; Igawa, N.; Zakaria, A.K.M.; Yamauchi, H.; Yunus, S.M., *Journal of Alloys and Compounds*, **454**, 10-15, (2008).
- [70] V.G. Simkin; D.Sangaa; M.S. Maschenko; I.A. Bobrikov; A.M. Balagurov, *Crystallography Reports*, **58**, 710 717, (2013).
- [71] Kawaminami, M.; Zheng, X.G.; Soejima, Y.; Yamada, H., Transaction of the Material Research Society of Japan 25, 1199-1202 (2000).
- [72] Kageyama, H.; Tabuchi, M.; Kobayashi, H.; Sukeshini, A.M., Materials Research Bulletin 32, 151-157 (1997).
- [73] A. S. Albuquerque, J. D. Ardisson, W. A. A. Macedo, J. L. L'opez, R. Paniago and A. I. C. Persiano, J. Magn. Magn. Mater. 226, 1379–1381 (2001).
- [74] S. T. Okuno, S. Hashimoto and K. Inomata, J. Appl. Phys. 71, 5926–5929 (1992).

- [75] E. V. Gopalan, P. A. Joy, I. A. Al-omari, D. S. Kumar, Y. Yoshida and M. R. Anantharaman, J. Alloys Compd. 485, 711–717 (2009).
- [76] N. Ponpandian, A. Narayanasamy, J. Appl. Phys. 92, 2770–2778 (2002).
- [77] R. P. Mahajan, K. K. Patankar, M. B. Kothale, S. A. Patil, Bull. Mater. Sci. 23, 273 (2000).
- [78] X. Meng, H. Li, J. Chen, L. Mei, K. Wang, and X. Li, J. Magn. Magn. Mater. 321, 1155-1158 (2009).
- [79] E. Tirosh, G. Shemer, and G. Markovich, Chemistry of Materials 18, 465 (2006).
- [80] Z. Iatridi, K. Vamvakidis, I. Tsougos, K. Vassiou, C. Dendrinou-Samara, and G. Bokias, ACS Applied Materials and Interfaces 8, 35059 (2016).
- [81] H. Gu, K. Xu, Z. Yang, C. K. Chang, and B. Xu, Chemical Communications 34, 4270 (2005).
- [82] U. Luders, A. Barthelemy, M. Bibes, K. Bouzehouane, S. Fusil, E. Jacquet, J. P. Contour, J. F. Bobo, J. Fontcuberta, and A. Fert, *Advanced Materials* 18, 1733 (2006).
- [83] G. Baldi, D. Bonacchi, C. Innocenti, G. Lorenzi, and C. Sangregorio, *J. Magn. Magn. Mater.***311**, 10 (2007).
- [84] Rajath, P.C., Manna, R.S., Banerjee, D., Varma, M.R., Suresh, K.G., Nigam, A.K.: J. Alloy. Compd. **453**, 155 (2006).
- [85] Tanaka, T., Shimazu, R., Nagai, H., Tada, M., Nakagawa, T., Shandhu, A., Handa, H., Abe, M.: J. Magn. Magn. Mater. **321**, 1417 (2009)
- [86] Lee, S.W., Bae, S., Takemura, Y., Shim, I.B., Kim, T.M., Kim, J., et al.: J. Magn. Magn. Mater. **310**, 2868 (2007)
- [87] Pita, M., Abad, J.M., Dominguez, C.V., Briones, C., Martí, E.M., Gago, J.A.M., Morales, M.P., Fernández, V.M.: J. Colloid Interface Sci. **321**, 484 (2008).
- [88] Huixia, F., Baiyi, C., Deyi, Z., Jianqiang, Z., Lin, T., J. Magn. Magn. Mater. 356, 68–72 (2014). https://doi.org/10.1016/j.jmmm.2013.12.033
- [89] Nlebedim, I.C., Melikhov, Y., Jiles, D.C., J. Appl. Phys. 115, 043903 (2014). https://doi.org/10.1063/1.4862300 043903
- [90] Swatsitang, E., Phokha, S., Hunpratub, S., Usher, B., Bootchanont, A., Maensiri, S., Chindaprasirt, P., *J. Alloys Compd.***664**, 792–797 (2016). https://doi.org/10.1016/j.jallcom.2015.12.230.
- [91] Franco, AJ, Silva, FC, Appl. Phys. Lett. 96, 172505–172508 (2010).
- [92] R. SatoTurtelli, M. Atif, N. Mehmooda, F. Kubel, K. Biernacka, W. Linert, R. Grössingera, Cz. Kapusta, M. Sikora, *Materials Chemistry and Physics* 132, 832–838 (2012).
- [93] W.S. Chiu, S. Radiman, R. Abd-Shukor, M.H. Abdullah and P.S. Khiew, J. Alloys Compd. 459, 291 (2008).
- [94] M. P. Gonzalez-Sandoval, A. M. Beesley, M. Miki-Yoshida, L. Fuentes-Cobas, and J. A. Matutes-Aquino, *Journal of Alloys and Compounds* **369** (1-2), 190–194 (2004).
- [95] T. Bala, C. R. Sankar, M. Baidakova, V. Osipov, T. Enoki, P. A. Joy, B. B. L. V. Prasad, and M. Sastry, *Langmuir* 21, 10638 (2005).
- [96] Fan X, Guan J, Cao X, Wang W, Mou F, Eur J Inorg Chem40, 419–426 (2010).

- [97] Saffari F, Kameli P, Rahimi M, Ahmadvand H, Salamati H., *CeramicsInternational.* **45**(6),7352-7358 (2015).
- [98] Ateia EE, Soliman FS., Applied Physics A: Materials Science and Processing. 123(5), 312 (2017).
- [99] E.V. Gopalan, I.A. Al-Omari, D.S. Kumar, Y. Yoshida, P.A. Joy, M.R. Anantharaman, Inverse magnetocaloric effect in sol–gel derived nanosized cobalt ferrite, Applied Physics A 99 (2010) 497–503.
- [100] T. Ibusuki, S. Kojima, O. Kitakami, Y. Shimada, Magnetic anisotropy and behaviors of Fe nanoparticles, IEEE Transactions on Magnetics 37 (2001) 2223–2225.
- [101] A. Franco, Jr., F. L. A. Machado, V. S. Zapf, and F. Wolff-Fabris, Journal of Applied Physics, 109 (2011) 07A745.
- [102] Y. Melikhov, J. E. Snyder, D. C. Jiles, A. P. Ring, J. A. Paulsen, C. C. H. Lo, and K. W. Dennis, J. Appl. Phys. 99, 08R102 (2006).
- [103] N. Ranvah, I. C. Nlebedim, Y. Melikhov, J. E. Snyder, P. I. Williams, A.J. Moses, and D. C. Jiles, IEEE Trans. Magn. 45 (2009) 2861.
- [104] C.G. Koops, *Phys. Rev.***83**,121–124 (1951).
- [105] Md.T. Rahman, M. Vargas, C.V. Ramana, J. Alloys Compd. 617, 547–562 (2014).
- [106] N. Sivakumar, A. Narayanasamy, and N. Ponpandian, G. Govindaraj J. Appl. Phys. 101 (2007) 084116.

Chapter 4

Structure and properties of cobalt ferrite (CoFe₂O₄) and copper doped cobalt ferrite (Co_{0.75}Cu_{0.25}Fe₂O₄) thin films

This chapter contains the experimental data on CoFe₂O₄ and Co_{0.75}Cu_{0.25}Fe₂O₄ films deposited by RF-magnetron sputtering under different sputtering conditions of RF power, thickness, and argon gas pressure are presented. The influence of annealing on structure, magnetic and optical properties of the deposited films is also presented in this chapter.

4.1 Effect of RF Power on Structural, Magnetic and Optical Properties of CoFe₂O₄ Thin Films

The magnetization and optical data on thin films of Co-ferrite deposited at RF power of 60 -120 W are recorded. Detailed systematic studies were undertaken on the as-deposited and annealed films of Cobalt ferrite. These studies are helpful in tuning the properties of the ferrite films.

Thickness of the as-deposited films is estimated by using profilometer. The thickness of the film increases as the RF power increases. This is due to the increase in deposition rate with the increase in RF power. A slight decrease in thickness of film was observed after annealing. This may be due to increase in packing density of the films on annealing. Film thickness for all films annealed at 500 °C for 3 h are shown in Fig. 4.8 and Table 4.3.

4.1.1 Structural analysis

The XRD patterns of the CoFe₂O₄ target and the grazing incident angle x-ray diffraction patterns measured on the as-sputtered films as well as on the films annealed at 500 °C for 3 h are shown in Fig. 4.1. The X-ray peaks of the target and the films are in accordance with those of a typical crystalline Co-ferrite, with spinel structure without a preferred orientation. The as-deposited films CFF-60 and CFF-80 are amorphous, while those deposited at higher RF-power (100 and 120 W) show a certain degree of crystallinity. After post-annealing at 500°C for 3 h, the major peaks corresponding to cobalt ferrite emerge, indicating the improvement in crystallization. The XRD line width and crystallite size are connected through the Debye-Scherrer equation [1] given b

$$D = \frac{0.9 \,\lambda}{\beta \cos \theta} \tag{4.1}$$

where, D is crystallite size in Å, λ is the wavelength of X-rays, β is the full width of the diffraction line at half the maximum intensity and θ is the diffraction angle.

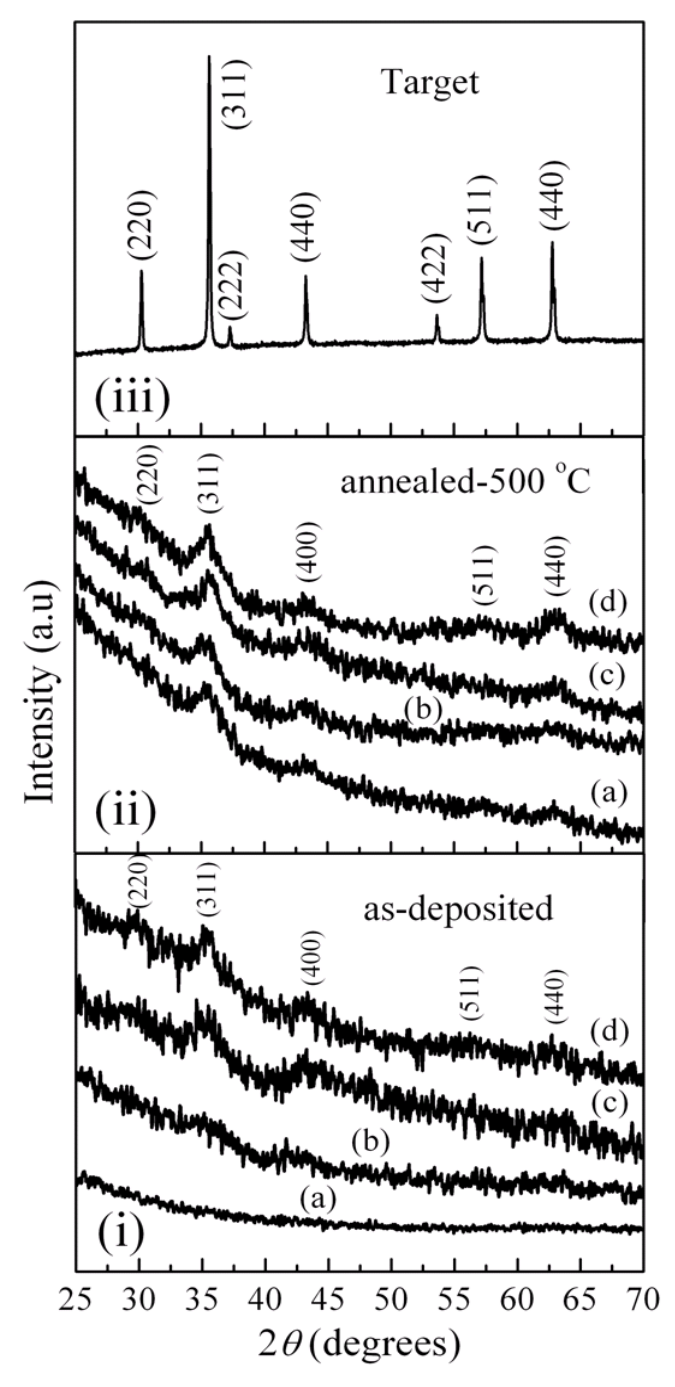


Fig. 4.1 The XRD patterns of the $CoFe_2O_4$ thin films grown at (a) 60 W, (b) 80 W, (c) 100 W and (d) 120 W RF powers, for as-deposited (i), annealed at 500° C (ii) and Target (iii).

The size of crystallites was calculated using the full width at half maximum (FWHM) of the (3 1 1) peak and the values are presented in Table 4.1. Nanocrystalline nature of Co-ferrite thin films is evident from the data. Lattice parameter (a) and X-ray density were evaluated using following formulae [2-4].

$$a = \frac{\lambda}{2\sin\theta} \sqrt{h^2 + k^2 + l^2} \tag{4.2}$$

$$\rho_{\chi} = \frac{zM}{N_A a^3} \tag{4.3}$$

where 'a' is lattice parameter, (hkl) are Miller indices, z represents number of molecules in unit cell (z=8), N_A , Avogadro's number and M is equal to molecular weight of CoFe₂O₄. The calculated lattice parameter of Co-ferrite target is 8.35 Å and that of the films varies between 8.39–8.48 Å.

Table 4.1 FESEM, TEM and structural properties of annealed CoFe₂O₄ thin films

Sample	Lattice constant 'a' (±0.01Å)	Crystallite size (±2 nm) XRD	Grain size (±2 nm) As-grown films FESEM	Grain size (± 2nm) FESEM	Particle size (±2 nm) TEM
CFF-60	8.43	11	44	18	11
CFF-80	8.48	19	38	28	19
CFF-100	8.34	10	47	22	11
CFF-120	8.39	13	42	21	9
Target	8.35	51	-	-	-

4.1.2 Surface morphology

Field emission scanning electron microscopy micrographs of the cobalt-ferrite films are shown in Figs. 4. 2(for as-deposited) and 4.3(annealed). The grain-size distribution was determined from the histogram obtained by measuring the size of around 100–200 individual grains using imageJ software. For the as-deposited films, the average grain size is 44, 38, 47, and 42 nm for CFF-60, CFF-80, CFF-100, and CFF-120, respectively. For the annealed films, the histogram of sample CFF-60 shows that the maximum size distribution is in the range of 15–20 nm, for CFF-80, 15–25 nm, and for CFF-100 and CFF- 120, it is in the range of 20–25 nm. Average grain size estimated by FESEM increases from 16 to 28 nm as RF power increases from 60 to 80 W and then it decreases to 22 and 21 nm with a further increase in RF power of 100 and 120 W, respectively. The average values of grain size are listed in Table 4.1. Both sample CFF-80 (Fig. 4.3b) and sample CFF-120 (Fig. 4.3d) have polycrystalline structure. The largest crystal grain and the best crystallinity were obtained for film deposited at RF power of 80 W. The surface morphology of the present film is very different from that reported by other group [5].

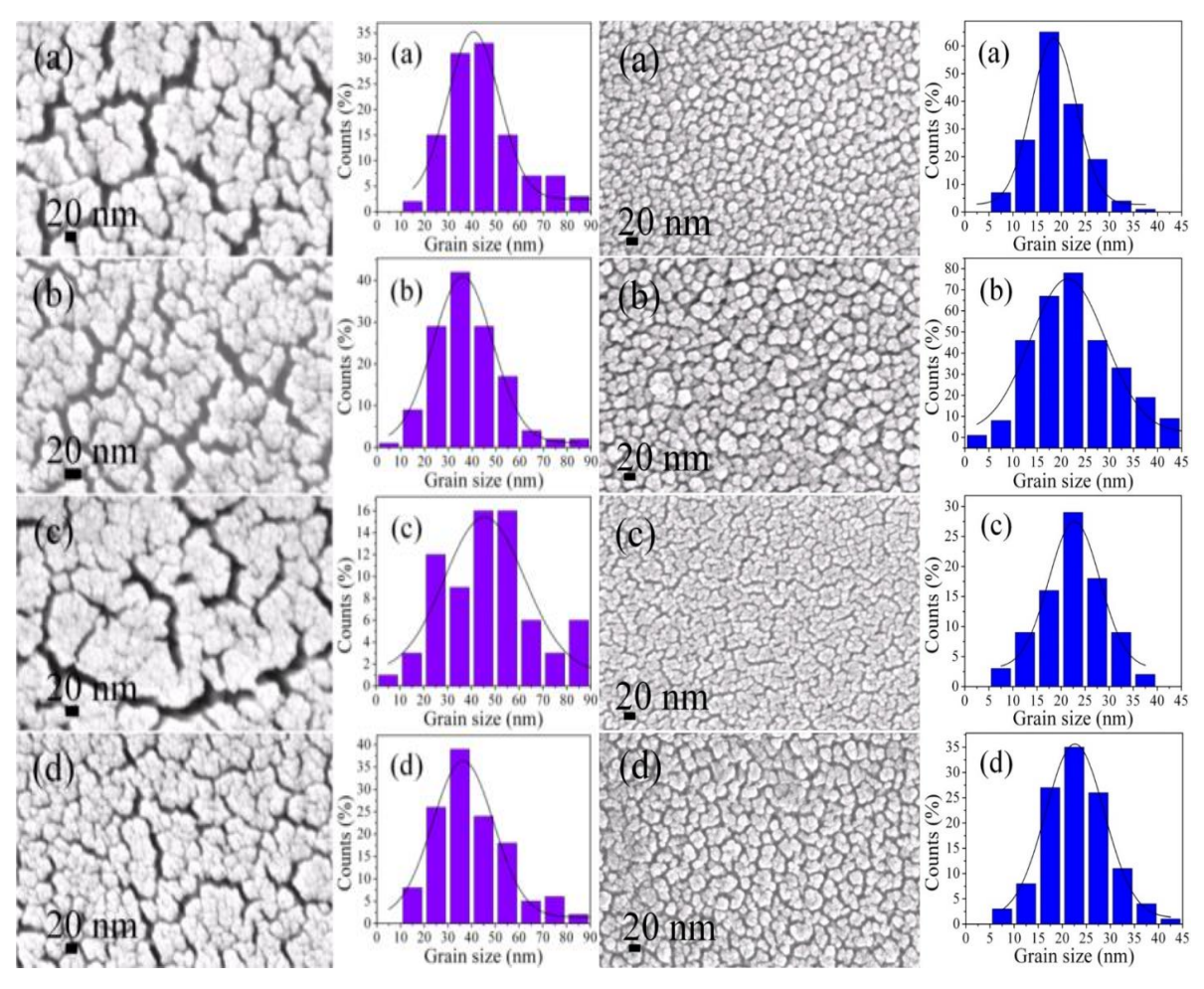


Fig. 4.2 FESEM images of the CoFe₂O₄ thin films grown at (a) 60, (b) 80, (c)100, and (d) 120 W RF powers and cluster-size distribution.

Fig. 4.3 (right) FESEM images of the annealed CoFe₂O₄ thin films and grain-size distribution.

4.1.3 Transmission electron microscopy

Transmission electron microscopy (TEM) and High Resolution microscopy have been used to confirm the nanoparticle size and to determine average particle size. Fig. 4.4 shows the TEM images of the annealed CoFe₂O₄ thin films. It can be seen that the particles are more or less spherical with an average size estimated to be 11, 19, 11 and 9 nm for CFF-60, CFF-80, CFF-100 and CFF-120, respectively (Table 4.1). These particle sizes are in good agreement with the particle size estimated from XRD data using Scherrer formula.

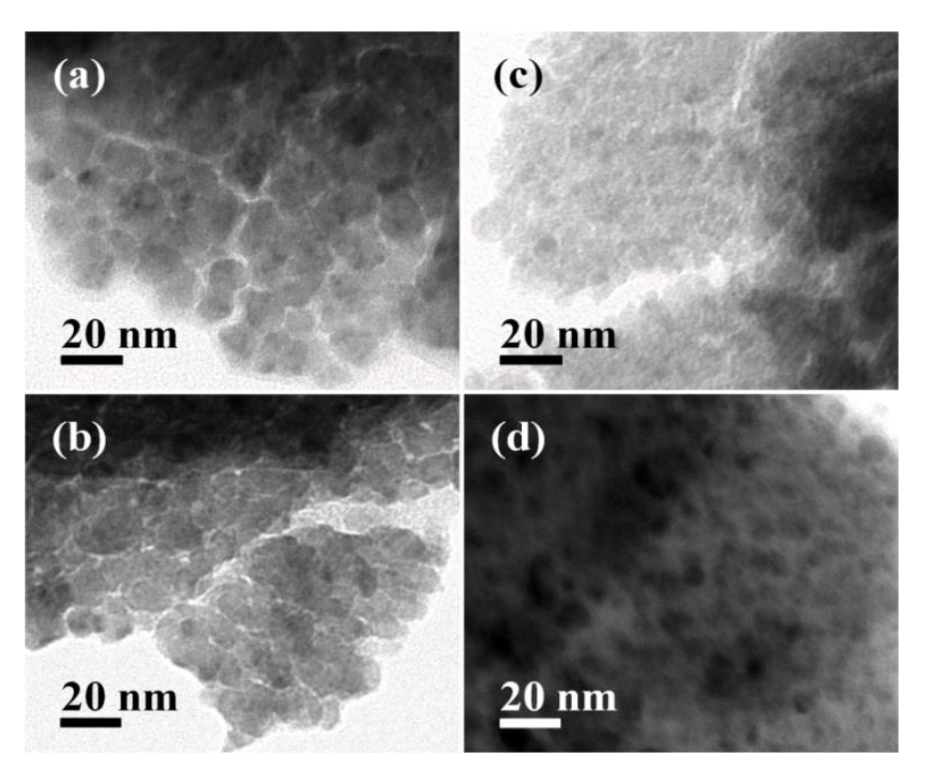


Fig. 4.4 Microstructure of annealed $CoFe_2O_4$ films by TEM, grown at various RF power: (a) 60 W; (b) 80 W; (c) 100 W and (d) 120 W.

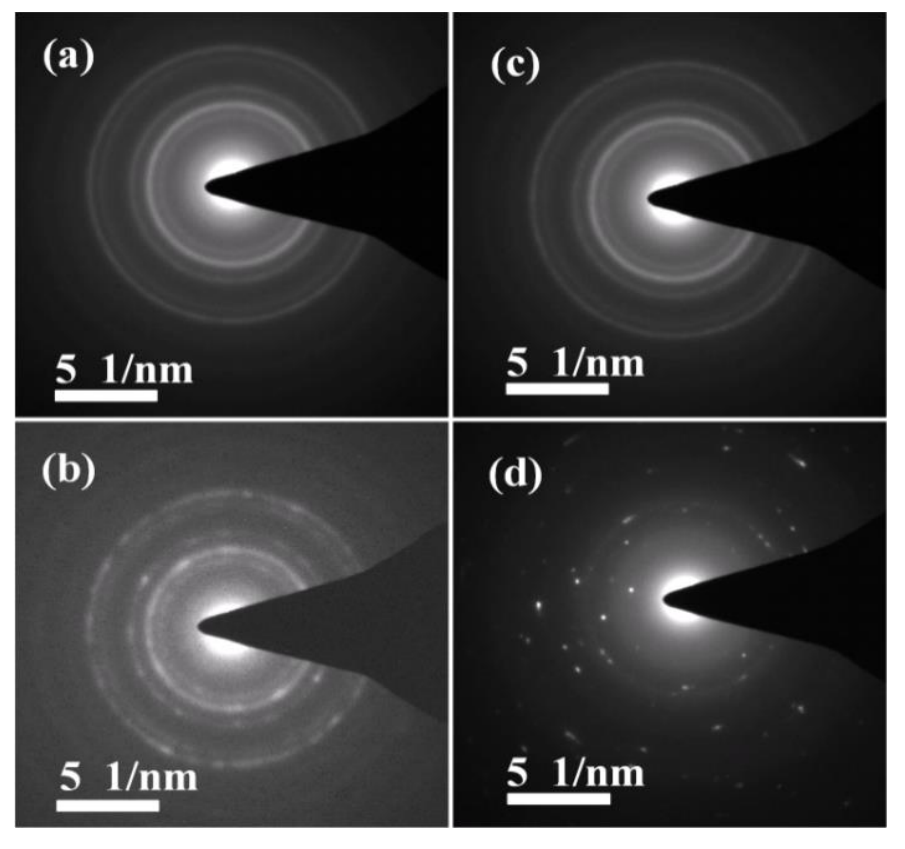


Fig. 4.5 Selected area diffractions of annealed $CoFe_2O_4$ films grown at various RF powers: (a)60, (b) 80, (c) 100, and (d) 120 W.

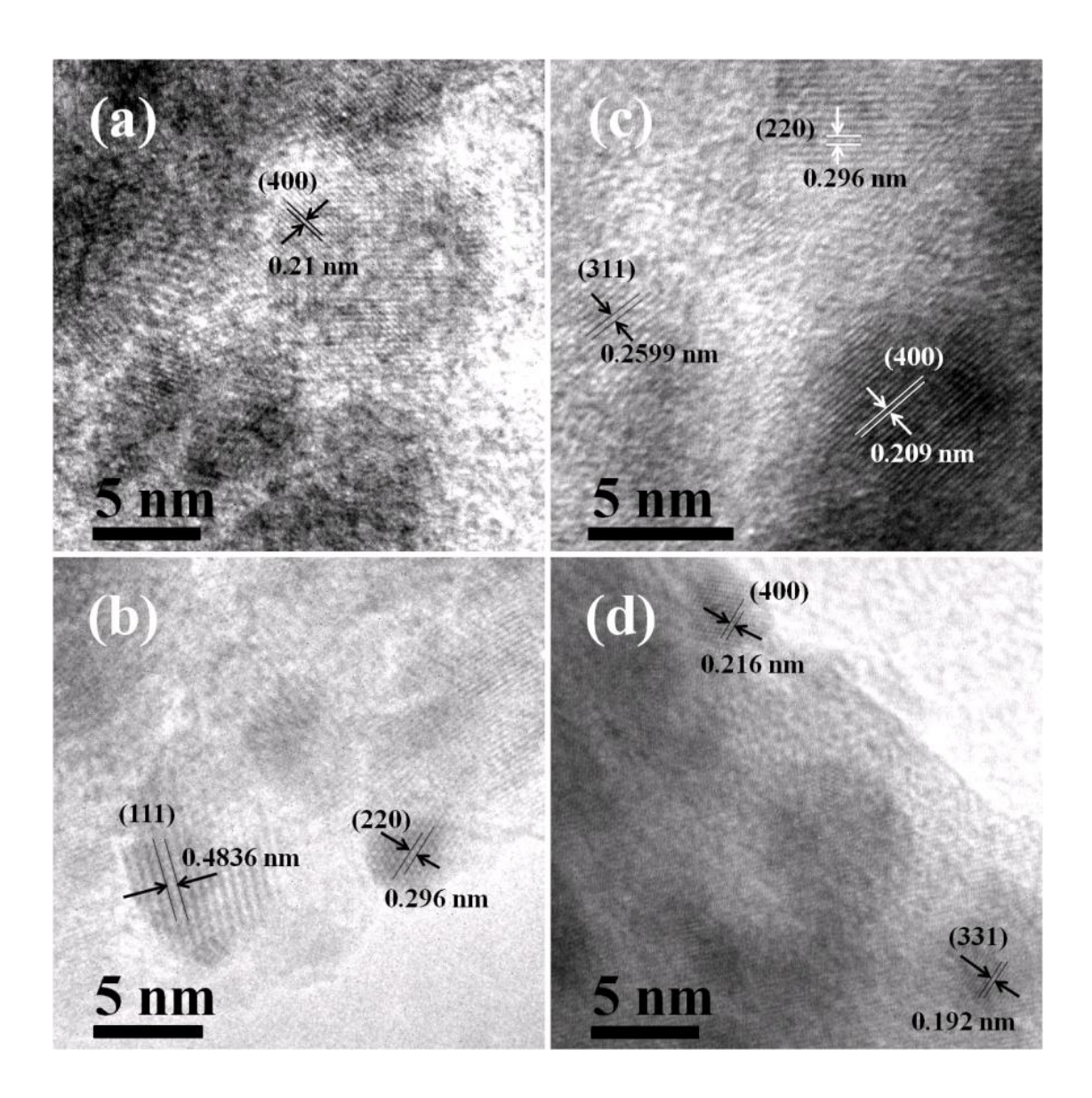


Fig. 4.6 HRTEM micrographs of annealed $CoFe_2O_4$ films grown at various RF power: (a) 60 (b) 80 (c) 100 and (d) 120 W.

The selected area diffraction (SAD) patterns are shown in Fig. 4.5. The diameter of the diffraction ring in SAD pattern is proportional to $\sqrt{h^2 + k^2 + l^2}$ where (hkl) are the Miller indices of the planes corresponding to the ring. Counting the rings from the center 1st, 2nd, 3rd, 4th and 5th rings correspond to (2 2 0), (3 1 1), (4 0 0), (5 1 1) and (4 4 0) planes, respectively. The high-resolution TEM image of the annealed films in Fig. 4.6 show the lattice fringes of the nanocrystallites. The nanocrystal formation on annealing can be seen in Fig. 4.6b for thin film

deposited at 80 W of RF power. These micrographs show details of the interplanar distance corresponding to different planes in spinel structure.

4.1.4 Magnetic and properties

Figure 4.7 show the magnetization hysteresis loops of the CoFe₂O₄ target, as-deposited and annealed thin films measured at room temperature. The loops were obtained with the magnetic field applied parallel to the plane of the films and corrected by subtracting the diamagnetic contribution from the substrate. Since the magnetization does not saturate even at 1.5 T, we have compared magnetization at the highest field value for different films. The magnetization at 1.5 T (M_s), remanent magnetization (M_R), and coercivity (H_c) of the films are tabulated in Table 4.2.

As-deposited films have a small magnetization compared with that of the target. This is probably related to the amorphous nature of the films. After annealing, the H_c and M_s values of the film increase significantly depending on film thickness. The target which has coercivity of 162 G and M_s of 272 emu/cm³. The in-plane coercivities of the annealed films increased as the RF-power increased from 60 W to 80 W and then decreased at 100 W followed by an increase with further increase in RF power up to 120 W. It is related to the increase in grain size up to 80 W followed by a decrease in grain size as RF power is increased to 120 W (Fig. 4.4).

Table 4.2 Magnetic and optical parameters of CoFe₂O₄ thin films deposited at various RF power

Sample	As-deposited			Annealed at 500 °C for 3 h		
	M _r (emu/cc)	M _s (emu/cc)	<i>H_c</i> (G)	M _r (emu/cc)	M _s (emu/cc)	H _c (Oe)
CFF-60	-	-	-	36	246	402
CFF-80	1.5	38	181	50	274	442
CFF-100	0.3	2	75	15	164	154
CFF-120 Target	2.4 18	14 272	313 162	12	136	220

Fig. 4.8 shows the dependence of saturation magnetization (M_s) at 1.5 T on RF power of the annealed films. The decrease in M_s of annealed films can be explained in two ways. It can be due to the change in microstructure of the film as RF power increases. The film deposited at 60 W has porosity, between cobalt ferrite particles (Fig. 4.4) show an M_s value of 246 emu/cm³.

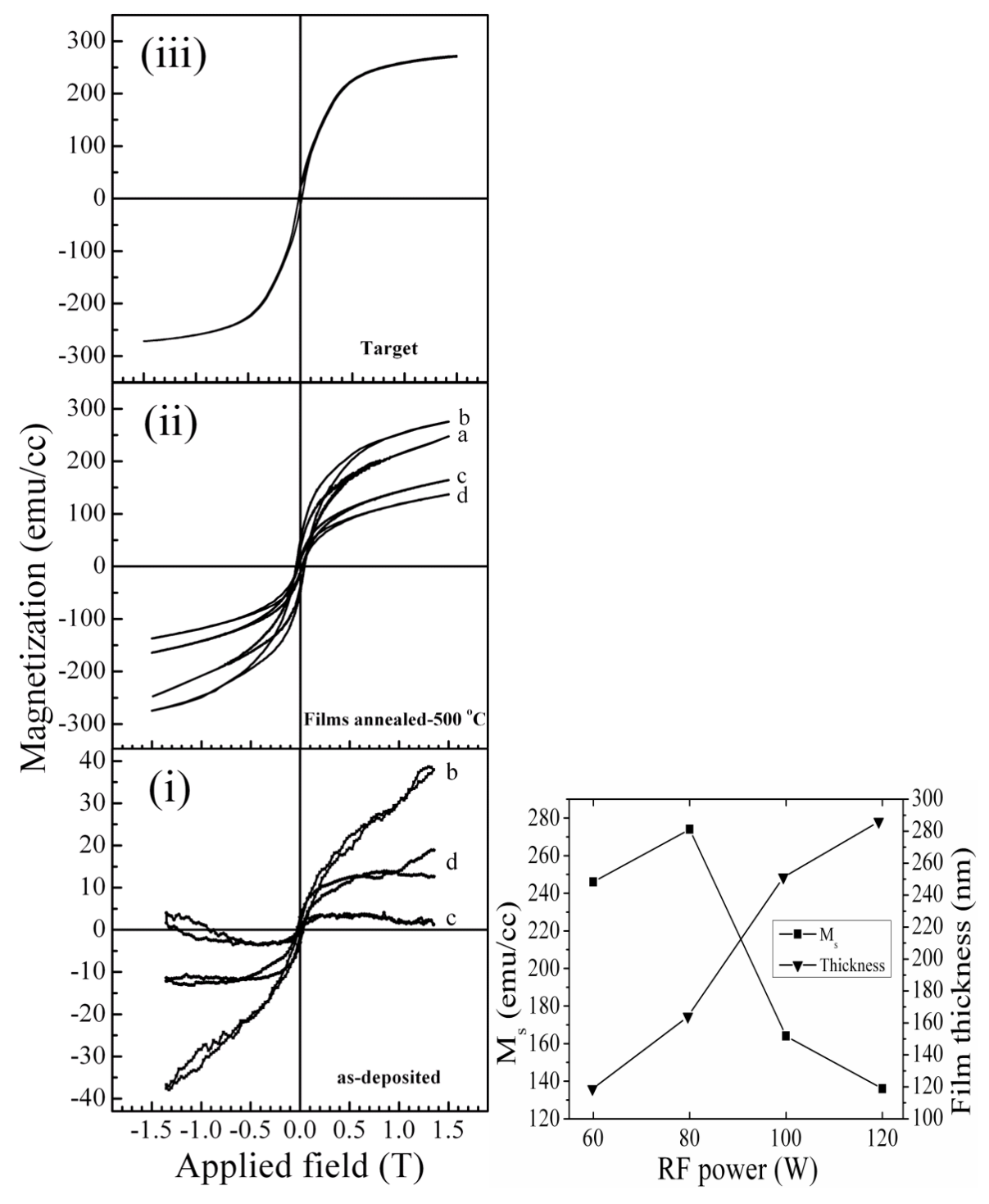


Fig. 4.7 The magnetization hysteresis loops of CoFe₂O₄ thin films grown at (a) 60 W, (b) 80 W, (c) 100 W and (d) 120 W RF power for as-deposited (i), annealed at 500 °C (ii) and CoFe₂O₄ target (iii).

Fig. 4.8 (right) Dependence of saturation magnetization and film thickness of CoFe₂O₄ films annealed at 500 °C deposited at various RF powers 60 W, 80 W, 100 W and 120 W.

For the film grown at 80 W, the porosity decreases due to the fusion of grains forming bigger dense grains which lead to an increase in M_s value to 274 emu/cm³ which is close to the bulk

value. As the RF-power is increased to 100 W, grains are loosely attached leading to a decrease in M_s to 164 emu/cm³. The film deposited at an RF power of 120 W exhibit appearances of very large grain boundaries and hence the M_s value is further decreased to 136 emu/cm³.

The variation in M_s can be due to redistribution of cations among the A and B sites due to heat treatment. The increase in M_s value of the film grown at 80W (CFF-80) could be due to disorder in the distribution of Fe³⁺ and Co²⁺ among A and B sites compared with a perfectly ordered inverse spinel structure. In the fully inverted structure, the Fe³⁺ moments are completely compensated, and the net moment arises only from Co²⁺ ions. The occupation of Co²⁺ ions to octahedral sites might be less than the full. The octahedral holes which are not occupied by the Co²⁺ ions might be filled with Fe³⁺ ions which lead to the increase in M_s of the film CFF-80. The decrease in M_s of CFF-100 and CFF-120 could be related to the increase in cation ordering among A and B sites. The 164 nm (CFF-80) thickness cobalt ferrite film has a coercivity (H_c) of about 442 Oe and saturation magnetization of 274 emu/cc, at room temperature (see Fig. 4.7; Table 4.2). Wang et al. [6] reported coercivity of 3.2 kOe and saturation magnetization of 291 emu/cc, for Co-ferrite films annealed at 900 °C and M_s value of 48 emu/cc and H_c value of 50 Oe for 100 nm-thick Co-ferrite film post-annealed at 500 °C for 2 h. Our studies show that H_c and M_s values strongly depend on film thickness when annealed at 500 °C for 3 h.

4.1.5 Optical properties

The optical transmittance spectra in the wavelength range of 200–2500 nm for CoFe₂O₄ thin films grown at various RF powers for the as-deposited CoFe₂O₄ thin films and annealed films are shown in Fig. 4.9. The fringes in the transmission spectra result from the interference of the incident light at the air-film, film-substrate, and substrate-air interfaces. Each spectrum can be roughly divided into three regions: (i) a zone of strong absorption in the near-UV region from 400 to 300 nm, transmittance decreases abruptly; (ii) a region of moderate absorption in the visible region from 400 to 750 nm, where the transmittance decreases drastically owing to the effect of the absorption coefficient; (iii) a transparent one with the interference pattern in the near-IR region between 760 and 2500 nm. The as-deposited films exhibit over 50% transmittance in the visible region and 84% in NIR region. The absorption edge of the as-deposited films is between 600 and 700 nm. The absorption edge shifts toward lower wavelength for the annealed films without any significant change in transmittance. In the

medium absorption region (λ <700 nm), the transmittance spectra of the annealed films are slightly shifted to shorter-wavelength (blue-shift) as compared with the as-deposited films.

The absorption coefficient α was determined from the optical transmission measurements at various wavelengths using the relationship given by Sunds [7,8].

$$\alpha = -\frac{1}{t}ln(T) \tag{4.4}$$

where *T* is transmittance and *t* is film thickness.

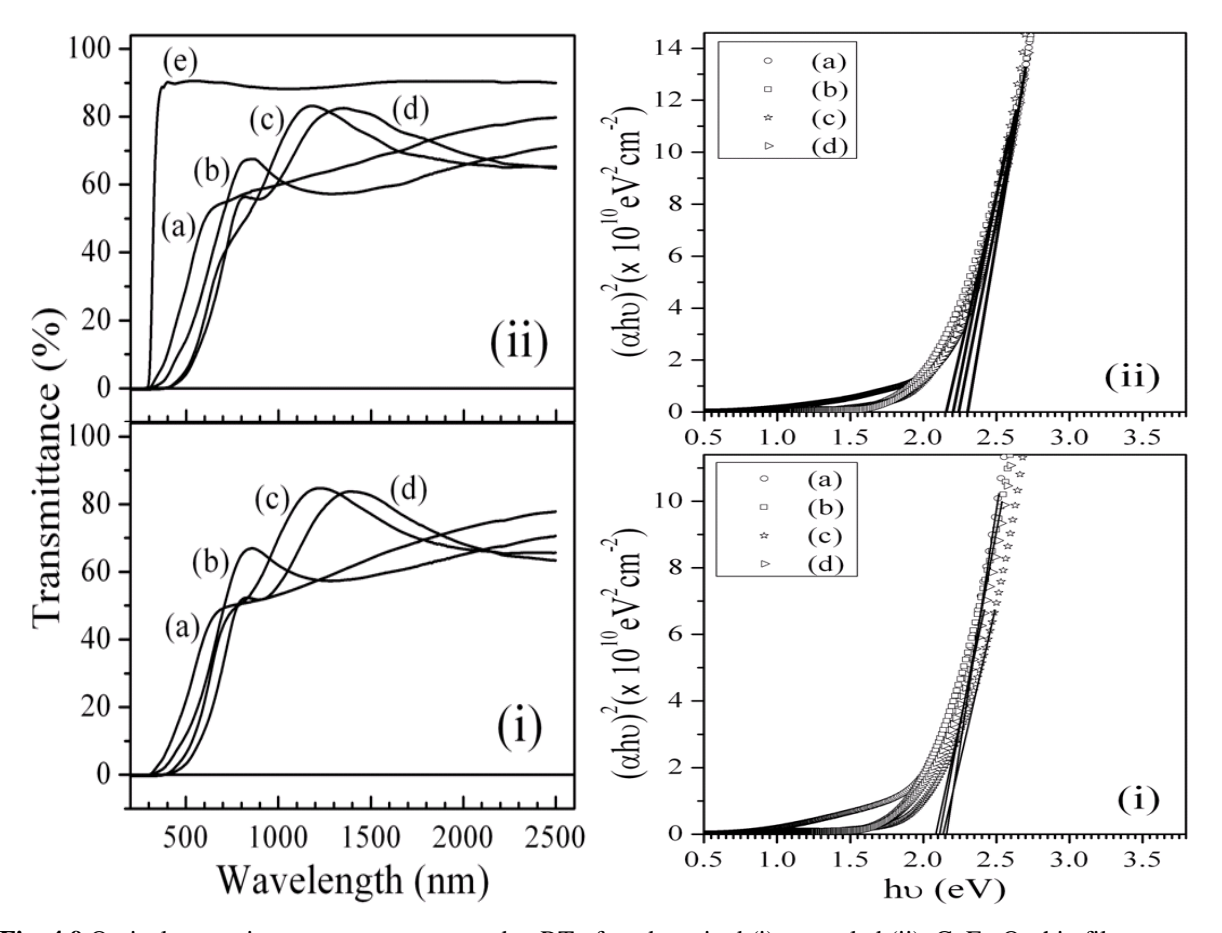


Fig. 4.9 Optical transmittance spectra measured at RT of as-deposited (i), annealed (ii), $CoFe_2O_4$ thin films grown at (a) 60 W, (b) 80 W, (c) 100 W,(d) 120 W RF power and (e) empty glass substrate.

Fig. 4.10 (right) Plots of $(\alpha h \upsilon)^2$ versus $(h \upsilon)$ for annealed CoFe₂O₄ thin films deposited at (a) 60, (b) 80, (c) 100, and (d) 120 W RF powers.

The thickness (t) of the thin film can be determined from the interference fringes of transmission data by calculating the refractive index of the thin film corresponding to two adjacent maxima (or minima) given as $n(\lambda_1)$ at λ_1 and $n(\lambda_2)$ at λ_2 [9],

$$t = \frac{\lambda_1 \lambda_2}{2[n(\lambda_2)\lambda_1 - n(\lambda_1)\lambda_2]} \tag{4.5}$$

where $n(\lambda_1)$ and $n(\lambda_2)$ are the refractive indices in two consecutive maxima (or minima) and λ_1 and λ_2 the corresponding wavelengths. The thickness of annealed films estimated from transmission measurements and surface stylus profilometer are listed in Table 4.3.

The band gap values were estimated considering the CoFe₂O₄ as a direct band gap material, by using the well-known Tauc's formula [9,10],

$$\alpha h \nu = A \left(h \nu - E_g \right)^{1/2} \tag{4.6}$$

where A is constant, α is the optical absorption coefficient, and hv is the energy of the incident photon. Figure 4.10 shows the plots of $(\alpha hv)^2$ versus (hv) for the annealed CoFe₂O₄ thin films. The extrapolation of the straight-line graphs to $(\alpha hv)^2 = 0$ gives the value of the optical gap. It can be seen that the plots of $(\alpha hv)^2$ versus (hv) varies linearly for all the films in the region of strong absorption near the fundamental absorption edge over a wide range of photon energies.

Table 4.3 Optical properties of CoFe₂O₄ thin films deposited at various RF power

Sample	Film thickne	ess (± 5 nm)	Band gap, E (± 0.05eV)	g	
	As-grown	Aı	nnealed	As-grown	Annealed
	Profiler	Profiler Calculated			
CFF-60	124	119	-	2.16	2.3
CFF-80	180	164	147	2.11	2.16
CFF-100	269	237	258	2.14	2.2
CFF-120	300	286	294	2.08	2.25

The linear variation of absorption coefficient at high frequencies indicates that these thin films have direct transitions across the energy band gap. The estimated values of energy band gap for the as-deposited and annealed films are listed in Table 4.3. The error in the optical band gap measurement by linear curve fitting is ± 0.02 eV. The band gap variation for films deposited at 80-120 W of RF power is within this measurement error limits. The increase in the optical band gap of $CoFe_2O_4$ thin films by annealing may be due to the removal of defect levels from the films. The optical band gap for annealed films shows a decrease from 2.3 to 2.16 eV as the RF power increases from 60 to 80 W and shows variations within the experimental error thereafter. This could be attributed to smaller average grain size in the thinner film (119 nm) deposited at 60 W, compared with that in the thicker film (164 nm) deposited at 80 W. The estimated E_g

value for the annealed CoFe₂O₄ thin film deposited at 60 W (120 nm) is 2.3 eV, which is smaller than 2.6 eV reported by Erdem et al. [11] for a 100-nm-thick CoFe₂O₄ thin film deposited by spin coating. The estimated direct band gap values for annealed films are greater than those reported by Rao et al. [12] and smaller than those reported by Ravindra et al. [13] and Holinsworth et al. [14].

4.1.6 Conclusions

Cobalt ferrite thin films were deposited on glass substrates by radio-frequency magnetron sputtering using ceramic CoFe₂O₄ target in Ar gas environment. The grazing incidence X-ray diffraction studies reveal the nanocrystalline nature of the films. The average grain size and particle size or crystallite size of the film is found to increase first and then decrease with increase in RF power. The saturation magnetization, remanence first increased at 80 W and then decrease with further increase in RF power while coercivity first increased at 80 W and decreased at 100 W followed by a decrease at 120 W. The films are highly transparent above 600 nm wavelength. The optical band increases on annealing the films. The optical band gap first decreases as the RF power increases from 60 to 80 W followed by an increasing trend with a further increase in RF power. The observed changes in the properties of the film are due to the combined effect of grain size and cation distribution.

4.2 Effect of thickness on structural, optical and magnetic properties of CoFe₂O₄ thin film.

In this study, the effect of film thickness and annealing on structure, magnetic and optical properties of CoFe₂O₄ thin films is carried out.

4.2.1 Structural analysis

Figure 4.11 shows grazing incidence X-ray diffraction patterns measured on the as-deposited films and on annealed films. The main peaks of cubic spinel structure can be seen in all the patterns. It can be seen from Fig. 4.11 that longer deposition times leads to slightly more intensity due to increase of the film thickness. As-deposited film CFF-1.5 is amorphous, while those deposited for 1 h and 2 h (CFF-1 and CFF-2) show a small degree of crystallinity. The films annealed at 500 °C showed well-defined (311), (400) and (440) peaks of cubic spinel structure CoFe₂O₄ phase. The (311) peak was used to estimate size of the crystallite from the FWHM (β) by using the Debye-Scherrer formula. The theoretical density of as-grown films CFF-1h and CFF-2h is 5.09402 g/cm³ and 5.22575 g/cm³, respectively. For annealed films the

X-ray densities are 5.37076 g/cm³, 5.39986 g/cm³ and 5.32684 g/cm³ for CFF-1h, CFF-1.5h and CFF-2h, respectively. This indicates a slight increase in the density of the films after annealing.

Table 4.4 FESEM, TEM, and structural properties of annealed CoFe₂O₄ thin films

Sample	mple Lattice constant 'a' (±0.005Å) XRD		Crystallite (±1 nm) XRD	'		Grain size (±1 nm) annealed films	Particle size (±1 nm) annealed films
	as-grown films	annealed films	as-grown films	annealed films	FESEM	FESEM	TEM
CFF-1h	8.487	8.34	5	10	47	22	11
CFF-1.5h CFF-2h	- 8.418	8.39 8.36	- 4	9 6	39 52	31 40	8 7

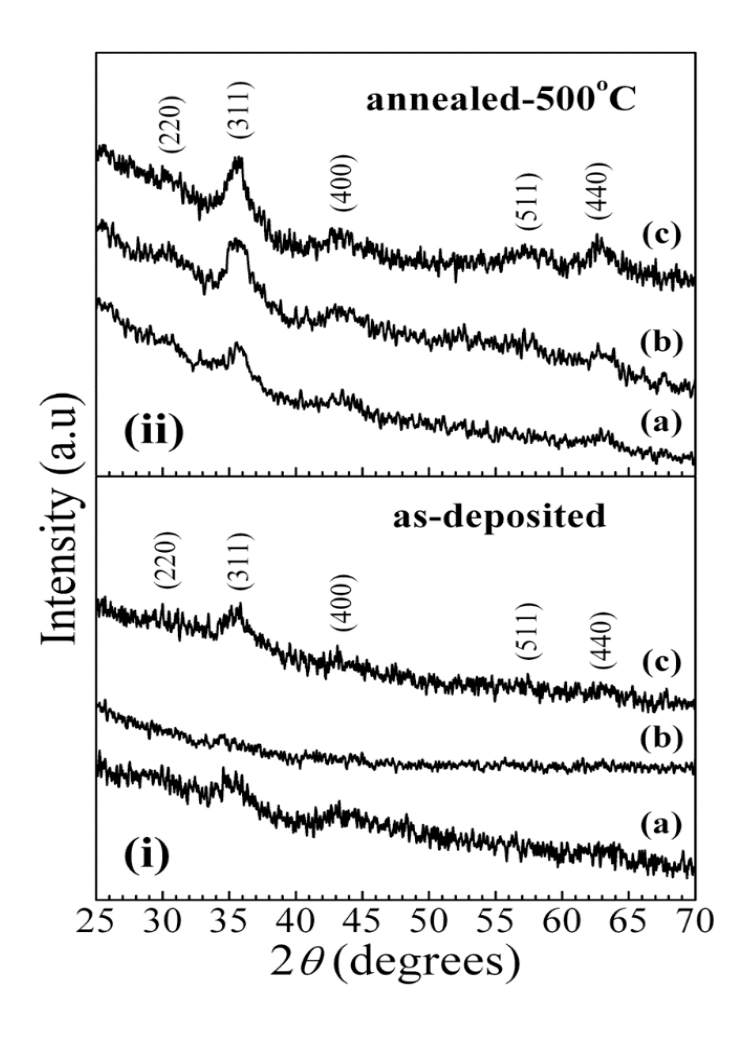


Figure. 4.11 The XRD patterns of $CoFe_2O_4$ films grown at 100 W for (a) 60 min, (b) 90 min, and (c) 100 min for as-deposited, (i) and heat treated at 500° C films (ii).

4.2.2 Surface morphology

Fig. 4.12 shows FESEM micrographs of the surface of as-grown films and films after annealing at 500°C for 3 h. The grain size distribution diagrams are shown in inset of the each FESEM images. Average grain sizes estimated for the as-deposited films are 49, 39 and 52 nm for CFF-1h, CFF-1.5h, and CFF-2h, respectively, and for annealed films average grain size is 22, 31 and 40 nm, respectively.

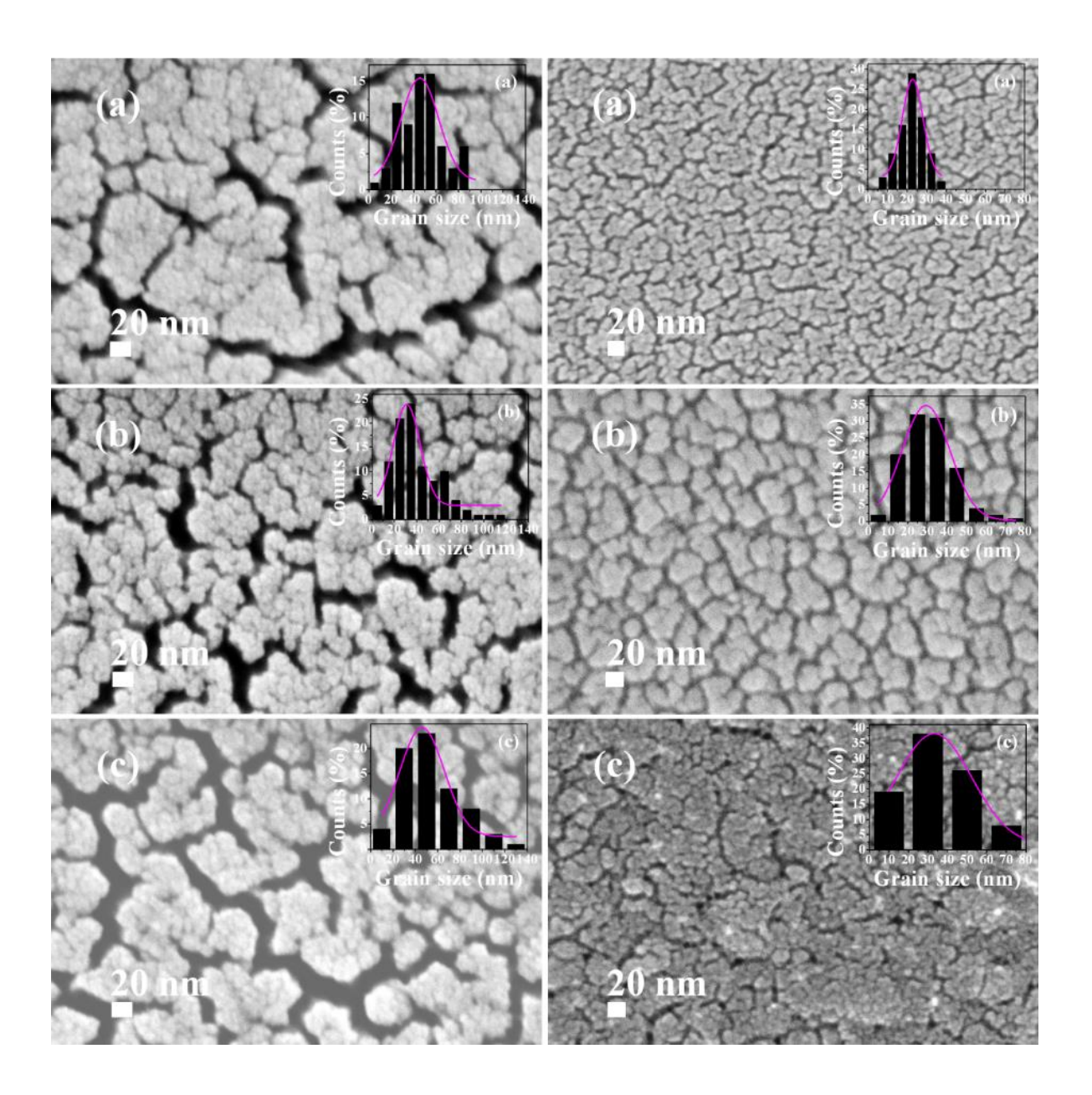


Figure 4.12 FESEM micrographs of the films deposited for (a) 1 h, (b) 1.5 h and (c) 2 h; as-grown CoFe₂O₄ thin films [left panel] and films annealed at 500°C [right panel].

The images have sufficient quality such that individual grains can be resolved and their sizes measured. ImageJ software was used for grain size analysis (measured at least 100 grains). It can be seen that films annealed at 500°C exhibit increase in grain size with increasing film thickness. After annealing the films at 500 °C, all the films possessed a uniform microstructure with improved crystallinity. Average grain sizes of all the films are found to be much greater than crystallite size (Table 4.4). The bigger grain size is due to the agglomeration of small crystallites.

4.2.3 Transmission electron microscope

Figure 4.13 shows TEM images of the annealed films (500°C). The average particle sizes estimated from TEM image are in agreement with the particle size estimated from XRD data using Scherrer formula (see Table 4.4). The average particle size decreases with increasing film thickness.

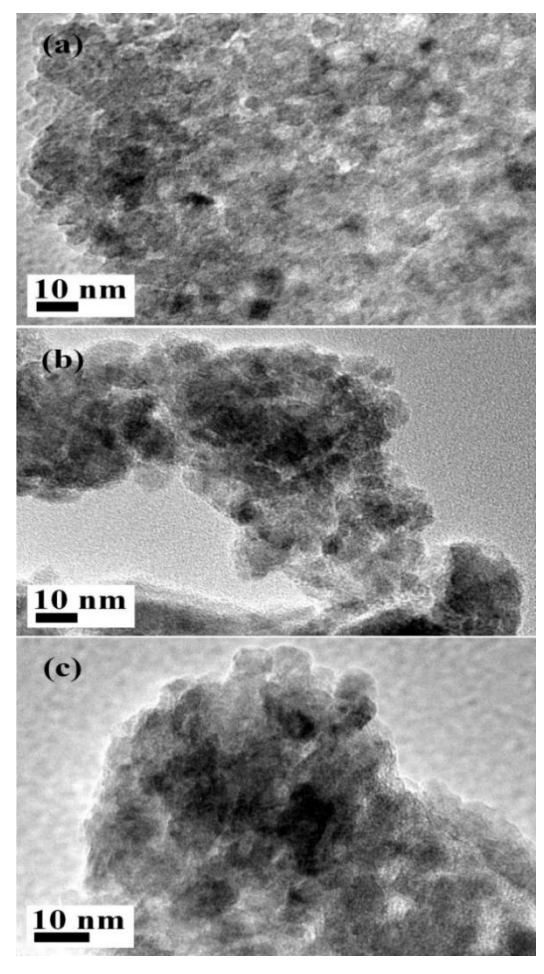


Figure 4.13 TEM micrographs for the annealed cobalt ferrite films deposited for (a) 1 h, (b) 1.5 h and (c) 2 h at 100 W.

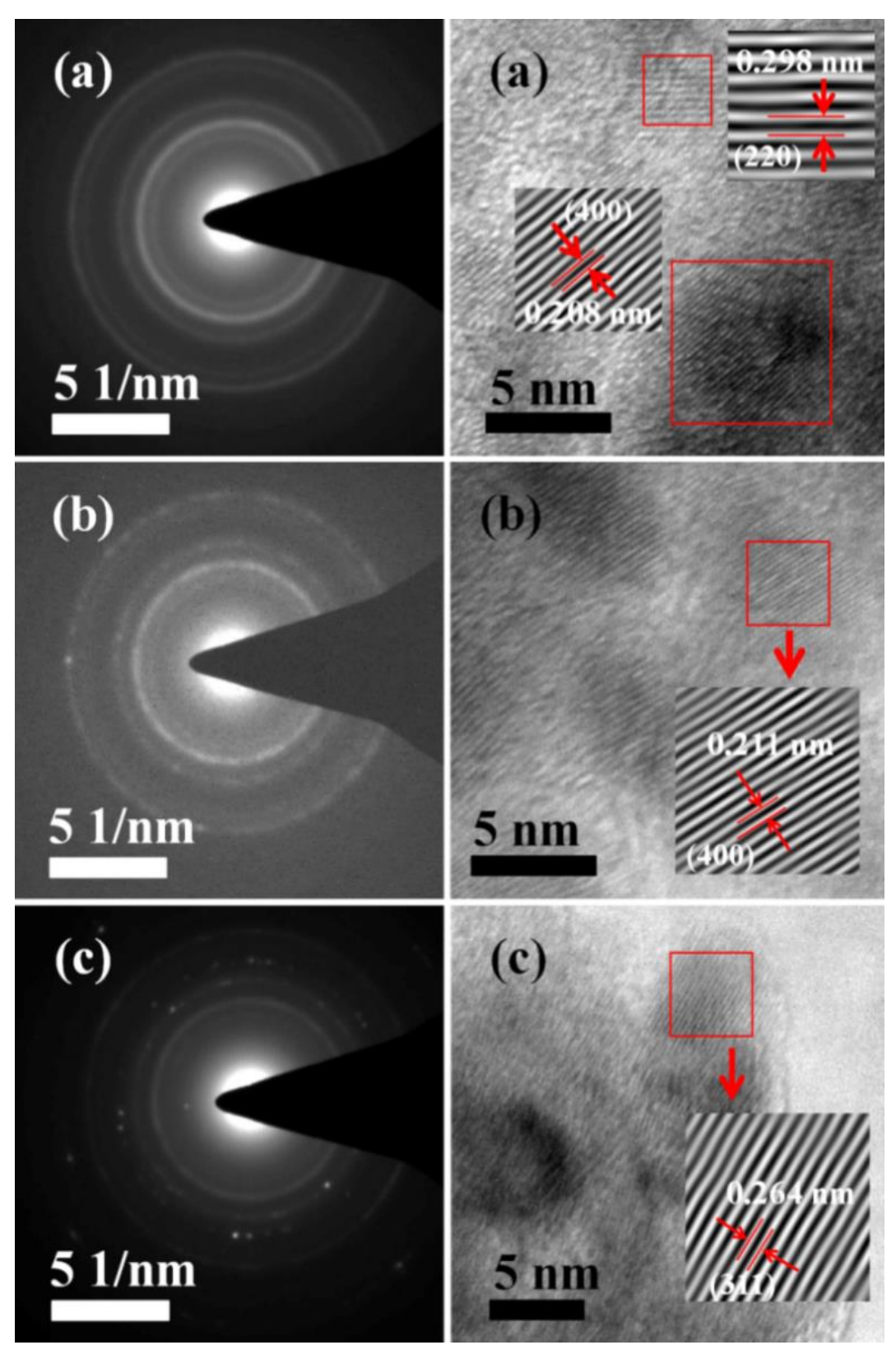


Figure 4.14 (**right**) Selected area electron diffraction (SAED) patterns [left panel] and HRTEM images [right panel] of the annealed cobalt ferrite films deposited at 100 W RF power for (a) 1 h, (b) 1.5 h and (c) 2 h

The selected area diffraction (SAD) patterns and HRTEM micrographs are shown Fig. 4.14. The SAED patterns of thin films demonstrate that the films have randomly oriented grains. The HRTEM analysis reveals that annealed Co-ferrite films have spherical/square shape. Using IFFT, interplanar distance was calculated from HR-TEM images. These micrographs show details of the interplanar distance corresponding to different planes in spinel structure.

4.2.4 Magnetic measurements.

Fig 4.15 shows the field-dependent magnetization (M–H) of the Co-ferrite films with different thicknesses at room temperature measured till applied field of ± 15 kOe. As a point of comparison, the magnetization of CoFe₂O₄ film deposited at 100 W in the previous section (M-H of Fig. 4.7(c) in Section 4.1) was shown as well. As can be seen from Fig. 4.15, the CoFe₂O₄ films exhibit ferromagnetic behavior. The obtained magnetic parameters are listed in Table 4.5. For the as-grown films CFF-1.5h and CFF-2h, the saturation magnetization M_S exhibits very low values of 14 and 37 emu/cm³, respectively, whereas the coercive field H_C of the samples decreased to half with increase of thickness from 236 nm to 353 nm for CFF-1h and CFF-1.5h, respectively, followed by a significant increase with further increase of thickness to 472.5 nm in case of CFF-2h.

As-deposited films exhibited an increase in saturation magnetization M_S with increasing film thickness i.e. increasing deposition time. M_S variation with film thickness might be ascribed to grain growth and reduced defect density of the as-deposited cobalt ferrite thin films. A reverse trend is observed between M_S and grain size with increasing film thickness in case of annealed films. For annealed films, with increase in film thickness, the grain sizes were 22, 31, and 40 nm for the films fabricated for 1 h, 1.5 h and 2 h, respectively. M_S decreases by 68 %, when the film thickness of annealed films increased from 236 nm (CFF-1h) to 353 nm (CFF-1.5h). With increase in film thickness to 472 nm, a slight increase in M_S is observed showing an overall decrease of 63%. Hence, with increasing film thickness, M_S decreases.

Annealing the films in air at 500 °C for 3 h results in an increase of M_S and also a decrease of H_C , and M_R . Only the film deposited for 1 h (CFF-1h) show a significant increase in H_C after annealing. A large increase in M_S is observed for CFF-1h (236.2 nm) film after annealing at 500 °C. The reason for increase in coercivity (H_C) of CFF-1h after annealing may be due to a decrease in grain size. The decrease in coercive field (H_C) of the annealed films with increasing film thickness beyond 236.2 nm (CFF-1h) is due to increase in grain size.

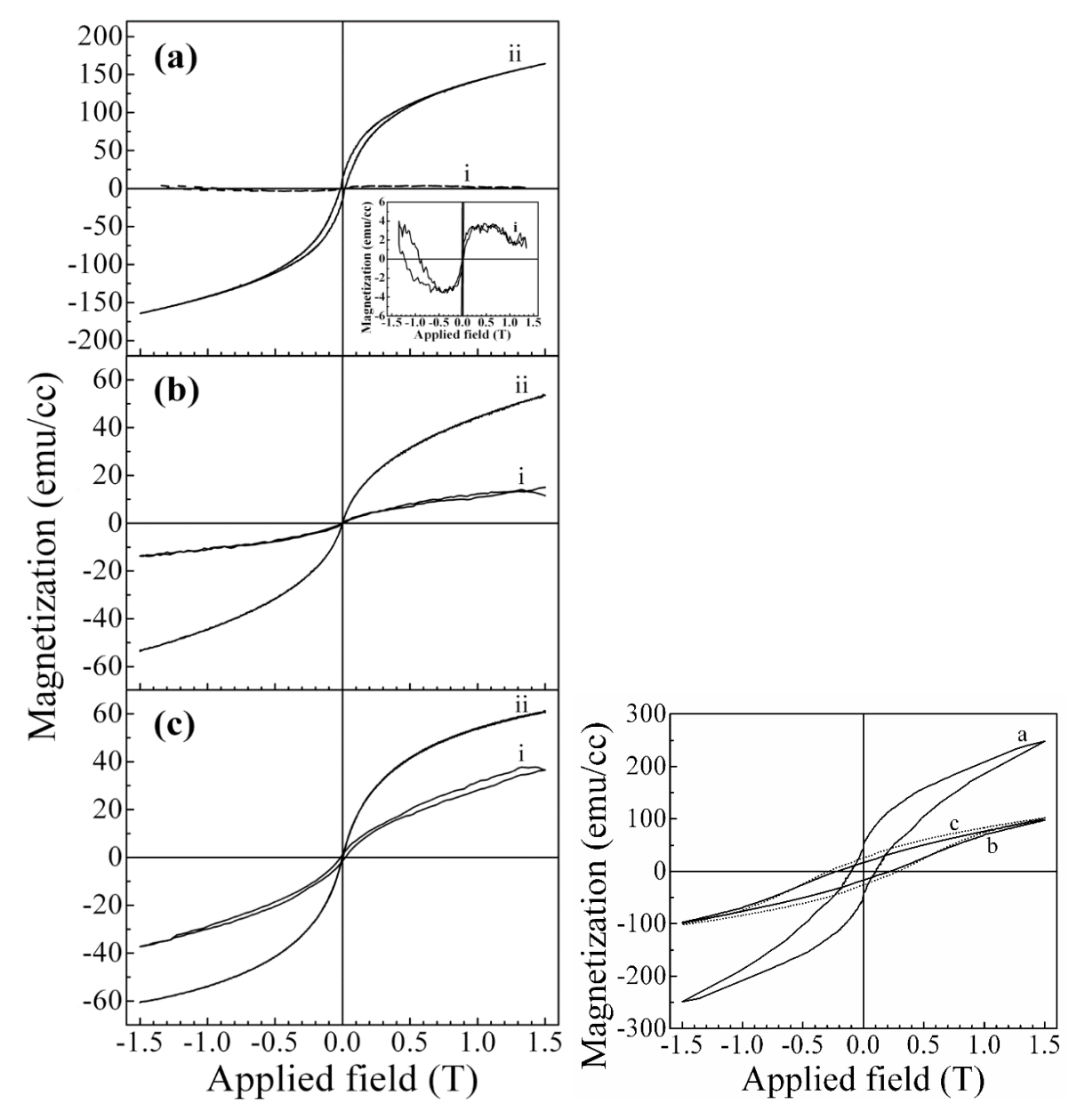


Figure 4.15 The M-H hysteresis cycles measured at room temperature on the (i) as-deposited and (ii) heat-treated CoFe₂O₄ films fabricated at 100 W for (a) 1 h, (b) 1.5 h, and (c) 2 h.

Figure 4.16 (right) The M-H hysteresis cycles measured at 100 K for (ii) heat-treated $CoFe_2O_4$ films deposited at 100 W for (a) 1 h, (b) 1.5 h, and (c) 2 h.

The increase in M_S after annealing the films at 500 °C for 3 h might be due to the redistribution of cations. Cation distribution in spinel sub-lattices may be altered with annealing. The increase in M_S might be due to increase in the B sub-lattice magnetization. Since net magnetic moment in inverse spinel CoFe₂O₄ is only due to Co²⁺ ions, because half of the Fe³⁺ cations (5µ_B) occupy

8 (of 64) tetrahedral (A) sites and the other half occupy 8 (of 32) octahedral (B) sites, and all Co^{2+} cations fill the remaining 8 octahedral (B) sites. Therefore, the net magnetization is given by M (μ_B) = M_B - M_A , here M_A and M_B are net magnetic moments of A (tetrahedral) and B (octahedral) sublattices, respectively. The increase in M_s values might be due to occupation of Co^{2+} ions in tetrahedral sites during annealing, forcing some of the Fe^{3+} ions to occupy octahedral (B) sites which increase net magnetization and hence the M_s . The low M_s than the bulk value may be due to occupancy most of Fe^{3+} ions on tetrahedral sites. Very large decrease in M_s might be due to the increase in defect density of the thicker films.

Table 4.5: Magnetic properties of annealed $CoFe_2O_4$ thin films deposited using 100 W RF power: for 1 h, 1.5 h and 2 h measured at 300 K

Sample		As-grown		Annealed at 50	Annealed at 500 °C for 3 h		
	M_r	M_s	H_c	M_r	M_s	H_c	
	(emu/cm^3)	(emu/ cm ³)	(G)	(emu/ cm ³)	(emu/cm ³)	(G)	
CFF-1h	0.11	-	102	15	164	154	
CFF-1.5h	0.13	14	49	0.05	53	3	
CFF-2h	1.3	37	257	0.4	61	23	

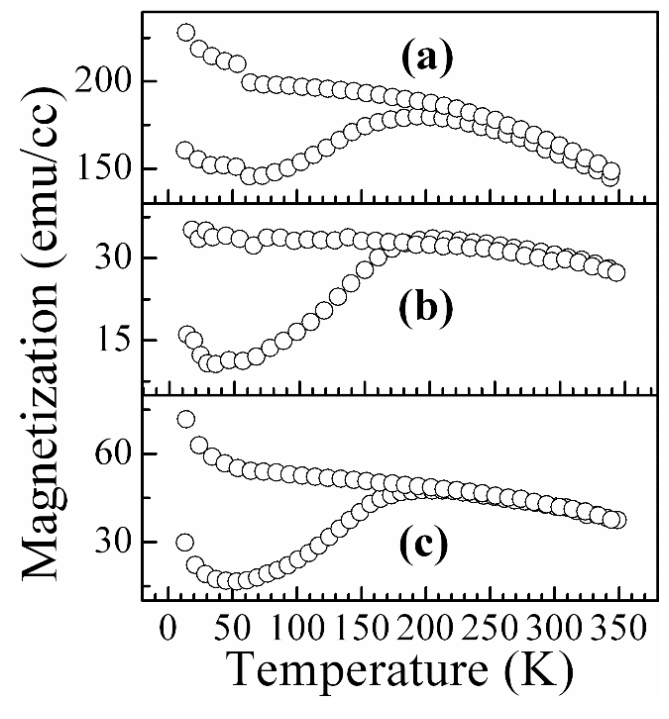


Figure 4.17: Temperature- and field dependent magnetization curves between 10-350 K at 5 kOe applied field obtained on annealed films deposited at 100 W RF power: for (a) 1 hour, (b) 1.5 hour and (c) 2 hours.

Figure 4.16 shows M(H) loops for annealed films measured at 100 K. Coercivity and saturation magnetization increased at 100 K. The H_c values of films grown for 1 hour, 1.5 hour and 2 hours are 1030, 2230 and 2888 Oe, respectively and M_s values are 248, 98 and 102 emu/cm³, respectively and M_r values are 44, 17 ad 25 emu/cm³, respectively. The reason for the increase in coercivity is due to increase of magnetic anisotropy.

Fig. 4.17 shows field-cooled (FC) and zero-field-cooled (ZFC) curves measured at 5 kOe in the temperature range 10-350 K. Fig. 4.17 shows the phenomenon of irreversibility. The irreversible (T_{irr}) temperature for CFF-1h, CFF-1.5h and CFF-2h is 220 K, 172 K and 190 K, respectively. Flattening of FC is due to interparticle interactions whereas increase of FC slope is due to non-interacting particle behavior [15].

4.2.5 Optical characteristics

The effect of thickness of Co-ferrite thin films and heat treatment at 500 °C has significant influence on band gap and crystalline structure. The transmission spectra in the wavelength range of 400–2600 nm of the as-grown CoFe₂O₄ films and films annealed at 500 °C are depicted in Fig. 4.18. A clear change of absorption edge is observed with increase in film thickness. After annealing absorption edge is shifted toward lower wavelength without any significant change in transmittance, i.e., the effect of annealing on the transmittance is a slight decrease because of the improved crystallinity and densification of the films after the annealing. This shift in absorption edges towards higher wavelength with increase in film thicknessis an indication of a decrease in optical bandgap. Absorption of light in short wavelength region is due to electronic transitions across energy levels in the band structure. The absorption coefficient α was determined from the optical transmission measurements at various wavelengths using the relationship given by Sunds [7,8] given by Eq. (4.4), $\alpha = -(1/t) \ln(T)$, where T is transmittance and t is film thickness.

The (t) of the thin film can be determined from the interference fringes of transmission data by calculating the refractive index of the thin film corresponding to two adjacent maxima (or minima) given as $n(\lambda_1)$ at λ_1 and $n(\lambda_2)$ at λ_2 [9] ascribed by Eq. (4.5),

$$t = \frac{\lambda_1 \lambda_2}{2[n(\lambda_1)\lambda_2 - n(\lambda_2)\lambda_1]}$$

where $n(\lambda_1)$ and $n(\lambda_2)$ are the refractive indices in two consecutive maxima (or minima) and λ_1 and λ_2 the corresponding wavelengths. The thickness of annealed films estimated by envelope

method [16] are 258, 395.4 and 483.8 nm for the films grown for 1 hour, 1.5 hour and 2 hours, respectively which were annealed at 500°C. The thickness of annealed films estimated from transmission measurements and surface stylus profilometer are listed in Table 4.6. Refractive indices of the annealed CoFe₂O₄ films were found to decrease with increasing wavelength from 820 nm to 1020 nm and then remain almost constant beyond 1050 nm as shown in Fig. 4.19. The increasing refractive index with film thickness is due to densification of the film. The increase in refractive index with increasing film thickness is also reported by other groups [17,18]. The estimated values of energy band gap for the as-deposited and annealed films are listed in Table 4.6. There is small decrease in band-gap with increase in film thickness for annealed films. This change is due to changes of structural defects, atomic distances and grain size in the films.

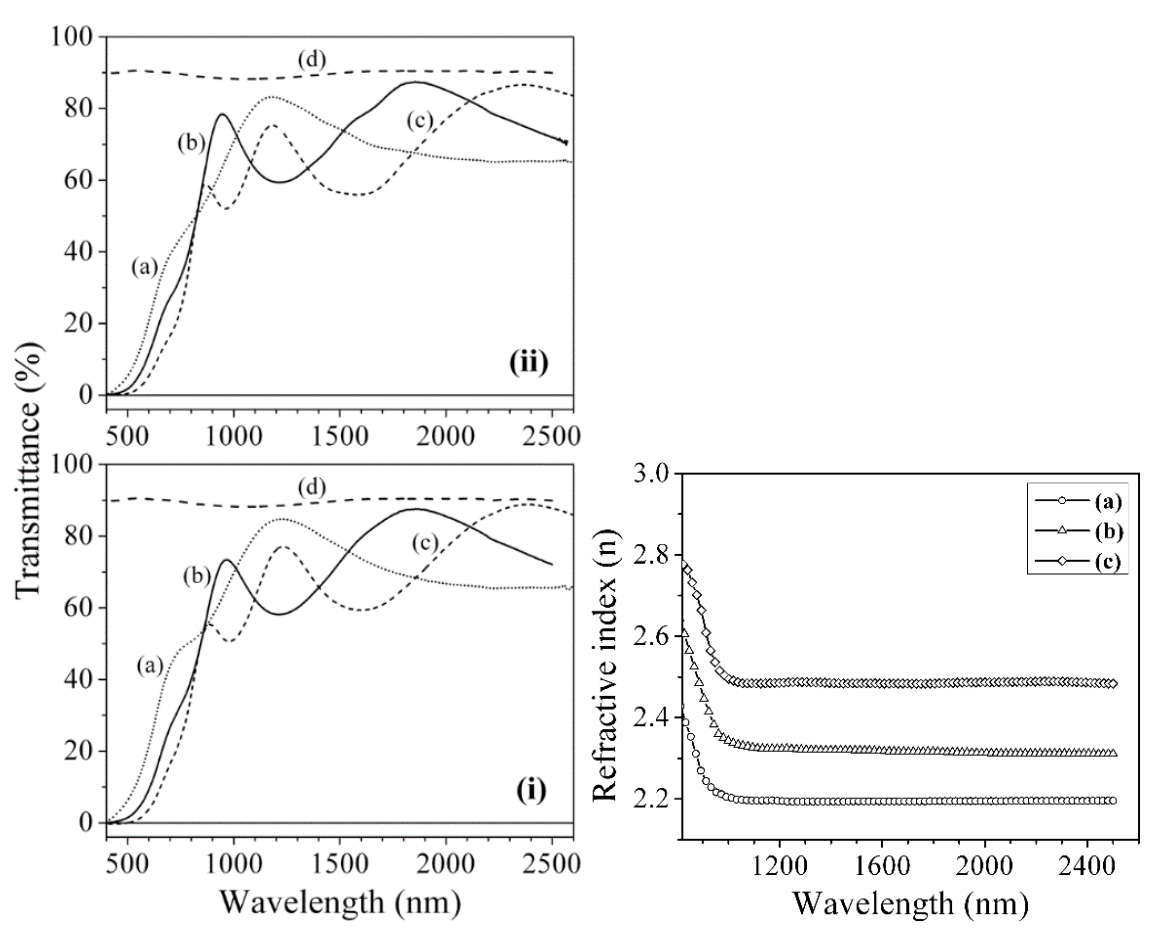


Figure 4.18: The optical transmission spectra of as-grown films, (i) and heat treated CoFe₂O₄ films, (ii); deposited for (a) 1 h, (b) 1.5 h, and (c) 2 h at 100W RF-power.

Figure 4.19(right) Plots of (n) versus (λ) for heat treated CoFe₂O₄ films grown for (a) 1 hour, (b) 1.5 hour, and (c) 2 hour.

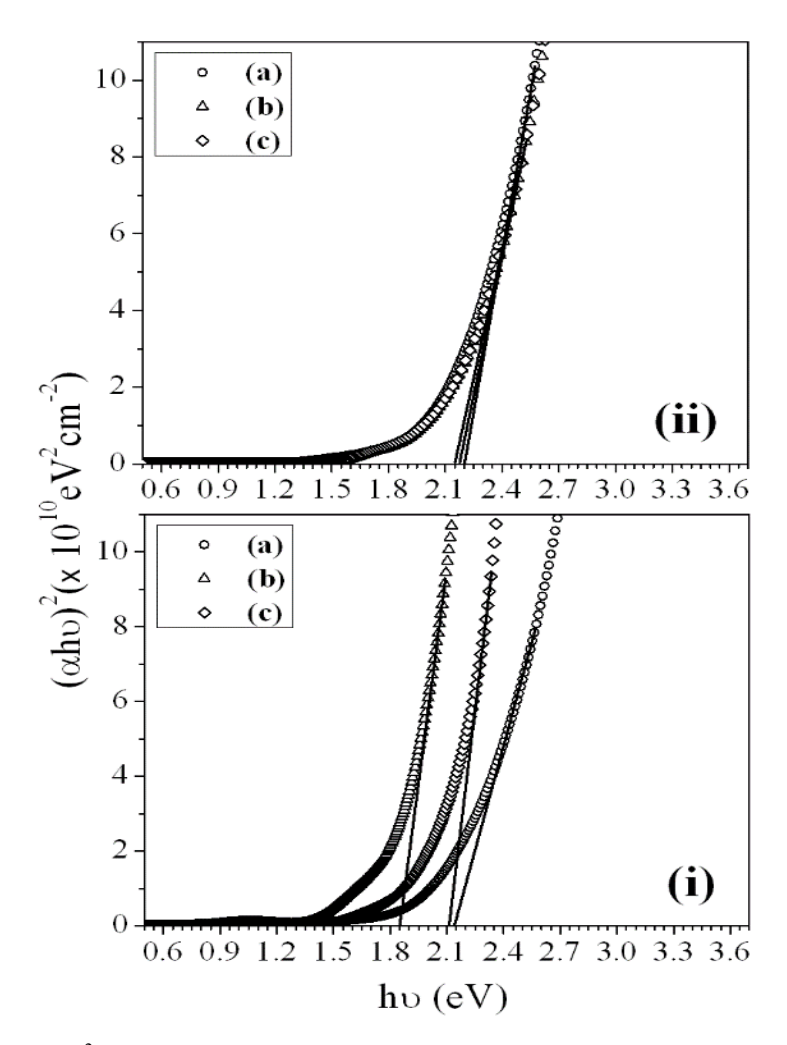


Figure 4.20: Plots of $(\alpha hv)^2$ versus (hv) for annealed CoFe₂O₄ thin films, (ii) and as-grown films, (i) deposited at 100 W for (a) 1 hour, (b) 1.5 hour, and (c) 2 hours.

Table 4.6 Optical properties of thin films of CoFe₂O₄ grown at various deposition times; 1 hour, 1.5 hour and 2 hours at 100 W RF-power.

Sample	Film	thickness (t	E_g (±0.0	01 eV)	
	As-grown	Annealed films		As-deposited	Annealed
	Profiler	Profiler	Calculated		
CFF-1h	269	237	258	2.14	2.2
CFF-1.5h	391	353	395	1.85	2.175
CFF-2h	512	472 484		2.11	2.15

These E_g results are less than the E_g values (ranging from 2.28 to 2.58 eV) of the CoFe₂O₄ films grown on glass substrates with thickness (400±20nm) by using chemical spray pyrolysis technique and annealed at different temperatures (500, 550) °C for (2h) by transmittance, absorbance and reflectance data [19].

4.2.6 Conclusions

The saturation magnetization M_S decreased by ~63% as film thickness increases from 236 to 482 nm. Decrease in M_S is due to decrease in particle size as observed from TEM and change in cation distribution over A and B sites of cobalt ferrite lattice. Optical band gap of annealed films decreases with increase in film thickness. The optical constants such as absorption coefficient, refractive index are affected by increase in film thickness. The decrease of E_g with increase in film thickness is due to increase in grain size.

4.3 Effect of argon gas pressure on structural, magnetic and optical properties of cobalt ferrite thin films.

The magnetization and optical data on thin films of Co-ferrite prepared at various argon gas working pressure of 8 (CFF-8), 10 (CFF-10) and 12 mTorr (CFF-12) were recorded. The saturation magnetization (M_s), remanence (M_r) and coercivity (H_c) decrease with the increase in argon gas pressure from 8 to 12 mTorr.

4.3.1 Structural analysis

The grazing incidence X-ray diffraction spectrum measured on the as-deposited CoFe₂O₄ films as well as on the films annealed at 500 °C is shown in Fig. 4.21. All peaks are in accordance with those of a typical crystalline Co-ferrite, with spinel structure. The as-grown films are amorphous with (3 1 1) peak as the most intense. After post deposition annealing at 500 °C for 3 h, the major peaks corresponding to cobalt-ferrite emerge, indicating the improvement of crystallization. Crystalline size calculated by using Debye-Scherrer equation calculated using the full width at half maximum (FWHM) of the (3 1 1) peak are listed in Table 4.7. The lattice constant 'a' was estimated for annealed samples and the values are presented in Table 4.7.

Table 4.7 TEM, FESEM and structural properties of CoFe₂O₄ thin films prepared at different argon gas pressure using 110 W RF power.

Sample (argon pressure)	Lattice constant 'a' (±0.01 Å)	Crystallite size (±1 nm) XRD	Grain size (±2 nm) as-deposited films FESEM	Grain size (±2 nm) annealed films FESEM	Particle size (±1 nm) TEM
8 mTorr	8.363	4.5	56	30	8
10	8.385	3.5	58	40	7
12	8.377	3.8	87	63	6

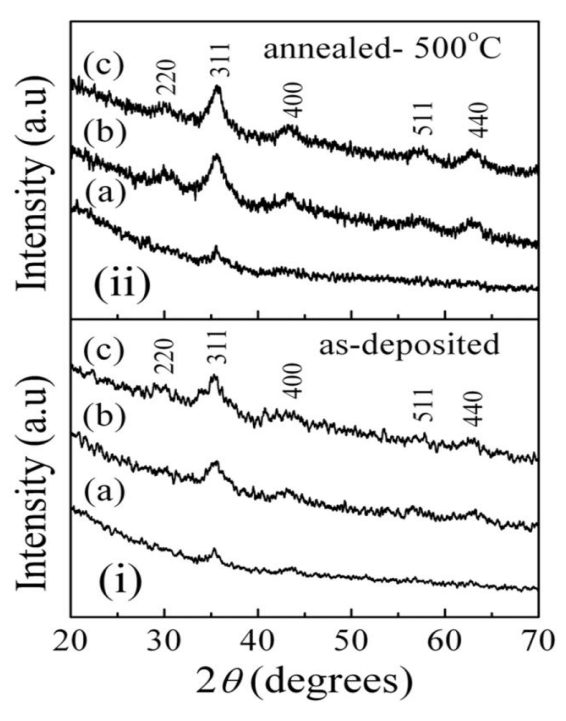


Fig. 4.21 XRD patterns of thin films $CoFe_2O_4$ grown at (a) 8, (b) 10 and (c) 12 mTorr of Ar gas pressure: for (i) as-deposited and (ii) annealed at 500° C.

4.3.2 Surface morphology

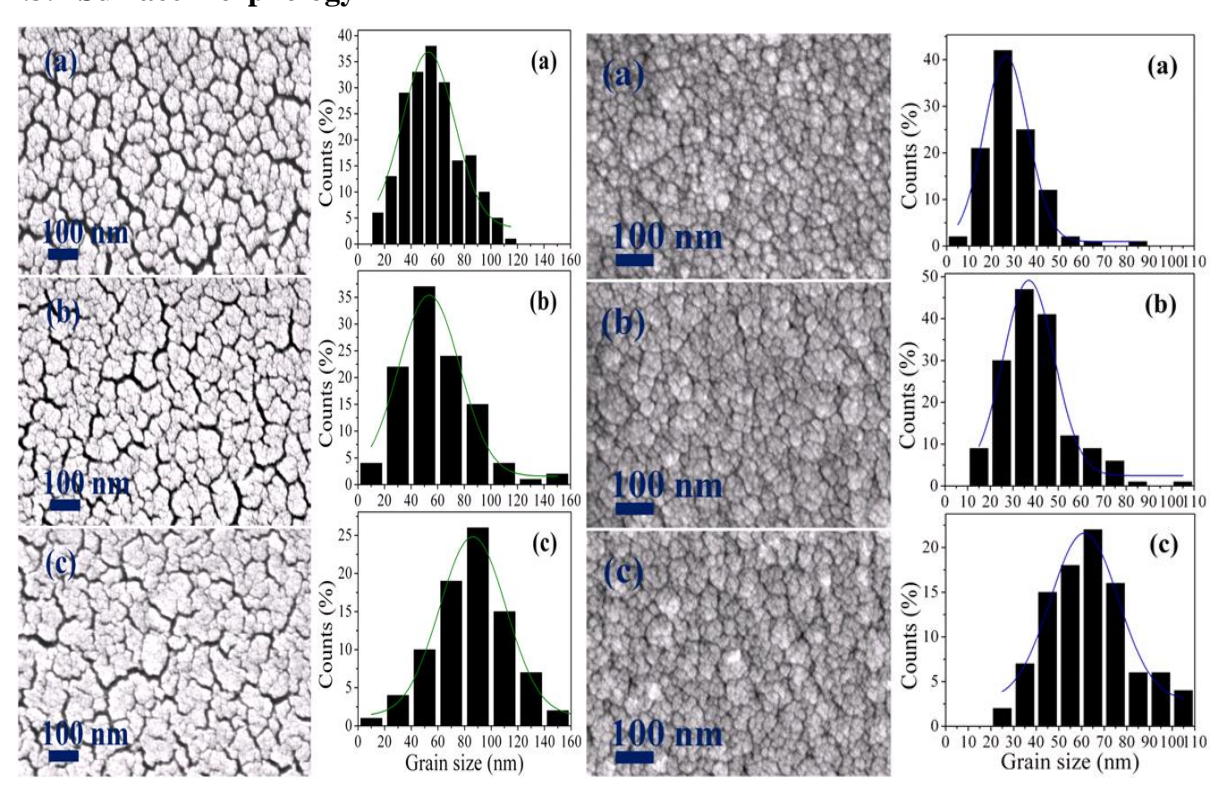


Fig. 4.22 FESEM images of the as-sputtered thin films of CoFe₂O₄ grown at (a) 8, (b) 10 and (c) 12 mTorr of Ar gas pressure.

Fig. 4.23 (right) FESEM images of annealed films of CoFe₂O₄ grown at (a) 8, (b) 10 and (c) 12 mTorr of Ar gas pressure.

Field emission scanning electron microscopy micrographs of the cobalt ferrite films are shown in Figs. 4.22(for as-deposited) and 4.23(annealed). FESEM images of annealed CoFe₂O₄ thin films deposited show spherical morphology. The estimated average grain size of the as-deposited films is 56, 58 and 87 nm, respectively, for films grown at 8, 10 and 12 mTorr argon pressure. Similarly, the average grain size increases as 30–40–63 nm for the annealed films as the argon gas pressure increases. For the annealed films, the histogram of sample CFF-8 shows that the maximum size distribution is in the range of 20–30 nm, for CFF-10, 30–40 nm, and for CFF-12, it is in the range of 60–70 nm. The average values of grain size are given in Table 4.7. The agglomeration in the sample may be due to the effect of post deposition annealing, giving the grains enough time to coalesce.

4.3.3 Transmission electron microscopy

Figure 4.24 shows TEM images and particle size distribution of annealed films. TEM images confirm the cluster formation of the films. From the TEM images, the measured mean diameter of particles by assuming that each particle was spherical, the CFF-8, CFF-10 and CFF-12 are 8, 7 and 6 nm, respectively. These values are in agreement with the particle size estimated from XRD data using Scherrer formula.

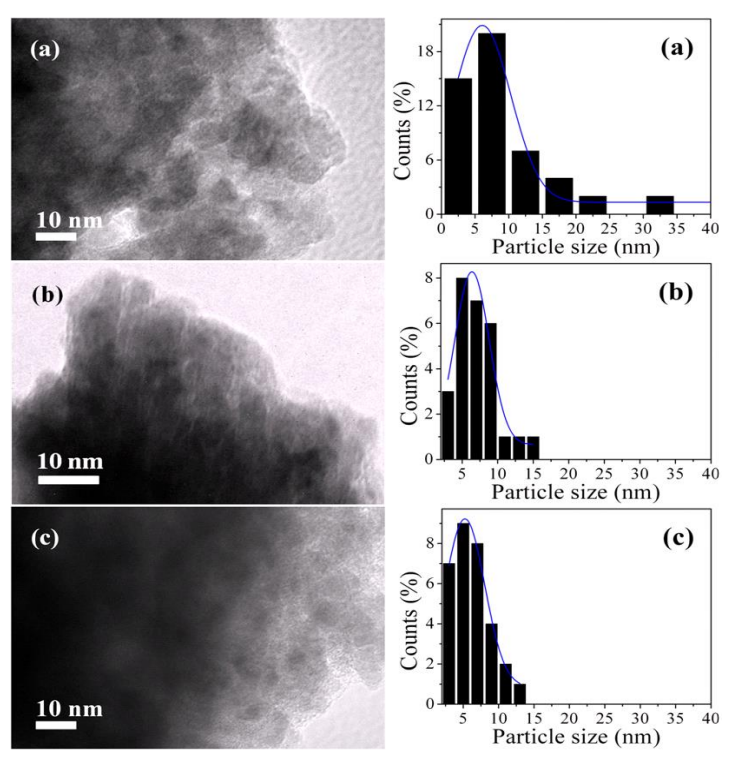


Fig. 4.24 TEM micrographs and corresponding particle size distribution of annealed CoFe₂O₄ films grown at various argon pressure: (a) 8, (b) 10 and (c) 12 mTorr.

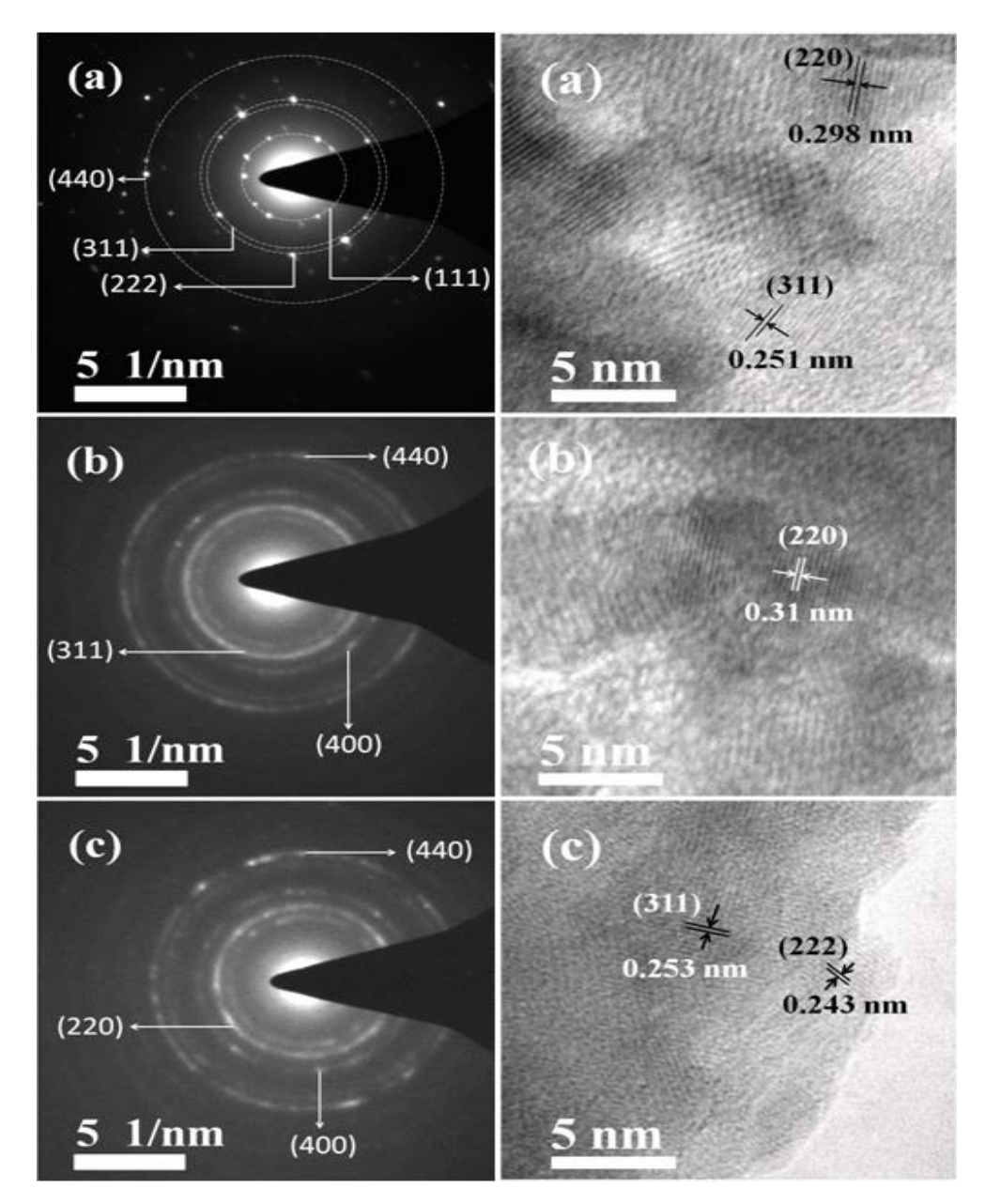


Fig. 4.25 Selected area diffractions [left panel] and HRTEM micrographs [right panel] of annealed CoFe₂O₄ films grown at various argon pressure: (a) 8, (b) 10 and (c) 12 mTorr.

Figure 4.25 depicts HRTEM images and selected area electron diffraction (SAED) pattern of the annealed films. SAED patterns confirm the polycrystalline nature of Co-ferrite thin films.

4.3.4 Magnetic properties

Figure 4.26 shows the magnetization hysteresis loops of as-deposited (Fig. 4.26(i)) and annealed (Fig. 4.26(ii)) thin films measured at room temperature. The values of coercivity, saturation magnetization and remanent magnetization increased significantly after annealing at 500 °C.

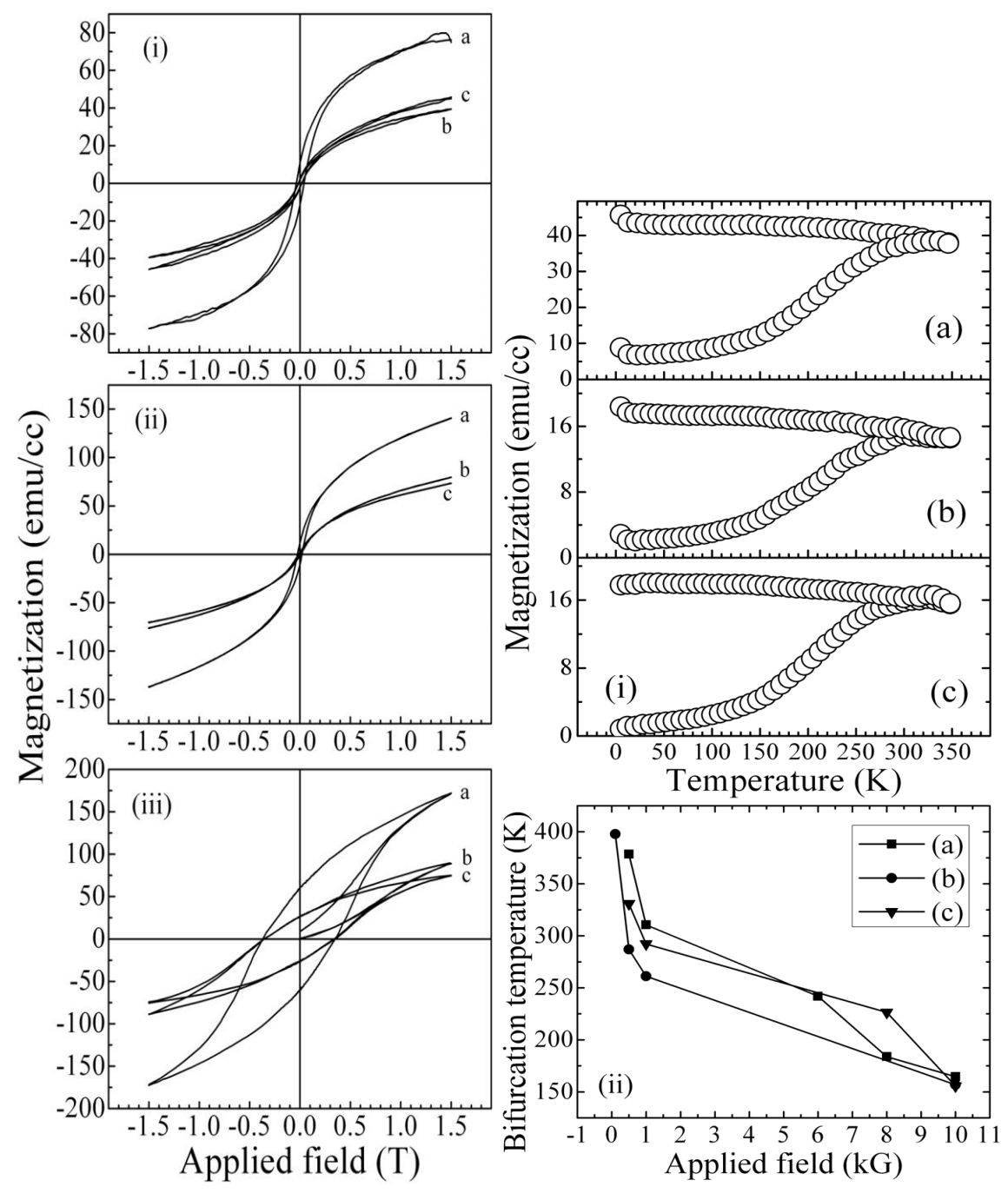


Fig. 4.26 The magnetization hysteresis loops of CoFe₂O₄ thin films grown at various Ar gas pressure: (a) 8, (b) 10 and (c) 12 mTorr for (i) as-deposited (RT) and (ii) annealed films (RT); (iii) M-H at 100 K.

Fig. 4.27 (right) Temperature- and field-dependent ZFC and FC magnetization curves (i), and bifurcation temperature vs. applied field (ii), obtained on annealed $CoFe_2O_4$ films, grown at different Ar gas pressure: (a) 8, (b) 10 and (c) 12 mTorr.

The M-H loops were obtained with the magnetic field applied parallel to the plane of the film and corrected by subtracting the diamagnetic contribution from the substrate. Since the

magnetization does not saturate up to a field of 1.5 T, so magnetization at the highest field value are compared for different films. The magnetic properties of these films are shown in Table 4.8. From Table 4.8 we observe that, the saturation magnetization (M_s) , remanence (M_r) and coercivity (H_c) decreases significantly with argon gas pressure. By comparing the structural results in Table 4.7 with the above magnetic properties, we see that H_c decreased, with increase of argon pressure, in heated Co-ferrite films probably is related to the increase of grain size. Films deposited at 8 mTorr shows a high coercivity H_c (222 Oe) and small saturation magnetization (M_s) (139 emu/cc) compared to that of bulk Co-ferrite target [20]. The low value of saturation magnetization (M_s) (139 emu/cc) is due to reduction in superexchange interaction between the nearest neighbor A-B ions. Decrease in M_s with increase in argon pressure is related to the increase in grain size. The present study shows that the H_c and M_s values strongly depend on thickness microstructure of the film when annealed at 500 °C for 3 h. The 408 nm cobalt ferrite film (CFF-8) has a H_c of 222 Oe and M_s of 139 emu/cm³, at room temperature (see Fig. 4.26; Table 4.8). Wang et al. [6] reported a H_c of 2.7 kOe and M_s of 345 emu/cm³ for 450 nm Co-ferrite films annealed at 900 °C for 2 h. Since the grain size determined (259.2 nm) from Scherrer's formula by Wang et al. [6] is very much greater than our estimated crystallite or particle size (4.5±1 nm from GIXRD or 8±1 from TEM and 30 nm from FESEM), our results are small than Ref. [6]. Horng et al. [21] reported M_s value of 121 emu/cm³ for 120-nm-thick CoFe₂O₄ film grown at 300 °C using oxygen-plasma-assisted molecular-beam epitaxy.

Figure 4.26 (iii) shows hysteresis loops measured at 100 K. The coercive field increases from 222 Oe at 300 K to 3923 Oe at 100 K for the film grown at 8 mTorr (CFF-8), and from 108 G to 3461 Oe for CFF-10 and from 80 G to 3493 Oe for CFF-12. We attribute this change to an increase in magnetic anisotropy with decreasing temperature.

4.3.5 Magnetization studies (FC-ZFC)

Figure 4.27(i) shows zero-field-cooled (ZFC) and field-cooled (FC) curves of the CoFe₂O₄ films measured in the temperature range of 5 K–400 K under an applied field of 1 kOe. The films with post deposition annealing were selected for these measurements, due to their good crystalline structure. The substrate effect from glass has been subtracted from the magnetization data. T_{irr}=330 and T_b=331 (CFF-8), T_{irr}=346, T_b=301 (CFF-10), T_{irr}=349 k, T_b=320 K (CFF-12). The irreversible temperature in ZFC and FC magnetizations is 330, 345 and 349 K, respectively, for annealed films CFF-8, CFF-10 and CFF-12. Bifurcation or irreversible

temperature (T_{irr}) increased with increase in argon pressure as film thickness increased. The blocking temperature (T_B) decreased from T_B =330 to T_B =301 with increase in argon pressure from 8 to 10 mTorr which increases to 320 at 12 mTorr. The thin films prepared in this study can be used in temperature sensor applications (FC curve) since there is a continuous variation in magnetization with changing temperature.

Table 4.8 Magnetic parameters of as-grown and annealed CoFe₂O₄ thin films measured at 300 K and 100 K deposited at various Ar gas pressure using 110 W RF power.

Sample (argon pressure)	_							nealed films red at 100 K	
	M _r (emu/cc)	M _s (emu/cc)	H _c (G)	M _r (emu/cc)	M _s (emu/cc)	H _c (Oe)	M _r (emu/cc)	M _s (emu/cc)	H _c (Oe)
8 mTorr	11	78	378	11	139	222	60	160	3923
10	1.9	45	150	1.7	78	108	26	89	3461
12	2.4	39	168	1.5	72	80	27	83	3493

Figure 4.27(ii) shows plot of bifurcation temperature versus applied field measured in the temperature range of 80 K–400 K under various applied field of 100 G, 500 G, 1 kG, 6 kG, 8 kG, and 10 kG by Lakeshore 7400 VSM. With increasing magnetic field the bifurcation temperature (T_B) decreased to lower temperatures.

4.3.6 Optical properties

The optical transmittance spectra in the wavelength range of 200–2500 nm for $CoFe_2O_4$ thin films grown at various argon pressures for the as-deposited $CoFe_2O_4$ thin films and annealed films are shown in Fig. 4.28. The optical transmittance of the as-deposited film CFF-8 (T = 64.508 at 967 nm and T = 77.865 at 1382 nm) has increased after annealing (T = 76.988 at 926 nm and T = 80.356 at 1310 nm) and shifted to shorter wavelengths. Similarly, CFF-10 (T = 63.742 at 965 nm and T = 77.1727 at 1379 nm) after annealing shows increased transmittance (T = 70.418 at 934 nm and T = 74.221 at 1332 nm) and finally, for CFF-12 (T = 43.8346 at 865 nm and T = 71.157 at 1063nm) also transmittance has increased (T = 57.86 at 858 nm and T = 80.331 at 1075nm). On an average as-deposited films exhibit over 58 % between 865–965 nm and 80 % in rest of NIR region. The absorption edge of the as-deposited films is between 850 and 950 nm. For the annealed films the absorption edge shifts toward lower wavelength with a remarkable increase in transmittance (>10%). In the medium absorption region (λ <800 nm),

the transmittance spectra of the annealed films are slightly shifted to shorter-wavelength (blue-shift) as compared with the as-deposited films.

It is clear that there are differences in the position of the absorption edge (position at which transmittance decreases). This difference corresponds to difference in band gap values.

Refractive indices and thicknesses of CoFe₂O₄ thin films by Swanepoel's method

Swanepoel method [22-23] was used to measure the refractive index (n) and film thickness of cobalt ferrite films. If $T_{max}(T_M)$ and $T_{min}(T_m)$ are maximum and minimum transmittance at any wavelength λ , then, refractive index n was calculated by relationship given by

$$n = \sqrt{N + \sqrt{N^2 - n_s^2}} \tag{4.7}$$

where

$$N = 2n_S \frac{T_M - T_m}{T_M T_m} + \frac{n_S^2 + 1}{2} \tag{4.8}$$

where n_s is refractive index of substrate (n_s =1.52 (glass)).

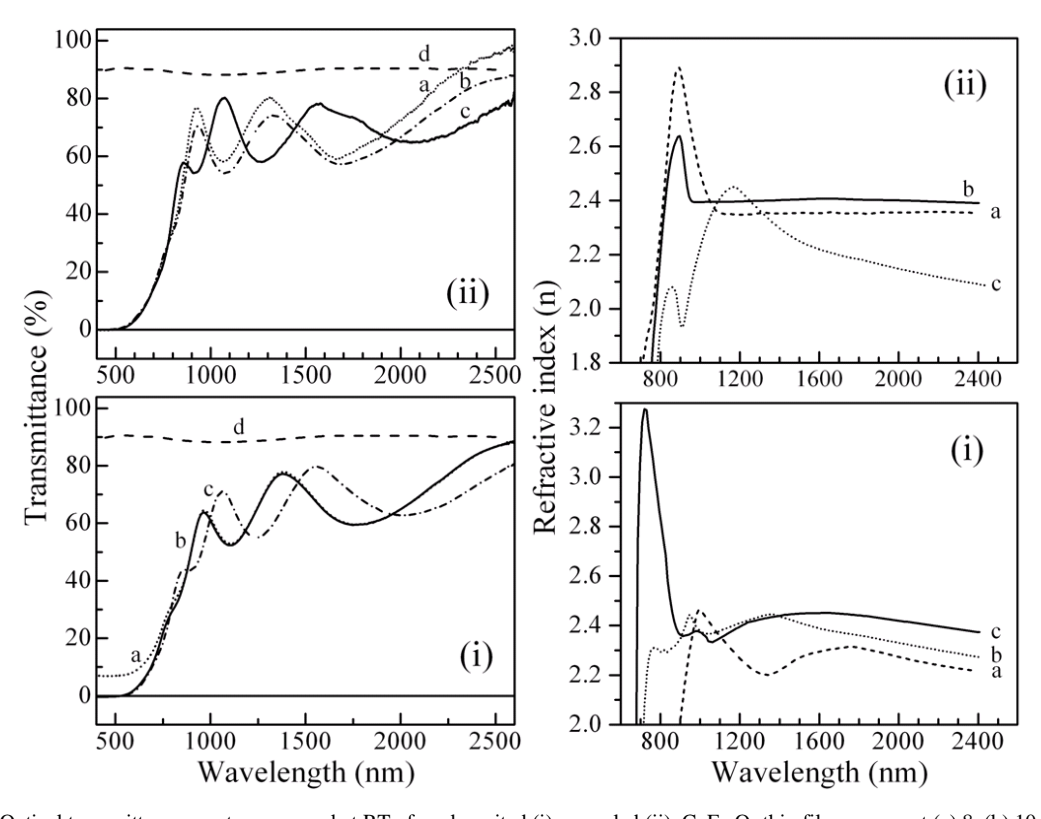


Fig. 4.28 Optical transmittance spectra measured at RT of as-deposited (i), annealed (ii), $CoFe_2O_4$ thin films grown at (a) 8, (b) 10 and (c) 12 mTorr of Ar gas pressure and (d) empty glass substrate.

Fig. 4.29 (**right**) Refractive index versus wavelength plots of as-deposited (i), annealed (ii), CoFe₂O₄ thin films grown at various Ar pressure: (a) 8, (b) 10 and (c) 12 mTorr.

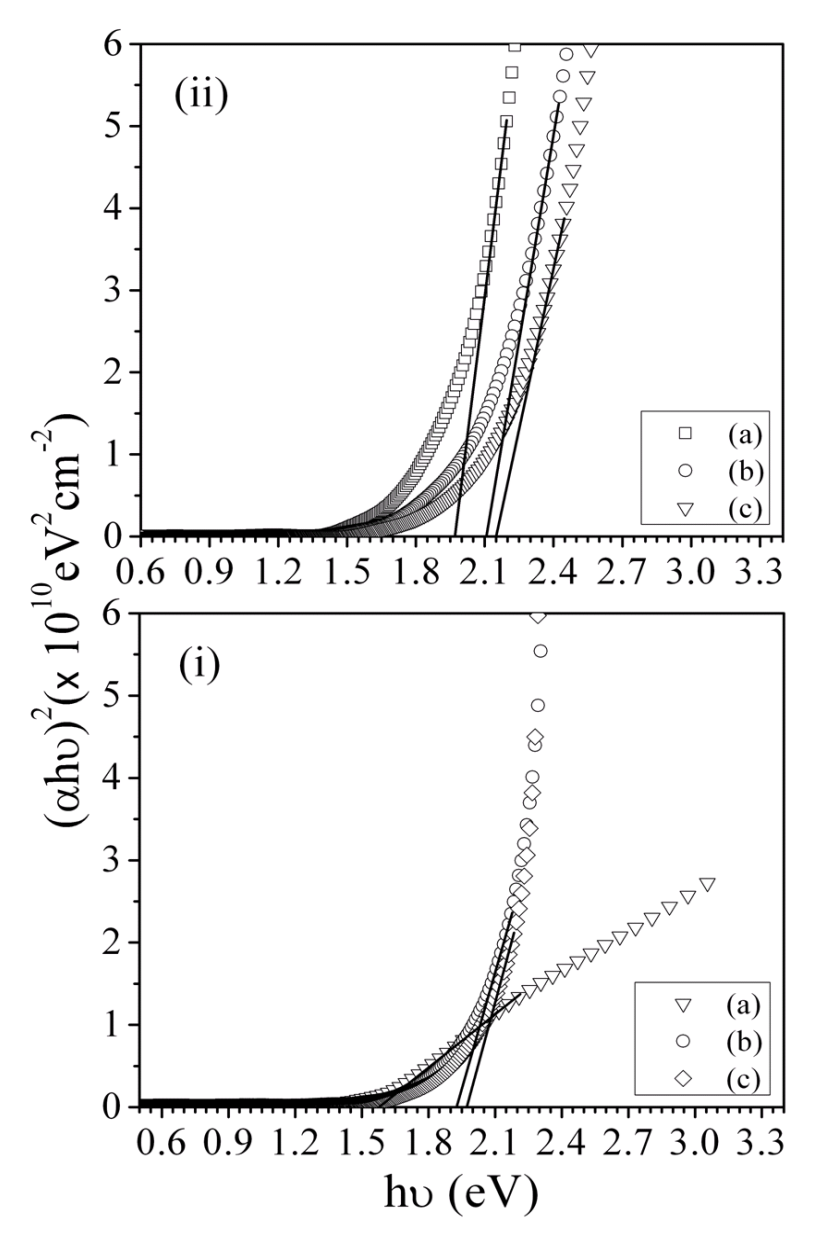


Fig. 4.30 Plots of $(\alpha h \upsilon)^2$ versus $(h \upsilon)$ for annealed CoFe₂O₄ thin films (ii) and for as-grown films (i), grown at (a) 8, (b) 10 and (c) 12 mTorr argon pressure.

Figure 4.29 shows refractive index versus wavelength graph. Since the average particle size decreases with increase of argon pressure (Fig. 4.24 and Table 4.7), there is a possibility of decrease in surface roughness and porosity of films with increasing argon gas pressure and hence results in a decrease of refractive index. Therefore, the surface roughness the films grown at 8 mTorr of argon pressure (408 nm) is more and shows a higher refractive index vary between 2.89 to 2.35. Refractive index for film grown at 10 mTorr (651.2 nm) is in the range of 2.64 to 2.4 and that of the film grown at 12 mTorr (808.5 nm) is in the range of 2.45 to 2.08.

The thickness of annealed films estimated from transmission measurements and surface stylus profilometer are listed in Table 4.9. The estimated values of energy band gap for the asdeposited and annealed films are listed in Table 4.9. From Table 4.9, optical band gap increases with increase in argon gas pressure. This increase in band gap is attributed to the decrease in particle size (Fig. 4.24;Table 4.7) and hence decreased disorder. The estimated direct band gap values for annealed films are slightly greater than those reported by Rao et al. [12].

Table 4.9 Optical properties thin films of CoFe₂O₄ grown at differentargon pressure using 110 W RF power.

Sample		Film thic	E _g (±0.01 eV)			
(argon pressure)	As-deposited		Annealed		As-deposited	Annealed
	Profiler	Calculated	Profiler	Calculated		
8 mTorr	450	495	408	410.7	1.58	1.98
10	700	680	651.2	598.9	1.93	2.10
12	870	798	808.5	800.6	1.98	2.16

4.3.7 Conclusions

CoFe₂O₄ thin films have been deposited onto glass substrates by RF magnetron sputtering technique at room temperature. Nanocrystalline cobalt ferrite thin films have been successfully deposited onto glass substrates at RT by RF-magnetron sputtering in argon atmosphere. The grazing incident X-ray diffraction patterns of sintered CoFe₂O₄ films indicates the formation of the desired single phase spinel structure. Saturation magnetization decreases with increase in argon pressure. The observed changes could are due to cation distribution and grain size present in the films after post annealing. Swanepoel method is successfully used to determine the refractive index, absorption coefficient, film thickness and energy gap of three films over the wavelength of 400–2600 nm. The optical energy band gap increased for annealed films as the argon gas pressure is increased. The increase in band gap is due to decrease in particle size as observed from TEM. Our results showed that the transmission decreased and refractive index decreased with increasing argon pressure. The study showed that the annealed cobalt ferrite film deposited at 8mTorr (CFF-8) can be used in temperature sensor applications.

4.4 Effect of annealing temperature on structure, magnetic and optical properties of C_{00.75}Cu_{0.25}Fe₂O₄ thin films.

4.4.1 Introduction

Magnetic properties of ferrite thin films also depend on their particle size, chemical composition and cation distribution. Tailoring magnetic properties is possible either by careful control of particle size or by changing cation distribution. This is possible by changing chemical composition and fabrication techniques and synthesis conditions. The electrical properties of cobalt ferrite films vary drastically with chemical composition. Hence, they are frequently used to investigate the conduction mechanism in ferrites. Even though thin films of CoFe₂O₄ are extensively studied by numerous researchers, there are only few reports about substitution of Cu²⁺ onto Co²⁺ site. The electrical and magnetic properties of cobalt ferrite films vary drastically with composition. Therefore, they can be used to study the conduction process in ferrites. Detailed systematic studies were undertaken on the as-deposited and annealed films of Co_{0.75}Cu_{0.25}Fe₂O₄. These studies are helpful in tuning the properties of the ferrite films.

4.4.2 Effect of Annealing Temperature

4.4.2.1 Film thickness

As-deposited films annealed at 600°C, 800 °C and 1000 °C were identified as 12403, 12403An6, 2403An8, and 12403An10, respectively. Thickness of the as-deposited and annealed Co_{0.75}Cu_{0.25}Fe₂O₄ films is estimated by using profilometer. A slight decrease in thickness of film was observed with annealing temperature. This may be due to increase in packing density of the films on annealing. The cross-sectional FESEM images of as-deposited and annealed films are shown in Fig. 4.33. The thickness of as-deposited films and films annealed at 600 °C, 800 °C and 1000 °C for 3 h estimated from cross-sectional FESEM images and surface stylus profilometer are listed in Table 4.11.

4.4.2.2 Structural Analysis

The XRD patterns of the $Co_{0.75}Cu_{0.25}Fe_2O_4$ target and the grazing incident angle X-ray diffraction patterns measured on the as-sputtered films as well as on the annealed films are shown in Fig. 4.31. The X-ray peaks of the target and the films are in accordance with those of a typical crystalline Co-ferrite, with spinel structure without a preferred orientation. The as-deposited films are amorphous. After annealing at 600 °C, 800 °C and 1000 °C for 3 h, the height of major peaks corresponding to cobalt-ferrite increased with annealing temperature, indicating

the improvement in crystallite size. The XRD line width and crystallite size are connected through the Debye-Scherrer equation [1] given by $D = 0.9\lambda/(\beta\cos\theta)$ where, D is crystallite size in Å, λ is the wavelength of X-rays, β is the full width of the diffraction line at half the maximum intensity and θ is the diffraction angle. The size of crystallites was calculated using the full width at half maximum (FWHM) of the (3 1 1) peak and the values are presented in Table 4.10.

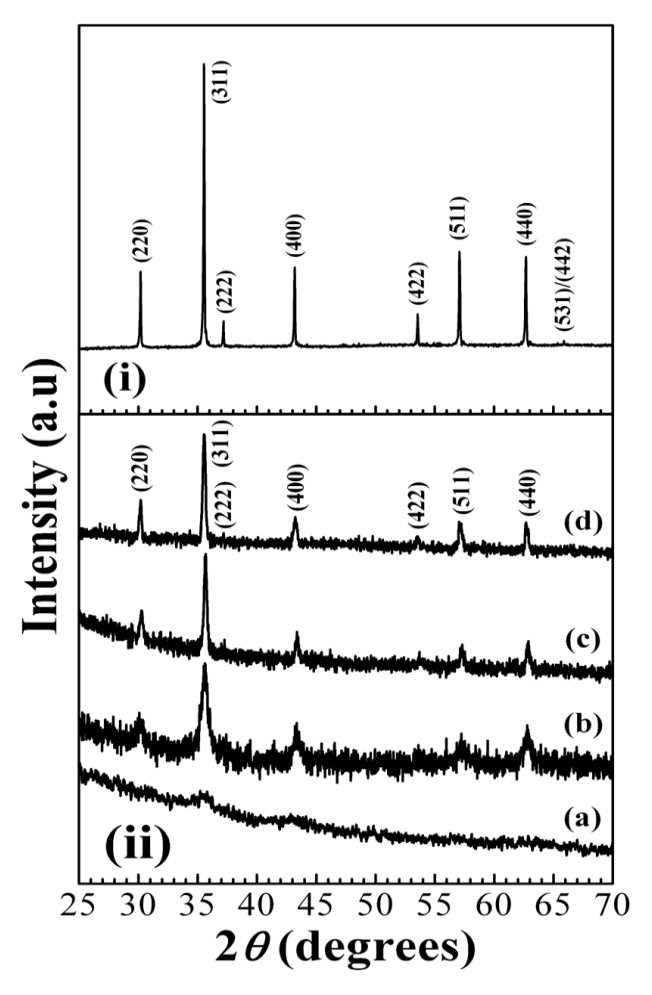


Fig. 4.31The XRD patterns of the $Co_{0.75}Cu_{0.25}Fe_2O_4$ target (i) and thin films (ii); (a) as-grown, (b) annealed at 600 °C, (c) annealed at 800 °C, and (d) annealed at 1000 °C.

4.4.2.3 Surface morphology

Field emission scanning electron microscopy micrographs of the Co_{0.75}Cu_{0.25}Fe₂O₄ films are shown in Fig. 4.32. The grain-size distribution was determined from the histogram obtained by measuring the size of around 100–200 individual grains using imageJ software. For the asdeposited films, films annealed at 600, 800 and 1000 °C the average grain size is 25, 30, 40 and

328 nm, respectively. The cross-sectional FESEM images of as-deposited films are shown in Fig. 4.33. The average values of grain size are listed in Table 4.10.

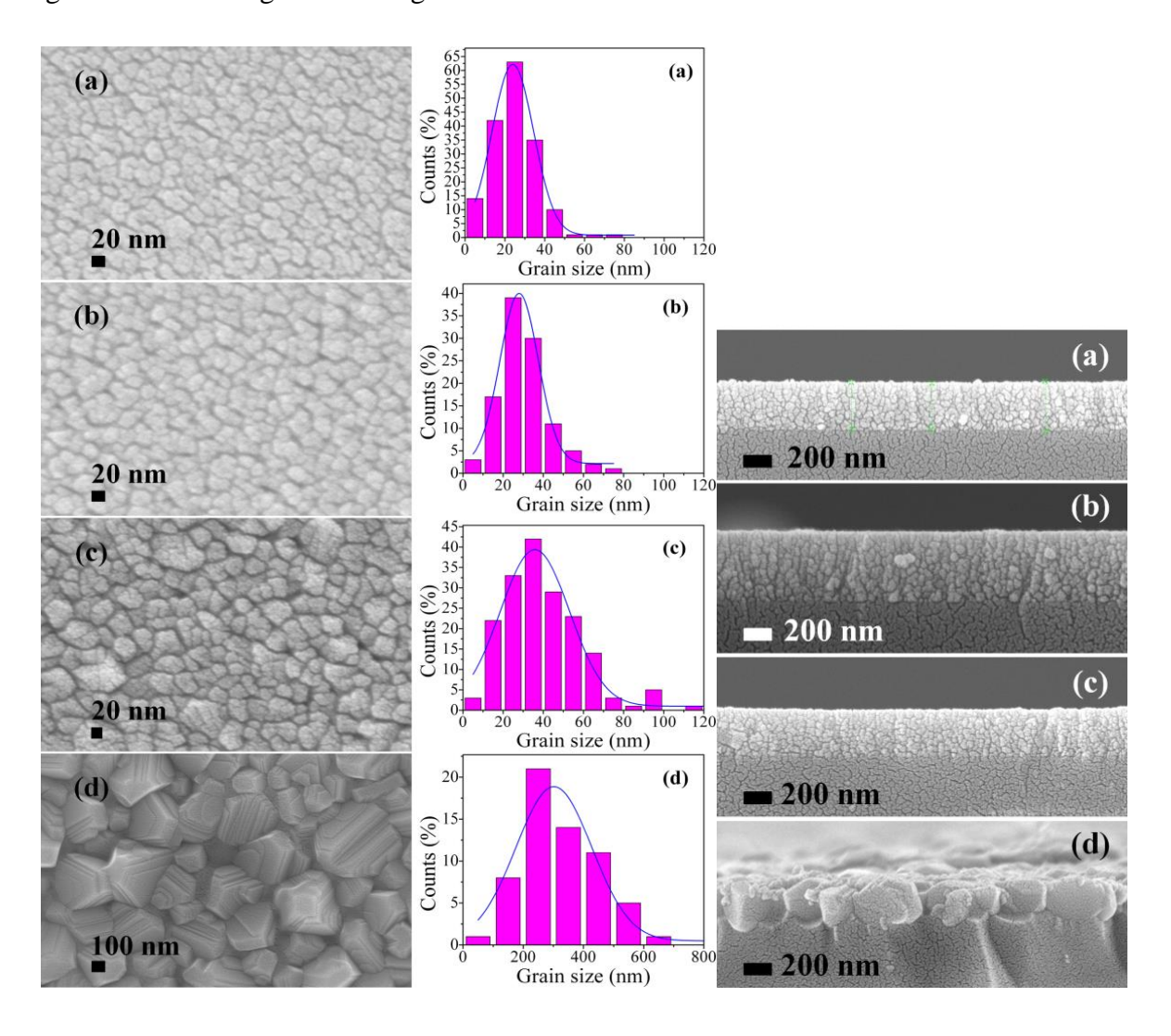


Fig. 4.32 FESEM images of the Co_{0.75}Cu_{0.25}Fe₂O₄ thin films grown at 40 W (a) as-grown, (b) annealed at 600°C, (c) annealed at 800°C, and (d) annealed at 1000°C and grain-size distribution.

Fig. 4.33 (**right**) FESEM cross-sectional images of the $Co_{0.75}Cu_{0.25}Fe_2O_4$ thin films grown at 40 W; (a) as-grown, (b) annealed at $600^{\circ}C$, (c) annealed at $800^{\circ}C$, and (d) annealed at $1000^{\circ}C$

Table 4.10 FESEM, TEM, and structural properties of annealed Co_{0.75}Cu_{0.25}Fe₂O₄ thin films deposited at 12 mTorr argon gas pressure using 40 W RF power

Sample	Lattice	Crystallite	Grain size	Particle size
(annealing	constant 'a'	size (± 1 nm)	$(\pm 1 \text{ nm})$	$(\pm 2 \text{ nm})$
temp. (°C))	(±0.01Å)	XRD	FESEM	TEM
As-deposited	8.38	7	25	-
600	8.36	14	30	16
800	8.34	31	40	7
1000	8.37	31.3	328	26
Target	8.33	30	64	-

4.4.2.4 Transmission Electron Microscopy

Transmission electron microscopy (TEM) and high resolution microscopy have been used to confirm the nanocrystalline nature of the films. Figure 4.34 shows the TEM images of the annealed films. It can be seen that the particles are more or less spherical with an average size of 7, 16 and 26 nm for films annealed at 600 °C (12403An6), 800 °C (2403An8), and 1000 °C (2403An10), respectively (Table 4.10).

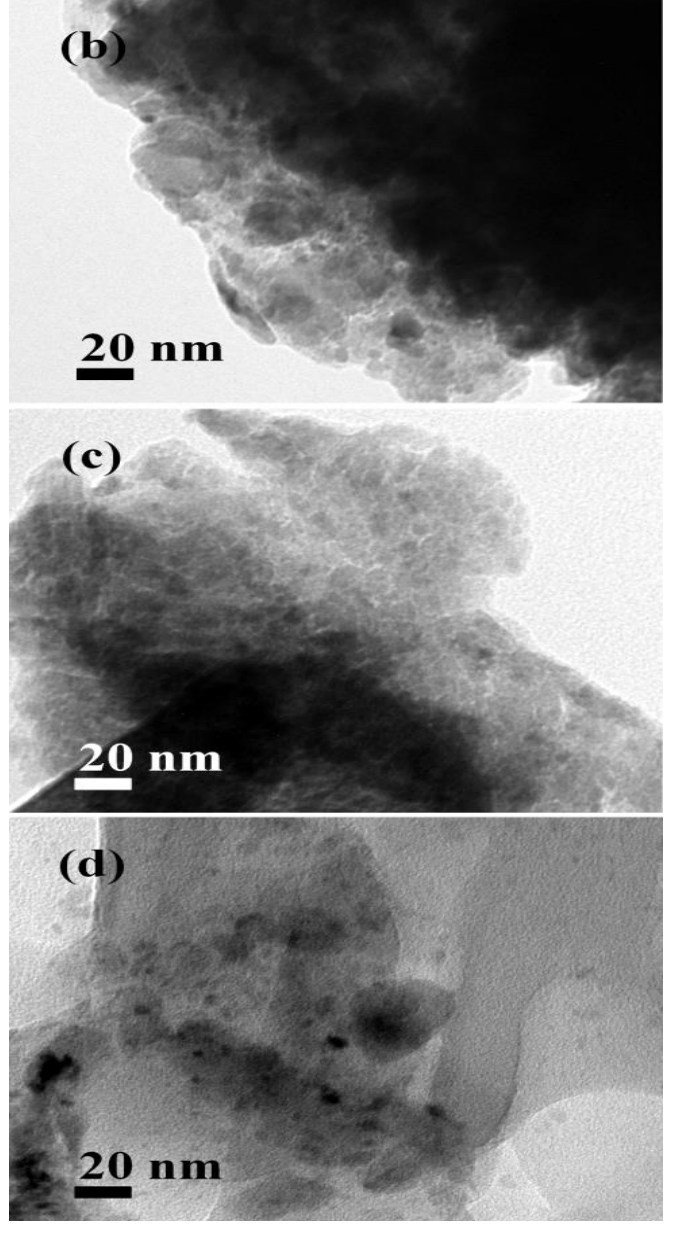


Fig. 4.34 Microstructure of $Co_{0.75}Cu_{0.25}Fe_2O_4$ thin films grown at 40 W; (b) annealed at 600 °C, (c) annealed at 800 °C, and (d) annealed at 1000 °C.

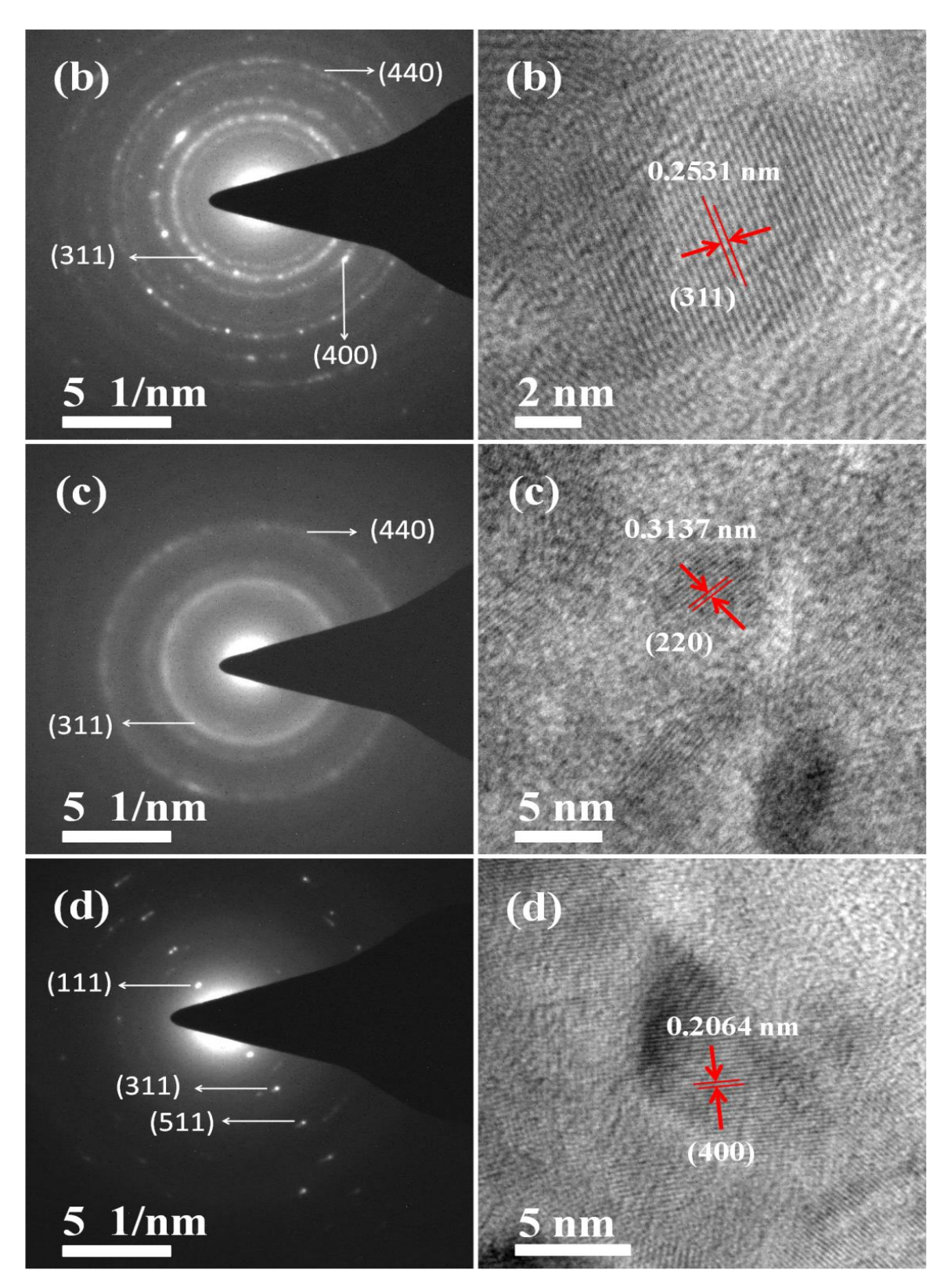


Fig. 4.35 Selected area diffractions [left panel] and HRTEM images [right panel] of $Co_{0.75}Cu_{0.25}Fe_2O_4$ thin films grown at 40 W; (b) annealed at 600 °C, (c) annealed at 800 °C, and (d) annealed at 1000 °C.

The selected area diffraction (SAD) patterns are shown in Fig. 4.35. The SAD patterns exhibit enhanced crystallinity with increase in annealing temperature. The high-resolution TEM image of the annealed films in Fig. 4.35 show the lattice fringes of the nanocrystallites. These micrographs show details of the interplanar distance corresponding to different planes in spinel structure.

4.4.2.5 Magnetic properties

Figure 4.36 shows the magnetization hysteresis loops of $Co_{0.75}Cu_{0.25}Fe_2O_4$ target, as-deposited, annealed thin films measured at room temperature. The loops were obtained with the magnetic field applied parallel to the plane of the film and corrected by subtracting the diamagnetic contribution from the substrate. The magnetization at 1.5 T (1.2 T for films) (M_s), remanent magnetization (M_R), and coercivity (H_c) of the films are tabulated in Table 4.11. The as-deposited films are amorphous and have a small magnetization compared with that of the target. The target has very low H_c of 57 G and M_s of 293 emu/cm³. After annealing at 600 °C, a large increase in M_s , H_c and M_r is observed due to increase in crystallinity and grain size (Table 4.10).

The in-plane coercivity of the annealed film increased as the annealing temperature increased from 600 °C to 800 °C and then decreases with further increase in annealing temperature up to 1000 °C. The high coercivity of the sample annealed at 800 °C is because of its small particle size which is observed from TEM micrograph and HRTEM images (Figs. 4.34 & 4.35) followed by a very large increase in grain size as annealing temperature is increased to 1000 °C (Fig. 4.32).

Table 4.11 Magnetic and optical parameters of Co_{0.75}Cu_{0.25}Fe₂O₄ thin films deposited at 12 mTorr argon gas pressure using 40 W RF power

Sample (annealing temp. (°C))	Film thick (±2 nm)	ness	Maş	Magnetic properties				
	Profiler	FESEM	M_r	M_s	H_c	E_g		
			(emu/ cm ³)	(emu/cm ³)	(G)	(eV)		
As-deposited	343	342	5	79	275.6	2.26		
600	332	328	59	227	1717	2.37		
800	321	323	55	166	2670	2.29		
1000	306	312	192	250	1499	2.04		
Target	-	-	11	293	57	-		

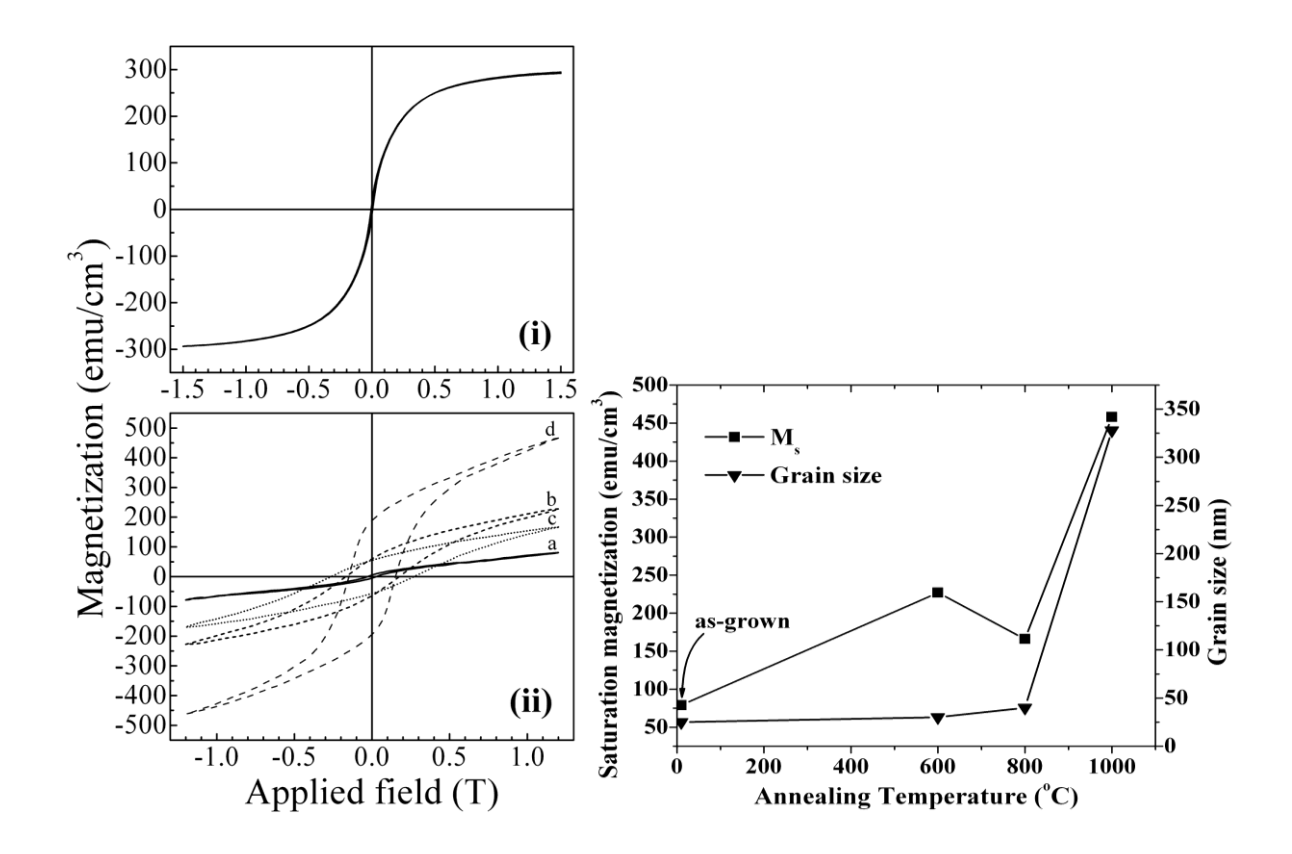


Fig. 4.36 The magnetization hysteresis loops of $Co_{0.75}Cu_{0.25}Fe_2O_4$ target (i), and thin films grown at 40 W (ii); (a) as-grown, (b) annealed at 600 °C, (c) annealed at 800 °C, and (d) annealed at 1000 °C.

Fig. 4.37 (**right**) Dependence of magnetization (M_s) at 1.2 T and grain size of annealed Co_{0.75}Cu_{0.25}Fe₂O₄ thin films annealed at different temperatures 600 °C, 800 °C and 1000 °C

Figure 4.37 shows the dependence of M_s at 1.2 T and grain size on annealing temperature. The increase in M_s of films annealed at 600 °C is due to the change in microstructure of the film. The as-grown film is amorphous (Fig. 4.32), having an M_s value of 79 emu/cm³. For the film annealed at 600 °C, the grain size increased due to the fusion of grains forming bigger dense grains leading to an increase in M_s value to 227 emu/cm³ as shown in Fig. 4.34 (b). As the annealing temperature is increased to 800 °C, grains are loosely connected as can be seen from TEM micrograph (Fig. 4.34 (c)) leading to a decrease in M_s to 166 emu/cm³. The film annealed at 1000 °C exhibits highly dense very large grains with no grain boundaries (Fig. 4.32 (d)) and hence the M_s value is increased to 250 emu/cm³. The M_s of this sample is found by extrapolation of linear portion of M(H) at high field to Y-axis and the value of y-intercept is taken as M_s value. The variation in M_s can be due to changes in cation distribution among the A and B sites due to heat treatment. The increase in M_s value of the film annealed at 1000 °C could be due to the

disorder in the distribution of Fe³⁺ and Co²⁺ among A and B sites compared with a perfectly ordered inverse spinel structure. In the fully inverted structure, the Fe³⁺ moments are completely compensated and the net moment arises only from Co²⁺ ions. The occupation of Co²⁺ ions to octahedral sites might be less than the full. The octahedral holes which are not occupied by the Co²⁺ ions might be filled with Fe³⁺ ions which lead to the increase in M_s of the film annealed at 1000 °C. Substitution of Co²⁺ by Cu²⁺ (1 μ_B) on tetrahedral sites leading to increase in M_s . Furthermore, non-magnetic Cu⁺ (0 μ_B) formed during heating at 1000 °C might occupy tetrahedral sites forcing Fe³⁺ ions to octahedral sites which lead to the increase in M_s of the film annealed at 1000 °C. The 311-nm Co_{0.75}Cu_{0.25}Fe₂O₄ film heated at 1000 °C has a H_c of 2.67 kOe and M_s of 250 emu/cm³, at room temperature (see Fig. 4.36; Table 4.11). Lee et al [6] reported saturation magnetization (M_s) of 220 emu/cm³ for CoFe₂O₄ films deposited by RF magnetron sputtering. The present study shows that the H_c and M_s values strongly depend on microstructure of the film when annealed at different temperatures 600 °C, 800 °C and 1000 °C for 3 h.

4.4.2.6 Optical properties

The optical transmittance spectra in the wavelength range of 300-2500 nm for $Co_{0.75}Cu_{0.25}Fe_2O_4$ thin films grown at 40~W~12 mTorr argon pressure for the as-deposited $Co_{0.75}Cu_{0.25}Fe_2O_4$ thin films and annealed films are shown in Fig. 4.38

Fig.4.39 shows the plots of $(\alpha h v)^2$ versus (h v) for the annealed $Co_{0.75}Cu_{0.25}Fe_2O_4$ thin films. The extrapolation of the straight-line graphs to $(\alpha h v)^2 = 0$ gives the value of the optical gap. It can be seen that the plots of $(\alpha h v)^2$ versus (h v) varies linearly for all the films in the region of strong absorption near the fundamental absorption edge over a wide range of photon energies. The linear variation of absorption coefficient at high frequencies indicates that these thin films have direct transitions across the energy band gap.

The estimated values of energy band gap for the as-deposited and annealed films are listed in Table 4.11. The error in the optical band gap measurement by linear curve fitting is ±0.02 eV. The band gap variation for films deposited at 40 W of RF power is within this measurement error limits. The increase in the optical band gap of Co_{0.75}Cu_{0.25}Fe₂O₄ thin films annealed at 600 °C may be due to the removal of defect levels from the films. The optical band gap for annealed films shows a decrease from 2.37 to 2.29 eV as the annealing temperature increases from 600 °C to 800 °C and decreased to 2.04 eV for film annealed at 1000 °C. This is because of increase

in grain size with increase in annealing temperature upto 1000 °C. This unfold the potentiality of band gap tuning by substitution in spinel ferrites.

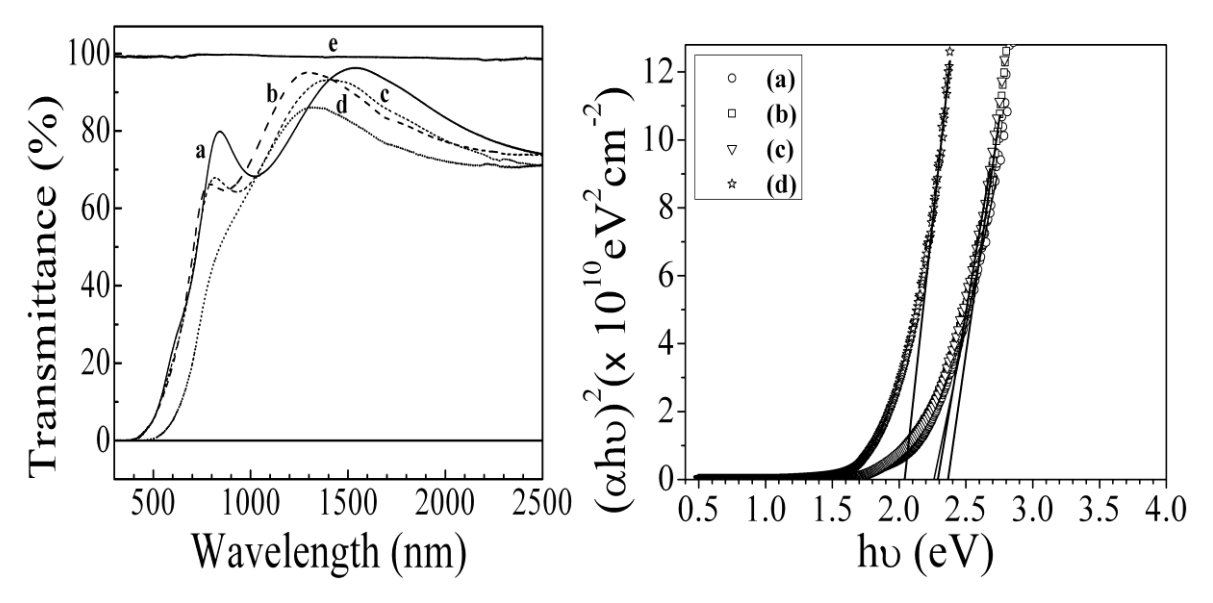


Fig. 4.38 Optical transmittance spectra $Co_{0.75}Cu_{0.25}Fe_2O_4$ films measured at RT; for as-deposited (a), annealed at 600 °C (b), annealed at 800 °C (c), annealed at 1000 °C (d), and empty quartz substrate (e).

Fig. 4.39 (right) Plots of $(\alpha h v)^2$ versus (h v) for annealed Co_{0.75}Cu_{0.25}Fe₂O₄ thin films; for as-deposited (a), annealed at 600 °C (b), annealed at 800 °C (c), annealed at 1000 °C (d).

The estimated E_g value for the annealed $Co_{0.75}Cu_{0.25}Fe_2O_4$ thin film deposited at 40 W annealed at 800 °C (320 nm) is 2.29 eV, which is smaller than 2.6 eV reported by Erdem et al. [11] for a 100-nm-thick $CoFe_2O_4$ thin film deposited by spin coating. The estimated direct band gap values for annealed films are smaller than reported value of 2.54 eV by Sultan et al. [24] for a 300-nm-thick $ZnFe_2O_4$ film deposited by RF magnetron sputtering.

4.4.2.7 Conclusions

The saturation magnetization (M_s) of Co_{0.75}Cu_{0.25}Fe₂O₄ films increased with increase of annealing temperature due to increase of average grain size. High saturation magnetization (M_s) of 250 emu/cm³ is obtained after annealing films at 1000 °C with H_c of 1500 G. High coercivity H_c of 2670 G is obtained after annealing films at 800 °C. The decrease in M_s after heat treatment at 800 °C is due to decrease in particle size as observed from TEM. The optical band gap first increases when films were annealed at 600 °C followed by a decreasing trend with a further increase in annealing temperature upto 1000 °C beause of increase in grain size.

4.4.3. Effect of RF power

4.4.3.1 Film Thickness

Thickness of the as-deposited films is estimated by using profilometer. The thickness of the film increases as the RF power increases. This is due to the increase in deposition rate with the increase in RF power [25]. A slight decrease in thickness of film was observed after annealing. This may be due to increase in packing density of the films on annealing. Film thickness for various as-grown films and films annealed at 800 °C for 3 h (Fig. 4.43) is shown in Table 4.14.

4.4.3.2 Structural Analysis

The grazing incident angle X-ray diffraction patterns of $Co_{0.75}Cu_{0.25}Fe_2O_4$ films measured on the as-sputtered films as well as on the annealed films are shown in Fig. 4.40. The X-ray peaks of the films are inaccordance with those of a typical crystalline Co-ferrite, with spinel structure without a preferred orientation. The as-deposited film grown at 30 W are amorphous, while those deposited at 40 W, 50 W and 60 W show a certain degree of crystallinity. After annealing at 800 °C for 3 h, the major peaks corresponding to cobalt-ferrite emerge, indicating the improvement in crystallization. The XRD line width and crystallite size are connected through the Scherrer equation [1] given by $D = 0.9\lambda/(\beta \cos \theta)$ where, D is crystallite size in Å, λ is the wavelength of X-rays, β is the full width of the diffraction lineat half the maximum intensity and θ is the diffraction angle. The size of crystallites was calculated using the full width at half maximum (FWHM) of the (3 1 1) peak and the values are presented in Table 4.12. The calculated lattice parameter of the films varies between 8.488 and 8.531Å for as-grown films and between 8.34 and 8.363 Å for annealed films.

Table 4.12 FESEM, TEM, and structural properties of as-deposited and annealed Co_{0.75}Cu_{0.25}Fe₂O₄ thin films deposited at 6 mTorr argon gas pressure using various RF power

Sample (RF power)	Lattice constant 'a' (± 0.002Å)		Crystallite si (± 2 nm) XRD	'			Particle size (± 2nm) TEM	
	As-grown	Annealed	As-grown	Annealed	As-grown	Annealed	Annealed	
30 W	8.531	8.340	6	30.7	22	42	40	
40 W	8.526	8.327	11	32	40	50	67	
50 W	8.508	8.352	16	30	32	42	49	
60 W	8.488	8.363	17	36	26	54	52	

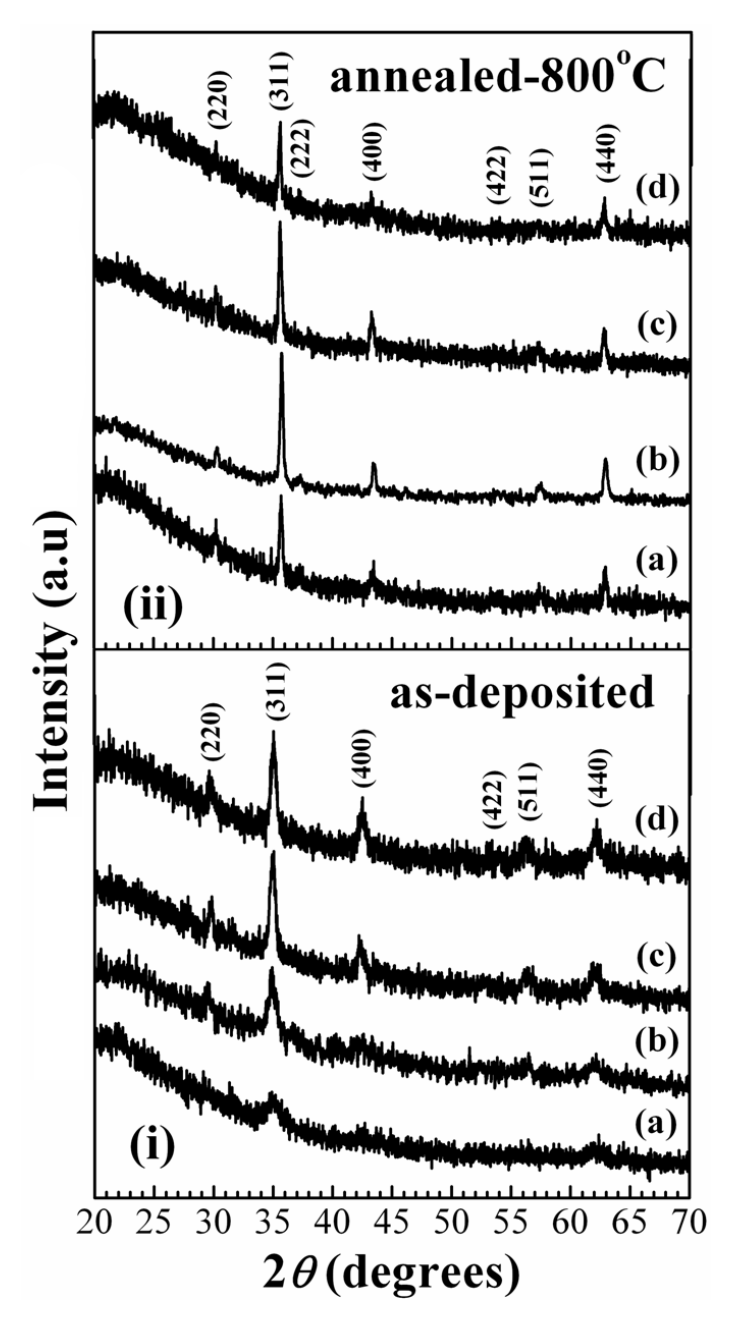


Fig. 4.40 The XRD patterns of the $Co_{0.75}Cu_{0.25}Fe_2O_4$ thin films grown at **a** 30, **b** 40, **c** 50, and **d** 60 W RF powers, for as-deposited (i), annealed at 800 °C (ii).

4.4.3.3 Surface morphology

Field emission scanning electron microscopy micrographs of Co_{0.75}Cu_{0.25}Fe₂O₄ films are shown in Figs. 4.41(for as-deposited) and 4.42(annealed). The grain-size distribution was determined from the histogram obtained by measuring the size of around 100–200 individual grains using imageJ software. For the as-deposited films, the average grain size is 22, 30, 32, and 26 nm for

films deposited using 30, 40, 50 and 60 W, respectively. For as-grown films, the histogram of sample deposited using 30 W shows that the maximum size distribution is in the range of 30–40 nm, for films deposited using 40, 50 and 60 W, it is in the range of 20–30 nm, respectively. For annealed films, the histogram of film deposited using 30 W shows that the maximum size distribution is in the range of 20–40 nm, film deposited using 40 W, 40–80 nm, for film deposited using 50 W, 30–40 nm and film deposited using 60 W, it is in the range of 40–60 nm, respectively. The average values of grain size are listed in Table 4.12. All the samples (Fig. 4.42) have polycrystalline structure. The cross-sectional FESEM images of annealed films are shown in Fig. 4.43.

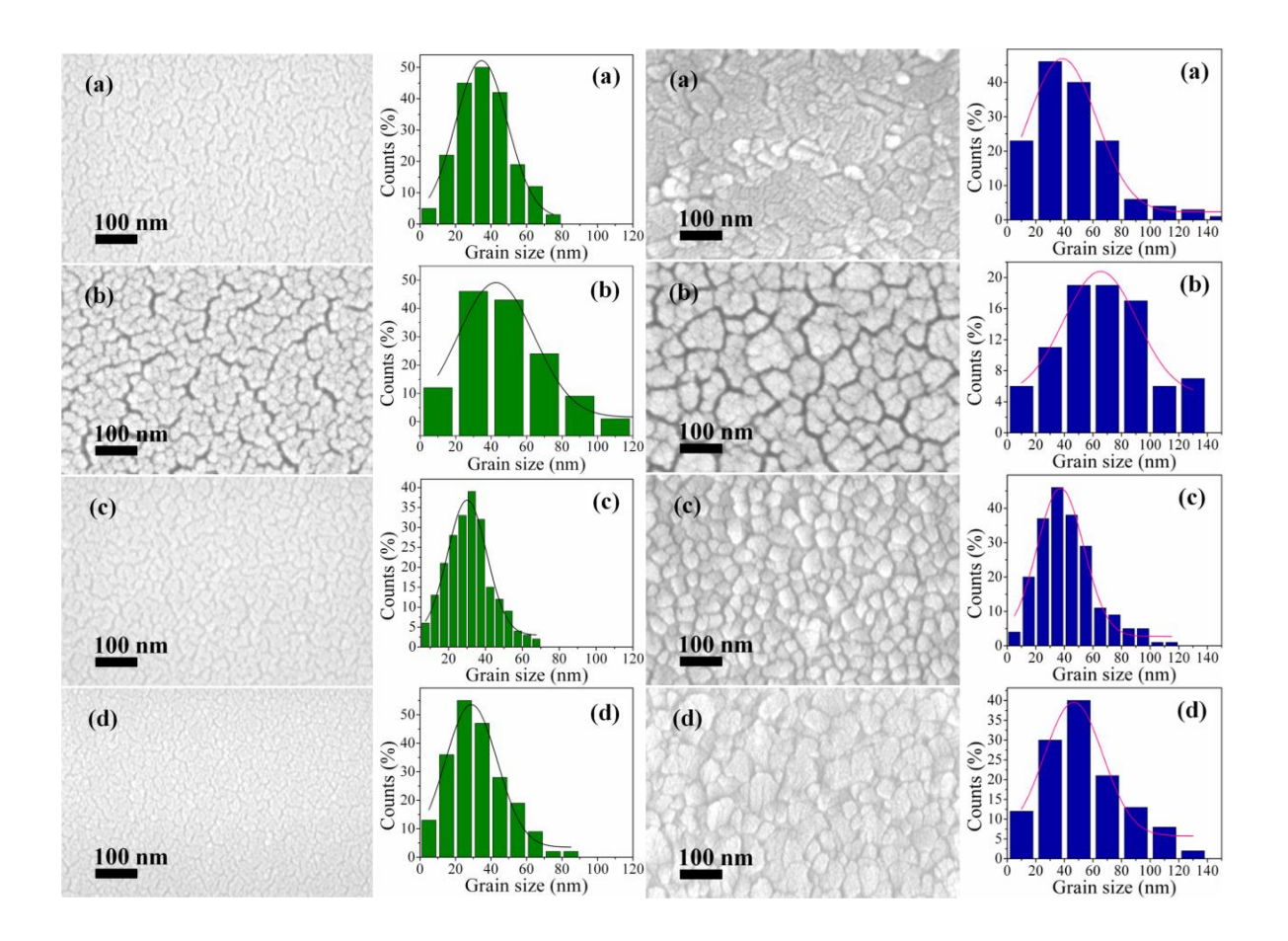


Fig. 4.41 FESEM images of the Co_{0.75}Cu_{0.25}Fe₂O₄ thin films (as-deposited) grown at **a** 30, **b** 40, **c** 50, and **d** 60 W RF powers and cluster-size distribution.

Fig. 4.42 (right) FESEM images of the annealed Co_{0.75}Cu_{0.25}Fe₂O₄ thin films grown at **a** 30, **b** 40, **c** 50, and **d** 60 W RF powers and cluster-size distribution

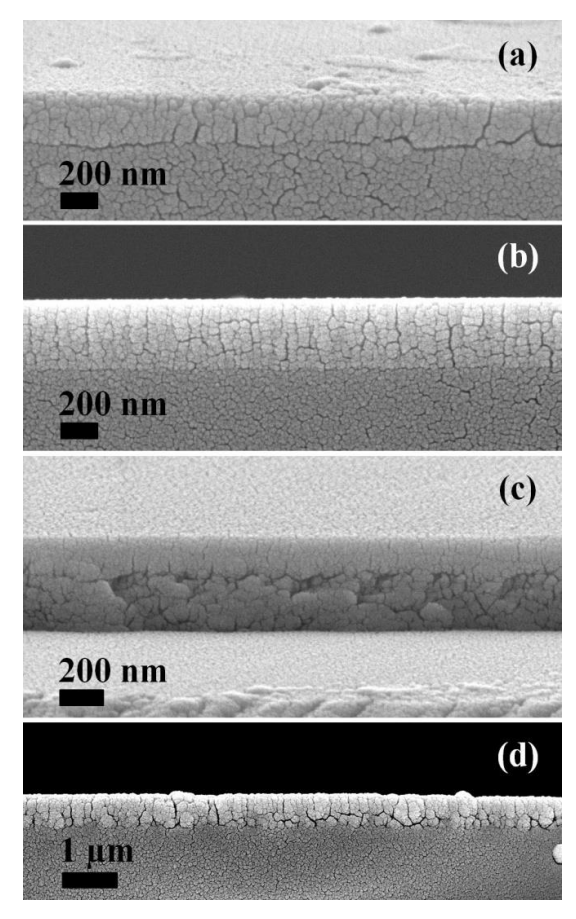


Fig. 4.43 FESEM cross-sectional images of the annealed Co_{0.75}Cu_{0.25}Fe₂O₄ thin films grown at a 30, b 40, c 50, and d 60 W RF powers

4.4.3.4 Transmission electron microscopy

Transmission electron microscopy (TEM) and high resolution microscopy have been used to confirm the nanocrystalline nature of the films. Figure 4.44 shows the TEM images of the annealed films. The average particle sizes of films deposited using 30, 40, 50 and 60 W are 40, 67, 49, and 52 nm, respectively (Table 4.12). These values are in agreement with the grin size estimated from FESEM images.

The selected area diffraction (SAD) patterns are shown in Fig. 4.45. The diameter of the diffraction ring in the SAD pattern is proportional to $\sqrt{(h^2 + k^2 + l^2)}$ where (hkl) are the Miller indices of the planes corresponding to the ring. Counting the rings from the center 1st, 2nd, 3rd, 4th, and 5th rings correspond to (2 2 0), (3 1 1), (4 0 0), (422) and (4 4 0) planes, respectively. The high-resolution TEM image of the annealed films in Fig. 4.46 show the lattice fringes of

the nanocrystallites. These micrographs show details of the interplanar distance corresponding to different planes in spinel structure.

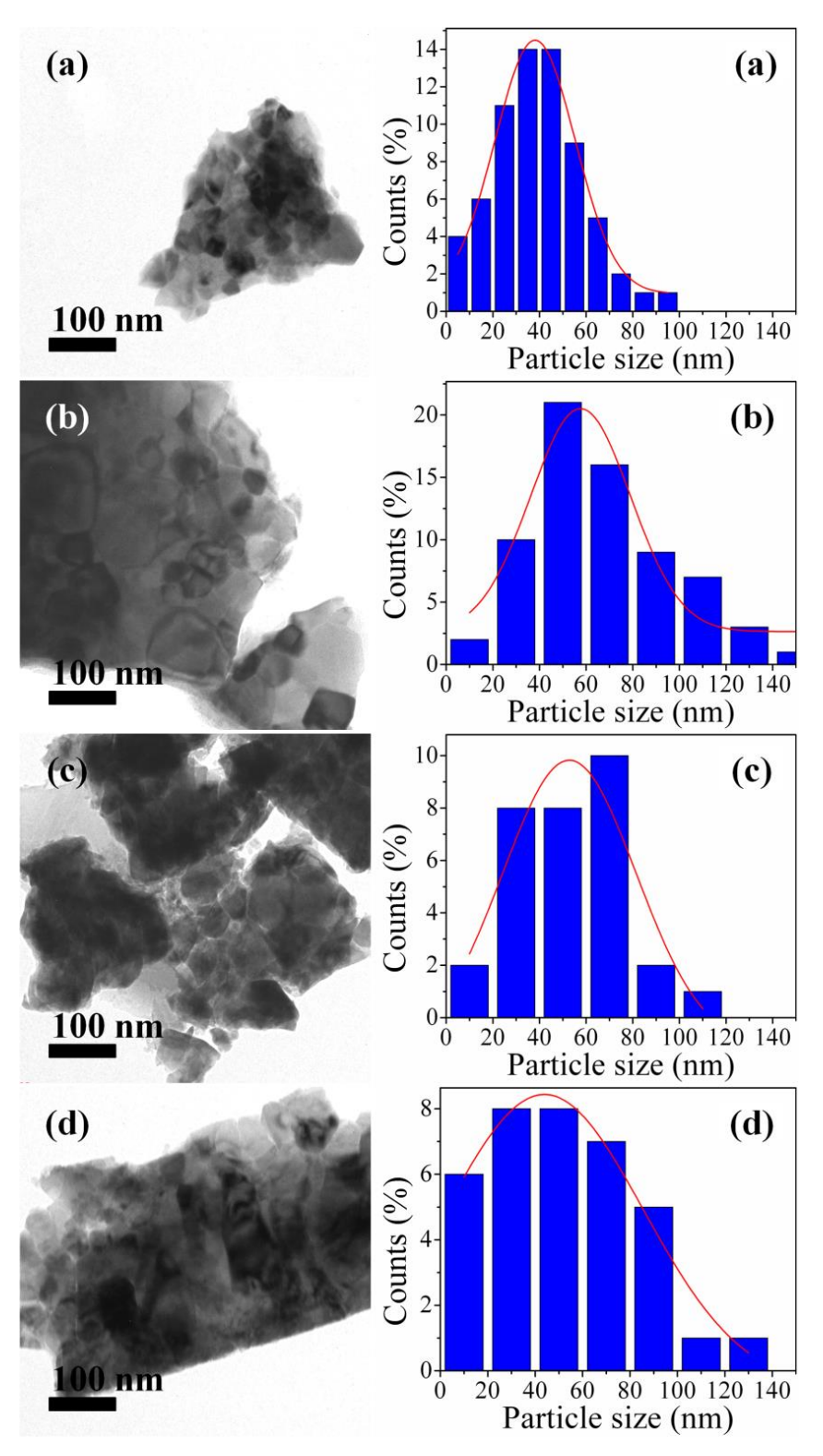


Fig. 4.44 TEM microstructure of the annealed Co_{0.75}Cu_{0.25}Fe₂O₄ thin films grown at a 30, b 40, c 50, and d 60 W RF powers.

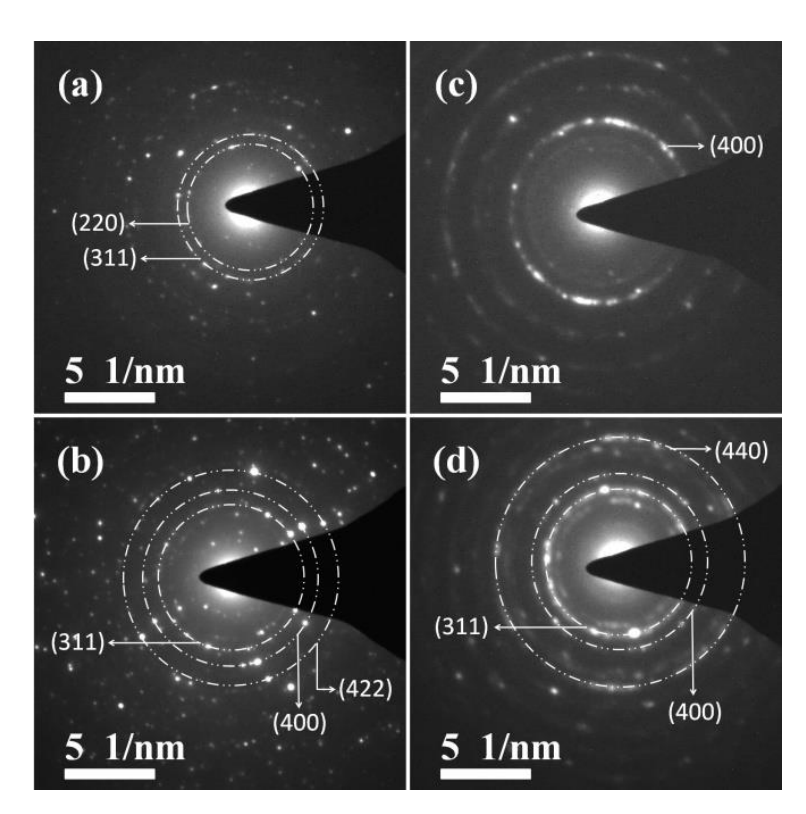


Fig. 4.45 Selected area diffractions of the annealed $Co_{0.75}Cu_{0.25}Fe_2O_4$ thin films grown at **a** 30, **b** 40, **c** 50, and **d** 60 W RF powers

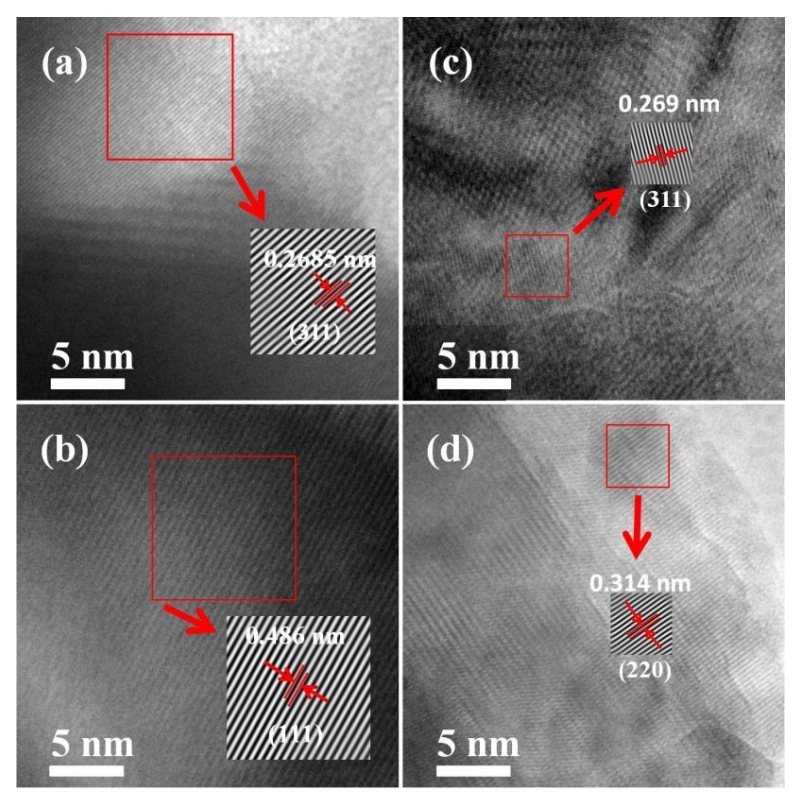


Fig. 4.46 HRTEM micrographs of the annealed Co_{0.75}Cu_{0.25}Fe₂O₄ thin films grown at **a** 30, **b** 40, **c** 50, and **d** 60 W RF powers.

4.4.3.5 Magnetic Properties

Figure 4.47 shows the magnetization hysteresis loops of as-deposited, and annealed $Co_{0.75}Cu_{0.25}Fe_2O_4$ thin films measured at room temperature. The loops were obtained with the magnetic field applied parallel to the plane of the film and corrected by subtracting the diamagnetic contribution from the substrate. Since the magnetization does not saturate up to a field of 2 T, so magnetization at the highest field value are compared for different films. The magnetization at 2 T (M_s), remanent magnetization (M_R), and coercivity (H_c) of the films are tabulated in Table 4.13. For as-deposited and annealed films M_s and M_R increase with increasing RF power because of increase in grain size, while coercivity (H_c) increased from 2.75 kOe to 3.45 kOe as the RF power increases from 30 to 40 W it decreases thereafter with further increase in RF power up to 60 W. Film deposited at 30 W RF power is amorphous. The high coercivity of the film grown at 40 W is due to increase in crystalline nature of the film with crystallite size of 11 nm.

After annealing, the M_s values of the film increased significantly with increasing film thickness. While H_c first increased as the RF power increased from 30 to 50 W followed by a decrease with further increase in RF power up to 60 W. It is related to the decrease in grain size of annealed film grown at 50 W followed by an increase in grain size as RF power is increased to 60 W (Fig. 4.44).

Table 4.13 Magnetic parameters of Co_{0.75}Cu_{0.25}Fe₂O₄ thin films grown at 6 mTorr argon gas pressure using various RF powers

Sample (RF power)	For as-de	posited film	S		For annealed films			
	M _r (emu/cc)	M s (emu/cc)	H_c (Oe)	M_R/M_S	M _r (emu/cc)	M s (emu/cc)	H _c (Oe)	M_R/M_S
30 W	33	71	2753	0.465	34	129	2001	0.264
40 W	62	115	3450	0.539	68	174	3449	0.39
50 W	86	176	2993	0.488	97	243	3866	0.399
60 W	112	205	2696	0.544	88	300	1934	0.293

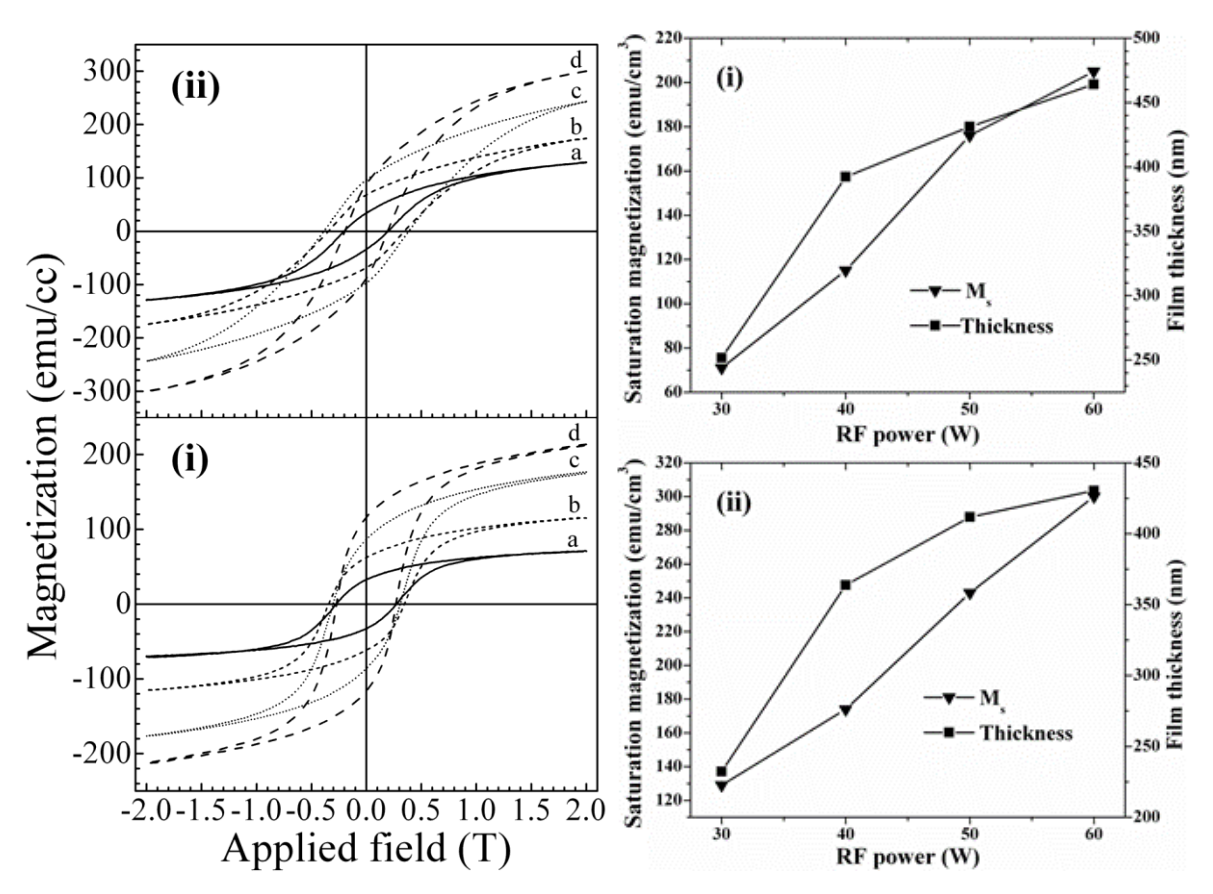


Fig. 4.47 The magnetization hysteresis loops of Co_{0.75}Cu_{0.25}Fe₂O₄ thin films grown at **a** 30, **b** 40, **c** 50, and **d** 60 W RF powers for as-deposited (i), annealed at 800 °C (ii).

Fig. 4.48 (right) Dependence of magnetization (M_s) at 2 T and film thickness of as-grown (i) and annealed (ii) $Co_{0.75}Cu_{0.25}Fe_2O_4$ thin films deposited at various RF powers.

Figure 4.48 shows the dependence of M_s at 2 T on RF power for as-deposited and annealed films. The increase in M_s of the annealed films can be explained in two ways. It can be due to the change in microstructure of the film as RF power increases. The film deposited at 30 W is porous with loose packing of grains (Fig. 4.42), showing an M_s value of 129 emu/cm³. The film grown at 40 W, show bigger dense grains (Fig. 4.44) leading to an increase in M_s value to 174 emu/cm³. As the RF power is increased to 50 W, grains are tightly connected leading to increase in M_s to 243 emu/cm³. The film deposited at an RF power of 60 W exhibits highly dense large grains and hence the M_s value is further increased to 300 emu/cm³ which is slightly greater than the bulk value. The variation in M_s can be due to changes in cation distribution among the A and B sites due to heat treatment. The increase in M_s value of the film grown at 60 W could be due to the occupation of Co^{2+} ions on tetrahedral sites forcing Fe^{3+} ions to octahedral sites

resulting in increase in net magnetic moment. Furthermore, any occupancy of Cu^+ (0 μ_B) on tetrahedral site may lead to the increase in M_s . The increase in M_s of films deposited using 30, 40 and 50 W could be related to the small increase in disorder in the distribution of Fe^{3+} and Co^{2+} among A and B sites with increase in RF power. The 410-nm annealed $Co_{0.75}Cu_{0.25}Fe_2O_4$ film deposited using 50 W RF power has a H_c of 3866 Oe and M_s of 243 emu/cm³, at room temperature (see Fig. 4.47; Table 4.13). Sartale et al. [26] reported a H_c of 0.2–0.27 kOe and M_s of 211–323 emu/cm³, measured at RT for cobalt ferrite films prepared by electrochemical deposition.

4.4.3.6 Optical Properties

The optical transmittance spectra in the wavelength range of 300–2500 nm for Co_{0.75}Cu_{0.25}Fe₂O₄ thin films grown at various RF powers for the as-deposited Co_{0.75}Cu_{0.25}Fe₂O₄ thin films and annealed films are shown in Fig. 4.49.

The estimated values of energy band gap for the as-deposited and annealed films are listed in Table 4.14. The error in the optical band gap measurement by linear curve fitting is ± 0.02 eV. The band gap variation for films deposited at 30–40 W of RF power is within this measurement error limits. For as-deposited films the optical band gap decreased with increasing RF power because of increase in grain size as the RF power increases from 30 to 50 W. The increase in the optical band gap of $Co_{0.75}Cu_{0.25}Fe_2O_4$ thin films by annealing may be due to the removal of defect levels from the films. The optical band gap for annealed films shows a slight increase from 2.14 to 2.16 eV as as the RF power increases from 30 to 40 W and then decreases with further increase in RF power up to 60 W.

Table 4.14 Optical properties of Co_{0.75}Cu_{0.25}Fe₂O₄ thin films deposited at 6 mTorr argon gas pressure using various RF powers

Sample (RF power, W)	Film thickr (± 4 nm)	ness	Band gap $E_g(\pm 0.01 eV)$		
	As-grown	Annealed	As-grown	Annealed	
	Profiler	FESEM	_		
30	252	232	2.07	2.14	
40	392	364	2.06	2.16	
50	431	412	1.90	2.01	
60	464	430	-	1.93	

This is attributed to the increase of grain boundaries in the film deposited at 40 W (364 nm), compared to the film (232 nm) deposited at 30 W. The decrease in band gap of the annealed films deposited at 50 and 60 W RF power is because of increase in grain size. The estimated E_g value for the annealed $Co_{0.75}Cu_{0.25}Fe_2O_4$ thin film deposited at 50 W (430 nm) is 2.01 eV, which is smaller than 2.6 eV reported by Erdem et al. [11] for a 100-nm-thick $CoFe_2O_4$ thin film deposited by spin coating. The estimated direct band gap values for annealed films are greater than those reported by Rao et al. [12].

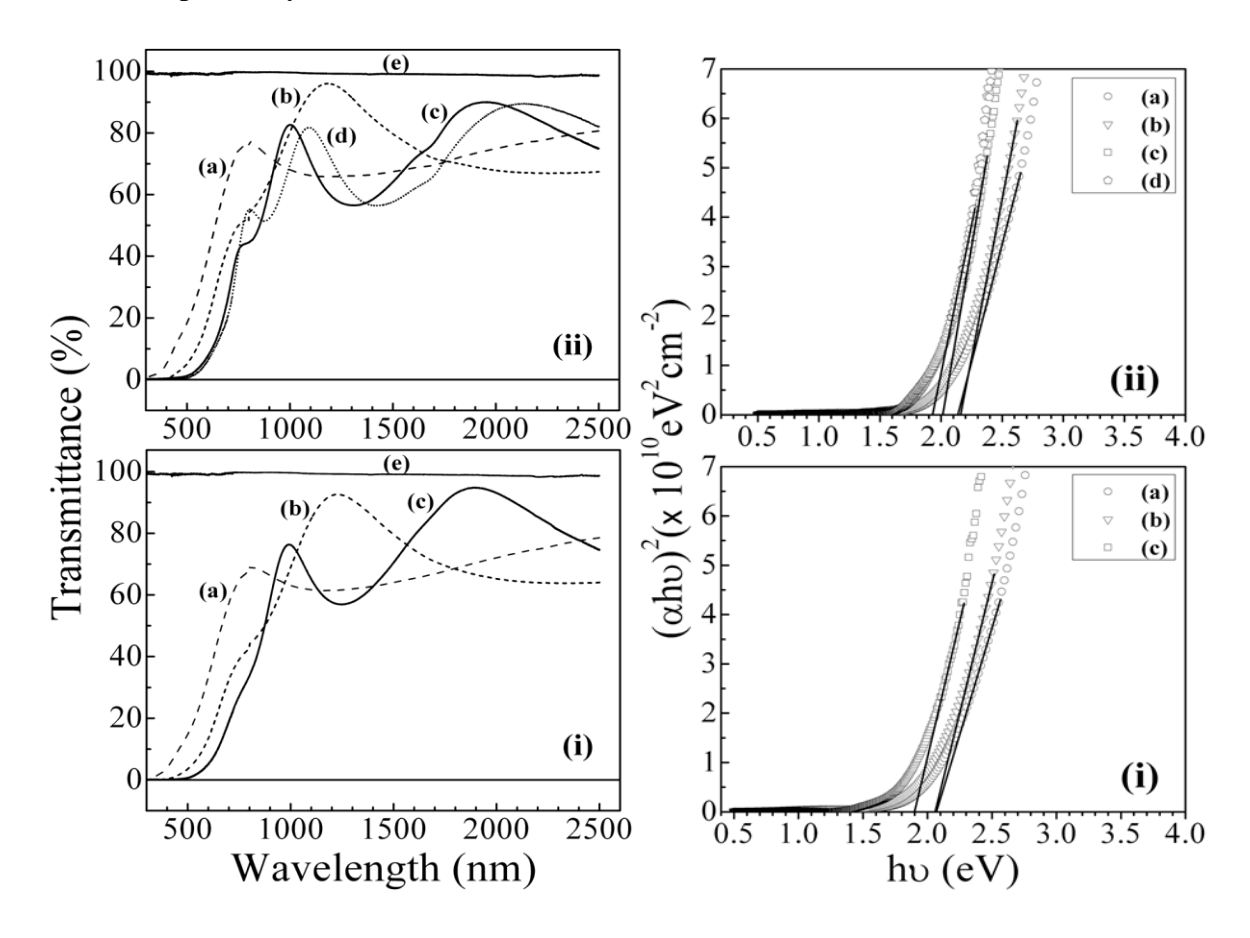


Fig. 4.49 (**left**) Optical transmittance spectra measured at RT of as-deposited (i), annealed (ii), $Co_{0.75}Cu_{0.25}Fe_2O_4$ thin films grown at **a** 30, **b** 40, **c** 50, and **d** 60 W RF powers and **e** empty quartz substrate.

Fig. 4.50 (**right**) Plots of $(\alpha h v)^2$ versus (hv) for as-deposited (i), annealed (ii), $Co_{0.75}Cu_{0.25}Fe_2O_4$ thin films grown at **a** 30, **b** 40, **c** 50, and **d** 60 W RF powers.

4.4.3.7 Conclusions

As-grown and annealed Co_{0.75}Cu_{0.25}Fe₂O₄ films exhibit increase in saturation nagnetization with increase of RF power from 30 W to 60 W because of increase in grain size. The average

grain size, particle size and crystallite size of the annealed films is found to increase first when RF power increased from 30 to 40 W and then decrease at 50 W followed by a small increase with further increase in RF power to at 60 W. The films are highly transparent above 800 nm wavelength. The optical band gap increases on annealing the films. The optical band gap first increases as the RF power increases from 30 at 40 W followed by a decreasing trend with a further increase in RF power. The annealed film deposited at 50 W exhibit high coercivity (3866 Oe) and M_s of 243 emu/cm³ which can be used for data storage applications.

4.4.4 Effect of Ar gas pressure

4.4.4.1 Film thickness

Thickness of the films is estimated by using surface stylus profilometer. The film thickness increased as argon gas pressure was increased from 5–10 mTorr. However, changing the argon gas pressure (5, 6, 8 and 10 mTorr), strongly affected the deposited film structure and properties. Film thickness for various films annealed at 800 °C for 3 h is shown in Table 4.17.

As described in Section 4.4.3, Co_{0.75}Cu_{0.25}Fe₂O₄ films were deposited on quartz substrates using various RF power 30, 40, 50 and 60 W at 6 mTorr argon gas pressure for a fixed duration of 3 hours. As a comparison study, we deposited three films using 40 W RF power at different argon gas pressure 5, 8, 10 mTorr, for 3 hours in the present study. To study the effect of argon gas pressure on structure, morphology, magnetic and optical properties of these films, the film deposited using 40 W RF power at 6 mTorr argon pressure for 3 h, of the previous Section 4.4.3 is also presented here. For comparison purpose once again we present here all the results such as XRD, TEM, FESEM, magnetic and optical data of the film deposited using 40 W RF power at 6 mTorr argon pressure for 3 h, which was presented in previous Section 4.4.3.

4.4.4.2 Structural Analysis

The grazing incidence X-ray diffraction spectrum measured on the as-deposited Co_{0.75}Cu_{0.25}Fe₂O₄ films as well as on the films annealed at 800 °C is shown in Fig. 4.51. All peaks are in accordance with those of a typical crystalline Co-ferrite, with spinel structure. The as-grown films are amorphous with (3 1 1) peak as the most intense. After post deposition annealing at 800 °C for 3 h, the major peaks height corresponding to cobalt ferrite emerge, indicating the improvement of crystallization. The size of crystallites was calculated using the full width at half maximum (FWHM) of the (3 1 1) peak and the values are presented in Table

4.15. The lattice constant 'a' was estimated for annealed samples and the values are presented in Table 4.15.

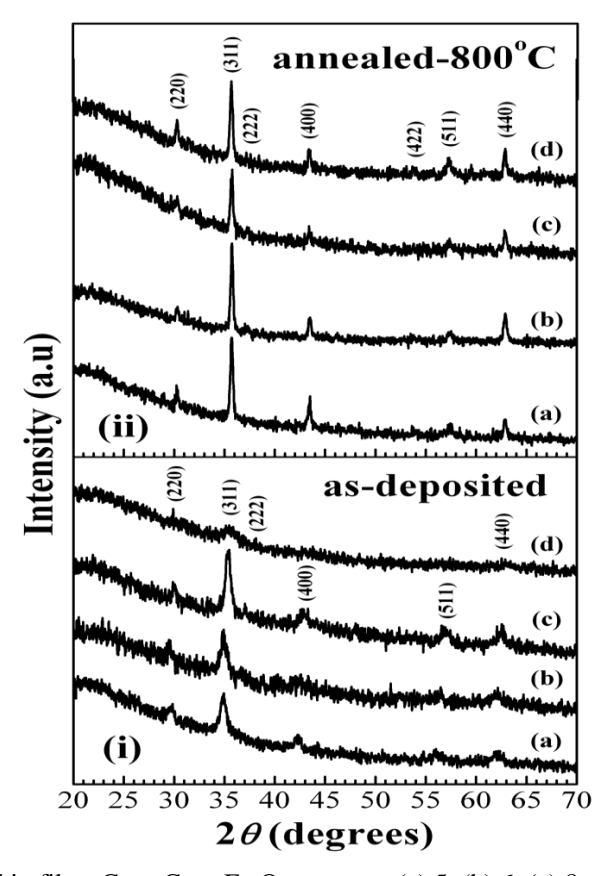


Fig. 4.51 XRD patterns of thin films $Co_{0.75}Cu_{0.25}Fe_2O_4$ grown at (a) 5, (b) 6, (c) 8 and (d) 10 mTorr of argon gas pressure: for (i) as-deposited and (ii) annealed at 800 °C.

Table 4.15 TEM, FESEM and structural properties of as-deposited and annealed Co_{0.75}Cu_{0.25}Fe₂O₄ thin films prepared at different argon gas pressure between 5-10 mTorr using 40 W RF power

Sample (argon pressure)	Lattice constant 'a' (±0.01Å)		Crystallite (± 2 nm)	size	Grain size (± 1nm) FESEM		Particle size (± 2 nm) TEM
	As-	Annealed	As-	Annealed	As-grown	Annealed	Annealed
	grown		grown				
5 mTorr	8.525	8.332	13	28.6	28	44	62
6	8.526	8.327	11	32	40	50	67
8	8.414	8.331	14	28.5	35	41	49
10	8.410	8.339	5	28	31	46	10

4.4.4.3 Surface morphology

Field emission scanning electron microscopy micrographs of the Co_{0.75}Cu_{0.25}Fe₂O₄ films are shown in Figs. 4.52(for as-deposited) and 4.53(annealed). FESEM images of annealed

Co_{0.75}Cu_{0.25}Fe₂O₄ thin films deposited show spherical morphology. The estimated average grain size of the as-deposited films is 28, 30, 35 and 31 nm, respectively, for films grown at 5, 6, 8 and 10 mTorr argon pressure. Similarly, the average grain size changes as 44–50–41–46 nm for the annealed films as the argon gas pressure increases.

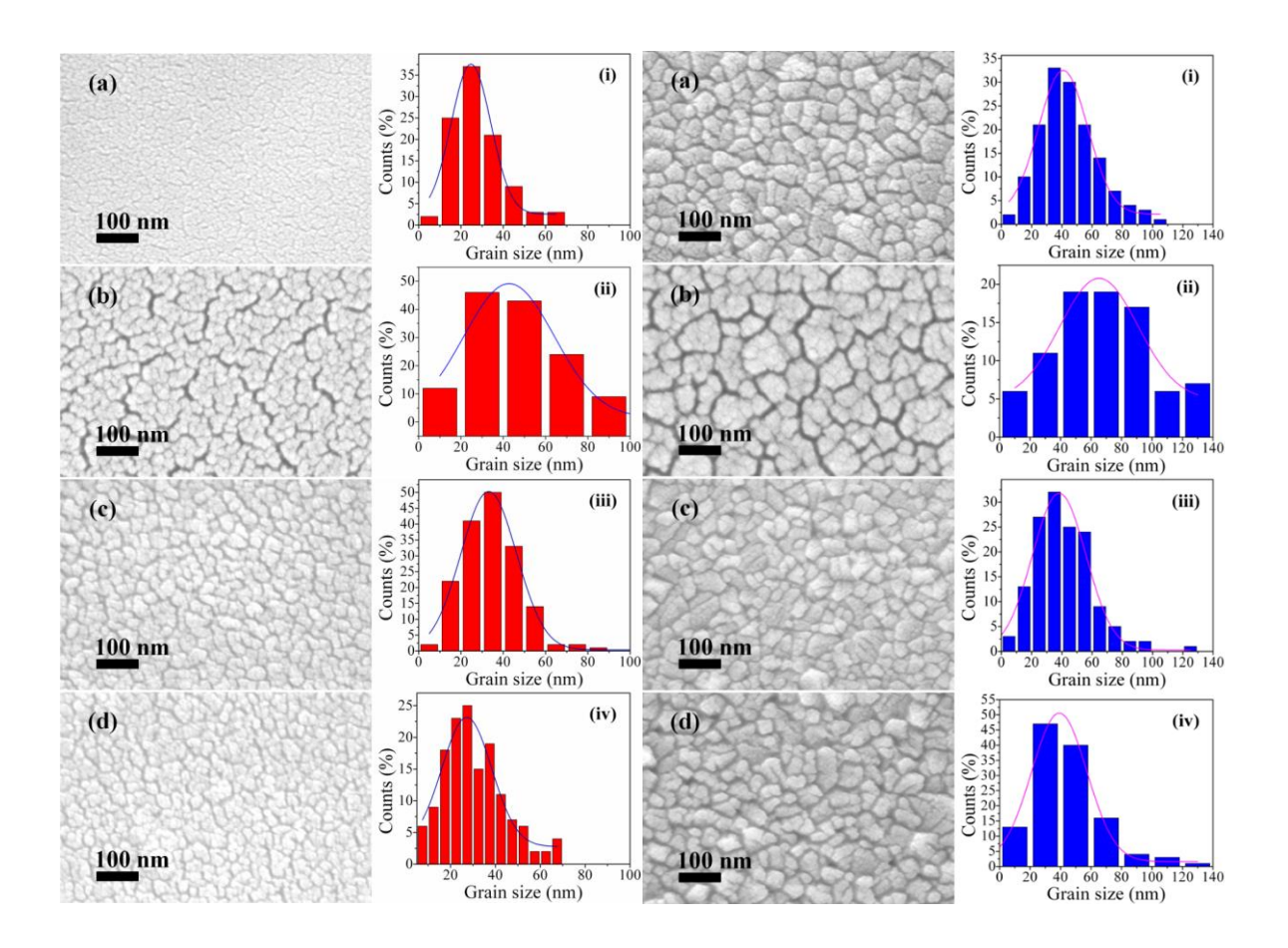


Fig. 4.52 FESEM images of the as-sputtered thin films of $Co_{0.75}Cu_{0.25}Fe_2O_4$ grown at (a) 5, (b) 6, (c) 8 and (d) 10 mTorr of argon gas pressure.

Fig. 4.53 (**right**) FESEM images of annealed thin films of Co_{0.75}Cu_{0.25}Fe₂O₄ grown at (a) 5, (b) 6, (c) 8 and (d) 10 mTorr of argon gas pressure.

For the annealed films, the histogram of sample grown at 5 mTorr shows that the maximum size distribution is in the range of 30–50 nm, for film grown at 6 mTorr, 40–80 nm, for film grown at 8 mTorr, 30–40 and for film grown at 10 mTorr, it is in the range of 20–40 nm. The average values of grain size were given in Table 4.15. The agglomeration in the sample may be due to

the effect of post deposition annealing, giving the grains enough time to coalesce. The cross-sectional FESEM images of annealed films are shown in Fig. 4.54.

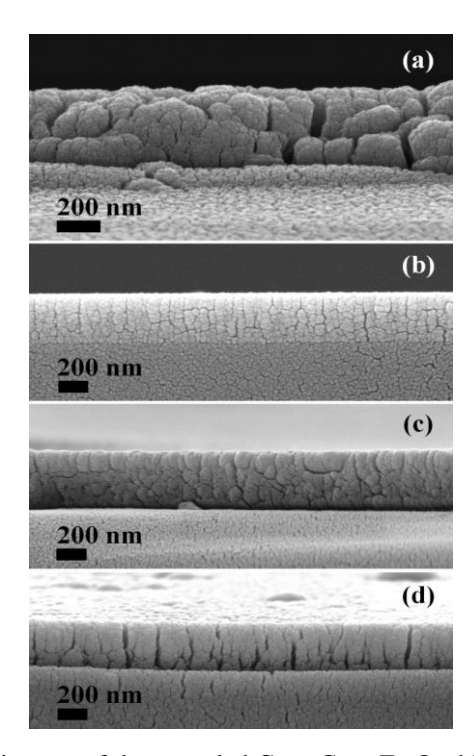


Fig. 4.54 FESEM cross-sectional images of the annealed $Co_{0.75}Cu_{0.25}Fe_2O_4$ thin films grown at (a) 5, (b) 6, (c) 8 and (d) 10 mTorr of argon gas pressure.

4.4.4.4 Transmission electron microscopy

Figure 4.55 shows TEM images and particle size distribution of annealed films. TEM images confirm the particle sizes of irregular shapes. From the TEM images, we measured the mean size of particles. The mean size of the films deposited at 5, 6, 8 and 10 mTorr argon pressures are 62, 67, 49 and 10 nm, respectively. These values are larger than the particle size estimated from XRD data using Scherrer formula. Figure 4.56 depicts selected area electron diffraction (SAD) pattern of the annealed films. SAD patterns confirm the polycrystalline nature of Co_{0.75}Cu_{0.25}Fe₂O₄ thin films. Determined radius of different rings show the formation of different lattice planes.

The high-resolution TEM image of the annealed films in Fig. 4.57 show the lattice fringes of the nanocrystallites. These micrographs show details of the interplanar distance corresponding to different planes in spinel structure.

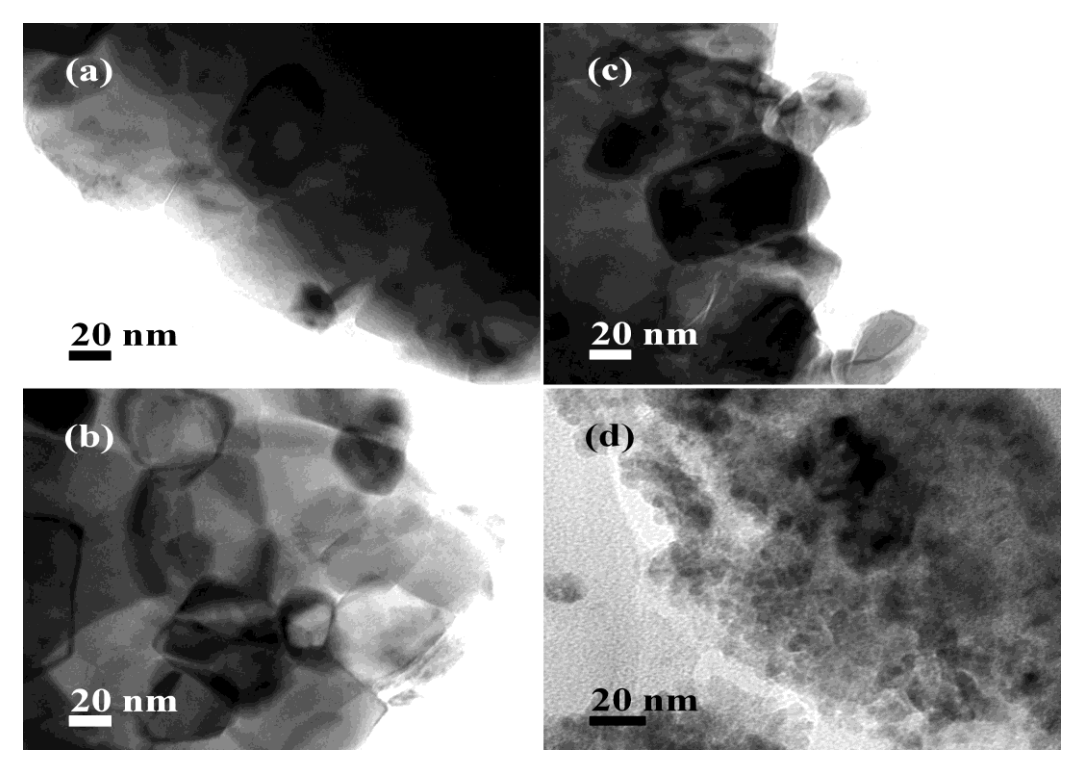


Fig. 4.55 TEM micrographs of annealed $Co_{0.75}Cu_{0.25}Fe_2O_4$ thin films grown at (a) 5, (b) 6, (c) 8 and (d) 10 mTorr of argon gas pressure.

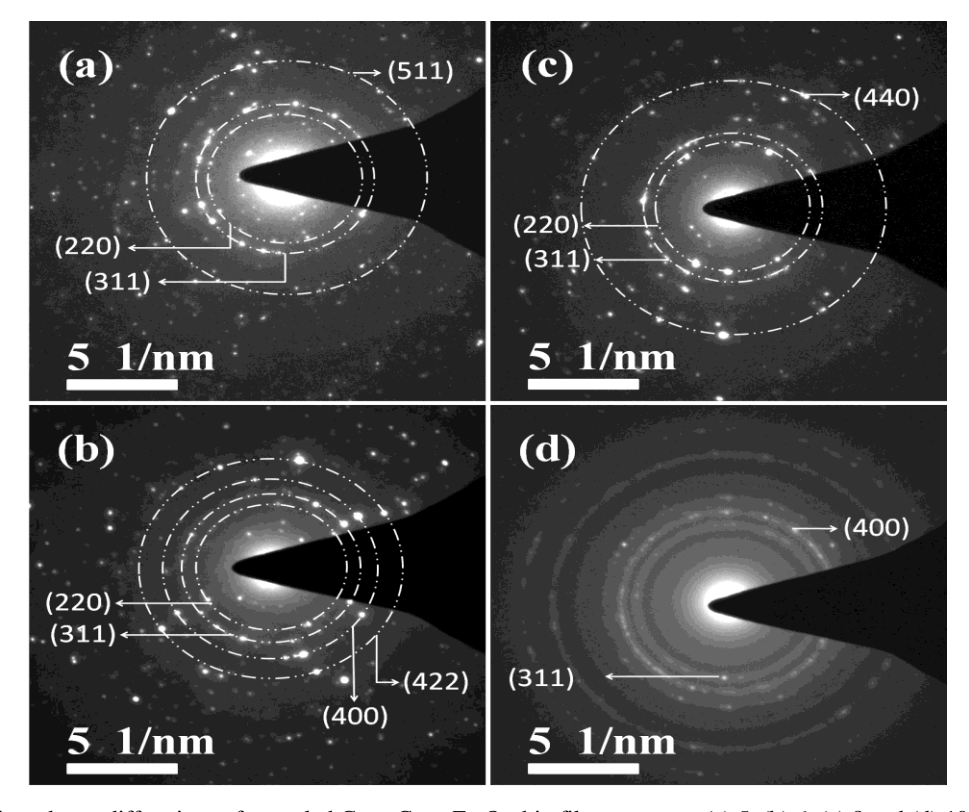


Fig. 4.56 Selected area diffractions of annealed $Co_{0.75}Cu_{0.25}Fe_2O_4$ thin films grown at (a) 5, (b) 6, (c) 8 and (d) 10 mTorr of Ar gas pressure.

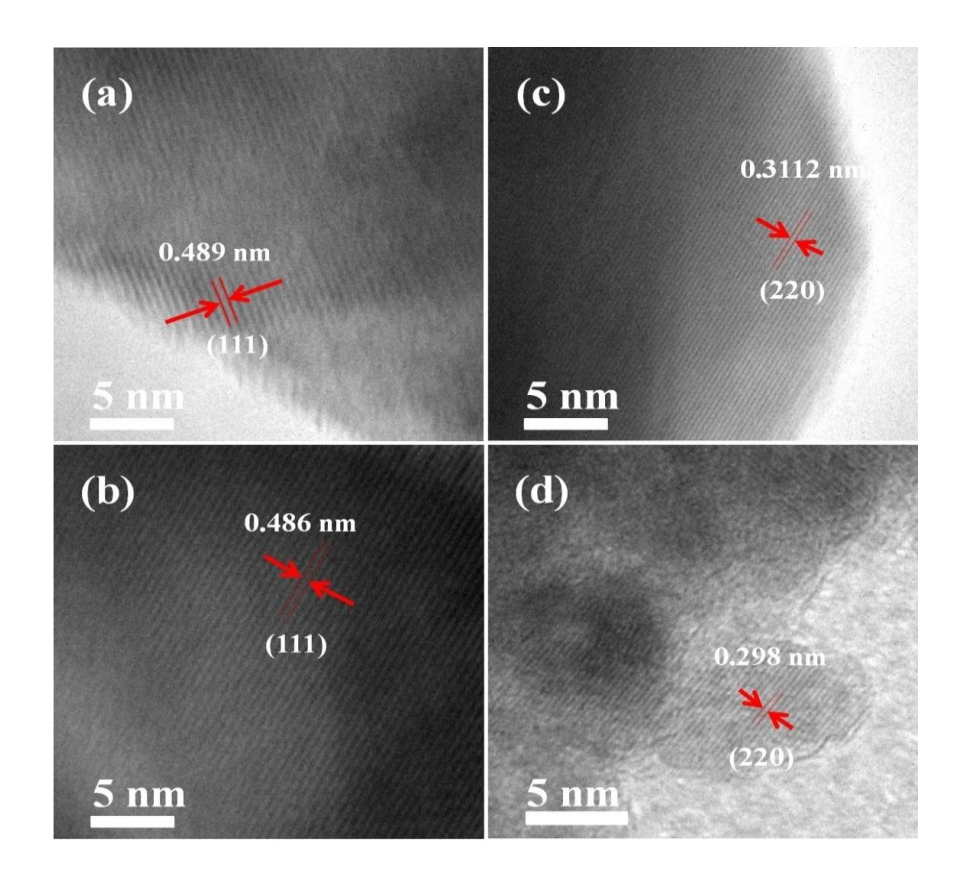


Fig. 4.57 HRTEM images of annealed $Co_{0.75}Cu_{0.25}Fe_2O_4$ thin films grown at (a) 5, (b) 6, (c) 8 and (d) 10 mTorr of Ar gas pressure.

4.4.4.5 Magnetic properties

Figure 4.58 shows the magnetization hysteresis loops of as-deposited (Fig.4.58 (i)) and annealed (Fig.4.58 (ii)) thin films measured at room temperature. The values of coercivity, saturation magnetization and remanent magnetization were increased significantly after annealed at 800 °C. The loops were obtained with the magnetic field applied parallel to the plane of the film and corrected by subtracting the diamagnetic contribution from the substrate. Since the magnetization does not saturate up to a field of 2 T, so magnetization at the highest field value are compared for different films. The magnetic properties of these films are shown in Table 4.16. From Table 4.16 we observe that, the saturation magnetization (M_s), remanence (M_r) and coercivity (H_c) decreases significantly with argon gas pressure for as-deposited films. The decrease in H_c with increasing argon pressure (Table 4.15), in as-grown $Co_{0.75}Cu_{0.25}Fe_2O_4$ films probably is related to the increase of grain size.

For as-deposited films, films deposited at 5 mTorr shows a high coercivity H_c (3716 Oe) and low saturation magnetization (M_s) (104 emu/cc) compared to that of bulk Co_{0.75}Cu_{0.25}Fe₂O₄ target. The low saturation magnetization (M_s) (104 emu/cc) is due to reduction in superexchange interaction between the nearest neighbor A-B ions. Decrease in M_s with increase in argon pressure is related to the decrease in superexchange because of the occupancy of less magnetic Cu2+ ion on B-sites resulting in a small difference between magnetizations of A and B sublattices. It is related to the increase in amorphous nature as pressure is increased. After annealing, the H_c and M_s values of the film increase depending on film thickness. The present study shows that the H_c and M_s values strongly depend on thickness and microstructure of the film after annealing at 800 °C for 3 h. The increase in M_s of the annealed films can be explained in two ways. It can be due to the change in microstructure of the film as argon pressure increases. The film deposited at 5 mTorr exhibit loosely connected grains (Fig. 4.53), showing an M_s value of 137 emu/cm³. For annealed film grown at 6 mTorr, grain size increases leading to an increase in M_s value to 174 emu/cm³. As the argon gas pressure is increased to 8 mTorr, grain size decreased leading to a decrease in M_s to 135 emu/cm³. The film deposited at argon pressure of 10 mTorr exhibits very small particles (Fig. 4.55 (d)) and hence the M_s value is further reduced to 120 emu/cm³. The variation in M_s can be due to changes in cation distribution among the A and B sites due to heat treatment. The increase in M_s value of the film grown at 6 mTorr could be due to the disorder in the distribution of Fe³⁺ and Co²⁺ among A and B sites compared with a perfectly ordered inverse spinel structure. The decrease in M_s of films deposited at 8 and 10 mTorr argon pressure could be related to the increase in cation ordering among A and B sites. Our M_s value 174 emu/cm³ for 392 nm $Co_{0.75}Cu_{0.25}Fe_2O_4$ film deposited at 6 mTorr with H_c of 3448 Oe is greater than the reported value. Horng et al. [27] reported M_s of 121 emu/cm³ at RT for 120-nm-thick cobalt ferrite films grown at 300 °C using oxygen-plasma-assisted molecularbeam epitaxy.

Table 4.16 Magnetic parameters of as-deposited and annealed Co_{0.75}Cu_{0.25}Fe₂O₄ thin films deposited at various argon pressures between 5-10 mTorr using 40 W RF power

Sample (argon pressure)	For as-depo	osited films	For annealed films					
	M _r (emu/cc)	M _s (emu/cc)	H_c (Oe)	M_R/M_S	M _r (emu/cc)	M _s (emu/cc)	H_c (Oe)	M_R/M_S
5 mTorr	53	104	3716	0.50	60	137	2966	0.44
6	62	115	3445	0.54	68	174	3448	0.39
8	17	86	549	0.19	47	135	2658	0.35
10	4	52	137	0.08	50	120	2540	0.41

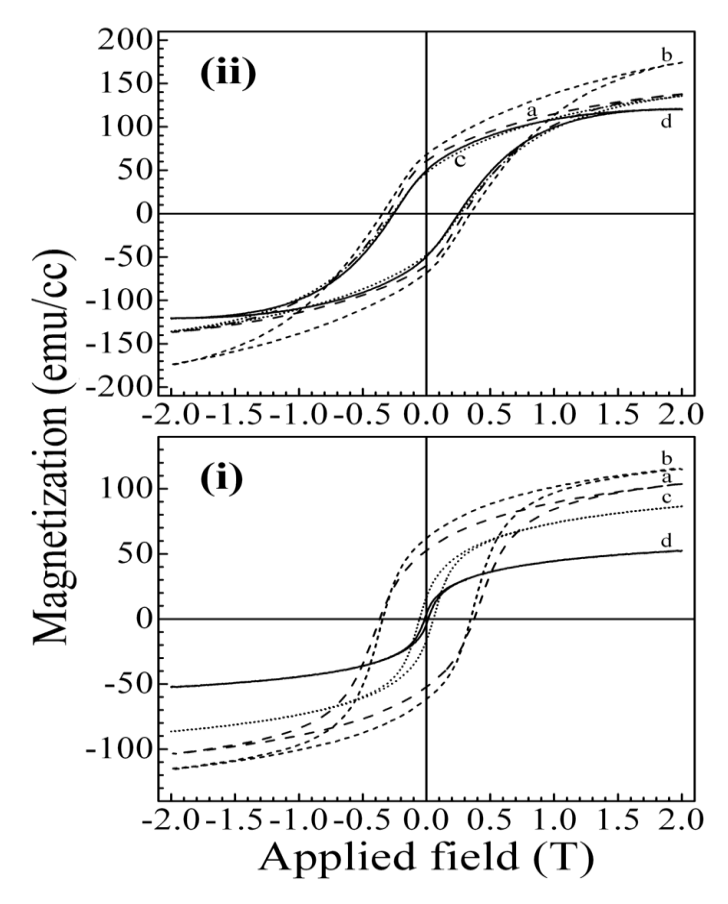


Fig. 4.58 The magnetization hysteresis loops of Co_{0.75}Cu_{0.25}Fe₂O₄ thin films grown at (a) 5, (b) 6, (c) 8 and (d) 10 mTorr of Ar gas pressures for as-deposited (i), annealed at 800 °C (ii).

4.4.4.6 Optical properties

On an average as-deposited films exhibit over 60 % transmittance in visible region 95 % in NIR region. The absorption edge of the as-deposited films is between 850 and 950 nm. For the annealed films the absorption edge shifts toward lower wavelength with a remarkable increase in transmittance (>10%). In the medium absorption region (λ <700 nm), the transmittance spectra of the annealed films are slightly shifted to shorter-wavelength (blue-shift) as compared with the as-deposited films.

The thickness of annealed films measured by FESEM cross-sections and surface stylus profilometer are listed in Table 4.17. The estimated values of energy band gap for the asdeposited and annealed films are listed in Table 4.17. The optical band gap for as-deposited films shows a slight increase from 2.13 to 2.06 eV as the argon pressure increases from 5 to 6 mTorr, increased slightly at 8 mTorr and then decreased with further increase in argon pressure up to 10 mTorr. Similarly, for the post deposition annealed films, the obtained optical band gap

values are 2.17, 2.16, 2.17 and 2.14 eV for films deposited under different argon gas pressure of 5, 6, 8 and 10 mTorr, respectively. The error in the optical band gap measurement by linear curve fitting is ± 0.01 eV. The increase in the optical band gap of films by annealing may be due to the removal of defects in the films. This slight decrease in band gap is attributed to the increase in grain size (Fig. 4.53; Table 4.17) and hence decreased disorder. The estimated direct band gap values for annealed films are slightly greater than those reported by Rao et al. [12]. The 164 nm-thick-cobalt ferrite film deposited at 80 W in our report [20] also exhibited direct band gap of 2.16 eV.

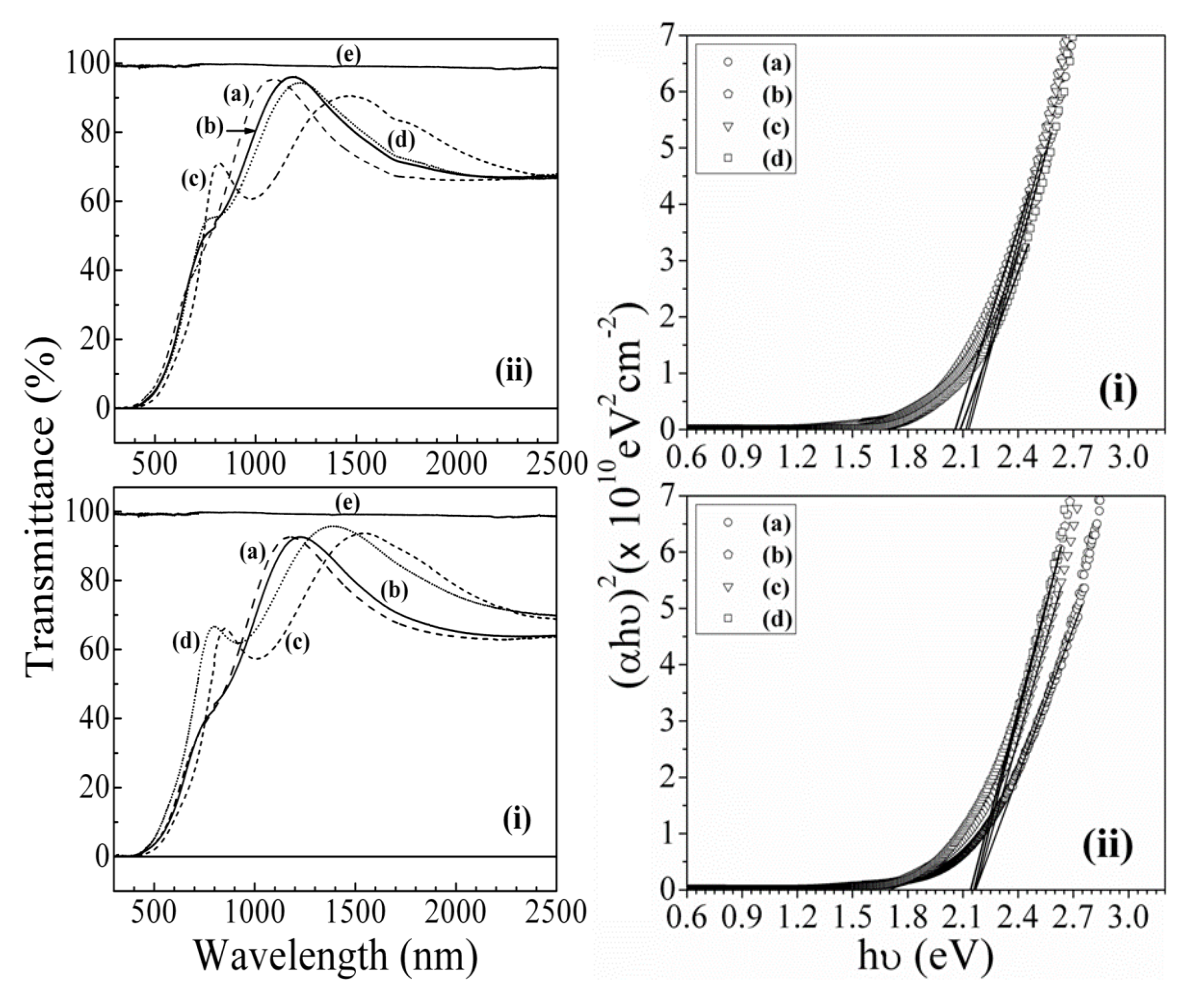


Fig. 4.59 Optical transmittance spectra measured at RT of as-deposited (i), annealed (ii), $Co_{0.75}Cu_{0.25}Fe_2O_4$ thin films grown at (a) 5, (b) 6, (c) 8 and (d) 10 mTorr of Ar gas pressure and (e) quartz substrate.

Fig. 4.60 (**right**) Plots of $(\alpha h v)^2$ versus (hv) for as-deposited (i), annealed (ii), $Co_{0.75}Cu_{0.25}Fe_2O_4$ thin films grown at (a) 5, (b) 6, (c) 8 and (d) 10 mTorr of Ar gas pressure.

Table 4.17 Optical properties thin films of $Co_{0.75}Cu_{0.25}Fe_2O_4$ grown at different argon pressure using 40 W RF power.

Sample (argon	Film thicknes (± 4 nm)	S	Band gap, E_g (±0.01eV)			
pressure)	As-grown	As-grown Annealed		Annealed		
	Profiler	FESEM				
5 mTorr	410	407	2.13	2.15		
6	392	364	2.06	2.16		
8	466	462	2.12	2.18		
10	381	370	2.09	1.14		

4.4.4.7 Conclusions

Saturation magnetization (M_s) first increases with increase in argon pressure from 5 to 6 mTorr due to increase in grain size followed by a decrease with further increase in argon pressure up to 10 mTorr. The 392-nm-thick $Co_{0.75}Cu_{0.25}Fe_2O_4$ film deposited at 6 mTorr exhibited high coercivity (H_c) of 3448 Oe. The observed changes could be due to change in the cation distribution over A and B sites of the ferrite lattice and change in grain size on annealing the films. The optical energy band gap (E_g) of annealed films increased with argon gas pressure from 5 to 8 mTorr followed by a decrease with increase argon pressure upto 10 mTorr. The increase in band gap is due to decrease in grain size. The decrease in band gap is due to increase in grain size as observed from FESEM.

References

- [1] Patterson, A. L., Phys. Rev. 56, 978 (1939).
- [2] B.D. Cullity, Second Edition Addison Wesley Publishing 42-46 (89), 92 (1978).
- [3] G. Mustafa, M. U. Islam, W. Zhang, Y. Jamil, A. W. Anwar, M. Hussain, M. Ahmad, J. Alloys Comp 618, 428 (2015).
- [4] B. D. Cullity, Elements of X-Ray Diffraction. (2nd edtn), Reading, MA: Addison Wesley. (1978).
- [5] Lee, J.-G., Chae, K. P., Sur, J.C., J. Magn. Magn. Mater. 267, 161 (2003).
- [6] Wang, Y. c., Ding, J., Yi, J. B., Liu, B. H., Yu, T., Shen, Z. X., Appl. Phys. Lett.84, 2596 (2004).
- [7] Sunds, R.H., Phys. Rev.99, 1222 (1955).
- [8] Davis, E.A., Mott, N.F., Philosophical Magazine 22, 903 (1970).
- [9] Tauc, J., Grigorovici, R., Vancu, A., Phys. Status Solidi15, 627 (1966).
- [10] Tauc (Ed.), J., : Amorphous and Liquid Semiconductors, Plenum, New York (1974).
- [11] Erdem, D., Bingham, N. S., Heiligtag, F. J., Pilet, N., Warnicke, P. Heyderman, L. J., Niederberger, M., *Adv. Func. Mater.* **26**, 1954(2016).
- [12] PratibhaRao, Godbole, R.V., Phase, D.M., Chikate, R.C., SunitaBhagwat, *Materials Chemistry and Physics***149-150**, 333 (2015).
- [13] Ravindra, A. V., Padhan, P., Prellier, W., Appl. Phys. Lett. 101, 161902 (2012).
- [14] Holinsworth, B. S., Mazumdar, D., Sims, H., Sun, Q.-C., Yurtisigi, M. K., Sarker, S. K., Gupta, A., Butler, W. H., Musfeldt, J. L., Appl. Phys. Lett. 103, 082406 (2013).
- [15] Imry, Y., Ma, S.-K., Phys. Rev. Lett. 35, 1399–1401 (1975).
- [16] E. Marquez, J. R. Malo, P. Villares, R. J. Garay, P. J. S. Ewen, and A. E. Owen, J. Phys. D25, 535 (1992).
- [17] E.R. Shaaban, Mater. Chem. Phys. 100, 411 (2006).
- [18] Revathi, P. Prathap, K.T. Ramakrishna Reddy, Solid State Sci. 11, 1288 (2009).
- [19] Sabah A. Salman, Asaad A. Kamil, Sahar J. Abed, J. Chem. Bio. Phy. Sci. Sec. C, 6(1); 124-134 (2016).
- [20] Babu, K.R. and Singh, R. J Supercond Nov Magn 31, 4029(2018).
- [21] L. Horng, G. Chern, M.C. Chen, P.C. Kang, D.S. Lee, J. Magn. Magn. Mater. 207, 389 (2004).
- [22] Swanepoel, R., J. Phys. E: Sci. Instrum. 16, 1214 (1983).
- [23] Swanepoel, R., J. Phys. E: Sci. Instrum. 17, 896 (1984).
- [24] Sultan, M. and Singh, R., Journal of Applied Physics, 105, 07A512 (2009)
- [25] Zhang, Y., Du, G., Liu, D., Wang, X., Ma, Y., Wang, J., Yin, J., Yang, X., Hou, X., Yang, S., *J. Cryst. Growth* **243**, 439 (2002).
- [26] S.D. Sartale, V. Ganesan, C.D. Lokhande, Phys. Stat. Sol (a) 202 (2005) 85.
- [27] L. Horng, G. Chern, M.C. Chen, P.C. Kang, D.S. Lee, J. Magn. Magn. Mater. 207 (2004) 389.

Chapter 5

Summary and Conclusions

The thesis contains synthesis and properties of nanoparticles, bulk and thin film of Cobalt ferrite and copper doped cobalt ferrite. The synthesized samples were heat treated at various temperatures to understand its effect on structure and properties of materials. The structural analysis of the synthesized samples was carried out by x-ray diffraction (XRD), FE-Scanning Electron Microscopy (FESEM) and Transmission Electron Microscopy (TEM). The magnetization and dielectric measurements on the samples heat treated at various temperatures were carried out to optimize these properties of the materials. The optical studies on the Cu doped and undoped cobalt ferrite thin films were carried out to estimate the optical band gap of the materials synthesized under various deposition conditions and subjected to various heat treatment temperatures. These extensive systematic studies have shown that very different values of physical parameters (like magnetization, dielectric constant, optical band gap) can be obtained for the nanoparticles, bulk and thin films of cobalt ferrite samples under different processing conditions of these materials.

Studies on nanoparticles and bulk samples:

Cobalt ferrite (CoFe₂O₄) and copper doped cobalt ferrite Co_{1-x}Cu_xFe₂O₄ (x=0.0, 0.2, 0.25 and 0.4) nanoparticles were prepared by co-precipitation method. Rietveld refined XRD patterns show single phase spinel structure with Fd-3m space group. As-synthesized nanoparticle size is in the range of 10-14 nm. After annealing particle size increases to 18-22 nm. As-prepared nanoparticles show saturation magnetization (M_s) values between 134-85 emu·g⁻¹ and coercivity (H_c) between 636-58 emu·g⁻¹. Nanoparticles of CoFe₂O₄ heated at 600 °C exhibit very high M_s value of 137 emu/g and H_c value of 582 G. The copper doped nanoparticles with composition x=0.2, 0.25 and 0.4 annealed at 600 °C exhibit M_s value of 119, 114 and 98 emu·g⁻¹, and H_c value of 1217, 1102 and 1081 G repectively. The as-prepared nanoparticles of cobalt ferrite and copper doped cobalt ferrite were pressed into pellets and heat treated at 100, 600 and 1200 °C for 4 hours. The M_s value increases significantly with increasing annealing temperature. The M_s values of CoFe₂O₄ heated at 100, 600 and 1200 °C are 134, 55 and 175 emu·g⁻¹, respectively. The M_s value of CoFe₂O₄ pellet heated at 600 °C for 3 h is 140 emu·g⁻¹.

The copper doped samples $\text{Co}_{1-x}\text{Cu}_x\text{Fe}_2\text{O}_4$ with x = 0.2, 0.25 and 0.4 annealed at 600 °C for 4 h exhibit M_s values of 50, 48 and 44 emu·g⁻¹, and H_c value of 891, 717 and 1010 G, respectively. While samples annealed at 600 °C for 3 h exhibited M_s values of 122, 120 and 107 emu·g⁻¹ with coercivity of 858, 970 and 939 G, respectively. The M_s values of samples annealed at 1200 °C for 4 h are 122, 120 and 107 emu·g⁻¹, with low coercivity of 76, 83 and 50 G respectively. The dielectric constant value is in the range 84.943 × 10³ to 14 when frequency of applied electric field increases from 100 Hz to 40 MHz. The dielectric constant and loss tangent show a decreasing trend with increasing frequency.

The copper-cobalt ferrite $\text{Co}_{1-x}\text{Cu}_x\text{Fe}_2\text{O}_4$ nanoparticles with x=0.0, 0.2, 0.25, 0.4, 0.9 and 1.0 prepared by co-precipitation (using high concentration solutions of nitrates of Fe³⁺, Co²⁺ and Cu²⁺) were pressed into pellets and heat treated at 100, 600 and 1200 °C for 4 hours with 3°C/min heating and cooling rates. Rietveld refined X-ray diffraction pattern reveals that the compositions with x=0.0 to 0.4 show single phased cubic spinel structure with Fd-3m space group and the compositions with x=0.9 to 1.0 show tetragonal spinel-(Cu,Fe) structure with I41/amd space group. The samples with x=0.9 and 1.0 had trace amounts of CuO, and Fe₂O₃ in as-synthesized nanoparticles dried at 90 °C and pellets heated at 100 and 600 °C. While samples heated at 1200°C indicate small amount of delafossite (Cu₁Fe₁O₂) phase. CoFe₂O₄ sample heated at 100, 600 and 1200 °C show M_s value of 48, 56 and 67 emu/g, and H_c values 1067, 880 and 277 G respectively.

As-prepared CuFe₂O₄ nanoparticles of 6 nm thickness heated at 90 °C and CuFe₂O₄ pellet heated at 100 °C exhibit superparamagnetism with M_s of 14 emu/g. Co_{0.1}Cu_{0.9}Fe₂O₄ annealed at 1200 °C also exhibit superparamagnetism with M_s of 37 emu/g, while CuFe₂O₄ annealed at 1200 °C exhibit M_s of 35 emu/g and low coercivity of 37 G. CuFe₂O₄ heated at 100 °C exhibits dielectric constant value of 10 and 9 at 10 MHz and 40 MHz with low loss tangent values of 0.078 and 006, respectively. CuFe₂O₄ heated at 1200 °C exhibits high dielectric constant of 1015 at 40 MHz with low loss tangent value (0.112). Low dielectric constant materials can be used for insulating materials application and high dielectric constant materials could be used as a medium in capacitors.

The properties of synthesized samples also depend on the starting materials for synthesis. Cobalt ferrite (CoFe₂O₄) nanoparticles of size 17 nm synthesized by co-precipitation method using

anhydrous FeCl₃ and CoCl₂·6H₂O as precursors and NaOH was compacted into pellets using mechanical press with 3 ton pressure and heated at 100, 400, 600 and 1200°C for 4 hours. Asprepared nanoparticles dried at 90 °C show H_c of 2.875 kG and M_s =39 emu/g. Cobalt ferrite heated at 100 and 1200°C show H_c of 3046 and 118 G and M_s of 39 and 71 emu/g, respectively. All the samples show a large increase in coercivity and a slight decrease in M_s value at 100 K. The CoFe₂O₄ sample heated at 600 °C exhibit high coercivity of 11.4 kG at 100 K. Dielectric constant of CoFe₂O₄ annealed at 1200 °C is 19 between 1 to 40 MHz with low loss tangent values (0.021-0.028). This sample can be used as an insulating material in high–frequency electrical circuits to reduce power losses and skin effect.

Studies on thin films:

Cobalt ferrite (CoFe₂O₄) thin films were deposited on glass substrates under different sputtering conditions i.e. RF power variation, deposition time (film thickness) and argon gas pressure. Asdeposited films were amorphous and were post-annealed at 500° C for 3 h. Cobalt ferrite target show an M_s of 272 emu/cm³ with low H_c of 162 G.

The thin films of CoFe₂O₄ deposited on glass substrates by (RF) sputtering using various RF power 60, 80, 100 and 120 W were post annealed at 500 °C. Film thickness of annealed films are 119, 164, 237 and 300 nm. The magnetic parameters of the film, i.e., in-plane coercivity (H_c), saturation magnetization (M_s), and remanence (M_r) increase as RF power is increased from 60 to 80 W followed by a decreasing trend with further increase in RF power to 120 W. Annealing of the film significantly improves the magnetic properties. The largest grain size and the best crystallinity of the film is obtained for the film deposited at 80 W of RF power. The M_s values of annealed films are 246, 274, 164 and 136 emu/cm³. The thin films exhibited 60–85% optical transmittance. For the as-deposited films optical band gap decreases with increasing RF power between 60 and 120 W as 2.16, 2.14, 2.11, 2.08 eV. The increase in the optical band gap of CoFe₂O₄ thin films by annealing may be due to the removal of defects from the films. For annealed films the band gap values are 2.3, 2.16, 2.2 and 2.25 eV, respectively. The study shows that RF power used for depositing the film has strong effect on the microstructure and properties of the film. The 164 nm (CFF-80) thick cobalt ferrite film has H_c of 442 Oe and M_s of 274 emu/cc which is equal to values for bulk CoFe₂O₄ target.

Thin films of CoFe₂O₄ were deposited using 100 W RF power at 10 mTorr of argon gas pressure for various deposition duration to study the effect of film thickness on magnetic and optical properties. The (M_S) of CoFe₂O₄ films annealed at 500 °C deposited for 1, 1.5 and 2 h are 164, 53 and 64 emu/cm³, respectively. The M_S of annealed film decreases by 63% when film thickness increases from 236 to 482 nm. The annealed films deposited for 1.5 h and 2 h show superparamagnetism with zero coercivity and remanence. Decrease in M_S is due to decrease in particle size as observed by TEM and cation distribution. Thickness of annealed films deposited for 1, 1.5 and 2 h are 237, 353 and 472 nm and these values match with the thickness estimated from transmission measurements. Optical band gap of annealed films decreases with increasing film thickness due to the increase in grain size.

CoFe₂O₄ thin films were deposited on glass substrates using 110 W RF power at various Ar gas pressure of 8, 10 and 12 mTorr for 2 h. The M_s values of as-grown films deposited at 8, 10 and 12 mTorr are 78, 45 and 39 emu/cm³, respectively. The M_s values of annealed films are 139, 78, 72 emu/cm³. Decrease in M_s with increase in argon pressure is due to decrease in particle size. Thickness of annealed films are 410, 650 and 809 nm. The optical band gap for films annealed at 500 °C are 1.98, 2.10 and 2.16 eV with increasing argon gas pressure. The increase in band gap is due to decrease in particle size. The study shows that (FC curve) for the 410-nm-thick annealed cobalt ferrite film deposited at 8 mTorr can be used for temperature sensor applications in the temperature range of 5-350 K.

The $Co_{0.75}Cu_{0.25}Fe_2O_4$ target show low H_c of 57 G and M_s of 293 emu/cm³. Thin films of $Co_{0.75}Cu_{0.25}Fe_2O_4$ were deposited on quartz substrates using 40 W RF power at 12 mTorr of argon gas pressure. As-deposited films were amorphous having low M_s of 79 emu/cm³. The films were heat treated at 600, 800 and 1000 °C. The M_s value increases with increasing annealing temperature due to increase in grain size. The film annealed at 600 °C, show M_s of 227 emu/cm³. A slight decrease in M_s after annealing at 800 °C is because the film is made up of loosely connected small particles as observed by TEM. The 311-nm-thick film annealed at 1000 °C exhibits high M_s of 250 emu/cm³ (and coercivity of 1.5 kG). With post annealing at 800 °C, films exhibit a high coercivity of 2670 G. The optical band gap decreases from 2.37 to 2.29 eV with increasing annealing temperature from 600 °C to 800 °C. This further decreases to 2.04 eV for film annealed at 1000 °C. The decrease in optical band gap is due to increase in grain size.

Thin films of $Co_{0.75}Cu_{0.25}Fe_2O_4$ were deposited on quartz substrates using various RF power at 6 mTorr argon gas pressure. As-deposited films were annealed at 800 °C. The M_s values of as-deposited films are 71, 115, 176 and 205 emu/cm³, respectively, for films deposited using 30, 40, 50 and 60 W. The annealed film exhibit M_s value of 129, 174, 243 and 300 emu/cm³. The H_c of as-deposited and annealed films are 2753, 3450, 2993 and 2696 Oe, and 2001, 3450, 3866 and 1934 Oe, respectively. The optical band gaps and thickness of the films deposited using 30, 40 and 50 W are 2.07, 2.06 and 1.9 eV and 232, 364, 412 and 430 nm respectively. The optical band gap of annealed films are 2.14, 2.16, 2.10 and 1.93 eV. The decrease in band gap on annealing the films is because of increase in grain size.

The Co_{0.75}Cu_{0.25}Fe₂O₄ films deposited on quartz substrates using 40 W RF power under different argon gas pressure of 5, 6, 8 and 10 mTorr, show M_s value of 140, 115, 86 and 52 emu/cm³ and H_c of 3716, 3445, 549 and 137 Oe, respectively. The M_s and H_c values of annealed films are 137, 174, 135, 120 emu/cm³ and 2966, 3448, 2658, and 2540 Oe, respectively. Thickness of annealed films deposited at 5, 6, 8 and 10 mTorr are 407, 364, 462 and 370 nm. These films can be used in data storage device applications.

Important results and Conclusions:

The detailed studies summarized above provide the clue to obtain materials with desired properties. $CoFe_2O_4$ nanoparticles of size 18 nm heated at 600 °C for 3 hours gives high magnetization (M_s) of 137 emu/g and coercivity (H_c) of 582 G. $CoFe_2O_4$ pellets heated at 1200 °C for 4 h show very high M_s of 175 emu/g. The nanoparticles of $Co_{0.8}Cu_{0.2}Fe_2O_4$ annealed at 600 °C exhibit high H_c value of 1217 G and M_s value of 119 emu/g.

CuFe₂O₄ pellets heated at 1200 °C exhibit high dielectric constant of 1015 at 40 MHz with low loss tangent of 0.112. This can be used as a filling material in capacitors.

As-prepared CoFe₂O₄ nanoparticles of size 17 nm show high H_c value of 2875 G at RT which can be used in data storage applications. At 100 K, cobalt ferrite pellet heated at 600 °C show very high H_c = 11.4 kG. CoFe₂O₄ pellet annealed at 1200 °C has dielectric constant of 19 in frequency range of 1MHz to 40 MHz and very low tangent loss (0.021-0.028). This material can be used as insulating material for practical applications in high–frequency electrical circuits.

The 164 nm (CFF-80) thick cobalt ferrite film exhibit M_s value of 274 emu/cc which is equal to the M_s of bulk CoFe₂O₄ target.

Thin films of $Co_{0.75}Cu_{0.25}Fe_2O_4$ show high saturation magnetization (M_s) of 250 emu/cm³ when annealed at 1000 °C with H_c of 1500 G. The H_c value of (2670 G) is obtained when annealing of the film is done at 800 °C.

The M_s value for Co_{0.75}Cu_{0.25}Fe₂O₄ thin film increases with increase in RF power (i.e. with increase in film thickness) from 30 to 60 W. The annealed film deposited at 50 W exhibit high H_c value of 3866 Oe and M_s of 243 emu/cm³. The films grown at 40 W show H_c of 3449 Oe and M_s of 174 emu/cm³. These films can be for data storage applications.

The thin films of doped and undoped cobalt ferrite have 60-85% optical transmittance with optical band gap values between 1.90-2.37 eV. The highest band gap value of 2.37 eV is obtained for Co_{0.75}Cu_{0.25}Fe₂O₄ film deposited on quartz substrate using 40 W RF power at 12 mTorr argon gas pressure and annealed post-deposition at 600°C for 3 h.

List of Publications:

1) Publication:

Kancharla RaviBabu, R. Singh, "Effect of RF Power on Structural, Magnetic, and Optical Properties of CoFe2O4 Thin Films", Journal of Superconductivity and Novel Magnetism (2018) 31:4029–4037

Manuscripts communicated and under preparation:

- 1. Structural and magnetic properties of Co_{1-x}Cu_xFe₂O₄ (x=0.0, 0.2, 0.25, 0.4) nanoparticles (communicated).
- 2. Effect of annealing temperature on magnetic and dielectric properties of cobalt ferrite synthesized by co-precipitation method (to be communicated).
- 3. Magnetic and dielectric properties cobalt-copper ferrites Co_{1-x}Cu_xFe₂O₄ (x=0.0, 0.2, 0.25, 0.4, 0.9 and 1.0) sintered at various temperature (to be communicated).
- 4. Effect of argon gas pressure on structural, magnetic and optical properties of cobalt ferrite thin films (to be communicated).
- 5. Effect of RF power and argon gas pressure on structure, magnetic and optical properties of Co_{0.75}Cu_{0.25}Fe₂O₄ thin films (to be communicated).

Conferences attended:

- 1) "Morphology of Co-ferrite synthesized by co-precipitation method" at EMSI-2014 during July 9-11, 2014 at University of Delhi, Delhi. (Poster presentation)
- 2) "Structure and magnetic properties of cobalt ferrite thin films synthesized by RF magnetron sputtering" at ICMAGMA-2015 during December 2-4, 2015. (Poster presentation)
- 3) "Effect of RF Power on Structural, Magnetic, and Optical Properties of CoFe₂O₄ Thin Films" at ICMAGMA-2017during February1-3, 2017 at Hyderabad, India (Poster presentation)
- 4) Kancharla RaviBabu and R. Singh, "Effect of cation distribution on structure and magnetic properties of sintered cobalt ferrite" presented at FIP-2014, organized by School of Physics, University of Hyderabad, Hyderabad during 17-18 October 2014. (Poster presentation)

5) Attended National Conference on Physics at Small Scales and Advanced Materials during 8-9 September 2017 organized by School of Physics, University of Hyderabad, Hyderabad.

Workshops:

- 1) Attended Electron Microscopy workshop (EMSI-2014) on 7th July 2014 at University of Chicago's Center in Delhi, Connaught Place, New Delhi.
- 2) Attended "Bringing the Nanoworld Together 2017 (BTNT-2017)" during December 5-6, 2017 held at University of Hyderabad, Hyderabad, in collaboration with Oxford Instruments, U.K
- 3) Attended Workshop on Processing and Characterization of Thin Films held during January 3 9, 2018 at UGC Networking Resource Centre, School of Physics, University of Hyderabad, Hyderabad.
- 4) Attended Workshop on Functional Magnetic Materials held during 26th February –3rd March, 2018 at UGC Networking Resource Centre, School of Physics, University of Hyderabad, Hyderabad.